



Plasmonic Nanorods and Nanoparticle-Assemblies

Synthesis, Characterization, and Usage as Sensors

Inga Zins

Mainz, 2011

Dissertation

zur Erlangung des Grades

“Doktor der Naturwissenschaften”

im Promotionsfach Chemie

am Fachbereich Chemie, Pharmazie und Geowissenschaften

der Johannes Gutenberg-Universität Mainz

Die vorliegende Arbeit wurde im Zeitraum von September 2007 bis Februar 2011 am Institut für Physikalische Chemie der Johannes Gutenberg-Universität Mainz angefertigt.

Dekan:

Erster Gutachter:

Zweiter Gutachter:

Tag der mündlichen Prüfung: 16.03.2011

Abstract

Plasmonic nanoparticles are subject to this study. They have the property that their interaction with light results in a plasma-oscillation, visible in bright colors of the nanoparticle suspensions. The color of the particles depends on intrinsic (material, size, shape), as well as on external features (refractive index of the surrounding, distance of neighbouring nanoparticles). They are therefore used as plasmonic sensors, reporting on changes in their environment. The demand for sensing applications is not only a good sensitivity. The ability to reproducibly synthesize plasmonic nanoparticles with designed features is important as well. Here, the growth of gold and silver-coated nanorods is studied, and the use of nanoparticles as orientation, refractive index, and distance sensor is explored.

A model for the growth of gold nanorods is developed. It turns out that there are several factors, which need to be fulfilled to do a successful synthesis. Besides the presence of surfactant to stabilize the growing particles, also bromide and silver are crucial, as well as a small electrochemical potential difference between reducing and oxidizing reaction partners to allow for slow selective anisotropic growth. Those gold nanorods are used to monitor the collapse of a gel matrix by recording polarization-dependent time traces of their scattering intensity.

A chemical modification of the gold nanorods by a silver-shell increases the sample quality with respect to the ensemble linewidth. The plasmonic focusing effect, a change in the slope of the plasmon-shape-relation, is discovered. The easy optical monitoring allows to study the kinetics of this reaction. Knowing reaction order and activation energy, the progress in the reaction is forecast and the quenching time for a desired resonance wavelength is predicted.

Besides the application of single nanoparticles, also assemblies of them are probed. The controlled arrangement of two particles of the same size is used to determine the interparticle distance by different methods of calibration, including light-scattering and TEM-techniques. The polarization of the scattered light along or perpendicular to the interparticle axis is used to measure both, refractive index and interparticle distance, at once. Furthermore, the dimers are a tool to characterize the behaviour of a thermoresponsive elastin-like linker-molecule upon changes in the temperature and concentration. Core-satellite structures, consisting of a big core particle surrounded by several smaller ones are used as refractive index sensor. It turns out that they are better suited for refractive index sensing applications than pure spherical particles of the same size, since their sensitivity is much higher.

Contents

| | |
|---|-----------|
| 1. Introduction | 1 |
| 2. Theory | 9 |
| 2.1. Spectra of Plasmonic Nanoparticles | 9 |
| 2.2. Localized Surface Plasmons | 11 |
| 2.3. Rods | 18 |
| 2.4. Coated Nanoparticles | 19 |
| 2.5. Dimers | 19 |
| 2.5.1. Sensing with dimers | 24 |
| 3. Why anisotropic? A Growth-Model for Gold Nanorods | 29 |
| 3.1. Motivation | 29 |
| 3.2. The Growth Model | 31 |
| 3.2.1. Anisotropic Growth | 34 |
| 3.2.2. High yield | 35 |
| 3.2.3. Trends | 37 |
| 3.3. Summary and Outlook | 47 |
| 4. Silver-Coating of Gold Nanorods | 51 |
| 4.1. Plasmonic Focusing Effect | 51 |
| 4.2. Kinetics | 59 |
| 5. Rotating Rods - Novel Probes for Local Viscosity | 69 |
| 5.1. Motivation | 69 |
| 5.2. Gold Nanorods in PNIPAM - Introducing the System | 71 |
| 5.3. Results | 73 |
| 5.4. Summary and Outlook | 74 |
| 6. Nanoparticle Assemblies | 77 |
| 6.1. Dimers | 77 |
| 6.1.1. Calibrating the Plasmon Ruler | 83 |
| 6.1.2. Distance and Refractive Index Sensor | 85 |
| 6.1.3. Characterization of Elastin-Like Polypeptides | 91 |

Contents

| | |
|---|------------|
| 6.2. Core-Satellite Structures | 96 |
| 6.2.1. Sensing Refractive Index Changes | 98 |
| 6.2.2. Synthesis and Separation | 99 |
| 6.2.3. Summary and Outlook | 101 |
| 7. Summary and Outlook | 103 |
| | |
| Appendix | 105 |
| | |
| A. Analytical Methods | 107 |
| A.1. Ensemble-Spectra | 107 |
| A.2. Single-Particle-Spectra | 108 |
| A.3. Dark-Field-Microscopy | 110 |
| A.4. Electron-Microscopy | 111 |
| A.5. Gel-Electrophoresis | 112 |
| A.6. Dynamic Light Scattering | 113 |
| | |
| B. Darkfield Setups | 115 |
| B.1. FastSPS Setup | 115 |
| B.2. Rotation Setup | 115 |
| B.3. Polarization Contrast Setup | 116 |
| | |
| C. Experimental Methods | 117 |
| C.1. General Synthesis of Gold Nanorods | 117 |
| C.1.1. Overview Over the Carried out Syntheses | 118 |
| C.1.2. Spectra of the Carried out Syntheses | 127 |
| C.1.3. TEM-data of the Carried out Syntheses | 134 |
| C.1.4. Electrochemical Potential of the Growth Solution | 142 |
| C.2. Silver-Coating | 147 |
| C.3. Gold Nanorods in Gels | 156 |
| C.3.1. PNIPAM-Gels | 156 |
| C.3.2. Rotational Data Acquisition and Analysis | 158 |
| C.4. Biological Coatings (Bio-functionalization) | 165 |
| C.4.1. Biotin-PEG | 165 |
| C.4.2. Streptavidin | 165 |
| C.4.3. ELP | 166 |
| C.4.4. Biotin-ELP | 168 |
| C.5. Dimers | 174 |
| C.5.1. Synthesis in Batch | 174 |

| | |
|---|------------|
| C.5.2. Synthesis in the Flow-Cell | 174 |
| C.5.3. Sensing with Dimers | 176 |
| C.5.4. TEM | 180 |
| C.5.5. DLS of monomers | 184 |
| C.6. Core-Satellite Assemblies | 185 |
| References | 191 |
| Acknowledgement | 203 |
| Curriculum Vitae | 205 |
| Publications | 207 |

List of Figures

| | |
|--|----|
| 1.1. Church Window in Notre-Dame-de-Paris | 2 |
| 2.1. Typical Ensemble Spectra | 10 |
| 2.2. Plasmons | 11 |
| 2.3. Real and Imaginary Part of the Dielectric Function of Gold | 13 |
| 2.4. Conditions for QSA | 14 |
| 2.5. Prolate and Oblate Shape | 18 |
| 2.6. Parameters to Describe a Nanoparticle Dimer | 20 |
| 2.7. Energy and Orientation Factor in the Exciton-Coupling Model | 22 |
| 2.8. Orientation of Dipoles in an Electric Field | 23 |
| 2.9. Spring Model | 24 |
| 2.10. Sensitivity of Dimers | 25 |
| 2.11. Dimer in Water (BEM) | 26 |
| 2.12. Resonance of Short and Long Axis over Refractive Index | 27 |
| 3.1. Pictures of the Gold Nanorod Synthesis | 32 |
| 3.2. Model for Gold-Rod Growth | 33 |
| 3.3. Anisotropic Growth | 36 |
| 3.4. High Yield | 38 |
| 3.5. Overview Over Trends | 39 |
| 3.6. Variations of Seeds | 40 |
| 3.7. Variation of Silver nitrate | 41 |
| 3.8. Concentration of Bromide for different CTAB-concentrations | 43 |
| 3.9. Resonance Wavelength over Concentration of Bromide in Solution | 43 |
| 3.10. Resonance Wavelength over Halides in Solution | 45 |
| 3.11. Resonance Wavelength over Electrochemical Potential of the Growth Solution | 46 |
| 3.13. Effective Electrochemical Potential Difference | 46 |
| 3.12. Variation of Nitrate | 47 |
| 4.1. Ensemble Linewidth | 52 |
| 4.2. Typical Silver Coating | 54 |
| 4.3. Single Particle Silver Coating | 55 |
| 4.4. Translation of Size-Distribution into Resonance Position-Distribution | 57 |

List of Figures

| | |
|--|-----|
| 4.5. Theoretical Modeling of the Measured Spectra | 58 |
| 4.6. General Features Ag-Coating | 60 |
| 4.7. Different Rod Concentrations | 62 |
| 4.8. Initial Constants for Different Goldrod Concentrations | 63 |
| 4.9. Different Ag-Concentrations | 64 |
| 4.10. Rate Constants for Different Silver Concentrations | 64 |
| 4.11. Ag-coating at Different Temperatures | 65 |
| 4.12. Decay Constant and Arrhenius Plot | 66 |
| 4.13. Activation Energy | 67 |
| 4.14. Quench the Coating Reaction | 68 |
| | |
| 5.1. PNIPAM | 71 |
| 5.2. Gold Nanospheres and -rods in PNIPAM | 72 |
| 5.3. Gold Nanorods in Microscopic PNIPAM | 72 |
| 5.4. Tau and Diffusion Coefficient for Different Temperatures | 73 |
| | |
| 6.1. Streptavidin and Biotin | 80 |
| 6.2. Biotin-PEG | 81 |
| 6.3. Structure of Elastin | 82 |
| 6.4. Flow Cell Setup | 83 |
| 6.5. Calibration Plasmon Ruler | 84 |
| 6.6. Shift of Long and Short Axis in Methanol | 87 |
| 6.7. Distances in Water and Methanol | 87 |
| 6.8. Shift of Long and Short Axis and Monomers in Glycerol | 88 |
| 6.9. Sensitivity and Resonance of Short and Long Axis | 89 |
| 6.10. Resonance Wavelength over Distance in Water and Glycerol | 90 |
| 6.11. Distances in Water and Glycerol | 90 |
| 6.12. ELP-Dimers at Different Temperatures | 92 |
| 6.13. Shift and Distance for Different ELPs | 93 |
| 6.14. Distance between Dimers over D_h and M_w | 94 |
| 6.15. Resonance Shift and Distance for Different % of ELP | 95 |
| 6.16. Comparing % ELP/Distance with Concentration/Transition Temperature | 96 |
| 6.17. Flowers | 97 |
| 6.18. Single Particle Resonance Positions of Spheres and Flowers | 98 |
| | |
| A.1. Typical Ensemble Spectra | 108 |
| A.2. Typical Single Particle Spectra | 109 |
| A.3. Dark-field Illumination | 110 |
| A.4. Transmission Electron Microscope | 111 |
| | |
| B.1. FastSPS-Setup | 115 |

| | |
|---|-----|
| B.2. Polarization Contrast Setup | 116 |
| C.1. $I_{\text{long}}/I_{\text{short}}$ Calculated by QSA | 133 |
| C.2. Seeds and Silver Variations | 134 |
| C.3. Distribution of Au^{3+} Complexes | 143 |
| C.4. Distribution of Au^+ Complexes | 143 |
| C.5. Fractional Charge | 144 |
| C.6. Halogenides in Solution | 146 |
| C.7. Extinction Spectra Au@Ag-Nanorods | 148 |
| C.8. Extinction Spectra Au@Ag-Nanorods | 149 |
| C.9. Quality Factor Au@Ag Nanorods | 150 |
| C.10. Polarization Anisotropy Au@Ag Nanorods | 150 |
| C.11. Modeled Ensemble Spectra Au@Ag Nanorods | 151 |
| C.12. Linewidth Narrowing for Au@Ag Nanorods | 152 |
| C.13. Different Ascorbic Acid Concentrations | 154 |
| C.14. Vary Silver and Ascorbic Acid | 155 |
| C.15. Adding HCl after the Coating Reaction | 155 |
| C.16. Heating Gold Nanorods and -spheres in PNIPAM | 157 |
| C.17. Spectra NIPAM and PNIPAM | 157 |
| C.18. Spectra Gold Nanorods and -spheres in PNIPAM | 158 |
| C.19. Snapshots of Rotating Rods in PNIPAM | 159 |
| C.20. Typical Time Trace of a Rotating Gold Nanorod | 160 |
| C.21. Reduced Linear Dichroism and Autocorrelation | 161 |
| C.22. Heating of ELP-Functionalized Gold Nanorods | 166 |
| C.23. Different ELPs Bind to Particles in a Flow-Cell | 167 |
| C.24. Streptavidin Binds Biotinylated ELP | 169 |
| C.25. PAGE gel of ELP, Bio-ELP, and Streptavidin | 170 |
| C.26. Spectra of ELP- and mPEG-Functionalized Spheres | 171 |
| C.27. Batch and Surface % ELP | 172 |
| C.28. Agarose Gel of ELP/mPEG Functionalized Particles | 173 |
| C.29. Typical Dimerization Experiment | 175 |
| C.30. Yield and Surface Coverage by Counting | 176 |
| C.31. Reversibility Methanol | 177 |
| C.32. Principle of Reversibility Measurement | 178 |
| C.33. Reversibility Sucrose, Glucose and Glycerol | 179 |
| C.34. Introducing the system | 180 |
| C.35. TEM-images of the 60nm Gold spheres | 181 |
| C.37. Evaluation of Cryo-TEM Images | 181 |
| C.36. Yield of Dimers by TEM | 182 |

List of Figures

| | |
|--|-----|
| C.38. Cryo-TEM images | 182 |
| C.39. Convert measured to real distance | 184 |
| C.40. Ensemble Spectra of Spheres and Flowers | 186 |
| C.41. TEM Images of Flower-Like Structures | 186 |
| C.42. Separation Gel | 187 |
| C.43. Number of Cores and Satellites after Gel-Electrophoresis | 188 |
| C.44. Number of Cores and Satellites for Different % Dithiol-PEG | 188 |

1. Introduction

“Nano” became one of the most popular words during the last decade, yielding over 70 million hits in a google search. Everything turns out to be better, faster, easier, smaller, and cheaper after it went “nano”. It seems that the “big questions” for society’s future - namely health, energy, mobility, and data processing - will all be answered with the help of nanoscience and nanotechnology. But is “nano” really a new and innovative concept? Or is it rather well-established and used already for billions of years by nature and it’s just us who are nowadays much more aware of how things work on that small length scale?

What exactly is “nano”? In general every object with one dimension in the range of some (tens) nanometers can be treated as a nanoobject or nanoparticle. Therefore, the word “nano” is not more or less than a prefix describing a size-regime, like micro or kilo do as well. Nano, originating from the Greek word *nannos* (dwarf), stands for the 10^{-9} part of a unit. In order to characterize now a certain magnitude of this unit, it is common to use prefixes before a SI-unit, e.g. nanometer means 0,000000001 m, nanogramm 0,000000001 g. A car for example weighs about 1 tonne or 1 *megagramm*. Parts of it, like tires or seats have a weight of several *kilogramms* and one light bulb in the headlight is about 50 gramms. The wire inside will have the weight of some *milli-* or *microgramms* and finally be covered by a thin coating, probably weighing only some ten *nanogramms*.

Nature is already able for billions of years to structure matter down to the nanoscale and to use effects occurring only there. Observing a lotus leaf or a fern frond in a rain shower, with water droplets running down and dragging dirt with them, the idea of a self cleaning surface is close at hand. They are hierarchically structured, combining micro- and nanostructures and keeping an air layer in between water and surface, which is responsible for the silver-shimmer these surfaces often exhibit when kept under water (Ensikar *et al.*, 2009). Also animals use nanoscopic “devices” to make their life easier. Geckos are an example of a very fruitful but on first glance surprising combination of characteristics concerning stickiness and cleanliness (Hansen & Autumn, 2005). They “stick” on the one hand (one toe can hold the whole body-weight) but are on the other hand able to run very fast (speed ≥ 3.6 km/h). Even optical properties of materials on the nanoscale are used by animals. While for a long time it was believed that starfish “see” via diffuse dermal receptors, a new study (Aizenberg *et al.*, 2001) showed that the whole body of some of them is covered with μm -sized lenses of calcit, which is nanoscopically crystallized in a fashion *not* showing birefringence.

1. Introduction

The step to use these principles in technological applications seems unavoidable but not at all easy and straightforward. After understanding the underlying principles of phenomena caused by nano-effects, a big amount of research needs to be done in order to artificially mimic nature's ideas. Besides applications where nano is just used as a synonym for "small" or "very small", there are already products on the market that have real nanoparticles in them and which take advantage from features only present in the nanostate: Sunscreens containing zinc- or titanium oxide nano particles (which act as UV-filters), T-shirts, socks, and wipes made anti-bacterial by silver nanoparticles, pregnancy tests that show blue or red stripes caused by the assembly of gold nanoparticles due to antigen-antibody interactions. Those products all use nanotechnology for their functionality. In contrast to organic or bio-chemistry, which deal with molecules that are smaller or in the same size-regime (e.g. the diameter of DNA is ~ 2 nm) as particles in nanotechnology, is the fact that nanoscience deals with properties resulting from architecture. The size itself of "hard" materials matters in nanoscience, whereas classical chemistry describes and alters "soft" characteristics. Though the boundaries between classical chemistry and nanoscience are fluid. An example for this are dendrimers. Hierarchically structured polymers, which branch and evolve different generations starting from a core. Growing them bigger and bigger, what matters for their functionality at some point is architecture and size over chemical composition. A change from chemical to nanoscience characteristics is observed (Tomalia *et al.*, 1990).

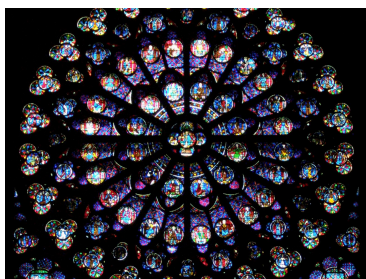


Figure 1.1.: Church Window in Notre-Dame-de-Paris

Metal nanoparticles embedded in glass show bright colors (geogebra, www.geogebra.org).

The first steps into nanotechnology and nanoengineering are done successfully. But not only new products use nanotechnology. With the deeper understanding and insight of the nanoscale, it became clear that already the Romans used metallic nanoparticles to produce colored glasses. During centuries, windows were built with "ruby glass" colored by gold nanoparticles inside the glass melt.

One special feature of nanoparticles is their enormous surface to volume ratio. Lets take a sugar-cube of edge-length 1 cm made of gold. It's mass is about 20 g and it contains the gigantic number of $59 \cdot 10^{21}$ atoms. But only 0.00015 % of them are on the surface. In contrast to this small amount of surface atoms, a gold-cube with an edge-length of 10 nm has 15% of its atoms (total number 59000) exposed to the surrounding. Since surface atoms have unsaturated bonds, they differ from those in the inside. Many nano particles are much more reactive than the same material in bulk, they show features which are not observed in other size regimes. Properties are not any longer exclusively connected to the material itself, but on the same time to structure and size.

Some examples for those size-depending properties are especially impressive. Already mentioned above, the color of gold depends on the size of it. Scaling it down to particles of some nanometers in size, no longer the shiny yellow color of bulk gold, but bright red, purple, and blue dispersions can be observed. But gold in its nano-state exhibits even more than only unique optical properties. The noble metal gold is known to last for eternity. Golden jewelery of ancient times is conserved and often looks, as if it was just manufactured. The inert properties of gold is the reason for this. Gold is known as one of the noble metals. On the other hand, gold nanoparticles are a well-known catalysts to perform the oxidation from carbon monoxide (CO) to carbon dioxide (CO₂) even at low temperatures (Sanchez *et al.*, 1999). The combustion of CO₂ is dependent on the size of the gold nanoparticles and found to start from a Au₈-cluster. Another very famous example of a property that mainly depends on size is the bright fluorescence colors of quantum-dots. Those small semiconductor spheres can have very different emission wavelengths, even when made out of the same material. In contrast to the bulk material, where electrons (and holes) are highly mobile, the small size of the particle confines motion in three dimensions, leading to a transition from continuous to discrete energy levels and therefore to specific colors of the emitted light. With increasing size, the color turns more into red, tunable only size, kind and degree of doping, and material composition, and nowadays, due to very defined synthetic routes, precisely adjustable (Murray *et al.*, 2000).

With all these effects and phenomena in mind, there is a huge demand to find and develop techniques in order to view what is happening on the nanoscale and to visualize processes and features that are far below the resolution of human eyes. The question of how to show things too small to be seen by eye is not new at all. The development of magnifying glasses and microscopes dates back to ancient times, but an even more challenging demand comes from nanoscience: Looking at objects smaller than the wavelength of light. Due to the physical diffraction limit, it is not possible to look at objects smaller than about 200 nm with simple optical imaging methods (Hecht, 2009). But it definitely is interesting to see objects or measure distances at much smaller length scales like 1 to 50 nm. Biochemical reactions happen on the nanoscale: DNA is transcribed, peptides are built, cells react to outer conditions, nerve cells transmit stimuli, tumors grow. All those actions either involve nanoscopic objects or are triggered by changes of nanometer size, nanomolar concentrations or nanonewton forces. In order to understand, manipulate, or mimic those reactions, a probe that is sensitive to those small changes is needed. At the same time, technological development is increasing in speed and power, but decreasing in size. This trend makes it necessary to build smaller and smaller objects, but on the same time characterize and test properties that rely on nanoobjects or nanometer thick films. Nanodefects might be the reason for a function or malfunction of a much bigger unit. Furthermore, local characteristics of samples at regions of square-nm or volumes of cubic- nm small evoke growing interest. But how to probe such small areas or volumes?

1. Introduction

There are different approaches for “nano-eyes”. Scanning techniques like atomic force microscopy (AFM) or scanning tunneling microscopy (STM) image samples due to forces acting between sample and a sharp probe-tip or current tunneling between them. They rely on an interaction between probe and sample and reconstruct the images, which contain information about topography, composition, charge, or chemical features of the samples. In electron microscopy (EM), one takes advantage of the fact that electrons have a much smaller wavelength than light and therefore smaller distances can be resolved (up to atomic resolution). There exist also optical techniques like super-resolution fluorescence microscopy, which rely on fluorescing samples and reconstruct an image from a stack of scans, having an effective resolution below the optical diffraction limit.

An encouraging far-field technique is plasmon scattering dark field microscopy and spectroscopy. With this technique, it is possible to image the light scattered by plasmonic particles and analyze it in a spectrometer. Therefore, an optical image that contains lateral information of the position with an accuracy of 400 nm down to 200 nm can be combined with spectral information, which contains information about size, shape and the surrounding of the particles.

Plasmonic nanoparticles show a distinct response to an incoming light wave, they scatter light of a certain color. This scattered light contains information about the particle itself (material, shape, size) as well as about the surrounding medium. Collection of the scattered light and dispersion via a prism or grating results in a signal, which represents the scattering intensity at different wavelengths. The scattering intensity of the plasmonic nanoparticles is the highest at its resonance frequency. This resonance frequency of the plasmon depends on intrinsic parameters (material, size, shape), as well as on external conditions (refractive index of the surrounding medium, existence and distance of neighboring nanoparticles). Gold and silver nanoparticles are therefore used as plasmonic sensors, reporting on changes in their environment.

In order to use (anisotropic) nanoobjects in any sensing or probing application, and to study the fundamental properties of them, it is crucial to have access to high quality plasmonic nanoparticles with low polydispersity and high yield. One of the best-known methods for the synthesis of gold nanoparticles was already published in 1951 (Turkevich *et al.*, 1951). Since then, the synthetic strategy for spherical gold nanoparticles was improved and revised (Kimling *et al.*, 2006), but in general the original route is still followed. Besides isotropic gold nanoparticles, anisotropic shapes (gold nanorods) were synthesized as well (Jana *et al.*, 2001), using a seeding-growth technique, in which pre-formed spherical gold seeds are grown into elongated rod-shaped nanoparticles. Various improvements of the synthesis were made to obtain high aspect ratio (length to width ratio, (Nikoobakht & El-Sayed, 2003)) gold nanorods in high yield (Johnson *et al.*, 2002). Besides the various studies performed to determine the growth mechanism, it is still unclear how anisotropic particles grow. Open and discussed questions are: the source and reason for anisotropic growth in general, accompanied by the surprisingly high yield of anisotropic particles. Different possible mechanisms are described and

discussed (Huang *et al.*, 2009), including electric-field- (Perez-Juste *et al.*, 2004), and surfactant-preferential-binding-directed growth (Murphy *et al.*, 2005), or under-potential deposition of silver (Liu & Guyot-Sionnest, 2005; Orendorff & Murphy, 2006). The ability to determine the mechanism of the growth, as well as the correlation between reaction additives and observed trends in the synthesized structures, are both topics with high importance. Tuning the resonance position of the gold nanorods, which is proportional to the aspect ratio of them, to external needs, is one of the key demands in order to use gold nanorods as plasmonic sensors. In order to understand the growth mechanism of the gold nanorods more precisely, a systematic study on the influence of internal parameters in the synthesis is performed. Using spectral data and transmission electron microscopy, a mechanistic model is proposed (chapter 3). Besides the role of the surfactant CTA⁺ as selective stabilizer of the growing nanoparticles, for the first time the electrochemical potential difference between reducing and oxidizing species, namely ascorbic acid and gold ions, is identified as essential parameter for anisotropic growth. With this new knowledge, fine-tuning of the synthesis of gold nanorods is possible in a more defined way. Using the electrochemical information, a possible reason for “good” or “bad” growth conditions is determined. Potentially, electrochemical conditions are important as well in the synthesis of different metallic nanoparticles, the (unsuccessful) growth of them might be influenced more than it was thought so far by the choice of reducing agent and electrochemical potentials.

The resonance position of plasmonic nanoparticles is not singly determined by their shape. The material or composition of the nanoparticles matters as well and can be used as additional tuning parameter for the resonance position, extending the region of accessible resonances. A combination of two noble metals in one nanoparticle by epitaxially growing a silver shell on top of gold nanorods alters the color of the nanoparticles (Liu & Guyot-Sionnest, 2004; Wang *et al.*, 2005; Tsuji *et al.*, 2006; Mandal *et al.*, 2004; Hodak *et al.*, 2000; Ah *et al.*, 2001; Song *et al.*, 2005). The thicker the silver shell, the lower the observed resonance position. Additionally (and so far overlooked), the peak-width of the resonance is decreased, which improves the quality of the nanoparticles in terms of sensing applications. Besides a big response to small changes, a good sensor also shows a narrow signal. There is high interest to understand how an existing nanoparticle sample can be processed further to make it more attractive as a sensor-candidate. In cooperation with Dr. Jan Becker, an effect termed “Plasmonic Focusing” is identified to be responsible for the decrease in ensemble-linewidth (chapter 4). Along with single particle measurements, transmission electron microscopy, and electrodynamical modeling, the degree of plasmonic focusing, cleaned from single-particle linewidth and size distribution changes, is determined. Knowing that the shift in the plasmon-shape-relation has the main influence on the ensemble spectra characteristics, one attribute for the search of the best plasmonic sensor is identified. The kinetics of the silver-coating of gold nanorods have not yet been subject to any study, although knowledge of the reaction kinetics allows to predict the product obtained at a certain point in time. Time-resolved spectra of the silver coating reaction are recorded for different reaction conditions, and a kinetic model is obtained. Knowing reaction order

1. Introduction

and activation energy, the progress in the reaction is forecast and the quenching time for a desired resonance wavelength is predicted. With this information of the reaction rate law, along with micro-fluidics and stop-flow techniques, plasmonic nanoparticles with different resonance wavelengths will be accessible from one reaction.

For isotropic (spherical) nanoparticles, an interpretation of the scattering signal is (relatively) easy. They don't show preferred directions of response to an outer trigger. Interpretation of signals does not depend on illumination angle or polarization, it does not matter on which side of a particle another molecule binds. But with this "simple" geometry, information is lost that is accessible with anisotropic objects. Rod-shaped gold nanoparticles "tell" their orientation by the polarization of the scattering signal (Sönnichsen & Alivisatos, 2005), even when illuminated with unpolarized light. They are used to characterize the local viscosity of the medium around them (Pierrat *et al.*, 2009). Gold nanorods are used as substitutes for conventional single-molecule probes, which are usually dyes that suffer from the fact that they are bleaching over time, might be photo-oxidized, or chemically unstable. Single-molecule studies have the big advantage that they are sensitive to rare events. They are therefore also used to study heterogeneous environments or processes, like polymers near glass transitions or polymer melts (Wei *et al.*, 2007; Deschenes & Vanden Bout, 2001; Uji-i *et al.*, 2006). In order to use gold nanorods as full substitutes for dyes as single-molecule/ particle sensors, they are introduced into a polymer-matrix and their rotational information is used to determine the transition temperature of the gel (chapter 5). With this proof-of-principle, the usage of gold nanorods as single particle rotational sensor is demonstrated as possible.

Besides the use of single nanoparticles as sensors for the orientation (Sönnichsen & Alivisatos, 2005; Pierrat *et al.*, 2009) and the refractive index (Baciu *et al.*, 2008; Jain & El-Sayed, 2008), assemblies of nanoparticles are explored concerning their sensing applications. The change of the resonance wavelength of a plasmonic particle if a second one is close by, can be used to determine either the presence of the second one at all (Rong *et al.*, 2008), or to distinguish the distance between them (Sönnichsen *et al.*, 2005). Aggregation, caused by the presence or absence of target molecules (Xia *et al.*, 2010), is also used in sensing applications. The promising fact of nanoparticle dimers is the dependence of their resonance position of the interparticle distance. With their help, small distances and distance changes, which appear in biological systems as well as in artificial ones, are accessible. A growing number of people are working on nanoparticle dimers (Ghosh & Pal, 2007; Anker *et al.*, 2008; Sheikholeslami *et al.*, 2010; Reinhard *et al.*, 2005; Brown *et al.*, 2010; Jain & El-Sayed, 2010), including in-vitro (Sönnichsen *et al.*, 2005; Reinhard *et al.*, 2007) and in-vivo (Rong *et al.*, 2008) applications. Different scaling laws, connecting the spectral shift to an interparticle shift, are found (Jain *et al.*, 2007; Encina & Coronado, 2010; Sönnichsen *et al.*, 2005). Since the resonance position of the nanoparticle dimer depends on the interparticle distance *and* the local refractive index, an internal calibration is required. Using external methods like dynamic light scattering and cryo-electron microscopy,

a new calibration for the distance dependency of the resonance position in water is established. With the help of numerical simulations, corrections for the local refractive index, which is determined in the same measurement, are included. The ability to measure an unknown distance in an unknown refractive index is achieved, which was not possible before (chapter 6). The here studied nanoparticle dimers are formed by a linking-strategy, which is reproducibly yielding a high fraction of dimers, while on the same time being generalizable. The nanoparticle dimers are used to study the behavior of a thermoresponsive polymer as linker under different conditions. Even the collapsed state of the polymer, not accessible with light scattering techniques, because macroscopic turbidity is observed, can be characterized. Having access to gold nanoparticle dimers linked by a switchable polymer, further characterization of the two states is possible. By high frequency time-resolved studies of the resonance position, fluctuations in the interparticle distance causing spectral fluctuations will be measurable.

The presented thesis is organized as follows:

Initially, a short theoretical introduction (chapter 2) gives selected fundamentals on electronic properties of metals, particle plasmons, and the scattering spectra of plasmonic particles. It includes features of the spectra of anisotropic particles like rods and dimers.

Chapter 3 and 4 deal with the synthesis of plasmonic nanoparticles. While in chapter 3 the anisotropic growth of gold nanoparticles is studied and a growth model is developed, chapter 4 shows how a thin silver layer on top of pre-formed gold nanorods improves their quality with respect to optical properties and how the kinetics of this coating-process work, including the development of a reaction rate law, which allows to predict the product of the reaction at a certain point in time.

The anisotropic gold nanorods are used to characterize the phase transition of a thermoresponsive polymer, using the polarization dependent scattering of the plasmon (chapter 5).

Assemblies of nanoparticles are discussed in chapter 6. While core-satellite structures are used for sensing of refractive index changes due to their increased sensitivity compared to single spheres, gold nanoparticle dimers are a versatile sensor for distance *and* refractive index changes, as well as a tool to characterize the linking polymer.

After a summary of the main results (chapter 7), a detailed appendix follows, which includes analytical methods (appendix A), a description of the used dark-field setups (appendix B), as well as synthetic methods and experimental details (appendix C).

2. Theory

Gold and silver nanoparticles have the special feature that, due to their small size and the fact that they are metallic and therefore have “free” conduction electrons, they show bright colors upon illumination with light. Embedded in glass (as windows), or as particle suspension, colors of the whole visible spectrum up to the IR-region are accessible. The physical reason for those colors is a phenomenon called “plasmon”, which will be explained in the following chapter. Starting from experimentally observed features and characteristics of gold nanoparticles spectra, a condensed physical background of metals is given and the main results for small spherical metal nanoparticles are explained. Later on, an extension to rod-shaped particles (chapter 2.3), coated particles (chapter 2.4), and nanoparticle assemblies (chapter 2.5) is given.

2.1. Spectra of Plasmonic Nanoparticles

“Plasmons” occur when light interacts with metals. They are the reason why dispersions of metal nanoparticles or church windows made of ruby-glass show bright colors. The quasi-particle *plasmon* is a term for the collective oscillation of electrons. It can be excited by light as well as by electrons (as observed in electron microscopy). There are different types of plasmons depending on where they emerge. Surface plasmons on thin metal films, localized surface plasmons or particle plasmons in metal nanoparticles, and volume plasmons, which do not occur on the interface between two materials with a dielectric constant of opposite sign, but inside a material (bulk plasmon). In the following, only particle plasmons (later on simply called plasmons) are considered, because they occur in plasmonic nanoparticles.

Using a conventional UV-Vis spectrometer, the suspensions of gold and silver nanoparticles show one (or two) distinct peaks (see figure 2.1). They are attributed to the resonance frequency of the plasmon, a collective oscillation of the conduction band electrons.

From the spectrum, different features can be extracted, namely the extinction E , the resonance position λ_{res} , and the width of the peak at half the extinction FWHM. Knowing the extinction coefficient, the extinction (scattering *and* absorption) can be used to determine the concentration of the particles in solution using Lambert-Beer’s law (see also appendix A). The FWHM gives a hint to the polydispersity of the sample, since it is a convolution of single-particle linewidth

2. Theory

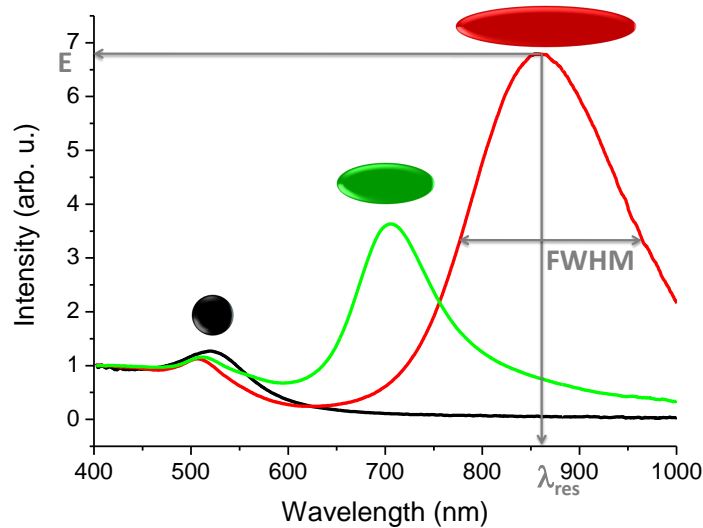


Figure 2.1.: Typical Ensemble Spectra

Ensemble spectra (normalized at 400 nm) for gold nanospheres (black), small (green), and large (red) aspect ratio gold nanorods.

and particle size distribution. The narrower the peak, the lower the polydispersity of the sample (or the shallower the plasmon-shape-relation, see chapter 4). The main feature of the ensemble spectrum is the resonance position λ_{res} (in a medium with refractive index n), since it accounts for the mean aspect ratio of the gold nanorods via an empirical formula (Becker, 2010):

$$\lambda_{\text{res}} (\text{nm}) = (91 \cdot \text{aspect ratio} + 138) \left(\frac{\text{nm}}{\text{RIU}} \right) \cdot n - (15 \cdot \text{aspect ratio} - 215) (\text{nm})$$

The difference between the spectra of spheres compared to rods, having one or two resonance peaks respectively, can descriptively be explained by the collectively oscillating electron cloud. Since spheres are isotropic, only one resonant oscillation can be excited. Nanorods, in contrast, have two distinct axis, which both have a different resonance condition (figure 2.2). The first (lower wavelength) peak in the nanorod spectrum is attributed to the transverse oscillation (perpendicular to the long axis), the second (higher wavelength) peak to the longitudinal one.

Besides ensemble spectra, with the help of dark-field microscopy (see appendix A.3) single particle *scattering* spectra of gold and silver nanoparticles can be recorded as well. In there, in principle similar features as in the ensemble spectrum are found. The scattering intensity corresponds to the scattering efficiency of the observed nanoparticle. A high scattering efficiency is desired in order to have a good scattering signal to record. In contrast to the FWHM of an ensemble spectrum, the single particle linewidth Γ accounts for the lifetime of the plasmon. The thinner the peak, the longer the plasmon lifetime (see also appendix A.2). The third and mainly used information from the single particle spectrum is the resonance position λ_{res} . The wavelength of the scattered light is connected to material, shape, and surrounding of the

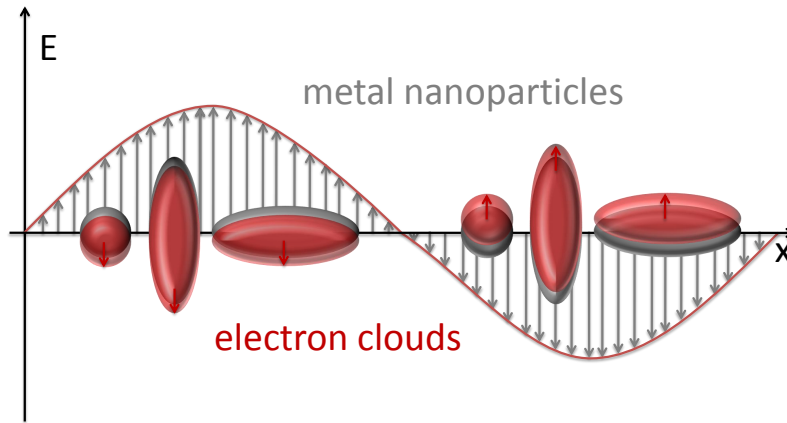


Figure 2.2.: Plasmons

Exposing gold nanoparticles to an oscillating electromagnetic field (light), the free conduction electrons are excited to a resonant oscillation. While for spheres only one resonance can be found, nanorods have two preferred oscillations, along both particle axes.

nanoparticle. If material and shape are known, the resonance position can be used to report on the local environment of the single nanoparticle and environmental changes. Increasing the refractive index of the surrounding medium (and with this its polarizability), the resonance wavelength is shifted to lower energies (higher wavelengths).

2.2. Localized Surface Plasmons

Complex dielectric function

Properties that depend on the frequency of a wave (ω) are called dispersive properties, materials that show those features are termed dispersive media. For metals, the dielectric constant or relative permittivity ϵ is such a property. $\epsilon(\omega)$ governs the optical response of metals to light. The fundamental relationship of relative permittivity and conductivity σ is (Maier, 2007):

$$\epsilon(\omega) = 1 + \frac{i\sigma(\omega)}{\epsilon_0\omega} \quad (2.1)$$

including the vacuum permittivity ϵ_0 . In general both, permittivity and conductivity are complex functions with a real and an imaginary part

$$\epsilon(\omega) = \epsilon_1(\omega) + i\epsilon_2(\omega) \quad (2.2)$$

2. Theory

$$\sigma(\omega) = \sigma_1(\omega) + i\sigma_2(\omega) \quad (2.3)$$

Knowing this, also a complex refractive index $\tilde{n} = \sqrt{\varepsilon}$ can be defined

$$\tilde{n}(\omega) = n(\omega) + i\kappa(\omega) \quad (2.4)$$

The extinction coefficient κ can be expressed as

$$\kappa = \frac{\varepsilon_2}{2n} \quad (2.5)$$

It is linked to the to the absorption coefficient α in Lambert-Beer's law via (Maier, 2007)

$$I(x) = I_0 e^{-\alpha x}$$
$$\alpha(\omega) = \frac{2\kappa(\omega)\omega}{c}$$

Since κ , and therefore α as well, only depends on ε_2 , it is clear that the imaginary part ε_2 of ε accounts for the amount of absorption inside the medium.

The plasma model - a Drude metal

In the plasma model, a free electron gas moves against a fixed background of positively charged ions. No details of the lattice potential or electron-electron interactions are taken into account. All electrons oscillate as a response to the applied electromagnetic field and are damped by collisions with other electrons. They are deflected from their equilibrium position and contribute to the overall polarization of the particle. From this model, an expression for the dielectric function of the free electron gas is derived, including the so called plasma-frequency $\omega_p^2 = \frac{ne^2}{\varepsilon_0 m}$ (n = number density of the electrons, m = effective optical mass of the electrons):

$$\varepsilon(\omega) = 1 - \frac{\omega_p^2}{(\omega^2 + i\gamma\omega)} \quad (2.6)$$

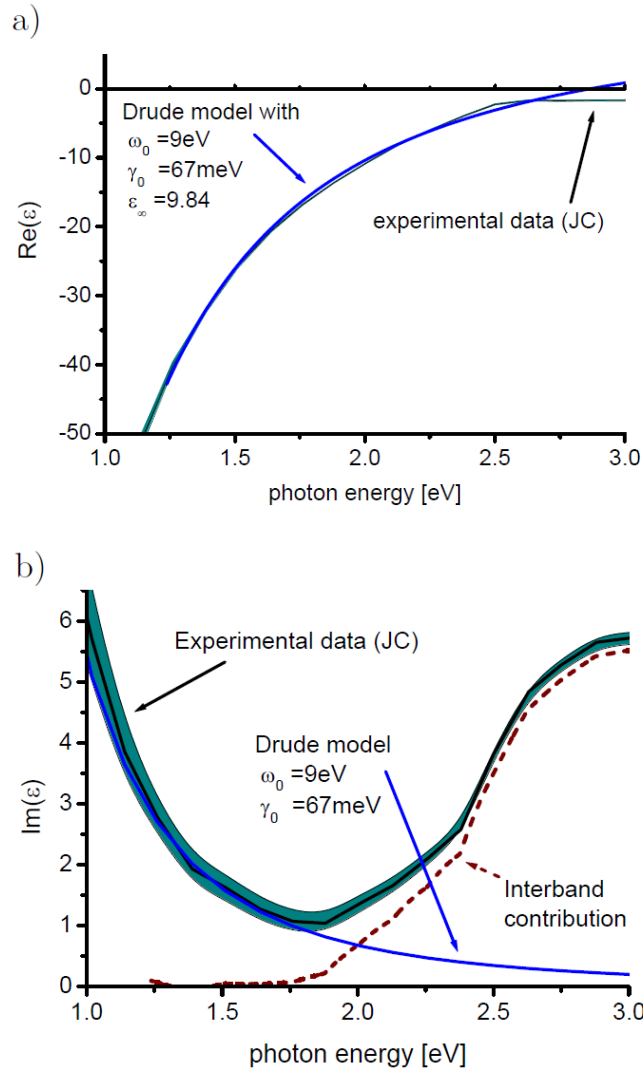


Figure 2.3.: Real and Imaginary Part of the Dielectric Function of Gold

Real (a) and imaginary (b) part of the dielectric function of gold. Blue lines show the calculated values from a Drude metal. The experimental data from Johnson and Christy (Johnson & Christy, 1972) are compared to the theoretical one to calculate the inter band contribution (red dashed line). Green shading represents the uncertainty of the experimental values (Sönnichsen, 2001).

Extension to real metals

For real metals like gold or silver, an extension of the above mentioned free electron description is needed, since at frequencies close to the plasma frequency, the response to an applied electromagnetic field is mainly governed by s-electrons. Johnson and Christy (Johnson & Christy, 1972) measured the real and imaginary part of the dielectric functions of gold, silver, and copper and compared them to the situation of a pure Drude metal. They used optical measurements on thin films in order to get values for the two optical constants and information about the film thickness. One can see (figure 2.3) that the imaginary part differs a lot from the ideal case when it comes to higher photon energies, where inter-band damping (excitation of electrons from d-bands into the conduction band) becomes relevant. The dielectric function in real metals has to be corrected by

2. Theory

the term ϵ_∞ , accounting for the background potential of the bound electrons.

$$\epsilon(\omega) = \epsilon_\infty - \frac{\omega_p^2}{(\omega^2 + i\gamma\omega)} \quad (2.7)$$

with ϵ_∞ usually in the range of $1 \leq \epsilon_\infty \leq 10$.

LSP- Localized surface plasmons (or particle plasmons)

So far, general features of metals are presented. In the following, plasmonic nanoparticles will be treated. The term localized surface plasmon is used for non-propagating excitations of conduction electrons of metallic nanostructures coupled to the electromagnetic field. They can be observed due to scattering events on sub-wavelength conductive nanoparticles in oscillating electromagnetic fields. Due to the (curved) surfaces of the particle, there is an effective restoring force on the driven electrons, which leads to resonance and field amplification. A direct excitation by light is possible.

QSA- quasi-static approximation

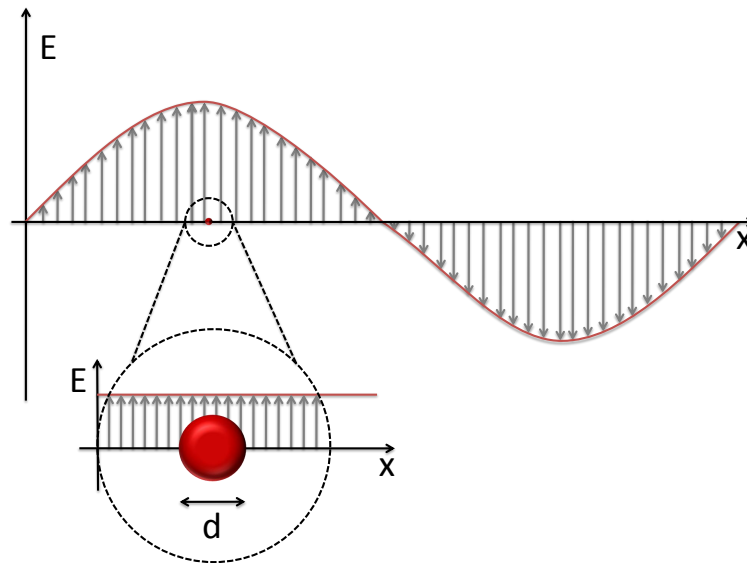


Figure 2.4.: Conditions for QSA

Not-to-scale schematic representation of the conditions for QSA. Treating a nanoparticle in the quasi-static approximation is valid, if the particle's dimension d is much smaller than the wavelength of the electromagnetic field. The field "felt" by the particle is quasi static, the phase inside the particle constant.

In the quasi-static approximation, the particle diameter d is much smaller than the wavelength of the electromagnetic field λ (see figure 2.4) . Therefore, the phase of the field inside the particle can be considered as constant and the problem simplifies to a particle in a quasi electrostatic field. The central result of the quasi-static approximation QSA is the complex polarizability α of a small sphere (radius a) of sub-wavelength diameter, including the medium dielectric constant

ϵ_m (Maier, 2007)

$$\alpha = 4\pi a^3 \frac{\epsilon - \epsilon_m}{\epsilon + 2\epsilon_m} \quad (\text{Clausius-Mosotti relation}) \quad (2.8)$$

It can be seen that the polarizability $\alpha \rightarrow \infty$ for $|\epsilon + 2\epsilon_m| \rightarrow 0$, the resonance condition is fulfilled. For dielectric constants with a small imaginary part of ϵ , the minimum condition around the resonance simplifies to (Maier, 2007)

$$\text{Re}[\epsilon(\omega)] = -2\epsilon_m$$

This condition is called the ‘‘Fröhlich criterion’’, its associated mode is called ‘‘dipole surface plasmon’’ of the metal nanoparticle. It shows that the resonance frequency strongly depends on the dielectric constant of the surrounding medium, which makes metal nanoparticles candidates for refractive-index sensors. The polarizability α is the fundamental characteristic, which needs to be calculated in order to derive further features of a plasmonic nanoparticle. Therefore, for different materials and shapes, it is a change in α , which affects other properties like absorption or scattering cross-sections.

Scattering and absorption cross-section

The fact that the polarizability α shows a maximum results in an enhancement of scattering and absorption efficiency of a metal nanoparticle at the resonance frequency. If the small metal sphere ($d \ll \lambda$) is treated as an ideal dipole, radiating an electromagnetic field due to scattering of a plane wave on the small sphere, the expressions for the magnetic and electric field of an oscillating dipole can be used to calculate the cross-sections of scattering C_{sca} and absorption C_{abs} . This yields (Bohren & Huffman, 1983):

$$\begin{aligned} C_{\text{sca}} &= \frac{k^4}{6\pi} |\alpha|^2 \\ &= \frac{8\pi}{3} k^4 a^6 \left| \frac{\epsilon - \epsilon_m}{\epsilon + 2\epsilon_m} \right|^2 \end{aligned} \quad (2.9)$$

$$\begin{aligned} C_{\text{abs}} &= k \text{Im}[\alpha] \\ &= 4\pi k a^3 \text{Im} \left[\frac{\epsilon - \epsilon_m}{\epsilon + 2\epsilon_m} \right] \end{aligned} \quad (2.10)$$

From these two cross-sections, the extinction cross-section can be calculated (Maier, 2007):

$$\begin{aligned} C_{\text{ext}} &= C_{\text{abs}} + C_{\text{sca}} \\ &= 9 \frac{\omega}{c} \epsilon_m^{\frac{3}{2}} V \frac{\epsilon_2}{[\epsilon_1 + 2\epsilon_m]^2 + \epsilon_2^2} \end{aligned} \quad (2.11)$$

2. Theory

It should be mentioned that all (scattering, absorption, and extinction) cross-sections are enhanced, if the Fröhlich criterion is fulfilled. Furthermore, it can be seen, that $C_{\text{sca}} \propto a^6$ and $C_{\text{abs}} \propto a^3$. It is therefore very hard to detect small scatterers in a background of bigger ones and by doubling the radius of the sphere, the scattering will increase much more than the absorption. In other words, small particles absorb with a higher efficiency compared to big ones.

The interaction of light with a nanoparticle - no matter if its absorption or scattering - results in a decrease of the detected light intensity after it interacted with the particle:

$$I_{\text{sca}}(\omega) = \frac{I_0(\omega)}{A} C_{\text{sca}}(\omega) \quad (2.12)$$

$$I_{\text{abs}}(\omega) = \frac{I_0(\omega)}{A} C_{\text{abs}}(\omega) \quad (2.13)$$

A is the area which is illuminated by the light intensity I_0 .

Mie-Theory

In general, QSA is not applicable in two cases: very small and very large particles. For very small ones (<10 nm), the particle's dimensions are smaller than the mean free path of the electrons that oscillate. In this regime, with a small absolute number of electrons, the quantization of electron levels becomes relevant and the picture of a plasmon as a coherent oscillation of electrons is no longer valid. Therefore, quantum-mechanical treatment is necessary, which will not be done in this thesis since no particles in this size regime were used.

The other regime in which the QSA breaks down is for bigger particles. Here two effects start to occur: retardation effects (opposite charges are separated, a change at one end of the particle leads to a time-delayed change on the opposite end, a red-shift of the resonance compared to the one calculated by QSA can be observed) and the finite skin-depth of metals for the penetration of light. Gustav Mie (German physicist, 1868-1957) was the first to analytically solve the situation of a sphere of arbitrary radius and dielectric constant in an oscillating electromagnetic field by solving Maxwell's equations in spherical coordinates. He found expressions for the scattering coefficients a_n and b_n (Bohren & Huffman, 1983):

$$a_n = \frac{m\Psi_n(mx)\Psi'_n(x) - \Psi_n(x)\Psi'_n(mx)}{m\Psi_n(mx)\xi'_n(x) - \xi_n(x)\Psi'_n(mx)} \quad (2.14)$$

$$b_n = \frac{\Psi_n(mx)\Psi'_n(x) - m\Psi_n(x)\Psi'_n(mx)}{\Psi_n(mx)\xi'_n(x) - m\xi_n(x)\Psi'_n(mx)} \quad (2.15)$$

with the size parameter $x = \frac{2\pi n_m r}{\lambda}$ (n_m is the refractive index of the medium) and the relative refractive index $m = \frac{n_{\text{particle}}}{n_m}$. Furthermore, he used the Riccati-Bessel functions Ψ_n and ξ_n . The index n accounts for the order of the functions, for $n = 1$ the dipole mode is described, $n = 2$ relates to the quadrupole mode. It is worth noting that for $m \rightarrow 1$ (the refractive indices of

particle and medium are the same) a_n and $b_n \rightarrow 0$. This means, if the particle disappears also scattering and absorption vanish. With the help of the coefficients a_n and b_n , new expressions for the scattering and extinction cross-sections can be found, which - in contrast to 2.9 and 2.11 - now include retardation effects as well (Bohren & Huffman, 1983).

$$C_{\text{sca}} = \frac{2\pi}{k^2} \Sigma (2n+1) (|a_n|^2 + |b_n|^2) \quad (2.16)$$

$$C_{\text{ext}} = \frac{2\pi}{k^2} \Sigma (2n+1) \text{Re}(a_n + b_n) \quad (2.17)$$

In here, $k = 2\pi \frac{\sqrt{\epsilon_m}}{\lambda}$ is the wave vector of the electromagnetic wave with wavelength λ .

Numerical Methods

In order to be able to calculate the optical response of an arbitrary shaped particle, numerical methods are needed. Very common is the discrete dipole approximation (DDA), in which the particle is represented by a cubic array of N polarizable dipolar elements, which exhibit a dipole moment as consequence of the incident and the local electric field, the latter one being an overlap of the fields from the other $N-1$ dipoles. Since the interaction between two dipolar elements has a long range, the interaction matrix includes *all* other dipoles. Therefore, the number of dipoles is the critical factor. The higher it is, the higher the accuracy of the calculation but also the longer the computational time. This method was implemented into the software DDSCAT by Draine and

simulation method is the boundary element method (BEM). In this technique, one describes the homogeneous field inside the particle by a system of surface integrals that account for fields and field changes at the boundary between particle and outer medium (surface of the particle). These field changes determine the field inside, therefore it is sufficient to model the surface instead of the whole volume of the particle by this method (Myroshnychenko *et al.*, 2008). Other computational methods include FDTD (finite difference time domain) methods, in which electric and magnetic fields are defined only at grid points and used to solve the differential forms of Faraday's and Ampere's law (Zhao *et al.*, 2008). Those methods have the drawback that they are limited in modeling capability due to the grid they are based on. Geometries will suffer from errors arising from the nature of the grid and computational time will increase with area, if fine structures still want to be resolved.

In chapter 6 (Nanoparticle Assemblies) BEM simulations are used to calculate the optical response of metal nanospheres and nanoparticle dimers in different refractive index media. The simulations were done by Dr. Jan Becker, using the BEM-software provided by Andreas Trügler (working group of Prof. Dr. Ulrich Hohenester, University of Graz).

2. Theory

2.3. Rods

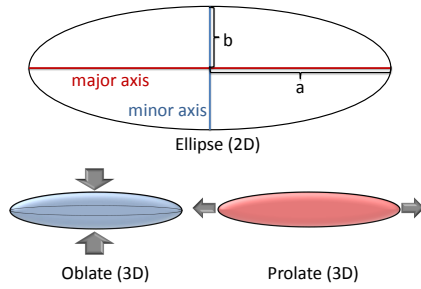


Figure 2.5.: Prolate and Oblate

Shape

Variables used to describe an oblate (compressed) and prolate (elongated) ellipsoid.

The quasi-static approximation cannot solely be used in the case of spherical particles, but it is also possible to analytically calculate the polarizability α_i along one of the axis i ($i = a, b$, or c) of a spheroid by introducing a geometrical factor L_i into the formula of the polarizability (see equation 2.8).

This was first done by Richard Gans (German physicist, 1880 - 1954), who expressed the polarizability of an ellipsoid as (Bohren & Huffman, 1983)

$$\alpha_i = 4\pi abc \frac{\epsilon - \epsilon_m}{3\epsilon_m + 3L_i(\epsilon - \epsilon_m)} \quad (2.18)$$

Comparing with the expression for the polarizability of a spherical particle 2.8, one can see that for a sphere $L_a = L_b = L_c = \frac{1}{3}$. For spheroids (ellipsoids with two of their axis being the same length) two cases can be differentiated, prolates ($a=b < c$, rugby-ball-shaped) and oblates ($a=b > c$, disk-shaped). For both, expressions for the geometrical factors are found (Bohren & Huffman, 1983):

$$L_{a,\text{prolate}} = \frac{1-e^2}{e^2} \left(-1 + \frac{1}{2e} \ln \left(\frac{1+e}{1-e} \right) \right)$$

$$L_{b,\text{prolate}} = L_{c,\text{prolate}} = \frac{1 - L_{a,\text{prolate}}}{2}$$

in the prolate case, with the eccentricity $e = \sqrt{1 - \frac{b^2}{a^2}}$, and

$$L_{a,\text{oblate}} = L_{b,\text{oblate}} = \frac{g(e)}{2e^2} \left(\frac{\pi}{2} - \arctan(g(e)) \right) - \frac{g^2(e)}{2}$$

$$L_{c,\text{oblate}} = 1 - 2 \cdot L_{a,\text{oblate}}$$

for oblate shaped particles, which include $g(e) = \sqrt{\left(\frac{1-e^2}{e^2}\right)}$ and the oblate eccentricity $e^2 = 1 - \frac{c^2}{a^2}$. One can now use these expressions to calculate the polarizability 2.18 and following this, also the scattering and absorption cross sections. In contrast to spheroids, where analytical solutions for the polarizability α_i are found, “real” rod-shaped nanoparticles can strictly not be treated like a spheroid. In fact, numerical methods like DDA are used in order to obtain the polarizations for rods. Prescott and Mulvany found that the scattering spectra of rods do not

purely depend on the aspect ratio (as in the case of spheroids), but also tremendously on the end-shape geometry (Prescott & Mulvaney, 2006).

The QSA for prolate shaped particles is used to calculate theoretical spectra of spheroids with a mean size and aspect ratio derived from TEM images for the particles synthesized in chapter 3 (Anisotropic Growth). These theoretical spectra are used to calculate the ratio $\frac{I_{\text{long axis}}}{I_{\text{short axis}}}$ and to calculate the yield of rods compared to spheres in a synthesis by comparing the theoretical with the experimentally determined value.

2.4. Coated Nanoparticles

It is furthermore possible to extend the QSA to coated particles, consisting of an inner core and an outer shell of a different material. As well as in the spheroid extension, the expression for the polarizability is modified. According to Liu and Guyot-Sionnest (Liu & Guyot-Sionnest, 2004), the expression for the polarizability α_i of a prolate shaped core-shell particle (dimensions core: $a_1=b_1<c_1$, dimensions whole particle: $a_2=b_2<c_2$, confocal conditions, the core is centered inside the shell, $c_2^2-a_2^2=c_1^2-a_1^2$) is

$$\alpha_i = \epsilon_0 V_{\text{total}} \frac{\left\{ (\epsilon_s - \epsilon_m) \left[\epsilon_s + (\epsilon_c - \epsilon_s) \left(L_i^{(1)} - f L_i^{(2)} \right) \right] + f \epsilon_s (\epsilon_c - \epsilon_s) \right\}}{\left[\epsilon_s + (\epsilon_c - \epsilon_s) \left(L_i^{(1)} - f L_i^{(2)} \right) \right] \left[\epsilon_m + (\epsilon_s - \epsilon_m) L_i^{(2)} \right] + f L_i^{(2)} \epsilon_s (\epsilon_c - \epsilon_s)} \quad (2.19)$$

including the dielectric constant of the core ϵ_c , the shell ϵ_s , and the surrounding medium ϵ_m . The factor f denotes for the fraction of the total volume which is occupied by the core ($f = \frac{a_1 b_1 c_1}{a_2 b_2 c_2}$), while $L_i^{(1,2)}$ are geometrical factors, influenced by the the eccentricity of the particle (see also (Liu & Guyot-Sionnest, 2004)). It can be seen that for uncoated spheroids (ϵ_c equals ϵ_s , $\epsilon_c - \epsilon_s = 0$) expression 2.18 is recovered.

The QSA theory for coated particles is used in chapter 4 (Silver Coating) to calculate the theoretical spectra of silver-coated gold nanorods, which are used to determine the plasmonic focusing effect.

2.5. Dimers

Single metallic nanoparticles (spheres, rods, other shapes) are by themselves interesting structures for two reasons, studying fundamental properties of plasmonic particles concerning material and shape, and as sensors for the environment they are embedded in. Introducing a second plasmonic nanoparticle nearby a first one, the spectrum of the assembly differs from the one of the single particles. Using polarization dependent illumination or detection, two observations

2. Theory

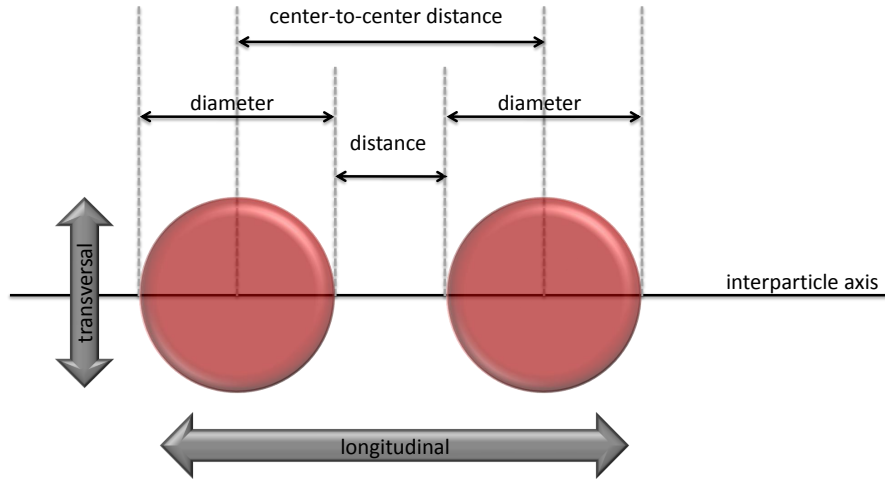


Figure 2.6.: Parameters to Describe a Nanoparticle Dimer

Main definitions needed to describe a system of a nano particle dimer.

are made: The resonance wavelength of the plasmon mode parallel to the inter particle axis (“longitudinal plasmon mode”) is red-shifted to higher wavelengths (lower energies), compared to the resonance position of the single nanoparticle. It is favored, less energy is needed to drive this oscillation. In contrast to the redshift of the resonance parallel to the inter-particle axis, a (small) blue-shift to lower wavelengths is measured for the polarization perpendicular to the inter-particle axis. This oscillation is hindered, more energy is needed to excite it. In principle two new features occur due to the interaction of the near-fields of the two particles, namely the appearance of two plasmon modes (parallel and perpendicular to the inter particle axis), and the field enhancement in the gap between the two particles. While the latter one is used to study the fluorescence enhancement of dyes situated around the particles (Bek *et al.*, 2008), the orthogonally polarized plasmon modes provide information about orientation and distance of the two particles.

If two plasmonic nanoparticles are close to each other, the field E felt by a particle consists of two parts, the incident field E_0 and the near-field of the neighboring particle E_{nf} .

$$E = E_0 + E_{\text{nf}} \quad (2.20)$$

The response of the conduction electrons to this “mixed” external field can be seen experimentally in the spectra of the nanoparticle assemblies, and can in principle be calculated using Maxwell’s equations. In order to have a more concrete picture of the situation of two plasmonic particles next to each other, different models can be referred to, which will be briefly discussed in the

following. All of them have in common that they provide pictures or comparisons to other phenomena, with the goal to clarify the observed effects. It turns out that the easy assumption, treating the two spheres as two point dipoles (which is doable for small sphere sizes and big separation distances, **exciton-coupling model**), qualitatively explains the observed shifts of longitudinal and transverse axis, but does not suffice to model the experimentally observed exponential decay of the longitudinal resonance for longer separation distances. This exponential behavior in turn can be best explained by the **tunneling model**, which connects the plasmon coupling to a coupling mediated by photons tunneling through the inter-particle gap.

The exciton-coupling model (Jain & El-Sayed, 2010)

This model derives from the coupling of two organic dyes, treated as two point dipoles. It is therefore strictly speaking only valid if the particle size \ll inter-particle distance. Upon dimerization, the excited state of the monomer splits into two levels. One with lower energy (accounting for the in-phase or symmetrical orientation) and one with higher energy (for the out-of phase or asymmetrical orientation, see figure 2.7a). The energy splitting $2U$ depends on the interaction energy between the two particles. This energy is approximated by the Coulomb interaction of the transition dipole moments μ of the monomers. The field E felt by the particle becomes

$$E = E_0 + \frac{\xi \mu}{4\pi\epsilon_0 s^3} \quad (2.21)$$

and the interaction energy U can be expressed as

$$U = -\frac{\xi |\mu|^2}{4\pi\epsilon_0 s^3} \quad (2.22)$$

with s the interparticle distance. Since the two dipoles in general do not have to be aligned in any direction, the near-field of the second particle includes the inter-particle distance between the dipoles and the orientation of them, expressed by the orientation factor

$$\xi = 3 \cos \theta_1 \cos \theta_2 - \cos \theta_{12} \quad (2.23)$$

This orientation factor (see figure 2.7b) involves the angle between the dipoles and the inter particle axis (θ_1 and θ_2) as well as the angle between the two dipoles (θ_{12}).

Two cases can now be treated separately (see figure 2.8) :

- Case 1 - the incident light is polarized parallel to the inter-particle axis.

The two dipoles will be aligned on their axis and the orientation factor ξ calculates to 2. Therefore, the interaction energy results in $U < 0$ and the interaction of the dipoles is attractive. This causes a shift of the excited state of the dimer to lower energies, the resonance wavelength of this mode shifts to higher wavelengths. For an antisymmetric alignment of the dipoles, they cancel out

2. Theory

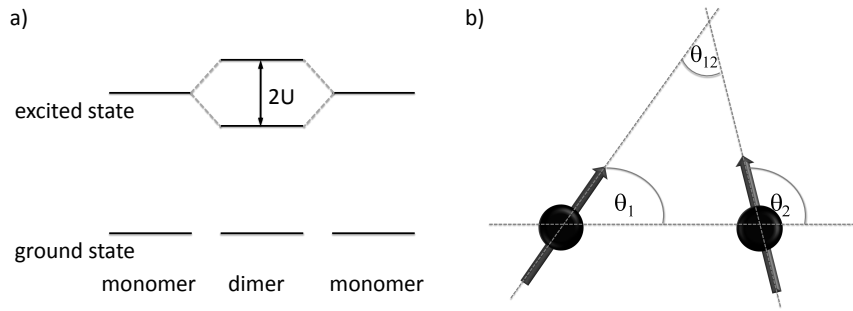


Figure 2.7.: Energy and Orientation Factor in the Exciton-Coupling Model

a) Schematic representation of states of the monomers and the dimer, including the interaction energy. b) Relative orientation of two dipoles.

(at least in a homodimer consisting of two identical spheres). Therefore, this configuration is optically forbidden and represents a dark plasmon mode in a homodimer. For heterodimers (different dipole moment for each dipole, represented by different size and/or composition of the two particles) this mode can be excited as well.

- Case 2 - the incident light is polarized perpendicular to the inter-particle axis.

In the symmetrical orientation of the dipoles, the orientation factor is -1, and therefore the interaction energy results in $U > 0$. The interaction between the dipoles becomes repulsive and a blue shift of the resonance wavelength of the transverse mode (to higher energies) can be observed. Again, the antisymmetric case is optically forbidden and results in a dark plasmon mode.

Using the exciton-coupling model, a coupling strength which is proportional to $\frac{1}{s^3}$ is expected. This is (experimentally observed) not the case, especially for separation distances smaller than $0.5 \times$ diameter of the particles. There a simple dipolar treatment is not sufficient any more and higher order multipole-multipole type interactions are considerably large, resulting in a much steeper increase of the coupling strength for short inter particle distances.

Orbital Hybridization Model (Nordlander *et al.*, 2004)

In this model, the coupling of plasmons in nanoparticle assemblies is compared to the hybridization of atomic orbitals in molecules. Upon hybridization, the plasmon modes of the single spheres form bonding (red-shifted to lower energies) and antibonding (blue-shifted to higher energies) plasmon modes of the dimer. The big advantage of this model is the possibility to extend it to assemblies of rod-shaped particles, resulting in σ , π , σ^* , and π^* orbitals, and to asymmetric dimers (so called heterodimers, for example consisting of two different sized spheres), similar to hetero-dimeric molecules. The conduction electrons are treated as a charged, incompressible liquid on top of the ion cores, which are represented by a rigid positive charge that is uniformly distributed within the particle boundaries (known as “jellium” approximation). A plasmon mode is then a self-sustained deformation of the electron liquid. Since this liquid is incompressible, deformations will cause surface charges σ . If any retardation effects are

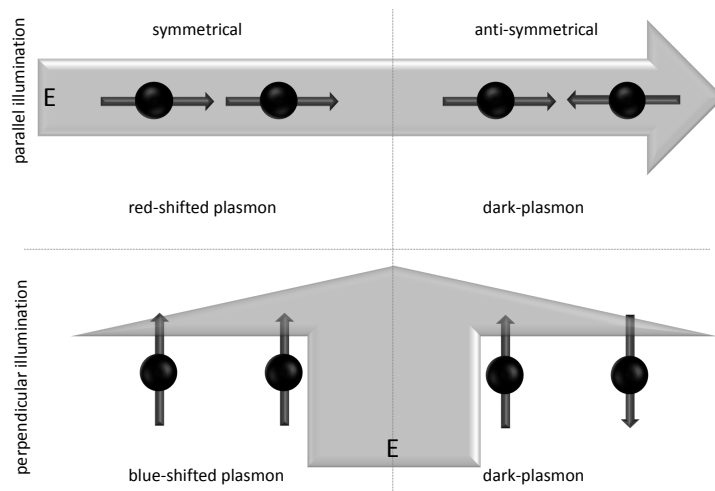


Figure 2.8.: Orientation of Dipoles in an Electric Field

Two cases are explored: Illumination parallel and perpendicular to the inter particle axis. In both cases, the symmetrical orientation of the dipoles results in bright plasmons, while the antisymmetrical one leads to dark plasmons. For parallel illumination, a red-shifted plasmon resonance is observed, while for perpendicular illumination a blue-shift of the plasmon is measured.

neglected (center-to-center distance + diameter $< \frac{\lambda}{4}$), the dynamics of the plasmon oscillation of a dimeric assembly of spheres are determined purely by the Coulomb interaction of the surface charges. The Coulomb interaction is a function of the center-to-center distance as well as of radii of the two spheres. Calculations for different quantum numbers (representing the orientation of the polarization relative to the dimer axis) end up with Eigenvalue problems of exactly the same form as if one calculates molecular orbitals from atomic ones (see also (Nordlander *et al.*, 2004) for further details).

Tunneling Model (Su *et al.*, 2003)

The two coupling particles are treated as two identical resonators in this model. Upon coupling, the resonance frequency will shift. This shift is proportional to the coupling coefficient (if one, shift or coupling coefficient, is small). Therefore, the measured shift (of the resonance in the far-field) reflects the plasmon coupling behavior. This coupling is promoted by photons tunneling through the gap between the particles. Comparing this tunneling to other quantum wave tunneling effects, the coupling coefficient can be approximated as an exponential function over gap size, as in many other quantum effects. The experimentally observed exponential dependency of the resonance position of the longitudinal plasmon mode (representing the coupling strength) agrees well with this exponential function.

Spring Model (Rechberger *et al.*, 2003)

The simple model of two interacting dipoles needs to be modified by additional forces that act due to the surface charges on the particles. Within one particle, a force is established if electrons and holes are separated by the particle diameter and accumulated on the opposite surfaces. This force can be represented by an elongated spring. If now a second particle is close to the first one, the sur-

2. Theory

face charges of the second will influence the forces acting inside the first particle (and vice versa).

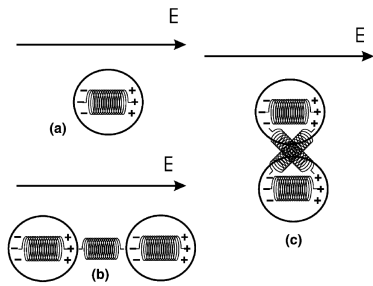


Figure 2.9.: Spring Model

Sketch to illustrate the electromagnetic interaction of a) an isolated particle, a pair of closely packed particles with the polarization of the exciting field b) parallel and c) orthogonal to the long particle pair axis (Rechberger *et al.*, 2003).

For the case of the driving field parallel to the long axis of the dimer, a weakening of the repulsive forces within one particle can be observed. The negative surface charges of particle one face the positive surface charges of particle two. Attractive forces between the particles act, a lower resonance frequency is observed. If the driving field is perpendicular to the inter particle axis, the surface charge distributions of the particles influence each other in a way that they enhance the repulsive action in both particles, which causes a repulsive action and an increased resonance frequency (see figure 2.9).

In conclusion, one can state that the exciton-coupling model as a simple one, treating the two plasmonic particles as dipoles, explains well the qualitative shifts for the longitudinal and transverse axis. It lacks an explanation for the

observed exponential decay of the longitudinal resonance wavelength of a nanoparticle dimer upon increasing interparticle distance, which is experimentally observed and predicted from the tunneling-model.

2.5.1. Sensing with dimers

In principle, all plasmonic structures -including dimers- are sensitive to changes in the local refractive index around the particle. Increasing n_{local} causes a shift of the resonance position to higher wavelengths. This is also true for both resonances of the dimer, transverse and longitudinal. Additionally to changes in the refractive index, dimers can also report on their orientation (as gold nano rods can as well) and on the inter particle distance between the two spheres, making them good candidates for nanoscopic distance sensors (nano-rulers).

Refractive index changes

For refractive index sensing applications, it is interesting to know how particle pairs behave in different refractive index environments and how the medium refractive index influences the coupling strength of the plasmons. One expects that the interaction energy scales with $\frac{1}{\epsilon_m}$. Higher dielectric constants would cause a decrease in interaction energy resulting in less or weaker coupling in higher refractive index media. But the opposite is observed: The higher the refractive index, the bigger the coupling of the plasmons. The reason for this result, observed experimentally and by simulations, is the fact that the interaction energy U depends quadratically on the dipole moment ($U \sim |\mu|^2$), which itself depends on the medium refractive index ($\mu \sim \epsilon_m$, (Jain *et al.*, 2006)). An increase in ϵ_m results in a decrease of the Coulomb restoring force within a particle. For an increase in ϵ_m , a net increase of the plasmon coupling strength is observed.

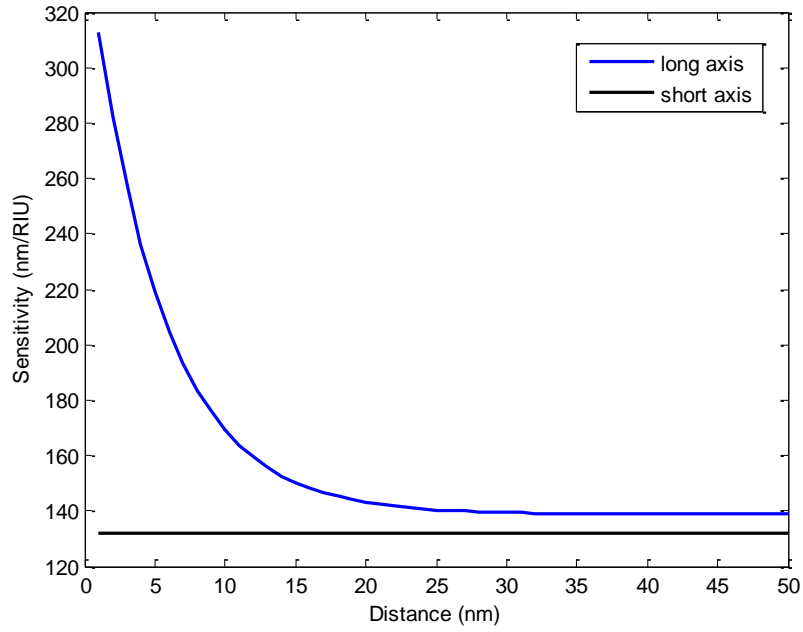


Figure 2.10.: Sensitivity of Dimers

Using BEM simulations, the sensitivity of the longitudinal (blue) and transversal (black) plasmon resonance to changes in the medium refractive index is calculated for increasing inter particle distances (Becker, 2010).

For sensing refractive index changes, the sensitivity S is a measure for the usefulness of the sensor. A high value of S is desired in order to be able to detect also small changes in the local environment.

$$S = \frac{\Delta\lambda}{\Delta n_m} \quad (2.24)$$

BEM simulations of gold nano particle dimers in different refractive index media (Becker, 2010) show that the sensitivity of the transverse plasmon mode is unaffected from the inter particle distance and calculates to $132 \frac{\text{nm}}{\text{RIU}}$. In contrast to this, the longitudinal plasmon mode's sensitivity is only constant for a fixed distance between the two spheres. Decreasing the inter-particle distance increases the sensitivity to refractive index changes (see figure 2.10).

$$S_{\text{longitudinal axis}} = 211.4 \frac{\text{nm}}{\text{RIU}} \cdot \exp\left(\frac{\text{interparticle distance (nm)}}{-5.15\text{nm}}\right) + 138.8 \frac{\text{nm}}{\text{RIU}} \quad (2.25)$$

Distance Changes

The longitudinal resonance of a dimer decreases almost exponentially with the reduction of the inter-particle gap, if the embedding refractive index stays constant. Using BEM simulations (Becker, 2010), the obtained data points for a dimer consisting of two gold spheres with a diameter of 60 nm in $n=1.33$ are fitted best by a stretched exponential function (see figure 2.11):

2. Theory

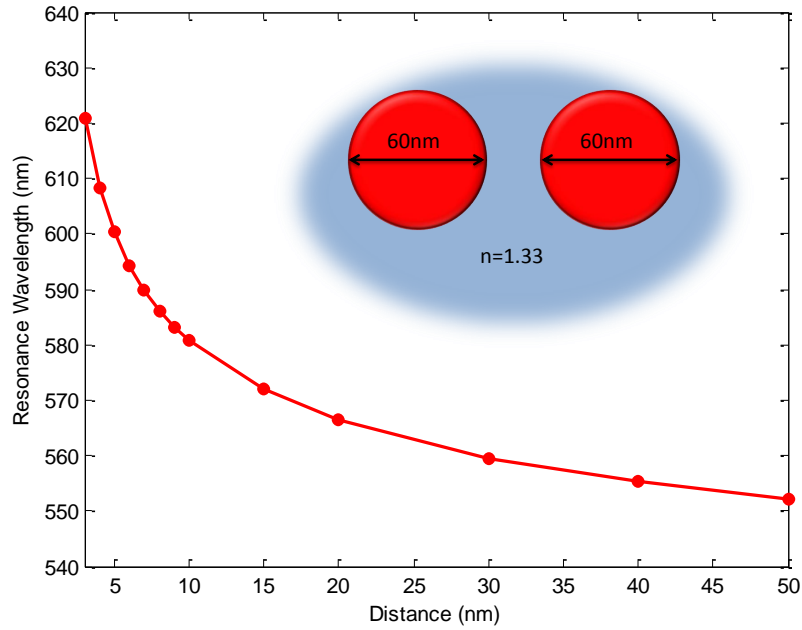


Figure 2.11.: Dimer in Water (BEM)

BEM-simulations of a dimers of two 60 nm gold nanoparticles in water for different inter particle distances show an exponential behavior.

$$\lambda = 552.7\text{nm} \cdot \left[1 - \exp\left(\frac{\text{interparticle distance (nm)}}{-15.2}\right) \right]^{-0.067} \quad (2.26)$$

Using equation 2.26 and the sensitivity 2.25 of the long axis, the resonance position of the longitudinal plasmon mode in various refractive index media for different inter particle distances can be calculated (see figure 2.12).

If both, inter-particle distance *and* refractive index change at once, the only way to determine both variables is to measure the resonances of the transverse *and* longitudinal axis. Using the information from the transverse axis to determine the refractive index first, the resonance of the longitudinal one can thereafter be used to calculate the inter particle distance.

So far only the inter-particle distance and the refractive index medium were varied in the simulations as well as in the experiments presented in chapter 6. Nevertheless, others also studied the behavior of nanoparticle pairs, if both, inter-particle gap *and* particle diameter change. Plotting the ratio of shift $\Delta\lambda$ (between dimer and monomer) over resonance wavelength of the monomer λ_0 versus inter-particle gap over diameter (of the monomer), a single exponential decay law is found, independent from the absolute size of the single particle or their shape (Jain *et al.*, 2007).

$$\frac{\Delta\lambda}{\lambda_0} \propto k \cdot \exp\left(\frac{-\text{interparticle distance (nm)}}{a \cdot \text{diameter single particle (nm)}}\right) \quad (2.27)$$

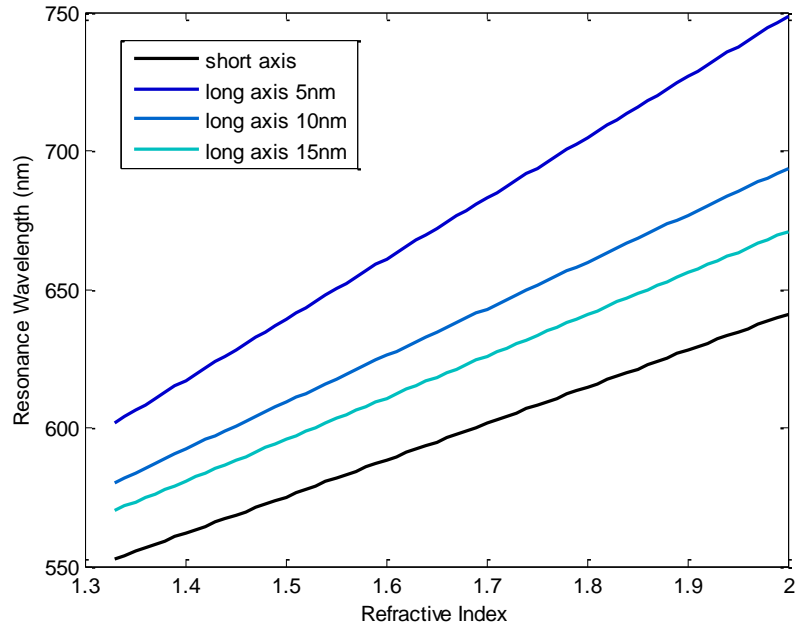


Figure 2.12.: Resonance of Short and Long Axis over Refractive Index

Using equations 2.26 and 2.25 and the sensitivity of the short axis, the resonance position of long and short axis for different separation distances of gold nanospheres in increasing refractive index media is calculated.

The pre-factor k (amplitude of the single exponential function) increases for increasing embedding refractive index, as well as the decay constant a . For a refractive index of 1, k calculates to 0.16 and a to 0.2 (other values see (Jain *et al.*, 2007)). If one assumes that $\frac{\Delta\lambda}{\lambda_0}$ only represents the near-field coupling strength, one can see that the coupling strength falls exponentially over $a \cdot \text{diameter}$ of the single particle in nm, meaning that for larger particles the near-field coupling extends over larger distances than for smaller ones. This scaling law is applicable no matter which material or shape is used. This can be explained by the simple picture of dipolar coupling. The strength of the inter-particle near-field $\frac{\Delta\lambda}{\lambda_0}$ is determined by two factors: the polarizability of the particles, which is proportional to the volume r^3 and the decay of the field with the distance s , that is expressed by $\frac{1}{s^3}$. Therefore the coupling strength is a function of $\left(\frac{r}{s}\right)^3$ and independent from further parameters. This general size-scaling is still valid, even if a more precise treatment of the inter particle interaction is done, by introducing higher multipole interaction (quadrupole, octupole,...). For example for octopoles, the polarizability is proportional to r^7 and at the same time the distance dependency scales with $\frac{1}{s^7}$. The resulting decay is of course steeper by including higher multipole interactions compared to a purely dipolar view.

3. Why anisotropic? A Growth-Model for Gold Nanorods

In order to use plasmonic nano particles in applications, it is crucial to have access to high-quality particles, which preferentially monodisperse and specially designed to fulfill external needs like given laser-wavelengths or pre-defined sizes. To do so, it is of high importance to know factors influencing the synthesis and to understand the mechanism behind the anisotropic growth. In the following chapter, a model for the anisotropic growth of gold nanorods is presented, which explains why anisotropic shapes form at all and how variations in the synthesis lead to higher (or lower) fractions of nanorods compared to spheres. It turns out that there are several factors, which need to be fulfilled to do a successful synthesis. Besides the presence of surfactant to stabilize the growing particles, also a certain amount of bromide and silver are crucial, as well as a small electrochemical potential difference between reducing and oxidizing reaction partners to allow for slow growth.

3.1. Motivation

Optical, catalytic and photothermal properties of noble metal nanoparticles attract much interest, thus size, shape and dielectric constant (or refractive index) of the metal surrounding environment become potential tunable parameters (Eustis & El-Sayed, 2006; Jain *et al.*, 2008). For anisotropic shapes such as gold nanorods, the plasmon mode splits into two bands, the longitudinal one tunable by the aspect ratio (nanorod length/width ratio) (Murphy *et al.*, 2005; El-Sayed, 2001). This provides the opportunity to tune the resonance band to match external experimental conditions like an excitation laser wavelength. The elongated shape, on the other hand, makes possible both, a spontaneous self-assembly into a close packed order with a side-by-side and end-to-end alignment (Nikoobakht *et al.*, 2000) and a guided assembly mediated by bifunctional ligands and biomolecules (Caswell *et al.*, 2003). Additional crystallographic facets, which are not present in a spherical nanoparticles and which exhibit different thermodynamic (Wang *et al.*, 1999) or catalytic properties (Zhang *et al.*, 2008; Lee *et al.*, 2006), originate from

3. Why anisotropic? A Growth-Model for Gold Nanorods

a rod-like shape. Different “synthetic” pathways like E-beam lithography, photo- and electro-chemical techniques (Kim *et al.*, 2002; Yu *et al.*, 1997), and soft-chemical routes (Nikoobakht & El-Sayed, 2003) are explored. The latter one being at the same time the most flexible, resulting in single-crystalline particles not restricted to any surface, but as well the most unpredictable one concerning influences of additives and reaction conditions. Open and discussed questions are: the source and reason for anisotropic growth in general, accompanied by the surprisingly high yield of anisotropic particles. Those fundamental questions are important not only for gold nanorod synthesis, but insights into the growth may also help to tune and understand growth of other materials or different shapes. Furthermore, in the light of the above mentioned effects, it is critical to carefully control and tune the gold nanorod growth in order to achieve a uniform nanoparticle distribution and thereby uniform properties.

In the seed-mediated growth approach, seed particles are added to a growth medium to facilitate the reduction of metal ions. Murphy *et al.* (Johnson *et al.*, 2002) have proven that the injection of 3-4 nm Au seeds in the presence of ascorbic acid as reducing agent, induces the heterogeneous nucleation on the gold precursor seed-particles. El-Sayed and coworkers reported the dependence of the aspect ratio (length to width ratio) of gold nanorods on the silver content (Nikoobakht & El-Sayed, 2003). However, the question remains how all reaction partners mechanistically work together in order to form long resonance wavelength gold nanorods in high yield. A deeper insight into the mechanism will allow to more specifically tune the outcome of a gold nanorod synthesis and will lead to fundamental understandings of nanoparticle growth, also applicable to other materials and shapes. Different possible mechanisms are described and discussed (Huang *et al.*, 2009), including electric-field- (Perez-Juste *et al.*, 2004), and surfactant-preferential-binding-directed growth (Murphy *et al.*, 2005), or under-potential deposition of silver (Liu & Guyot-Sionnest, 2005; Orendorff & Murphy, 2006), but none of them answers all mechanistic questions.

In this chapter I present a model for the growth of gold nanorods, which answers three main questions concerning the growth mechanism, namely the reason for anisotropic growth, the high yield of anisotropic particles, and the observed trends upon changes in the synthetic pathway. A systematic study on the influence of internal parameters in the synthesis is performed, using spectral data and transmission electron microscopy for sample analysis. Besides the role of the surfactant CTA⁺ as selective stabilizer of the growing nanoparticles in the unusual *anisotropic growth*, for the first time the electrochemical potential difference between reducing and oxidizing species, namely ascorbic acid and gold ions, is identified as essential parameter for anisotropic growth. *High yield* due to the adsorption of silver bromide and the slow growth speed due to the small electrochemical potential difference, as well as the observed *trends* like an increased aspect ratio due to ionic strength increases, charge screening of the micelles, and changes in the electrochemical potential/ environment are explained.

With this new knowledge, fine-tuning of the synthesis of gold nanorods is possible in a more defined way. Using the electrochemical information, a possible reason for “good” or “bad” growth conditions is determined. Potentially, electrochemical conditions are important as well in the synthesis of different metallic nanoparticles, the (unsuccessful) growth of them might be influenced more than it was thought so far by the choice of reducing agent and electrochemical potentials.

3.2. The Growth Model

The general route to produce gold nano rods is briefly described in the following:



In a first step, small gold seeds are formed by reducing tetrachloro-auric acid (HAuCl_4) in cetyltrimethylammonium bromide (CTAB) with sodium borohydride, a strong reducing agent. These preformed seeds are single crystalline (Liu & Guyot-Sionnest, 2004). In a second step, a small amount of seed solution is injected into the growth solution, containing HAuCl_4 , AgNO_3 , ascorbic acid and CTAB, in order to promote the growth of gold nanorods. Their growth can be observed optically (see figure 3.1). The addition of CTAB to the HAuCl_4 solution causes a color-change from pale yellow to orange, an indication that gold bromide complexes are formed. Ascorbic acid reduces Au^{III} to Au^{I} , which is finally reduced to elemental gold on the surface of the seeds to form gold nanorods. The color of the formed gold nanorods depends on their aspect ratio. The higher the aspect ratio, the further in the red the corresponding resonance wavelength of the plasmon is.

These nanorods exhibit different facets of the gold fcc-lattice on the sides and the tips. All proposed structural models (Murphy *et al.*, 2005; Wang *et al.*, 1999; Johnson *et al.*, 2002; Huang *et al.*, 2009) have in common that the crystal facets on the sides are of higher surface energy than the tips (Wang *et al.*, 2000). Beside those similar crystallographic models, a new model proposed by Garg *et al.* (Garg *et al.*, 2010) claims that the final gold nanorod consists of four {111} and two {100} facets on the sides and of {110} facets on the tips. They explain the anisotropic growth by the etching of less stable facets with bromide ions and therefore growth along the high surface-energy facets is observed. This is an innovative new idea and not (yet) well established in literature. Since in the following experiments it is shown that gold nanorods can as well be formed without any bromide, this model is not regarded further. A precise description of the carried-out syntheses and the variation parameters, including UV-Vis spectra and TEM-data is

3. Why anisotropic? A Growth-Model for Gold Nanorods

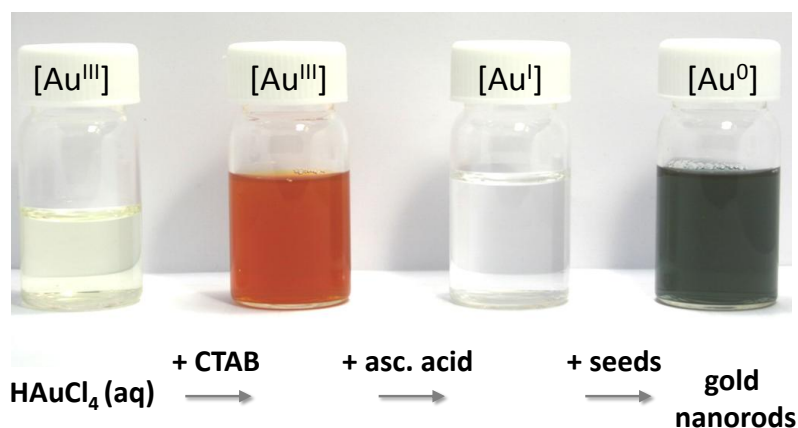


Figure 3.1.: Pictures of the Gold Nanorod Synthesis

True color pictures of the steps in the synthesis of gold nanorods. After the addition of CTAB to HAuCl_4 a color change from light yellow to orange is observed, indicating the formation of gold-bromide complexes. The addition of ascorbic acid causes decolorization, Au^{III} is reduced to Au^{I} . Finally gold nanorods are formed on the surface of the seeds.

given in appendix C.1.

The proposed model to explain the growth of the gold nanorods contains the following reaction partners and mechanisms: Gold is reduced in two steps. The initial Au^{3+} ions are reduced to Au^+ by ascorbic acid which forms a diketon (Pérez-Juste *et al.*, 2005). This can be seen by the decolorization of the solution. Formerly colored charge-transfer complexes that were built with CTAB and Au^{3+} are destroyed, the color fades. Since ascorbic acid is not “strong” enough to reduce Au^+ to elemental gold, seeds need to be added to provide a catalytic surface (Murphy *et al.*, 2005), on which via underpotential deposition (UPD) elemental gold is deposited, while ascorbic acid is oxidized. In order to induce anisotropic growth, CTAB is added in a concentration above the first cmc (1 mM (Tong *et al.*, 2010)). This ensures the presence of CTA^+ micelles, which can diffuse to the side facets to passivate those from further growth (Gao *et al.*, 2003; Murphy *et al.*, 2005; Johnson *et al.*, 2002). Additionally, these micelles might be loaded with metal-salt complexes (Pérez-Juste *et al.*, 2005) and provide them to the places (sides and/or tips) where growth happens. Introducing silver into the reaction mixture gives the possibility to form silver bromide and silver bromide-complexes (along with the bromide that came with the CTAB), which helps the CTA^+ to passivate the surfaces (Nikoobakht & El-Sayed, 2003). Increasing the ionic strength via chloride or nitrate ions increases the size and alters the shape of the CTA^+ micelles (Ono *et al.*, 2005). They are bigger and less charged, which makes them slower diffusing. Therefore, the reaction is slower and more selective, meaning the preferred growth at certain facets is even more pronounced. Furthermore, the electrochemical potential of the growth solution is tuned below 1.12 V, ensuring slow growth and high selectivity/ anisotropy.

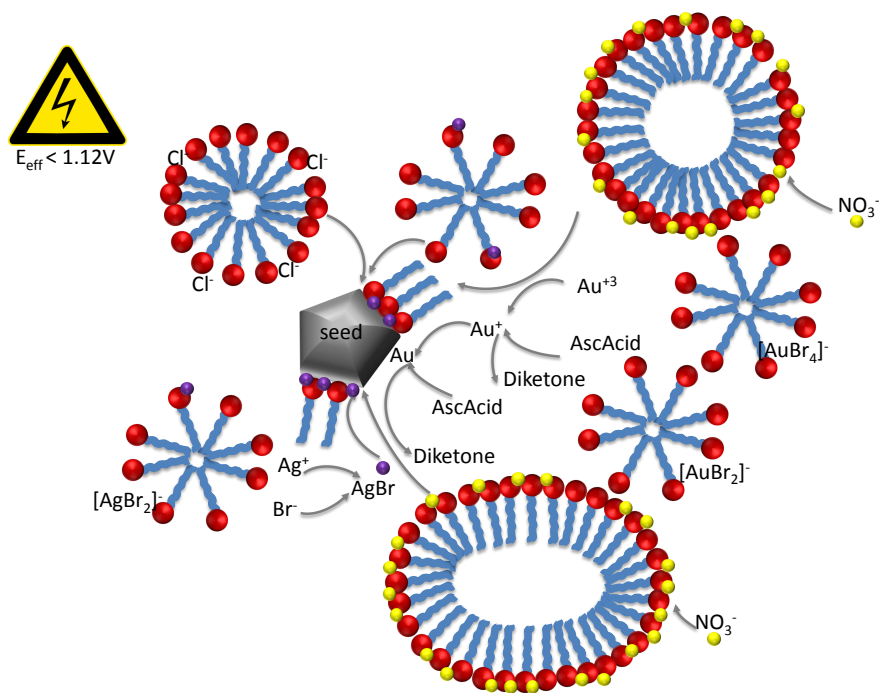


Figure 3.2.: Model for Gold-Rod Growth

Gold nano rods are grown via the surface-catalyzed reduction of gold ions by ascorbic acid. The anisotropic growth is promoted by CTA^+ micelles via the passivation of side facets by CTA^+ molecules, which are helped by silver bromide that reduces electrostatic repulsion between the charged headgroups. Nitrate and chloride ions increase the aspect ratio of the rods by slowing down the reaction speed due to bigger and elongated CTA^+ micelles. The overall electrochemical potential of the growth solution has to be below 1.12 V.

3. Why anisotropic? A Growth-Model for Gold Nanorods

The effective electrochemical potential is calculated using the electrochemical potentials of AuCl_2^- / AuBr_2^- , weighted by their molar fraction and corrected for the concentration of chloride and bromide in solution. A detailed description of the calculation is given in appendix C.1.4.

A complete mechanistic model for the growth of the gold rod synthesis has to fulfill three main demands: It has to explain 1) the anisotropic growth, 2) the yield of the desired anisotropic shape, and 3) trends due to variations/ additions of reactants. The two former ones are possible to be explained by a minimalistic model. The anisotropic growth happens, if CTA^+ is present in the solution in a concentration above the first cmc (see figure 3.3). Therefore, not only the adsorption of CTA^+ at the side facets, but also the existence of micelles in solution is critical. In growth solutions with the CTAB concentration below the first cmc (1mM), the effective electrochemical potential (for further details see C.1.4) is 1.13 V. This coincides with the fact that for successful gold nanorod growth the E_{eff} needs to be tuned below 1.12 V. The yield of rods is tremendously increased by the addition of silver *and* bromide (see figure 3.4). A better adsorption and closer packing of CTA^+ molecules on the side facets accompanied by AgBr is possible, increasing the strength of passivation.

3.2.1. Anisotropic Growth

In order to explain purely the anisotropic growth of rods, a simplified system compared to the above stated model (see figure 3.2) can be used. The reaction partners gold and ascorbic acid meet at the surface of the preformed seed, ascorbic acid reduces gold to elemental one, autocatalyzed by the surface, to promote growth. Additionally, the cationic surfactant CTAB is added to the solution in concentrations above the first cmc (1mM, (Tong *et al.*, 2010)) in order to provide CTA^+ to passivate the side facets from growth, and therefore direct the growth into one direction. The selective adsorption of CTA^+ on different gold surfaces seems to have the most influence (Johnson *et al.*, 2002). CTA^+ selectively accommodates specific crystallographic facets of the fcc Au nanostructure, energetically stabilizing them and allowing the unidirectional growth of the higher energy surfaces (Gao *et al.*, 2003; Murphy *et al.*, 2005). Furthermore, the CTA^+ micelles can be loaded with metal ions or metal halides (complexes). These CTA^+ micellized gold ions and the collisions between the rods' tips and the gold ions (CTA^+ micellized) are believed to act as the determining step in the rod formation (Pérez-Juste *et al.*, 2005; Pérez-Juste *et al.*, 2004). It seems that in this minimalistic mechanism, already all crucial aspects for rod-formation are included. Indeed, one finds rod shaped nanoparticles in syntheses, where the CTAB (or CTAC) concentration is raised above 1 mM (see figure 3.3 and TEM and spectrum of sample 12ii in appendix C.1). This accounts for a strong influence of CTA^+ micelles on the growth mechanism. It cannot be stated, if CTA^+ micelles are more attracted to the sides and therefore passivation is better. Or if metal-loaded micelles are more attracted to the tips and therefore growth there is faster. It seems reasonable that the formation of a densely packed CTA^+ layer on the sides of the growing rod is energetically favored since the hydrophobic tails can perform

Van-der-Waals interaction. Furthermore, if CTA^+ is used in concentrations below the CMC, single CTA^+ molecules instead of whole micelles diffuse. This would make the overall reaction speed much faster, selectivity of passivation or directed growth is reduced, isotropic reaction products are observed. If no CTAB is added, spherical reaction products form, which aggregate briefly after the synthesis, since neither steric nor electrostatic stabilization is provided. Also the electrochemical potential of the growth solution is taken into account. It can be calculated using a combination of law of mass action, stability constants of the gold-halide complexes, and fractional charge of CTA^+ micelles (for details see appendix C.1.4). Doing this, an effective electrochemical potential of the growth solution of less than $E_{\text{eff}} = 1.12 \text{ V}$ is needed in order to create an environment to form gold nanorods. This is also seen when looking at mixtures of CTAB and CTAC, where rods are only grown if the chemical potential is low enough, even though in all cases the concentration of CTA^+ is the same (well above the first cmc). It seems that the potential difference between E_{eff} and ascorbic acid needs to be small to ensure a slow reduction of gold and along with this a low reaction speed and high selectivity, leading to an anisotropic growth. Nevertheless, the yield of rods without the presence of bromide *and* silver in the reaction mixture is low compared to a “full” synthesis including all chemicals.

3.2.2. High yield

In addition to the system mentioned in figure 3.3, introducing silver *and* bromide ions in the solution leads to an increased yield of rods (see spectra and TEM figure 3.4). This increase in yield can have different reasons: The reduction of silver on the surface, charge screening of the micelles due to bromide, or the formation and adsorption of silver bromide. The reduction of elemental silver on the surface of the seed or growing rod, as proposed by Guyot-Sionnest and Orendorff (Liu & Guyot-Sionnest, 2005; Orendorff & Murphy, 2006) via "under potential deposition" (UPD), seems unlikely, since in the experiment where silver is present but no bromide, the yield of rods is not measurable (for example sample 20i, see appendix C). The charge screening of the CTA^+ micelles by Br^- is more reasonable. Ono et al. (Ono *et al.*, 2005) found that anions have some effect on size and shape of the CTA^+ micelles. The more chaotropic the anion, the higher the effect and the bigger the CTA^+ micelles. Since in the experiment where no silver but bromide was present, a reasonable amount of rods is found, it sounds likely that the more chaotropic anion bromide alters the micelles in higher extent, gold nanorod growth is promoted. Chloride is more kosmotrop than bromide. In the case where only chloride is present and *no* silver (see figure 3.3, gray spectrum and TEM-image), much less rods are formed, whereas in the experiment that has silver *and* chloride no rods at all can be seen in the TEM images. Therefore, a pure effect on the micelles due to bromide or chloride is not possible. The combination of silver *and* bromide, and the formation of AgBr and $[\text{AgBr}_2]^-$, which might be incorporated between the CTA^+ headgroups as AgBr pairs (Nikoobakht & El-Sayed, 2003) to reduce the repulsion between the headgroups on the gold surface; or to the epitaxial formation of

3. Why anisotropic? A Growth-Model for Gold Nanorods

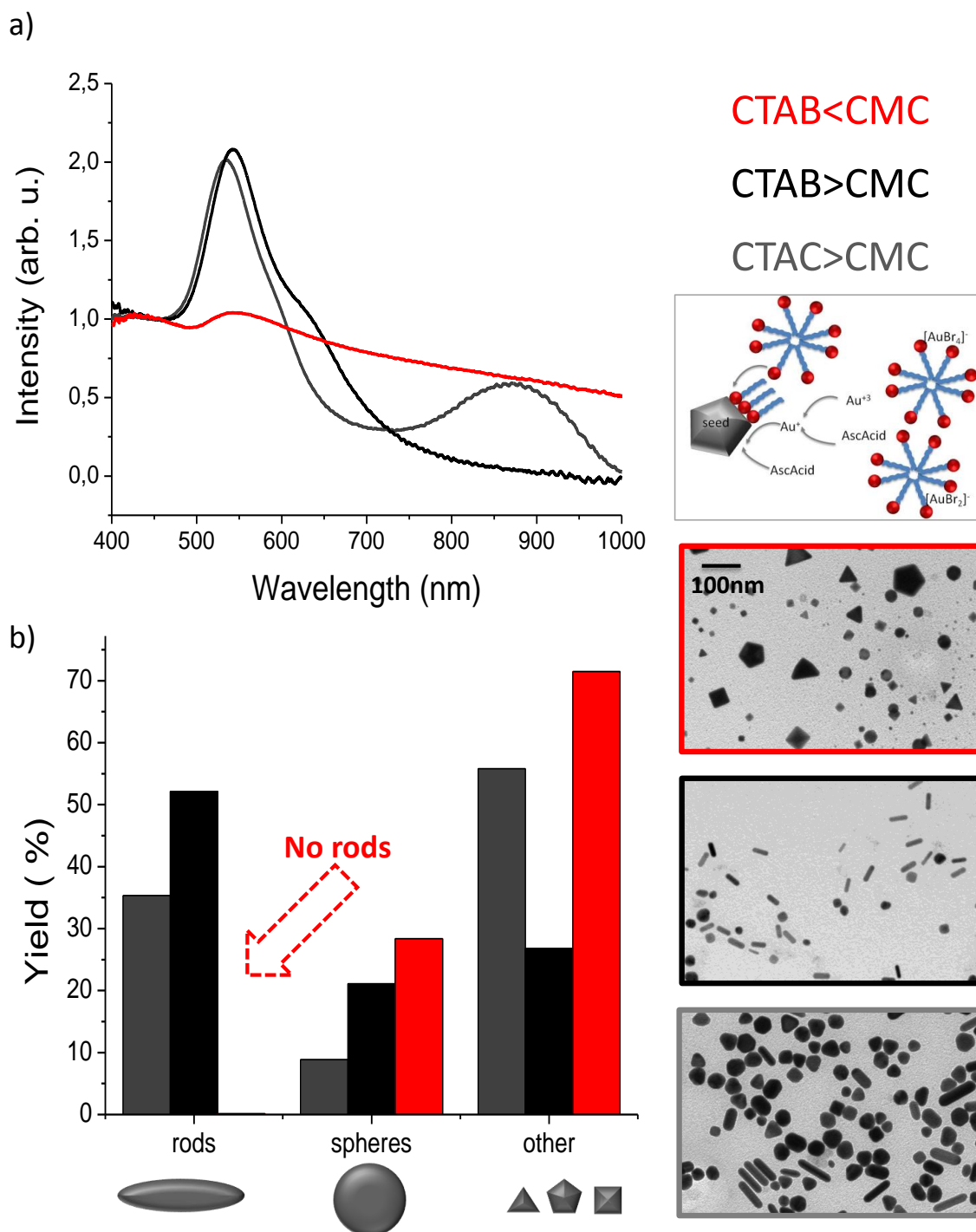


Figure 3.3.: Anisotropic Growth

Optical spectra (a) and TEM statistics (b) of three gold-nano rod syntheses carried out in CTAB < CMC (0.5 mM, red), CTAB > CMC (2 mM, black) and CTAC > CMC (100 mM, gray) without AgNO₃ present. The scalebar of all TEM-images is 100 nm. In the two syntheses with CTA⁺ > CMC (1 mM), rods are formed.

AgBr monolayers on specific faces inhibiting their growth (Murphy *et al.*, 2005) seems to be the case. Silver chloride seems not to fit onto the gold surface or between the CTA⁺ headgroups in the same manner as silver bromide. An unselective adsorption of AgCl on all gold facets and hindered growth in all directions, resulting in relatively small spheres, is expected and seen by experiments (see figure 3.4 gray spectrum). Besides [AgCl₂]⁻ and [AgBr₂]⁻ complexes, halides can also form complexes with gold ions and bind to the surface of the growing nanoparticle, which end in an effective electrochemical potential of the growth solution E_{eff} . Other experiments (see chapter C.1.2) show that the potential needs to be below 1.12 V in order to form rods. It is found that in both cases, CTAB+Ag and CTAC+Ag, the potential is below this threshold. Therefore, the existence of AgCl (and its unselective adsorption) is most likely the reason for the sphere-growth in this case (figure 3.4 gray spectrum).

Therefore, in the presence of chloride, kinetics might be changed (see also trends). Furthermore, discussed here is only the “final” structure of the particle: rod-shape or spherical. The internal crystallographic design might be different for cases with or without silver, with chloride and/or bromide. It might be unavoidable to study and discuss this in more detail in future experiments.

3.2.3. Trends

After understanding the reason for the anisotropic growth as well as the possibility to have high yields of rods, it is important that the above stated model (figure 3.2) also explains the observed trends upon variations and additions of reactants. Looking at the general reaction, there are plenty of things to be varied (see figure 3.5). Increasing the seed concentration increases the resonance position of the gold nanorods. A similar trend can be seen for an increase in CTAB concentration as well as for an increased bromide or chloride concentration. In contrast to those, increasing silver or nitrate, the resonance position has an optimum and decreases again if the concentration is too high. Furthermore, the ratio between silver, bromide, and chloride has a big influence to the finally prepared rods. In the following the trends will be treated separately from each other in more detail.

Variation of Seeds

The use of more seeds for the synthesis of gold nanorods results in the formation of rods with higher resonance wavelengths until a plateau is reached. The yield (measured by the ratio of the intensities between longitudinal and transverse peak, corrected for the theoretical value of 100 % yield of monodisperse rods, see also appendix C.1.2) of the rods stays more or less constant (see figure 3.6). According to the model (figure 3.2), the surface of the seed (or later on the surface of the growing gold nano rod) is the crucial location for reduction of gold ions to elemental gold. Providing more surface should speed up the reaction. In SAXS experiments (Henkel *et al.*, 2009) combined with optical spectroscopy it is found that initially the gold rods grow longer but at a certain point in time (where width- compared to length-growth-speed exceeds

3. Why anisotropic? A Growth-Model for Gold Nanorods

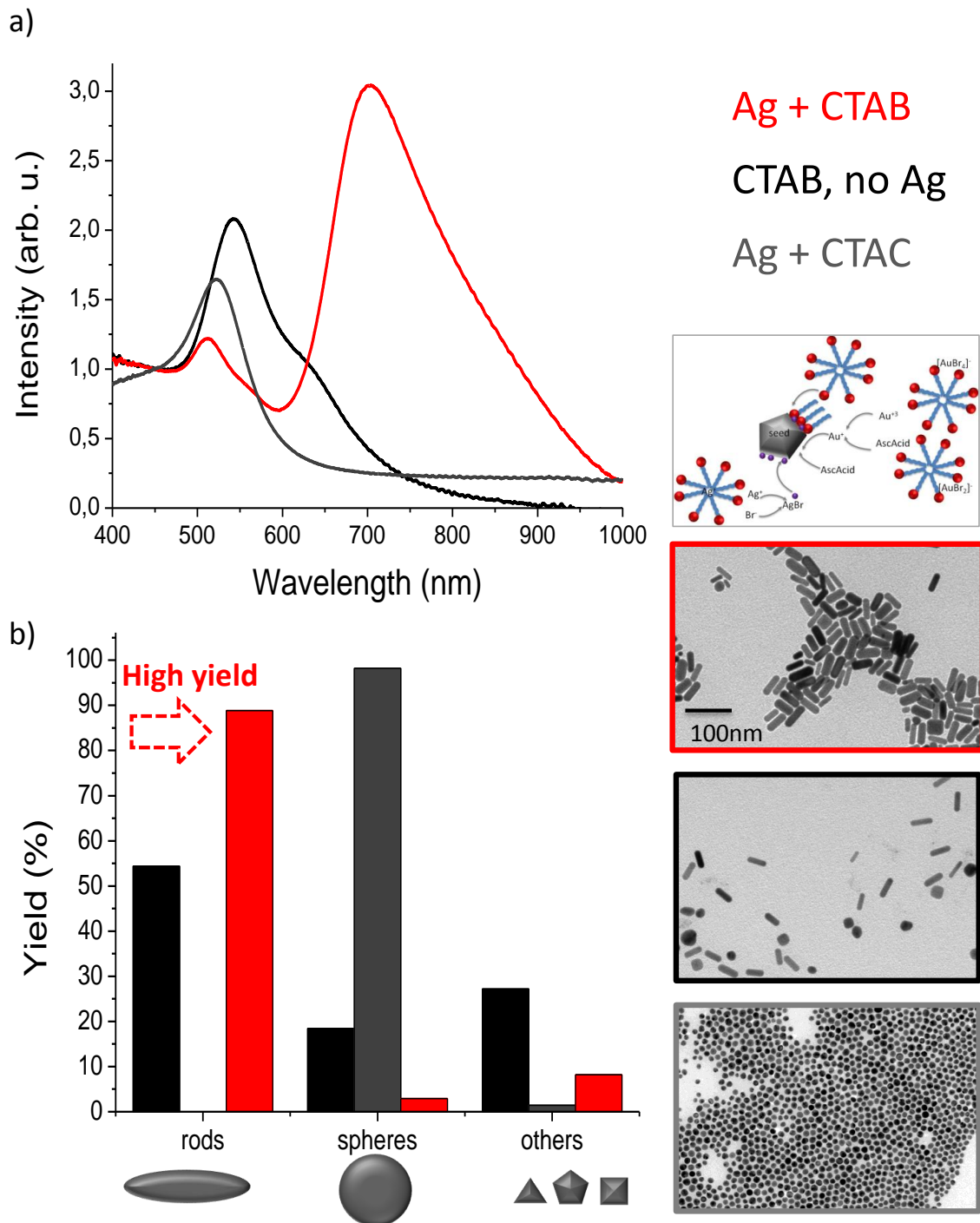


Figure 3.4.: High Yield

Optical spectra (a) and TEM statistics (b) of three gold nano rod syntheses carried out with AgNO_3 and CTAB (red), no AgNO_3 in CTAB (black), and with AgNO_3 in CTAC (gray). The scalebar of all TEM-images is 100 nm. The concentration of CTA^+ is 0.1 M. Only the combination of AgNO_3 and CTAB results in a high yield of rods, while pure CTAB produces less rods and the combination AgNO_3 and CTAC yields only spheres.

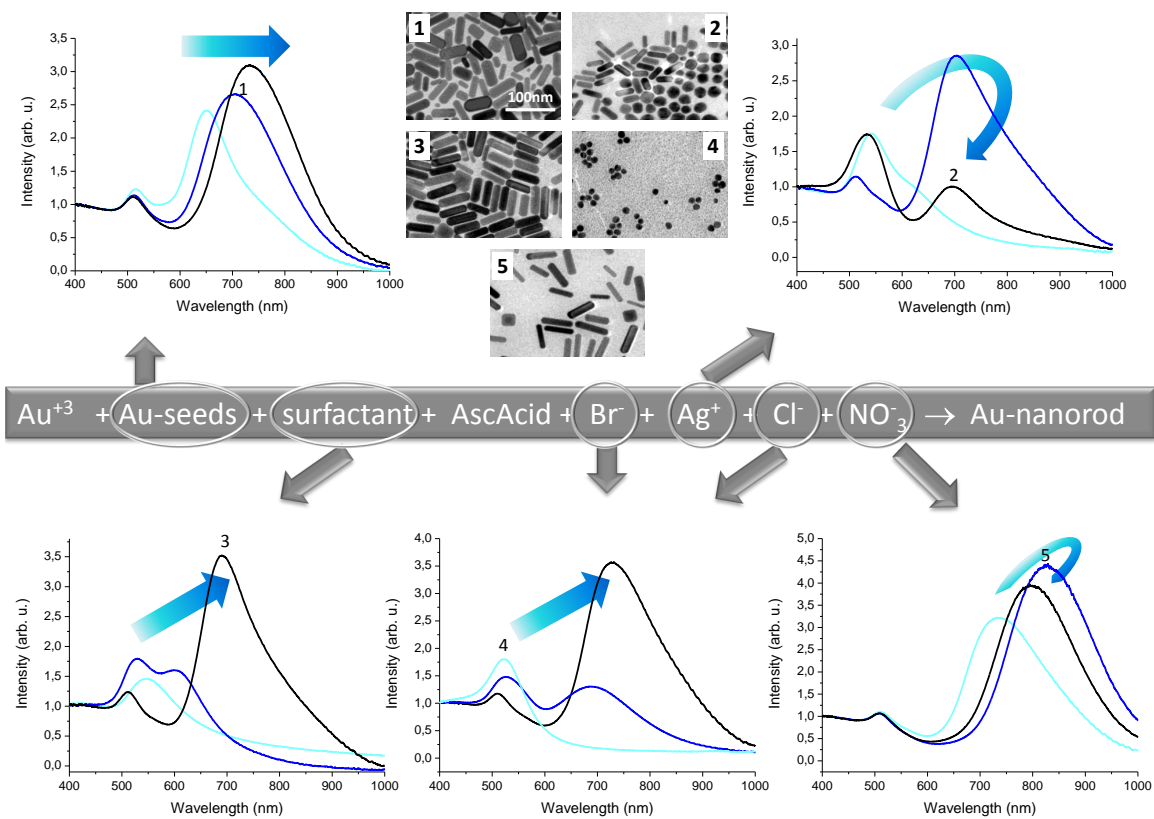


Figure 3.5.: Overview Over Trends

Overview over the trends observed upon variation of different parameters in the synthesis. Besides optical spectra, some selected TEM images are shown. The scalebar (100 nm) is the same for all images. Spectra and TEM images of all syntheses are given in appendix C.1.2 and C.1.3.

3. Why anisotropic? A Growth-Model for Gold Nanorods

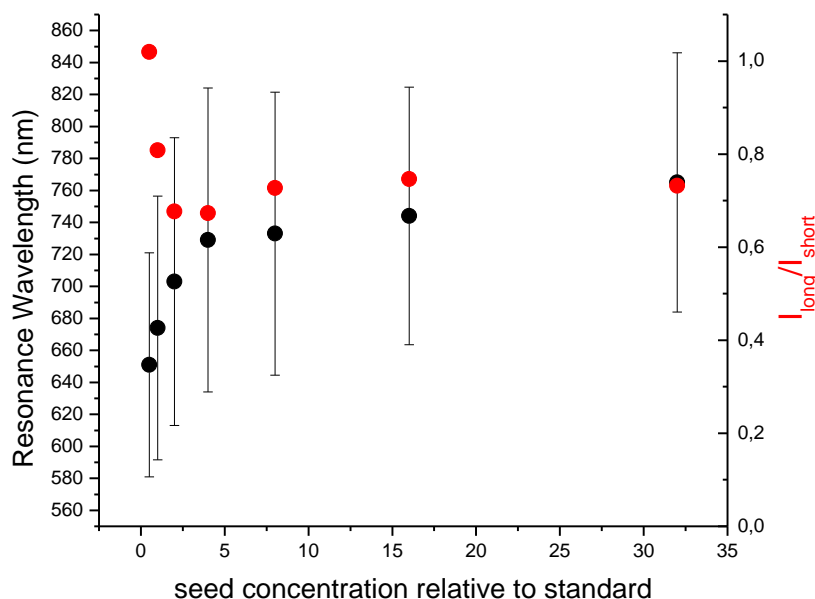


Figure 3.6.: Variations of Seeds

Increasing the concentration of seeds (given as factor compared to standard synthesis with 12 μl seeds) leads to an increase in the resonance wavelength (black) while the yield of rods (red) stays high. The errorbars correspond to the line width of the ensemble spectrum. The yield of rods is calculated from the ratio between longitudinal and transversal peak, corrected by theoretical values (see appendix C.1.2).

the current aspect ratio) they grow fatter. Increasing the reaction speed by increasing the seed concentration means as well that the reaction is over earlier, eventually before or close after this turning point. Therefore, the rods don't have a chance to grow in width again, an increased resonance wavelength is observed for increasing seed concentration. If more reaction centers are present in the beginning, the depletion in Au-ions concentration is faster. For later times in the reaction it is easier to form one more monolayer of gold on the tips than on the sides, since the absolute number of ions needed for one more layer of atoms on the lateral shell is 3 times higher than on the tips, already for an aspect ratio of 1.5 (Seyed-Razavi *et al.*, 2011). The lack of kinetic information in the presented experiments does not allow to clarify this effect in more detail.

Silver

The addition of silver nitrate to the growth solution is essential to form gold nanorods in a reasonable yield (see chapter 3.2.2). Increasing its concentration (at a given bromide concentration, which is at least 250 x higher than the concentration of silver) leads- up to a certain limit- to an increase of the resonance wavelength (see figure 3.7a). Doing a TEM analysis of the samples with varying AgNO_3 concentration, a similar trend can be observed as seen in the spectra before. The aspect ratio increases up to a certain point (AgNO_3 concentration 0.2 mM) and decreases slightly afterward (figure 3.7a). Looking at the fraction of rods compared to spheres by comparing peak intensities (corrected for the theoretical value of 100 % rod yield, see appendix C.1.2), one can see that the yield of rods decreases when overcoming a silver concentration of 0.1 mM.

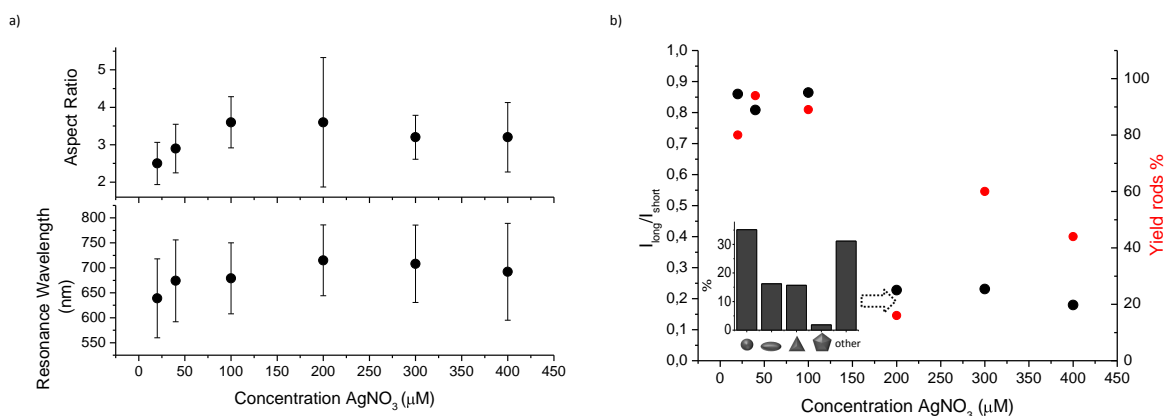


Figure 3.7.: Variation of Silver nitrate

(a) Increasing the AgNO₃ concentration leads to a maximum in the resonance wavelength (black) and the aspect ratio (red) at a concentration of 0.2 mM. (b) The yield of rods measured by TEM (red) or optical spectra (black) has an optimum at a silver concentration of 0.1 mM. The inset shows that for 0.2 mM AgNO₃ a significant amount of triangles is grown.

Supporting this, the fraction of rods in TEM measurements decreases after its maximum (see figure 3.7b). It is interesting to notice that photochemical (Kim *et al.*, 2002), electrochemical (Yu *et al.*, 1997) and seeded-growth- method (Nikoobakht & El-Sayed, 2003) rely on the Ag⁺ ion addition for promoting the rod-shaped-growth. Recent results assign to Ag⁺ ions a possible role in precipitating on {110} GNR surfaces preferentially than on {100} or {111} as under-potential reduced Ag (Liu & Guyot-Sionnest, 2005; Orendorff & Murphy, 2006) or as AgBr reacting with Br⁻ ions from CTAB (Murphy *et al.*, 2005). A robust confirmation of the favorable silver deposition on the {110} of a gold nanorods comes from the growth of a thick shell of silver on GNRs (Becker *et al.*, 2008). Nevertheless, the confirmation of silver in the particles (by elemental analyses) is not well affirmed.

The observed trends, having an optimum silver concentration for high aspect ratio rods as well as for high yield syntheses underpin the above stated role of silver bromide in the solution. If it is not present, CTA⁺ may provide some passivation of the side facets, but not very strongly. Rods can be formed, but their yield and aspect ratio are low. If an adequate concentration of silver bromide can be formed, the side facets are better passivated than the tips, an elongation of the rod is favored. High yields of high aspect ratio rods are observed. If too much silver bromide is there, sides and tips are similarly passivated, growth is not hindered in one direction more than in the other, the yield of rods decreases again. Interestingly, the aspect ratio is not significantly reduced, meaning that the rods that form are similar to those under optimum reaction conditions. A possible explanation might be that those rods that are formed grow with the help of AgBr, provided via micelles, in the same manner as under optimum conditions. For statistical reasons, they meet silver- and gold-loaded micelles, growth along the rod is promoted. If too many micelles are loaded with AgBr or [AgBr₂]⁻, there will be rods that only meet silver loaded micelles and not gold-loaded ones. Therefore, they will grow into spheres rather than rods. A

3. Why anisotropic? A Growth-Model for Gold Nanorods

different explanation might be the fact that a once grown rod easily grows further in a rod-shaped fashion (CTA⁺ building a (double)layer on the sides, stabilized by Van-der-Waals interaction), whereas spherical ones don't. Therefore, the presence of [AgBr₂]⁻ might be crucial in the very beginning of the synthesis, in order to produce a high amount of small rods from the seeds, which can further on enlarge and form bigger rods. In all the syntheses the concentration of Ag and Br exceeds the solubility product of AgBr ($5 \cdot 10^{-13} \frac{\text{mol}^2}{\text{l}^2}$, (CRC, 2004)). Nevertheless, no AgBr precipitate is found. The reason might be that in the presence of CTA⁺-micelles, AgBr rather sticks to the micelles than precipitates (Hubert *et al.*, 2008).

It seems that the described trends for increasing seeds (increasing aspect ratio) and increasing silver concentration (increasing aspect ratio) contradict, since in the ratio silver/seed is decreasing in the former case, whereas it is increasing in the latter one. This is not the case, since in the two experiments different regimes of silver/seed ratio are tested (see appendix C.1.2).

Increasing CTAB-concentration

According to the model (figure 3.2), it is crucial to have CTA⁺ in the solution in a concentration above the first micellar concentration to form rods at all. In order to increase their yield, bromide ions (and silver) need to be added. In the original synthesis, bromide and CTA⁺ are introduced simultaneously by CTAB. It has to be taken care that the concentration of bromide in solution is not equal to the concentration of CTAB used. The fractional charge of CTAB ($\beta = \frac{Z}{N}$, Z=charge micelle, N=aggregation number) can be calculated from its concentration (see appendix C.1.4 and (Aswal & Goyal, 1998; Berr *et al.*, 1992)). A surprising low concentration of bromide is found in solution, while most of the bromides are bound to the micelles (see figure 3.8). Therefore, the concentration of bromide in solution is calculated for each concentration of CTAB used. Varying the CTAB concentration shows that already at a concentration of 2 mM, which corresponds to 0.44 mM bromide in solution (double the 1st cmc which is about 1 mM (Tong *et al.*, 2010)), a rod-peak is visible in the spectrum (see spectrum of sample 14iii in appendix C.1.2). Increasing the CTAB concentration (and simultaneously the bromide one) further causes an increase of the resonance position (see figure 3.9). This might have two reasons. At higher CTAB concentrations, more (and bigger (van Stam *et al.*, 1998)) micelles are present, which seem to promote the growth on the tips rather than on the sides of the rod or lead to better passivation. For bigger micelles, the diffusion constant is bigger, the micelles diffuse slower, the reaction slows down. Therefore, selectivity for the passivation of side facets is higher. Second, the increase in resonance wavelength can also be due to the increase in bromide concentration in solution. Evidence for this is the fact, that for increasing bromide concentrations at a constant CTA⁺ concentration, an increase in resonance wavelength can be seen as well (see figure 3.10). For increasing bromides in solution the effective electrochemical potential decreases, the difference ΔE between E_{eff} and ascorbic acid decreases, the reaction slows down and is more selective.

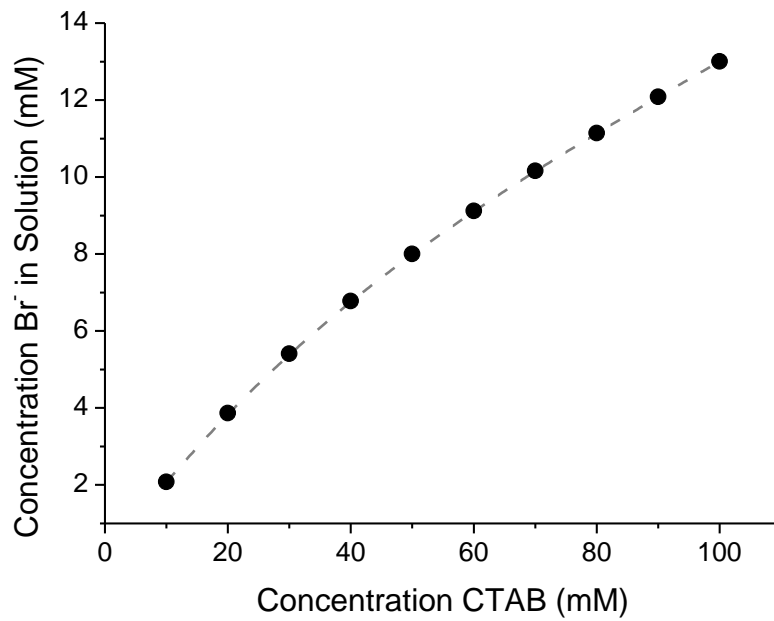


Figure 3.8.: Concentration of Bromide for different CTAB-concentrations
 The concentration of bromide in solution varies a lot with the concentration of CTAB used. Most of the bromide ions are bound to micelles, only a minor fraction stays in solution.

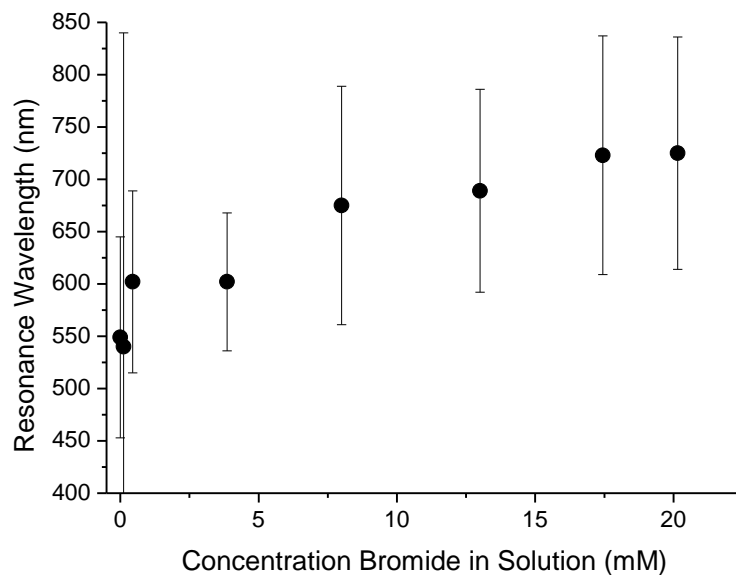


Figure 3.9.: Resonance Wavelength over Concentration of Bromide in Solution
 Increasing the concentration of CTAB increases the resonance wavelength of the formed rods, due to bigger and slower diffusing micelles and/or a smaller effective electrochemical potential in solution.

3. Why anisotropic? A Growth-Model for Gold Nanorods

Variations of CTAB, CTAC, NaBr, and NaCl

In order to test the influence of bromide and chloride separately from each other, syntheses were carried out, which have all 0.1 M CTA⁺, but differ in source and concentration of halides. Three cases are studied: CTAB and CTAC mixtures, CTAB and adding NaCl, and CTAC and adding NaBr. In order to compare the results, the resonance wavelength is plotted versus the total halide concentration in solution (see figure 3.10a), the ratio of bromide to chloride in solution (see figure 3.10b), and the calculated electrochemical potential of the growth solution (see figure 3.11). If chloride and bromide ions are present, the fractional charge of the mixture can be approximated by the mean of the fractional charges of the two components. Furthermore, the exchange constant between chloride and bromide is known (Gamboa *et al.*, 1981). With those two information, one can calculate the concentration of bromide and chloride in solution (and on the micelles). For further details of the calculations of halides in solution and the electrochemical potential, see appendix C.1.4.

Garg *et al.* (Garg *et al.*, 2010) found bromide to be the crucial factor for the growth of gold nanorods. They report that rods can be grown in conditions where CTA⁺ < CMC, but additional bromide is added. This was not tested in the study presented here. They also show that without bromide (but chloride, in the presence of silver) no rods can be grown. Since in our experiments rods in low yield could be synthesized in pure CTAC (without silver), the argument of Garg that bromide is crucial, only holds for syntheses with silver. Also the influence of iodide as a third halide element was studied (Millstone *et al.*, 2008; Rayavarapu *et al.*, 2010) but contradicting results are reported. While Millstone *et al.* report a minimum amount of iodide is crucial to form rods at all, Rayavarapu *et al.* claim even traces of iodide lead to sphere formation.

CTAB/NaCl

Increasing the overall halide concentration in solution by adding NaCl to 0.1 M CTAB, an increase in λ_{res} is observed (figure 3.10, blue triangles). More Cl⁻ ions in solution alter the size and shape of the CTA⁺ micelles, the micelles are less charged, they are bigger and therefore have a smaller diffusion constant (Berr *et al.*, 1992). The reaction speed decreases, the reaction is more selective, longer rods can be grown. This is seen in an increase of the resonance wavelength upon increasing the concentration of total halides in solution.

CTAB/CTAC (black triangles) and CTAC/NaBr (green spheres)

It is possible to increase the bromide concentration in solution by changing either the ratio between CTAB and CTAC (see black triangles figure 3.10) or by adding NaBr to a given concentration of CTAC (see green spheres figure 3.10). In both cases, an increase of the resonance wavelength can be seen. After overcoming a threshold, the formed gold nanorods increase in resonance wavelength. Interestingly, the observed threshold of bromide to chloride ratio is different in the two cases. While for the CTAB/CTAC variation the last synthesis which yields spheres has a ratio of 0.05 (Br to Cl), the CTAC/NaBr case produces the first rods if a

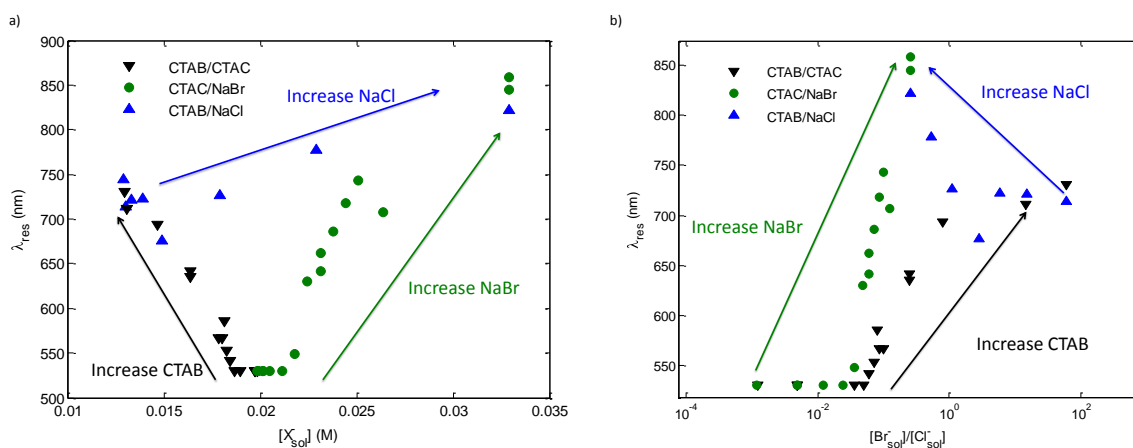


Figure 3.10.: Resonance Wavelength over Halides in Solution

a) Increasing the total halide concentration in solution leads to an increase in the resonance wavelength, if enough bromide is present in solution (blue and green data labels). b) Increasing the ratio of bromide to chloride in solution leads to an increase in the resonance wavelength of the synthesized gold nano rods in the presence of AgNO_3 . If no bromide is present, no rods are formed. The bromide can be provided by CTAB (blue triangles), a combination of CTAB and CTAC (black triangles), or the addition of NaBr to CTAC (green dots).

ratio of 0.024 for Br to Cl is overcome. Since there is no obvious explanation why different ratios are observed, additionally to the halogenides in solution, the electrochemical potential of the growth solution is calculated for each of the syntheses (see appendix C.1.4). Plotting the resonance wavelengths of the produced rods versus this effective potential (averaged redox potential of the Au^+ complexes), the two points for the syntheses which produce spheres fall close together (1.122 V for the CTAC/CTAB case, 1.121 V for CTAC/NaBr). In the plot versus the electrochemical potential, they therefore mark the same value of ~ 1.12 V which needs to be fallen below in order to grow rods. Comparing this value to the “usual” synthesis with only CTAB, for a CTAB concentration of 0.1 M, a potential of 0.987 V is calculated, well below the here stated threshold. On the other hand, for a CTAB concentration of 0.5 mM (which is below the first cmc), the electrochemical potential of the growth solution calculates to 1.125 V, which is above the 1.12 V. Indeed, this synthesis yields only spheres.

A reason for the importance of the electrochemical potential of the growth solution might be the difference between the calculated E_{eff} and the one of ascorbic acid, acting as reducing agent. The redox potential of ascorbic acid depends on the pH (Ando *et al.*, 1997). The higher the pH, the lower the potential. For pH 3, a value of 0.4 V is given.

The growth solution of the gold nanorod synthesis has a pH of ~ 5 , the ascorbic acid’s potential calculates to 0.3 V. The lower the calculated E_{eff} of the gold-complexes, the smaller the difference to the ascorbic acid potential. Smaller differences account for slower reactions, which are in general more selective. A more anisotropic growth is expected and seen in the syntheses. The potential difference ΔE acts as a measure for selectivity. Lowering ΔE , a better selectivity and therefore a higher anisotropy is seen.

3. Why anisotropic? A Growth-Model for Gold Nanorods

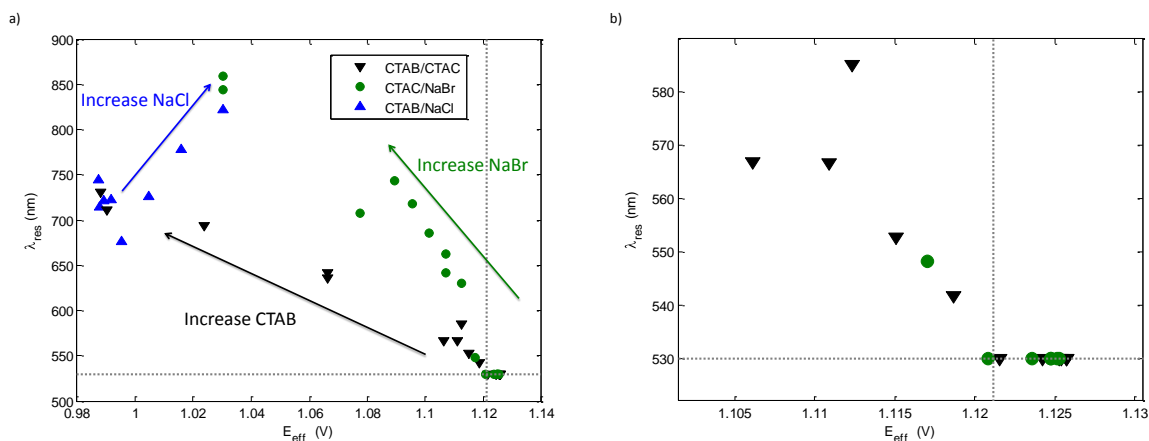


Figure 3.11.: Resonance Wavelength over Electrochemical Potential of the Growth Solution
 a) Plotting the resonance wavelength over the electrochemical potential of the growth solution, one can see that the potential of 1.12 V has to be under-run in order to form rodshaped particles. b) Enlargement of graph a) in the region of interest, around 1.12 V.

Variation of Nitrate

Since silver is introduced as AgNO_3 , also the nitrate ions might have some influence on the formation of gold nanorods. Therefore, a synthesis is carried out at constant CTAB and AgNO_3 concentrations, but with additional HNO_3 (appendix C.1, series 8-11). Increasing the HNO_3 concentrations leads to an increase in resonance wavelength, while the yield of rods stays high (figure 3.12).

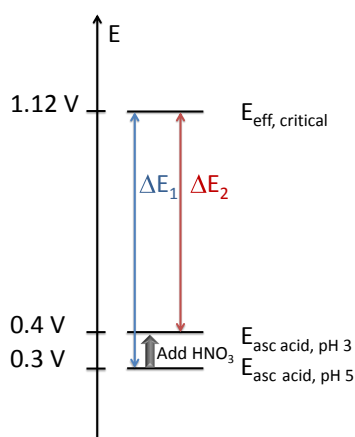


Figure 3.13.: Effective Electrochemical Potential Difference

The redox-potential of ascorbic acid is increased by decreasing the pH. Addition of HNO_3 causes a decrease of the pH, the electrochemical potential difference between ascorbic acid and the effective electrochemical potential of the growth solution is decreased.

As mentioned before, nitrate increases the size of CTAB micelles (Ono *et al.*, 2005) since it incorporates efficiently between the charged hydrophilic head groups and therefore a more dense packing of the molecules is possible. The bigger micelles diffuse slower (indeed, the synthesis takes longer), the directed growth is pronounced and the aspect ratio is increased. This trend might not solemnly be attributed to the presence of NO_3^- , but in addition the pH changes as well by adding nitric acid. For the trends upon variation of halide ions, the electrochemical potential of the growth solution or rather the potential difference between E_{eff} and ascorbic acid turned out to be important. Adding HNO_3 to the growth solution decreases the pH. A decrease in pH increases the potential of ascorbic acid, which causes

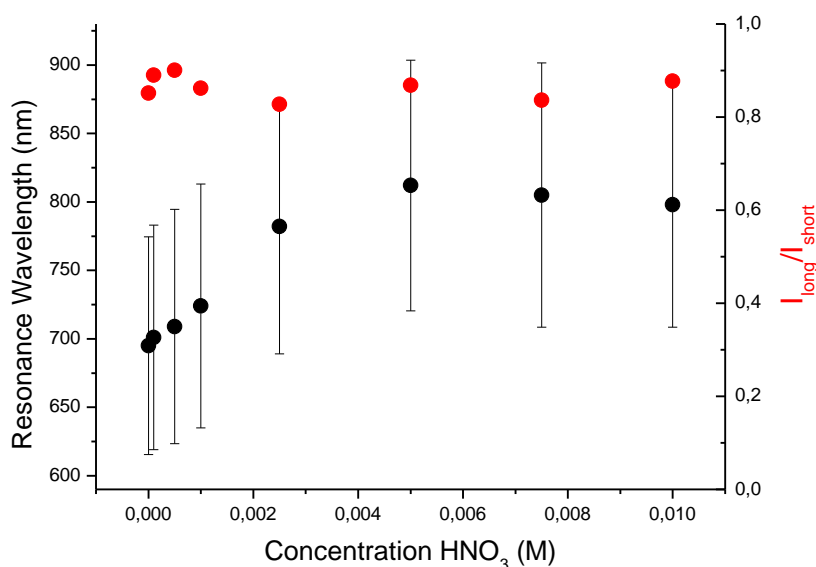


Figure 3.12.: Variation of Nitrate

Increasing the concentration of nitrate by adding HNO₃ increases the resonance wavelength of the gold nano rods (black), while the yield (red) stays high.

a decrease in the difference E_{eff} -ascorbic acid (see figure 3.13). As shown before, smaller differences cause slower reactions, which are more selective and therefore a higher anisotropy is expected (and observed). However, it has been shown by Wu et al. (Wu *et al.*, 2005) that in a three-step growth method for gold nanorods, the addition of nitric acid also causes an increase in resonance wavelength due to nitrate ions. They rule out the influence of pH by experiments with other acids. Furthermore, HNO₃ might serve as oxidizing agent, which makes its influence even more complex. In order to test if the shown effect is due to nitrate or some of the other factors mentioned above, a test series which contains different silver and nitrate salts might be of interest, maybe accompanied by a study adjusting the pH by other acids or introducing different oxidizing agents.

3.3. Summary and Outlook

In summary it can be said that the effects of the different reaction partners are complex and hard to separate. The proposed reaction model seems to include all critical parameters for the formation of rods, the high yield of the synthesis, and the trend seen by the increase of seeds, silver, bromide, chloride, surfactant, and nitrate. Some additional effects like the influence of pH, or oxidizing conditions are still not understood completely.

3. Why anisotropic? A Growth-Model for Gold Nanorods

The most crucial factor in the synthesis of gold nanorods is the presence of CTA⁺ micelles next to a preformed gold seed. The micelles diffuse to the side facets to passivate them from further growth. Therefore, elongation of the rod is favored. Furthermore, the effective electrochemical potential of the growth solution needs to be below 1.12 V. Otherwise the reaction speed is too high, only spherical particles are formed. Besides the fact that in this fashion rods can be grown in general, a high yield of high aspect ratio rods is achieved with the addition of silver nitrate. This allows for the existence of silver bromide, which helps to passivate side facets more efficiently. The aspect ratio can be increased even more if the ionic strength of the solution is increased and the effective electrochemical potential decreased, by the addition of chloride or nitrate ions, which slow down the reaction speed. Therefore, selectivity of the passivation of the side facets by CTA⁺ is increased. In order to clarify the effect of CTA⁺ micelles, experiments connecting the yield of rods and the aspect ratio directly with the rheology and diffusive properties of the micelles need to be done. The role of silver bromide might be better understood if direct electrochemical and redox potential measurements on growing rods (or on growing gold-surfaces) were possible. In order to confirm the importance of the electrochemical potential difference between oxidizing and reducing species, a reducing agent with a redox-potential different from ascorbic acid or the influence of increasing pH (lowering the redox-potential of ascorbic acid and increasing the potential difference) can be explored.

For practical reasons, some trends for the synthesis of long-wavelength rods are summarized in the following.

- For a variation in the concentration of silver, an optimum in both, resonance wavelength and rod-yield can be seen. For seeds, the increase in resonance wavelength levels out after a certain amount of seeds introduced, while the yield stays high. Therefore, these two parameters can be combined to synthesize rods with a long resonance wavelength in a high yield.
- The influences of bromide, chloride and cetyltrimethylammonium ions are hard to separate. For bromide, increasing the concentration leads to an increase in resonance wavelength. This trend is also shown by the addition of chloride, but in contrast to bromide, rods in a high yield can also be formed if no chloride is present.
- Nitrate ions are present in the synthesis by silver nitrate. Increasing their concentration by HNO₃ leads to an increase of the resonance wavelength up to an optimum. It is not excludable that this effect might be a result of other features of nitric acid instead of the pure presence or absence of NO₃⁻ ions.

If a desired wavelength of gold nanorods is pre-set by experimental reasons (resonance position in the visible part of the spectrum, absorption in the infrared, extreme dimensions in length or width, laser frequency, ...) it is advisable to do a test synthesis including the above mentioned trends and, relying on this test-synthesis, vary one or two factors more specifically to fine-tune

the properties of the sample.

4. Silver-Coating of Gold Nanorods

The silver-coating chapter divides into two parts. The first one, entitled Plasmonic Focusing Effect, shows the effects of silver coating on the spectrum of the plasmonic nanoparticles. An ensemble-linewidth narrowing is observed and explained by a change in the plasmon-shape relation for silver coated gold nanorods compared to pure ones. Those results are published in reference (Becker *et al.*, 2008). The second part deals with the kinetics of the coating process. Knowing that the reaction is first order in silver and zero order in gold nanorods, the activation energy of the reaction is calculated. A relationship between resonance wavelength and reaction time is established, which allows to predict the time at which the reaction must be stopped in order to obtain particles with a desired resonance wavelength.

4.1. Plasmonic Focusing Effect

The ensemble linewidth of a suspension of plasmonic nanoparticles is a convolution of the line width of individual particles and the distribution of their resonance wavelength. A narrow ensemble plasmon linewidth is desirable for most plasmonic applications such as sensors (McFarland & Van Duyne, 2003; Raschke *et al.*, 2003; Elghanian *et al.*, 1997), the enhancement of nonlinear optical effects (Kneipp *et al.*, 1997; Nie & Emory, 1997; Campion & Kambhampati, 1998) light guiding (Maier *et al.*, 2001; Quinten *et al.*, 1998), labeling (Schultz *et al.*, 2000), or tissue targeting (Brigger *et al.*, 2002; Hirsch *et al.*, 2003). A small single particle plasmon linewidth implies a long plasmon lifetime, a large field enhancement, and a high sensing sensitivity. This intrinsic single particle plasmon linewidth is determined by the amount of damping and mainly due to inter-band and intra-band excitation of electron-hole pairs, thus temperature, frequency, and material dependent (Sönnichsen *et al.*, 2002). The plasmon resonance wavelength is strongly dependent on the nanoparticle shape; a narrow ensemble linewidth indicates therefore a low polydispersity of the plasmonic particles.

The main factor influencing the resonance wavelength of rod-shaped particles is the aspect ratio via a linear relationship we term the ‘plasmon-shape relation’. Hence, three factors effectively determine the ensemble plasmon linewidth: (I) the single particle linewidth, (II) the width of the distribution in aspect ratios in the sample, and (III) the slope of the plasmon-shape relation connecting aspect ratio to resonance wavelength (Figure 4.1).

4. Silver-Coating of Gold Nanorods

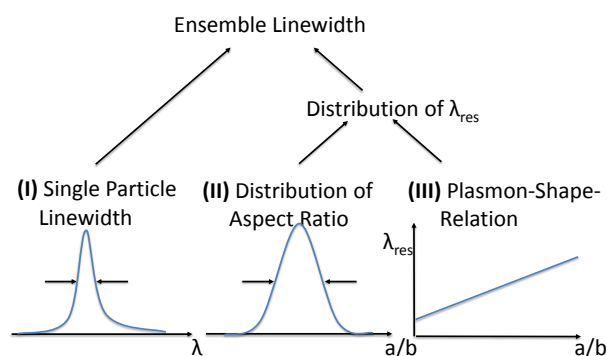


Figure 4.1.: Ensemble Linewidth

The three factors contributing to the ensemble plasmon linewidth: (I) the single particle linewidth, (II) the width of the distribution in aspect ratios (a/b) in the sample, and (III) the slope of the plasmon-shape relation connecting aspect ratio (a/b) to resonance wavelength (λ_{res}). A change in the slope of the plasmon-shape relation (III) is responsible for the ensemble linewidth narrowing of gold nanorods after silver coating.

We find that coating gold nano rods with a thin shell of silver leads to a strong reduction of the ensemble linewidth. The quantitative examination of this effect leads to the surprising finding that it is caused by a change in slope of the plasmon-shape relation (factor III), an effect we term ‘plasmonic focusing’. The silver coating leaves the shape and size of the original gold nanorods intact, excluding factor (II) from the discussion. The contribution of the single particle linewidth to the observed ensemble linewidth (factor I) is complex due to simultaneous shifts in the central resonance wavelength. However, we are able to show by single particle experiments together with theoretical modeling that the single particle linewidth contribution actually counteracts plasmonic focusing.

Plasmonic Focusing

To explain our terminology ‘plasmonic focusing’ we first note that during nanoparticle crystallization in solution, the shape and size polydispersity of the ensemble typically increases by statistical variations over time. An exception is the well-known (chemical) focusing regime during nanocrystal growth (Peng *et al.*, 1998; Reiss, 1951; Yin & Alivisatos, 2005), where a faster growth of small compared to larger particles lets small particles ‘catch up’. This effectively narrows or focuses the nanoparticle size distribution. The plasmonic focusing we observe, where the plasmon resonance linewidth of an ensemble of gold nanorods is smaller after silver coating than before, leaves the gold nanoparticles shape undisturbed but rather changes the way their shape polydispersity translates into spectral polydispersity. A shallower slope of the plasmon-shape relation narrows or focuses the distribution of plasmon resonances. In the ideal case of a completely flat plasmon-shape relation, all particles would have the same resonance wavelength regardless of their aspect ratio leading to an ensemble linewidth only limited by the intrinsic single particle linewidth. Another way of looking at plasmonic focusing is observing the spectral shift induced by the silver coating. Silver coating generally leads to a blueshift – but

the shift is stronger for particles with resonances further in the red.

Note the non-trivial choice of units in the discussion of linewidth changes accompanied with a resonance shift: a linewidth narrowing in energy or frequency units may correspond to a linewidth narrowing or broadening in wavelength units, depending on the magnitude of the resonance shift. Length or wavelength units have to be chosen here because of the almost linear relationship between aspect ratio and resonance wavelength (Link & El-Sayed, 2005; Pérez-Juste *et al.*, 2005). Other geometric factors besides aspect ratio, namely end-cap geometry and particle volume, have a weak influence on the plasmon resonance compared to the aspect ratio (Bryant *et al.*, 2008; Prescott & Mulvaney, 2006). An ensemble linewidth in length units therefore relates to a certain polydispersity in aspect ratio regardless of the mean resonance wavelength. For other discussions, linewidth in energy units may be more appropriate, e.g. the single particles energy linewidth corresponds to the plasmon decay time.

Synthesis and Characterization

We produce silver-coated gold nanorods according to literature (Liu & Guyot-Sionnest, 2004) by adding preformed gold nanorods (Nikoobakht & El-Sayed, 2003) to a coating solution containing silver ions (see appendix C.2). Increasing the silver concentration in the coating solution leads to a strong color shift (from green to orange-yellow, figure 4.2). The different electron density of silver and gold makes it possible to visualize clearly the silver shell around the original gold nanorod in transmission electron microscopy (TEM). The images confirm the expected increase of the silver shell thickness with increasing concentration of silver in the coating solution. When the silver concentration gets too high, the shell grows homogeneously (figure 4.2). High resolution TEM and spatially resolved elemental analysis by nano-spot energy dispersive X-ray spectroscopy (figure 4.2 and appendix C.2) confirms the mono-crystalline of the particles, the epitaxial growths of the silver shell on the gold particles.

Extinction spectra of the solutions reveal a blueshift of the plasmon resonance wavelength of up to 150 nm (figure 4.2 and appendix figure C.7), which is approximately linearly dependent on the amount of silver present (slope about -1.15 nm/ μ M). The extinction spectra also show the strong narrowing of the plasmon resonance in the particle ensemble spectra after silver coating when compared to the linewidth of the original gold nanoparticles – at least for thin silver coating. This narrowing has to the best of our knowledge not been reported before and is only observable if the silver shell is very homogeneous (Liu & Guyot-Sionnest, 2004; Wang *et al.*, 2005; Tsuji *et al.*, 2006; Mandal *et al.*, 2004; Hodak *et al.*, 2000; Ah *et al.*, 2001; Mock *et al.*, 2003; Becker *et al.*, 2007; Song *et al.*, 2005). As is evident from figure 4.2, a slightly thicker silver layer typically leads to more inhomogeneous coating resulting in a broadening of the ensemble linewidth compared to the optimal silver thickness.

4. Silver-Coating of Gold Nanorods

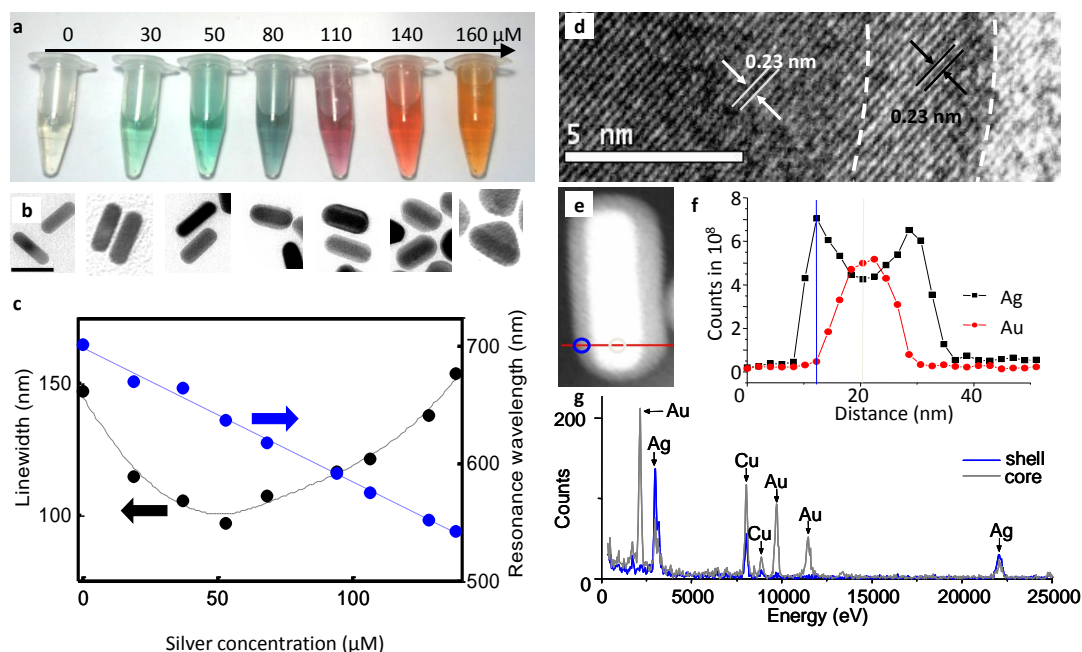


Figure 4.2.: Typical Silver Coating

a) True color photograph showing the color change of the pure gold nanorods (mean diameters 51x18 nm) (left sample) upon increasing silver concentration in the coating solution. The number above each vial indicates the concentration. b) Representative TEM images corresponding to the samples shown above. They show the increasing thickness of the silver shell with increasing silver concentration becoming inhomogeneous at very high silver concentrations (scalebars for all images 50 nm). c) Linewidth (black dots) and resonance wavelength (blue dots) as a function of silver concentration in the coating solution for a gold nanorod sample with a starting resonance wavelength of 700 nm and an initial linewidth of 148 nm. The shift in the resonance wavelength is approximately linearly dependent on the amount of silver present with a slope of $-1.15 \text{ nm}/\mu\text{M}$ (dashed blue line). The linewidth is the full width at half maximum (FWHM) as determined directly from the spectra (see figure C.7). It shows a minimum at 53 μM , where it is reduced to 97 nm from the initial 148 nm (dashed black line is a guide to the eye). d) High resolution TEM image of a silver coated gold nanorod. Dashed lines indicate the borders of the silver shell. Equal lattice spacing (0.23 nm) in the Au core and the Ag shell confirms epitaxial growth ([111] planes). e) STEM image of the silver coated gold nanorod with the position of the EDX linescan (red line) f) Profile of the Au and Ag elemental distribution. g), Two representative EDX spectra (at the positions indicated in e) and f)).

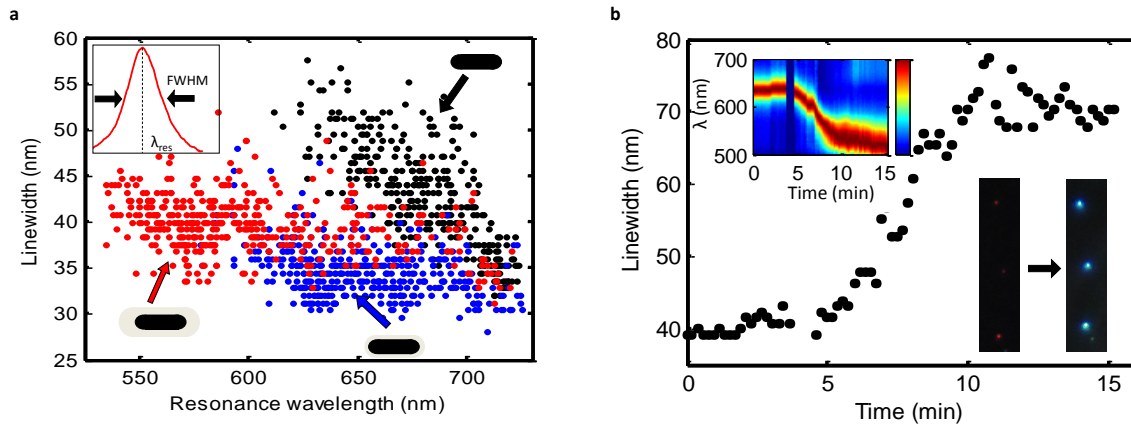


Figure 4.3.: Single Particle Silver Coating

a) Linewidth of gold nanorods (without coating (black dots), with a thin (blue dots) and thick (red dots) silver shell) plotted against their resonance wavelength, both extracted directly from scattering spectra (inset). On average, the linewidth (FWHM) of particles with silver coating is smaller than the linewidth of pure gold nanorods with similar resonance wavelength. The thicker silver shell shows a higher linewidth than the thin shell due to an anisotropic shell thickness. b) Observation of the linewidth change over time of a single gold nanorod exposed to the silver-coating solution. The inset on the upper left shows the full spectra (color coded) over time and the inset on the lower right a true color photograph of the same particles in the dark-field microscope before and after coating.

Linewidth

Before discussing the ensemble linewidth narrowing by plasmonic focusing in detail, we will first examine the single particle linewidth for coated and uncoated nanoparticles by observing the scattered light of individual nanoparticles in a dark-field microscope (Sönnichsen *et al.*, 2002; Wang *et al.*, 2005; Mock *et al.*, 2003). Our setup is automated to allow the spectral investigation of several hundred nanoparticles with reasonable effort (Becker *et al.*, 2007). For each particle spectrum, we extract the mean resonance position (λ_{res}) and the full linewidth at half of the maximum intensity Γ_{SP} (cf. figure 4.3 inset). Because the excitation of d-band electrons into the conduction band requires a threshold-energy, the linewidth increases for higher frequencies or smaller wavelengths. Hence, a plot of single particle linewidth Γ_{SP} as a function of the resonance wavelength λ_{res} shows an increase of linewidth at smaller wavelengths (figure 4.3 and appendix figure C.12). Most importantly, we observe a decrease of the single particle linewidth Γ_{SP} after silver coating compared to uncoated particles at the same resonance wavelength λ_{res} . This decrease is largest for thin coating and less pronounced for a thicker silver shell. The silver shell reduces the plasmon damping due to the higher energy required to excite d-band electrons into the conduction band in silver compared to gold. The interface between the gold core and the silver shell causes apparently no additional damping. A smaller single particle linewidth means lower plasmon damping, thus a longer plasmon lifetime (see appendix figure C.8) and a higher field enhancement, which is beneficial for many plasmonic applications. The quality factor Q (relevant for the field enhancement around plasmonic particles) increases for silver-coated rods compared to gold rods at the same resonance energy (see appendix figure C.9). For example, at 670 nm, we find silver-coated gold rods with quality factors above 20, whereas uncoated rods show quality factors below 15. The enhancement of Raman signals is believed to depend on

4. Silver-Coating of Gold Nanorods

Q^4 , so the silver coated gold rods should show an improvement of more than $(20/15)^4 \approx 3$. The increase of the single particle linewidth for a thick silver coating (compared to a thin coating) is probably due to the variation in the shell thickness around each particle – as already observed in TEM (figure 4.2). If the silver layer becomes too thick, the particles start to lose their rod-like shape. Affirming the hypothesis of decreasing ‘rod-like’ shape, we observe a decrease in the optical polarization anisotropy for rods with thicker silver coating (see appendix figure C.10).

The smaller linewidth of silver-coated gold rods compared to uncoated gold rods at the same resonance wavelength is, however, not responsible for the observed linewidth narrowing of the ensemble linewidth. The reason is the simultaneous shift in resonance wavelength towards regions with intrinsically higher plasmon damping. Depending on the initial and final wavelength, this shift in resonance wavelength often results in a broadening of the linewidth of a given particle after coating with silver. We observe such plasmon linewidth broadening of an individual particle by continuously monitoring individual particles exposed to a coating solution (see figure 4.3b) and appendix C.2).

If the single particle linewidth of particles become broader after silver coating, why do we observe a narrowing of the ensemble linewidth? The answer is a change in the plasmon-shape relation, which converts the distribution of particle aspect ratios into a distribution of plasmon resonances. In chemical focusing during nanocrystal growth, the growth of small particles is favored. Here, the silver coating shifts the plasmon resonances stronger for rods with higher aspect ratio than for particles with lower aspect ratio. Therefore, the same particle distribution leads to a narrower distribution of plasmon resonances after coating due to a different slope in the plasmon-shape relation (figure 4.4).

This purely electrodynamic effect that we call plasmonic focusing is responsible for the observed narrowing of the ensemble linewidth. The shallower slope of the plasmon-shape relation for silver-coated particles is caused by the strong wavelength dependency of the dielectric function of silver due to the plasma of the quasi-free conduction band electrons. There are two equivalent ways to look at plasmonic focusing: by noting the change in the slope in the plasmon-shape relation or by considering the plasmon shifts after coating. The latter lets us verify the theoretical model by spectrally investigating the same particles before and after coating without knowing the precise aspect ratio. We expect to find that particles with longer resonance wavelengths (i.e. larger aspect ratio) show a larger plasmon shift than those with a shorter starting wavelength. Indeed, we observe this trend (figure 4.4).

The plasmon-shape relation in figure 4.4 is derived from an electrodynamic model based on the quasi-static approximation (Liu & Guyot-Sionnest, 2004) (see appendix C.2). We test whether this model is able to predict the measured ensemble spectra from a known particle shape distribution, which we obtain by measuring the width and length of about 150 particles per sample on TEM images (figure 4.5). The simulation using our electrodynamic model reproduces the observed spectrum well, both for the uncoated and for the coated particles (figure 4.5). The

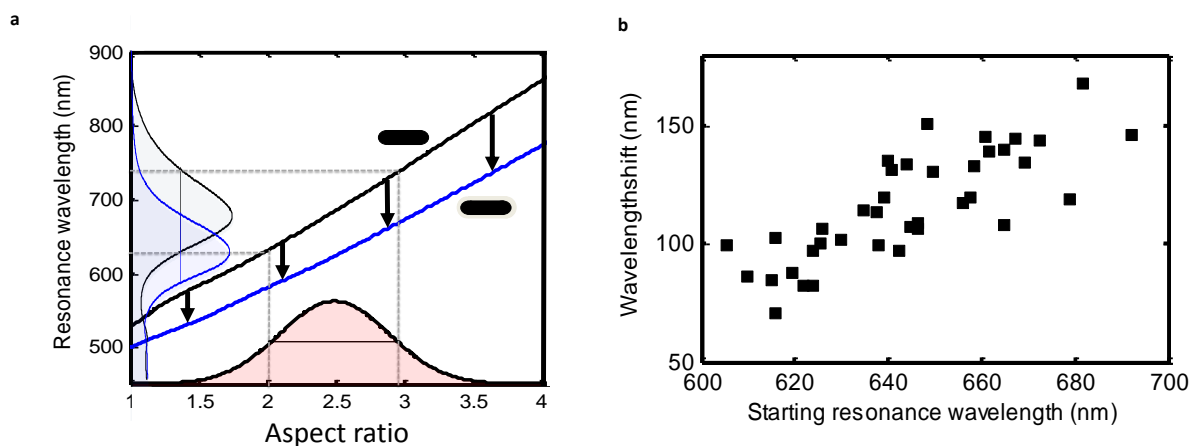


Figure 4.4.: Translation of Size-Distribution into Resonance Position-Distribution

a) The plasmon-shape relation shows how the resonance wavelength depends on aspect ratio. Values derived theoretically within the quasi-static approximation are shown for gold rods in water (black line, $n=1.33$) and with a 2.3 nm silver coating (blue line). The plasmon-shape relation converts an ensemble of particles with a distribution of aspect ratios (indicated by pink shading) into a distribution of resonance wavelengths (indicated by the gray shaded spectrum). The plasmon-shape relations are almost linear, i.e. a distribution of aspect ratios with a given width (polydispersity) gives a certain linewidth regardless of the mean aspect ratio. The smaller slope of the plasmon-shape relation for the silver coated rods leads to a smaller spectral linewidth (blue shaded spectrum). An alternative way to look at the effect of coating is to observe the vertical differences between the two plasmon-shape relations (indicated by black arrows). Rods with higher aspect ratio shift more on silver coating than those with a smaller aspect ratio. b) Experimental data for the wavelength shifts of gold nanorods upon coating with silver as a function of the starting resonance wavelength. Each data point is extracted from two single particle measurements of the same particle before and after coating. Higher starting resonance wavelengths, i.e. rods with higher aspect ratio, result in larger wavelength shifts.

shell thicknesses used here are inferred from TEM analysis, there are therefore no free parameters entering the calculation. Hence, we are confident that this simple method predicts ensemble plasmon wavelength and linewidth accurately. The model lets us theoretically analyze how strong the plasmonic focusing effect would be if the single particle linewidth remained constant after coating. Since the single particle linewidth increases after coating, it effectively reduces the amount of linewidth narrowing observable in the ensemble spectra. The convolution of single particle linewidth with the distribution of resonances in the ensemble further weakens the effect of any reduction of either of the two parameters. We show the values for the ensemble linewidth with and without the single particle contribution in the inset to figure 4.5. The plasmonic focusing alone would reduce the linewidth from 97 nm to 66 nm, the single particle linewidth increases from 28 nm to 29 nm. Their convolution then changes from 113 nm to 92 nm, which compares well to the measured change from 112 nm to 88 nm. Other samples show similarly good agreement of theory and experiment (see appendix figure C.11).

Summary

Our analysis of the plasmon linewidth of silver-coated gold nanorods shows two surprising and important results: ensemble linewidth narrowing by plasmonic focusing and single particle linewidth narrowing, comparing particles with the same resonance wavelength. Even though silver-coated nano particles have been prepared and studied before, the linewidth narrowing of both the ensemble and of single particles has not been reported – probably because it is only

4. Silver-Coating of Gold Nanorods

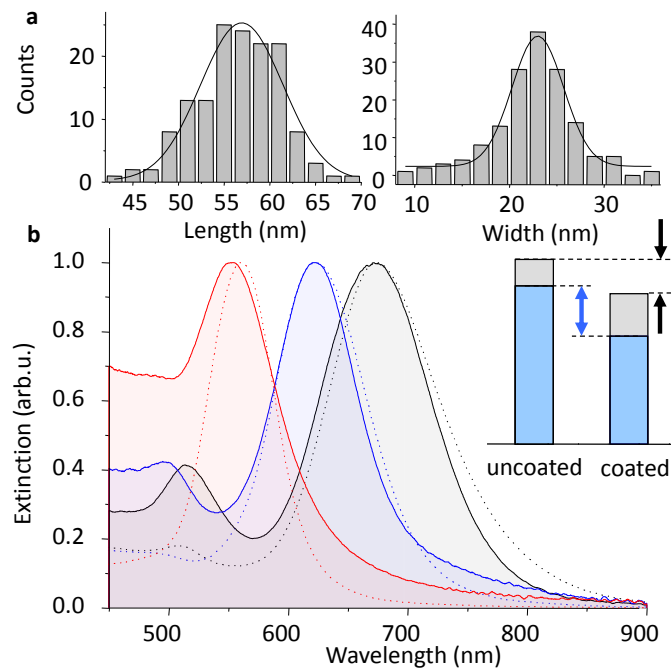


Figure 4.5.: Theoretical Modeling of the Measured Spectra

a) Length and width distribution of a sample of uncoated gold nanorods as determined from TEM images of 145 particles. The length and width show a mean of 56.4 ± 4.4 nm and 22.8 ± 3.4 nm, respectively. b) Ensemble extinction spectra of this gold nanoparticle sample (black), with a thin (2.3 nm) silver coating (blue) and a thick coating (6.9 nm, red), solid lines measured, dashed lines calculated. Only one free parameter enters all three calculations: the eccentricity e used to calculate the geometrical “L factor”,¹⁸ here $e = 0.95$. All other parameters are determined by TEM. The calculated spectra show good agreement to the measurement both in resonance position and linewidth. The inset illustrates the (calculated) linewidth for the uncoated and thinly coated nanorods, in black/gray including the single particle contribution, in blue without this contribution (i.e. pure plasmonic focusing).

present for very homogeneous silver shells. Only the spectroscopic investigation of several hundred single particles using an advanced single particle spectroscopy approach made it possible to obtain enough statistics to compare particles at the same resonance wavelength. Each individual particle shifts in resonance wavelength after silver coating, but observing many different particles allows comparing pairs with the same resonance wavelength. Since the damping (and thus the single particle linewidth) changes with resonance wavelength, only this direct comparison at the same wavelength makes sense. In combination with extensive particle size analysis by TEM, our electrodynamic model allows to entangle the contributions of single particle linewidth and plasmonic focusing for the observed ensemble linewidth changes. Plasmonic focusing alone would reduce the ensemble linewidth by about 30%, the convolution with single particle linewidth reduces the effect to about 20%. Plasmonic focusing is a new feature of bimetallic core-shell structures, interesting from a fundamental point of view. A sample preparation strategy with plasmonic focusing provides a simple method to obtain high quality plasmonic particles with tunable resonance energy over the entire visible spectrum. The silver-coated gold nano particles we produce are among the best plasmonic structures known with up to 50% longer plasmon lifetime than gold nanorods at the same resonance energy, which will make them ideal candidates for the enhancement of nonlinear effects, sensing and light guiding applications.

4.2. Kinetics

So far, only the end-product of the coating process was studied in terms of spectral position and linewidth, and thickness and composition of the silver shell. The information was used to explain the plasmonic focusing effect, meaning the narrowing of the ensemble linewidth upon coating gold nano rods with a thin silver shell. The coating reaction lends itself to follow it over time, since upon coating a color change is observed, easily detectable optically. The progress of the coating reaction can be attributed to the spectral position or spectral shift, time traces are recorded. Those time-traces are used to stop the reaction at a certain point in time (when the desired end-wavelength is reached). Furthermore, by varying reaction conditions such as concentrations or temperature, details of the reaction mechanism are explored. It is shown that the resonance position over time follows an exponential behavior. By varying the initial silver and rod concentration separately from each other and using the method of initial rates, the reaction orders of the two components are determined. It is found that the reaction is zero order for the gold nanorods (at least if silver is in large excess) and $\sim 1^{st}$ order for silver. With this knowledge, the activation energy is determined (65kJmol^{-1}) using an Arrhenius plot.

The kinetics of chemical reactions depend on many parameters like physical state of the involved components, concentrations, temperature, mixing, or pH. Therefore, in order to get information about the reaction kinetics, an isolated variation of each of those parameters is needed/desired.

4. Silver-Coating of Gold Nanorods

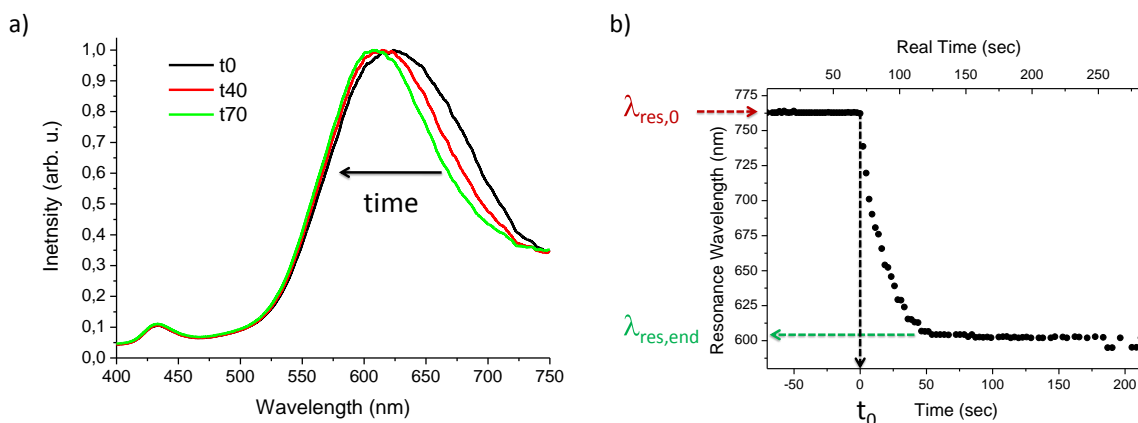


Figure 4.6.: General Features Ag-Coating

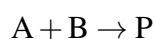
a) Selected spectra of a silver coating reaction of gold nanorods at three different times. The further in time the reaction advances, the bigger the shift of the resonance position compared to the initial one. b) Time trace of the resonance position of the same coating reaction. The real time of the experiment is transformed into a relative time, with $t_{\text{start}}=t_0=0$ sec. From the time trace, the initial resonance wavelength $\lambda_{\text{res},0}$ (of the uncoated gold nanorods) as well as the end-resonance wavelength $\lambda_{\text{res,end}}$ can be read off.

In the following, different conditions in the silver coating reaction are varied.

The silver-coating reaction is initiated by the addition of sodium hydroxide (NaOH) to the coating solution, which contains pre-formed gold nanorods, silver nitrate (AgNO_3), PVP as a stabilizing agent and ascorbic acid for reduction of Ag^+ to Ag^0 . Upon coating of the gold nanorods with a silver shell, a shift of the resonance position to smaller wavelengths is observed (see figure 4.6a). The further the reaction advances, the bigger the shift. The redox potential of ascorbic acid depends on the pH (Ando *et al.*, 1997). Increasing the pH of the solution causes a decrease in the oxidation potential, ascorbic acid becomes a stronger reducing agent. Therefore, sodium hydroxide is added to start the reaction. The start of the reaction (the addition of NaOH) is set to $t=0$ sec. Plotting the resonance position over time, a time trace of the resonance wavelength is obtained. As indicated in figure 4.6b), the start resonance wavelength (of uncoated gold nanorods) $\lambda_{\text{res},0}$ as well as the end resonance wavelength $\lambda_{\text{res,end}}$ can be read off this graph.

Method of Initial Rates

The rate v of chemical reactions is often found to be proportional to the concentration of the reactants to a certain power. Assuming a simple reaction



the rate law is given as

$$v = k [\text{A}]^a [\text{B}]^b$$

The coefficient k is called the rate constant. It is independent from the concentration of the reactants, but depends on the temperature. Therefore, in order to determine the rate constant,

experiments have to be carried out at constant temperature. From a practical point of view, it is interesting to know the rate constant in order to predict the rate of the reaction for a given mixture of reactants. a and b are called order of the reaction with respect to species A or B. The overall order of a reaction is the sum of all individual reaction orders. In order to determine the rate law, the *method of initial rates* can be used (Atkins & de Paula, 2006, chapter 22, page 797ff). In this method, all reactants except one are in large excess. Therefore, their concentration can be regarded as constant.

$$v = k' [A]^a \quad k' = k [B]_0^b$$

The rate at the beginning of the reaction is measured for different initial concentration of the reactant A, its initial rate v_0 is determined by the initial concentration $[A]_0$

$$v_0 = k' [A]_0^a$$

$$\ln v_0 = \ln k' + a \cdot \ln [A]_0$$

Plotting the logarithm of the initial rate v_0 against the logarithm of the initial concentration $[A]_0$ gives a straight line with slope a , the reaction order with respect to A. Doing now the opposite, using A in excess and varying B, results in the reaction rate b for the reactant B.

Variation of Gold Nanorods

For the silver coating reaction, silver is used in great excess over the gold nanorods. Typical silver concentrations are $\sim 8 \cdot 10^{-5} \text{M}$, whereas rods are used in concentrations around 10^{-11}M (assuming a typical concentration of gold rods from the synthesis of $10^{11} \frac{\text{particles}}{\text{ml}}$). Therefore, the method of initial rates can directly be applied to syntheses with varying rod concentrations, since at the beginning of the reaction the silver concentration does not significantly change. Since this concentration is unknown (depending on the initial gold rod synthesis), I express the concentration of gold nanorods as multiples of the lowest used concentration.

Before analysing the reaction order, some general features of the coating reaction are observed. Increasing the concentration of rods (and therefore decreasing the amount of silver per rod) results in a decrease of the shift (or an increase in the end-resonance wavelength, see figure 4.7a). A plot of the end-resonance wavelength over rod-concentration shows a saturation behavior. I expect that finally, for really high rod-concentrations, the end-resonance will show a tendency towards the start-resonance position before coating (if the rod concentration is so high that “no” silver per rod is deposited). The observed resonance wavelengths correspond to the resonance position of the coated gold nanorods. Strictly speaking, they show the development of the product of the reaction. Nevertheless, they can also be interpreted as a measure for the decrease in gold rod concentration. In order to determine the reaction order, the initial rate is calculated

4. Silver-Coating of Gold Nanorods

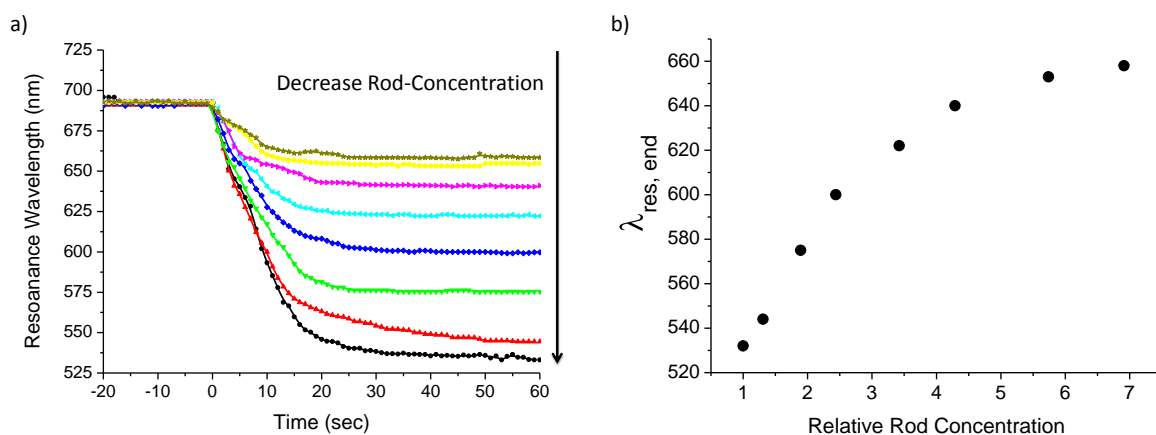


Figure 4.7.: Different Rod Concentrations

a) A decrease in the concentration of gold nanorods (relative rod concentration given as factor to the lowest one used) increases the shift of the resonance wavelength from uncoated to silver-coated nanorods. b) A plot of the end-resonance wavelength over the concentration of gold nanorods shows a saturation behavior.

by using the first data points in the time trace for different gold nanorod concentrations to fit a linear function (with slope v , ($\frac{nm}{sec}$), rate of the reaction, figure 4.8). Since the position of the resonance wavelength is used as a measure for the concentration of gold nanorods, units of the rates need to be converted $\frac{nm}{sec} \rightarrow \frac{mol}{l \cdot sec}$.

Plotting the logarithm of this rate versus the logarithm of the (relative) rod concentration (figure 4.8b), two regimes can be seen. In the low-concentration regime (where the excess of silver compared to gold rods is high), a linear function with slope 0 can be fitted (axis intercept = 2.03). The reaction order is zero, as expected for surface reactions. The second regime (high gold nanorod concentration) shows a decrease in the rate and a deviation from this zero-reaction-order behavior. In this regime, the condition for the method of initial rates - having one of the components (here: silver) in large excess- does not hold anymore. Therefore, those points can be excluded from the rate-determination process. The reaction order for gold nanorods is zero.

Variation of Silver-Nitrate

In a usual silver coating reaction, the concentration of rods is never in excess compared to the concentration of silver. Nevertheless, the method of initial rates can still be used to determine the reaction order for silver in the silver-coating reaction. Since the reaction order for gold nanorods is already found to be zero, the reaction rate is independent from the gold rod concentration. Therefore, also in conditions with no excess of gold rods, variations of the initial silver concentrations can be used to determine the reaction order using the method of initial rates. For this, the shift in the resonance position is equated with the consumption of silver.

Variation of the silver content results in a variation of the resulting end-resonance wavelength. Adding more silver causes an increase in the shift and therefore a decrease in the end-resonance position (see figure 4.9b). Furthermore, it can be noticed that even with no silver present in the solution, a shift is observed upon addition of sodium hydroxide. This might be due to a

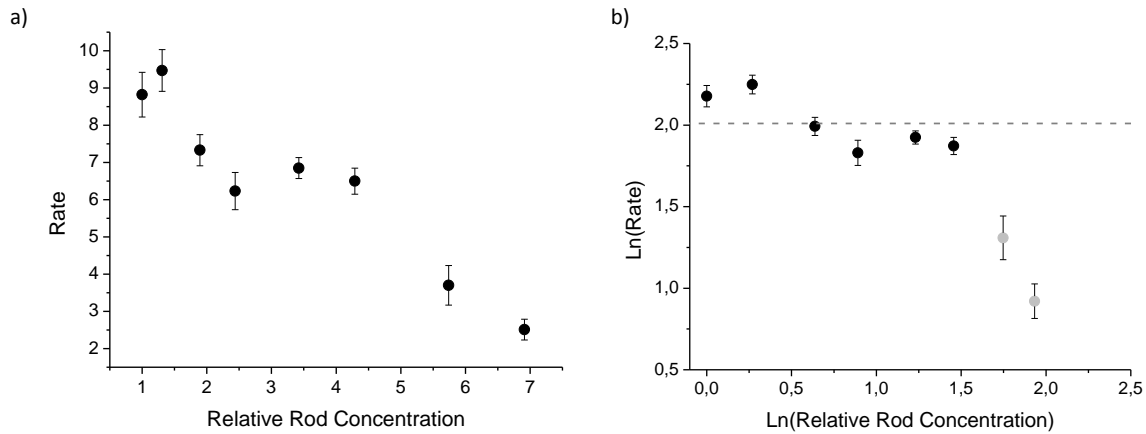


Figure 4.8.: Initial Constants for Different Goldrod Concentrations

a) The initial rate of the silver coating reaction can be determined by varying the initial goldrod concentration and fitting the first data points of the resonating-over-time graph linear. The slope of the fit is the reaction rate. b) Plotting the logarithm of the reaction rate versus the logarithm of the relative rod concentration, two regimes can be determined. At low rod-concentrations (up to 4.3), the rate does not depend on the concentration, the slope of the linear fit is zero. At high rod concentrations, the excess of silver (the condition to use the method of initial rates) is not fulfilled anymore. Those data-points are excluded from the analysis.

response of the plasmon to the changed pH-condition, due to charging or due to some reaction on the surface of the gold nanorod except for the growth of the silver shell (black data points figure 4.9a). This contribution is ignored in all following experiments which contain silver in the growth solution. Plotting the resulting resonance wavelength against the concentration of silver in the coating solution, a clear trend can be observed. Higher amounts of silver cause a smaller end-resonance wavelength (see figure 4.9b). This trend is not linear but follows more an exponential decay. The thicker the silver shell grows, the more spherical the resulting particles become (Becker *et al.*, 2008). Therefore, a saturation of the resonance wavelength into the resonance of big silver spheres is expected. Using the first data points of the resonance wavelength vs. time graph (figure 4.9a) for a linear fit, the rate of the reaction can be determined from the slope of this fit (figure 4.10a). Plotting the logarithm of the rate versus the logarithm of the silver concentration, a line with slope $a = 0.76 \pm 0.04$ is obtained. Since the slope determines the reaction order, the coating reaction has a reaction order in silver of about 1 and a reaction constant k of 5432sec^{-1} (at 23°C). The overall rate law is:

$$v \left(\frac{\text{mol}}{\text{l} \cdot \text{sec}} \right) = 5432 \text{sec}^{-1} [\text{Ag}]$$

or in its integrated form

$$[\text{Ag}] = [\text{Ag}]_0 e^{-\frac{t}{5432 \text{sec}}}$$

The silver coating reaction can be described as quasi-first order in silver. With this knowledge, the resonance position over time data can be fitted with an exponential function, characterized by the decay constant. For this fitting, only one parameter k (rate constant of the reaction) is variable, since the end- and start-resonance wavelength are fixed:

4. Silver-Coating of Gold Nanorods

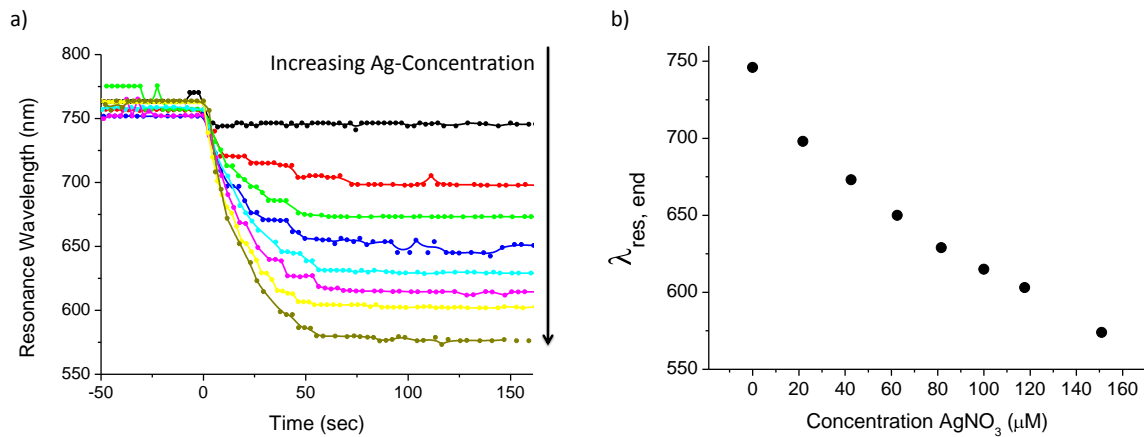


Figure 4.9.: Different Ag-Concentrations

a) An increase in the concentration of silver nitrate in the growth solution increases the shift of the resonance wavelength from uncoated to silver-coated nanorods. b) A plot of the end-resonance wavelength over the concentration of silver nitrate shows almost linear behavior.

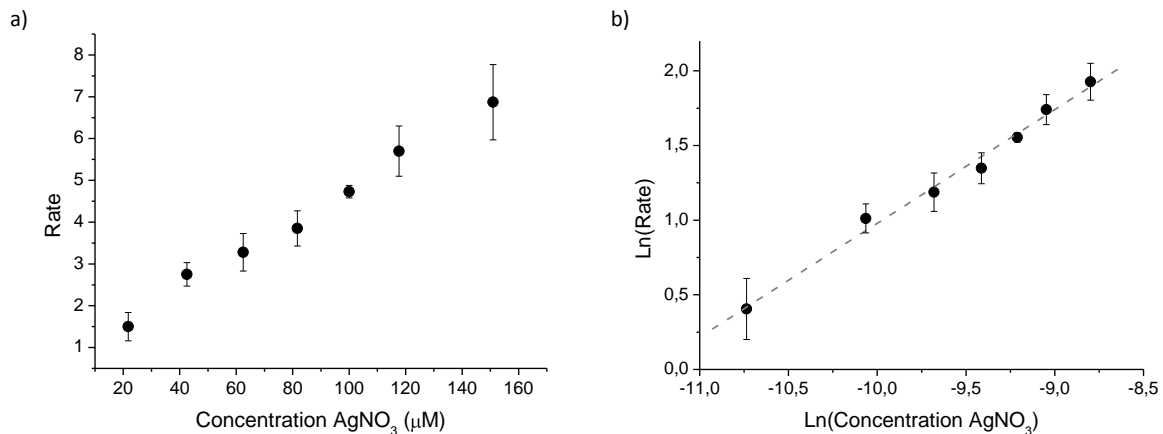


Figure 4.10.: Rate Constants for Different Silver Concentrations

a) The initial rate of the silver coating reaction can be determined by varying the initial silver nitrate concentration and fitting the first data points of the resonance-over-time graph linear. The slope of the fit is the reaction rate. Plotting the logarithm of the reaction rate versus the logarithm of the silver nitrate concentration, a linear behavior is found, the slope of the linear fit is 0.76. This slope can be approximated as one, meaning the reaction is first order in silver concentration.

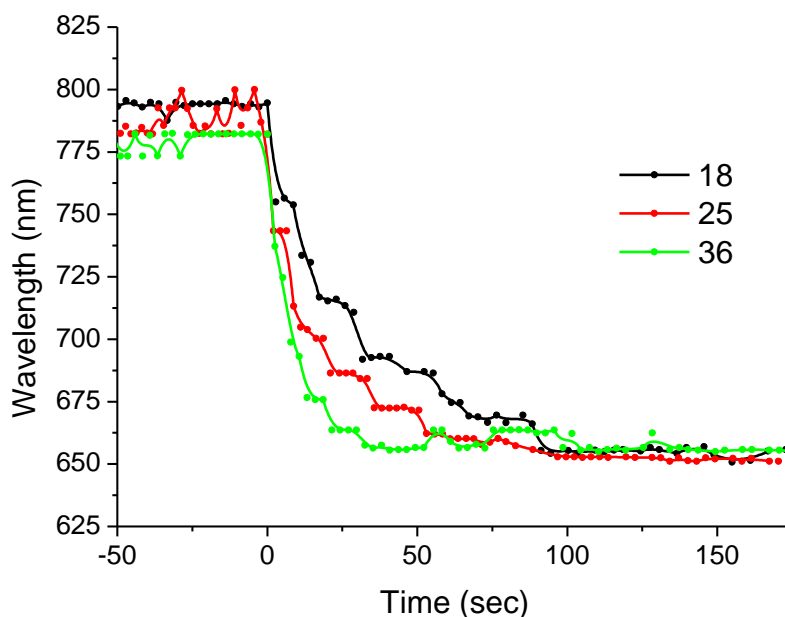


Figure 4.11.: Ag-coating at Different Temperatures

Doing the silver coating of gold rods at different temperatures (for the same rod and silver concentration) does not change the end-resonance wavelength, but an increase in reaction speed for increasing temperatures is observed.

$$\lambda_{\text{res}}(t) = \lambda_{\text{res, end}} + (\lambda_{\text{res, 0}} - \lambda_{\text{res, end}}) \cdot \exp(-kt)$$

Fitting the spectral position over time is favorable with respect to the prediction of a final (desired) resonance wavelength, at which the reaction might be stopped. For $T=23\text{ }^{\circ}\text{C}$ (temperature at which the Ag-variations are carried out), $k=0.051\pm 0.003\text{sec}^{-1}$ and for $T=30\text{ }^{\circ}\text{C}$ (temperature at which the rod-variations are carried out) $k=0.132\pm 0.007\text{sec}^{-1}$. For most reactions in chemistry, the rate constant shows the (also here observed) trend: by increasing the temperature, the rate constant increases as well. A systematic study of the rate constant for different temperatures can be used to determine the activation energy of the reaction and the Arrhenius parameter.

Arrhenius Plot

The temperature at which a reaction is carried out is one of the most prominent conditions to be varied, if the reaction speed should be influenced. If the silver coating reaction is carried out at various temperatures, two observations can be made (see figure 4.11). First, all reactions end at the same end resonance wavelength. A hint that the reaction itself is not changed. Second, the time needed until this end-resonance wavelength is reached, decreases with increasing temperature. The reaction speeds up by increasing the rate constant k . Using the simple exponential fit of resonance wavelength over time and extracting the decay constant, an increase of the decay constant with increasing temperature is observed (see figure 4.12a). Using the Arrhenius-type plot of showing the data, a linear behavior can be found. Furthermore, the pre-exponential factor A and the activation energy E_a can be calculated:

4. Silver-Coating of Gold Nanorods

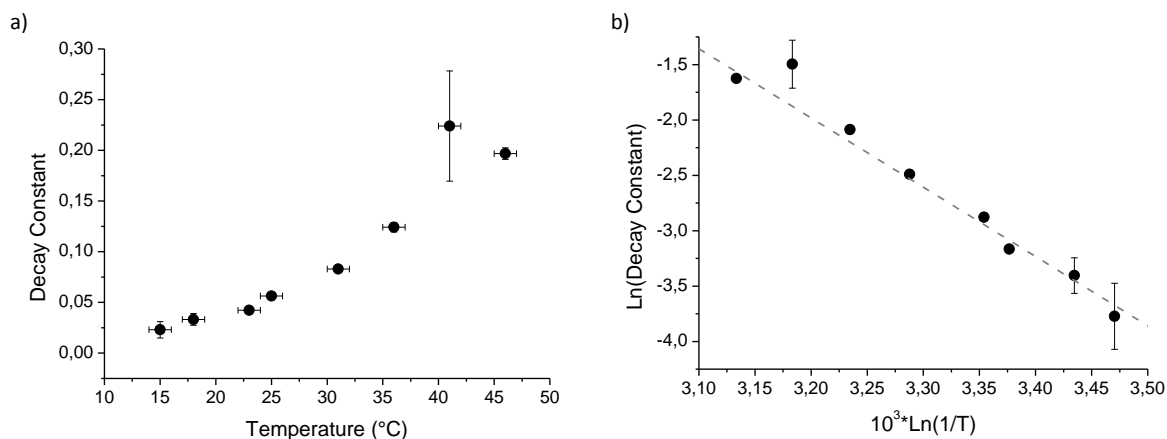


Figure 4.12.: Decay Constant and Arrhenius Plot

a) The decay constant of the silver coating reaction (determined from an exponential fit from graph 4.11) increases with increasing temperature. b) Using an Arrhenius plot, the activation energy of the reaction (52 kJ mol^{-1}) and the Arrhenius parameter ($6.74 \cdot 10^7 \text{ sec}^{-1}$) are determined.

| | |
|--------------------|--|
| A | $6.74 \pm 4 \cdot 10^7 \text{ sec}^{-1}$ |
| E_a^{red} | $52 \pm 1 \text{ kJ mol}^{-1}$ |

Table 4.1.: Arrhenius Parameter and Activation Energy

$$\ln k = \ln A - \frac{E_a^{\text{red}}}{RT}$$

The here-determined activation energy of the silver-coating reaction E_a^{red} can be compared to the activation energy E_a^{ox} found by Liu and Hurt (Liu & Hurt, 2010) for the oxidation of colloidal silver nanoparticles and the release of Ag^+ ions into aqueous media. They determine an activation energy of 77 kJ mol^{-1} , which is in good agreement with the value found here, if the calculated Gibbs energy for the redox-pair Ag/Ag^+ ($G=26.5 \text{ kJ mol}^{-1}$, see appendix C.2) is added (see figure 4.13).

$$\begin{aligned} E_a^{\text{ox}} &= E E_a^{\text{red}} + G \\ &= 52 \frac{\text{kJ}}{\text{mol}} + 26.5 \frac{\text{kJ}}{\text{mol}} \\ &= 78.5 \frac{\text{kJ}}{\text{mol}} \approx E_a^{\text{ox}} (\text{Liu}) \end{aligned}$$

For the gold nanorod growth an activation energy of $90 \pm 10 \frac{\text{kJ}}{\text{mol}}$ is reported (Zijlstra *et al.*, 2006), which is in similar magnitude to the one observed.

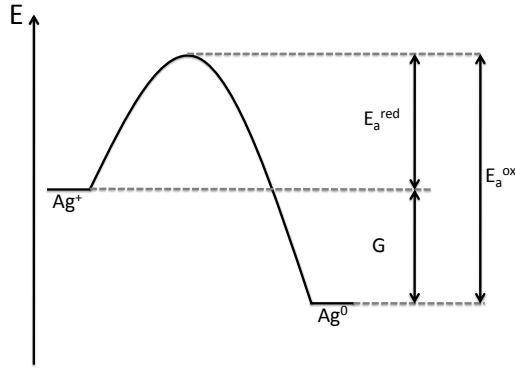


Figure 4.13.: Activation Energy

Schematic representation of the activation energy for the reduction of silver E_a^{red} . The activation energy needed for the oxidation is the sum of activation energy of the reduction E_a^{red} and the Gibbs-Energy G .

Stop the reaction at certain point of time

As already mentioned before, the redox potential of ascorbic acid depends on the pH (Ando *et al.*, 1997). In the Ag-coating reaction, it is adjusted by the addition of NaOH. If the pH is not high enough, the reaction doesn't start. This can be used to stop the reaction at a certain point of interest, for example at a specific desired resonance wavelength. Addition of HCl to the reaction provides a tool for this stop. For a given concentration of gold rods, silver, and a temperature of 23 °C, the following behavior of the resonance position over time is predicted, using the above stated model:

$$\lambda_{\text{res}}(t) = 516\text{nm} + (660\text{nm} - 516\text{nm}) \cdot \exp(-0.0452t)$$

From this equation, a resonance position of 568 nm is expected, if stopped 15 sec after the start of the reaction. The experimentally determined resonance wavelength (figure 4.14) is 600 nm, which is in very good agreement with the theoretical prediction.

Adding NaOH again, the reaction can be re-activated, until all silver is reduced. The additional H^+ and Cl^- ions do not further disturb the reaction as it can be seen if HCl is added after completion of the reaction (see figure C.15 appendix).

In summary it could be shown that the silver coating of gold nanorods is a reaction, which is quasi-first order in the concentration of silver and zero-order in the concentration of rods (at least for low rod-concentrations). The activation-energy of the reaction is determined to be 52 kJmol^{-1} , which is in agreement with theoretical and literature values. Furthermore, the kinetic model is used to predict the time needed for a specific set of parameters (silver concentration, temperature, known start and end-resonance wavelength) to be stopped at a certain point of interest. This is proven experimentally.

4. Silver-Coating of Gold Nanorods

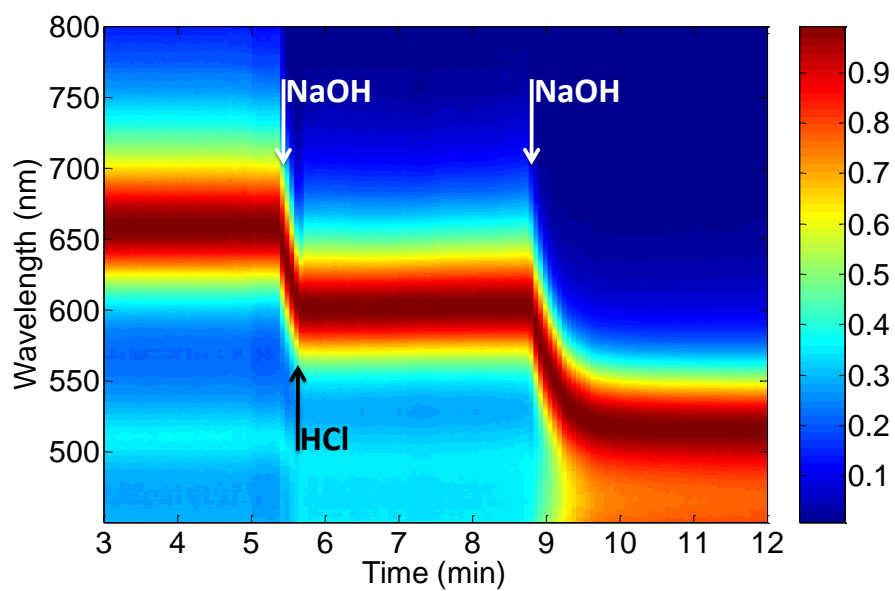


Figure 4.14.: Quench the Coating Reaction

Time-trace of a silver-coating reaction. Adding HCl after 15 seconds, the reaction stops at a wavelength of 600 nm. The reaction is re-activated with NaOH. The final resonance wavelength does not differ from the reaction where no quenching and re-activation step were included.

5. Rotating Rods - Novel Probes for Local Viscosity

Gold nanoparticles have the unquestionable advantage compared to fluorescent dyes that they neither bleach nor blink. Therefore, along with semiconductor nanoparticles, their application as markers is desirable. Besides the high scattering efficiency and the sensitivity towards the embedding refractive index, gold nanorods scatter polarized light, which makes them candidates to characterize their environment in terms of viscosity, using rotational information. In the following chapter it is shown that rotating gold nanorods in a gel matrix can in principle be used to characterize a gel at different temperatures and to measure the transition temperature of it.

5.1. Motivation

Gold nanorods are extremely small. Used as sensors, they probe a local environment of $\sim 10^{-15}$ ml, which makes them interesting when thinking of probing local features like viscosity of ultra-small systems like cell-membranes or micro- (and nano-) fluidic devices. They can be embedded into bigger systems without disturbing the system itself and be used as “internal” sensors for changes on ultra-small length (and volume) scales. Comparable to single-molecule studies, gold nanorods can act as single-particle sensors and allow for the observation of rare events, which would be averaged out by ensemble techniques, or for the study of heterogeneous systems, as many biological samples are. Another sector where local probes are interesting is the study of materials (polymers, glasses) near a phase- or glass-transition. The collapse itself is often visualized by microscopic pictures derived from theoretical models, not experimentally proven in single-molecule (single-particle) measurements, but rather adopted to fit macroscopic observations.

In order to probe the collapse of a gel or the transition from a glassy to a soft state, ensemble techniques suffer from the fact that they only represent averaged data. By introducing probes which are small enough to account for locally different environments, the question remains, if the observed dynamics of the rotation of the probe result from heterogeneities in the system (the molecule experiences different environments during the observation time, but each environment is characterized by an exponential reorientation), or if the transition itself exhibits non exponential behavior. In order to determine if an observed transition is heterogeneous or homogeneous, the

5. Rotating Rods - Novel Probes for Local Viscosity

Kohlrausch-Williams-Watt (KWW) analysis can be used. This stretched exponential function is fitted to the correlation function (of the reduced linear dichroism), one obtains two fitting parameters, β_{KWW} and τ_{KWW} . τ_{KWW} can easily be transformed into the correlation time τ_c (see appendix C.3.2). For an ideal homogeneous system, the parameter β_{KWW} is 1, resulting in a single exponential fit. For systems that are heterogeneous, meaning the observed molecule experiences different environments during the observation time, each characterized by a different correlation time, β_{KWW} decreases (Deschenes & Vanden Bout, 2001). Further (more detailed) theoretical treatment of this analysis (including for example the numerical aperture of the collecting objective, finite observation times, and inherent statistical errors) show that even for ideal rotational dynamics $\beta_{\text{KWW}} < 1$ can be found (Wei *et al.*, 2005), or that also single exponential fits might work, even for heterogeneous environments (Deschenes & Vanden Bout, 2001; Wei *et al.*, 2007).

In single particle spectroscopy, the probe used is usually a dye molecule that emits polarized light according to its orientation. Common probes are Rhodamine 6G (Wei *et al.*, 2007; Deschenes & Vanden Bout, 2001) or perylendiimide (Uji-i *et al.*, 2006). As always in fluorescence studies with dyes, those probes suffer from the fact that they are bleaching over time, might be photo-oxidized or chemically unstable. The experimental setup has to allow to read out the fluorescence intensity in two channels (polarized perpendicular to each other). Furthermore, the lateral diffusion of the dyes needs to be orders of magnitude lower than the rotational one, in order to use low excitation powers along with high integration times to obtain long time traces. Low temperatures and vacuum conditions need to be established in many cases.

Gold nanoparticles are already used as optical probes for the local refractive index (Baciu *et al.*, 2008) and the interparticle distance (Sönnichsen *et al.*, 2005). The polarization of the light scattered by gold nanorods can be used to determine their orientation (Sönnichsen & Alivisatos, 2005). Collecting signals from the orthogonally polarized channels allows to calculate their rotational time and by this characterize the local viscosity around them (Pierrat *et al.*, 2009). In order to use gold nanorods in an optical dark-field setup as sensors to characterize the collapse or glass-transition of a matrix, several requirements have to be fulfilled by the system. The matrix itself needs to be non-scattering, and allow the rods to rotate. On the other hand the lateral diffusion must be extremely hindered or non-existing, since otherwise long time-traces are not realizable.

In the following, gold nanorods, embedded in the thermoresponsive polymer-gel Poly(N-isopropylacrylamide) (PNIPAM), are used to characterize the polymer around its transition temperature. The system allows for dark-field investigation of the scattered light of the gold nanorods since the gel-matrix itself does not scatter light, the particles are locally fixed and rotate in the gel. Furthermore, it is possible to fabricate thin samples (necessary to avoid overlap of spectra of particles on top of each other), which have a high amount of non-aggregated particles inside the gel matrix. It is found that for small observation times the auto-correlation

of the reduced linear dichroism can be fit by a single exponential decay law, with an increasing correlation time τ_c . The sigmoidal behavior of the correlation time over temperature has its inflection point at 29 °C, close to the lower critical solution temperature (LCST of PNIPAM) stated in literature. For longer observation times, β_{KWW} deviates significantly from 1, indicating that the gold nanorods do either experience different environments or that the observation times are too small.

5.2. Gold Nanorods in PNIPAM - Introducing the System

PNIPAM

Poly(N-isopropylacrylamide) (PNIPAM) is a polymer, which undergoes a collapse when heated above its lower critical solution temperature (LCST). Consisting of polyacrylamide-subunits (NIPAM), cross-linked by N,N'-Methylene-Bis-Acrylamid (BIS), at temperatures below the LCST, the PNIPAM is in a swollen and well-hydrated state, stabilized by the enthalpy of amide-water hydrogen bonding. If the temperature is raised above the LCST, the polymer expels water and turns into a compact state, macroscopically observable by a dramatic increase in turbidity (Ahmed *et al.*, 2009). Water is released from the polymer into the bulk. The observed “volume-phase-transition” (VPT) is the reason why PNIPAM has been used for example as drug-delivery agent (Gu *et al.*, 2007). This VPT is similar to the phase transition of ELPs, which turn upon heating from a stretched and highly mobile into a collapsed structure (see also chapter 6.1.3).

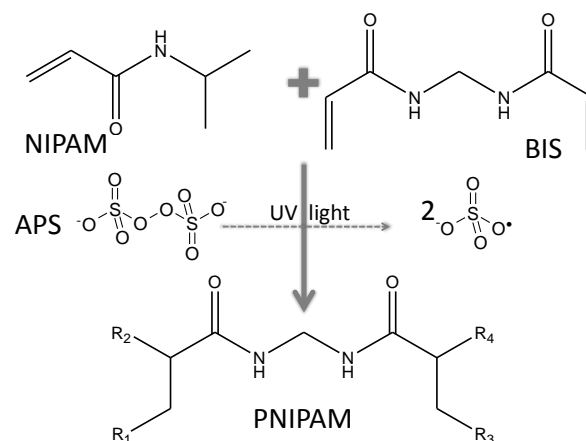


Figure 5.1.: PNIPAM

NIPAM is polymerized in the presence of the cross-linker BIS. The radical polymerization is started by the photoinitiator APS under UV-light, resulting in a cross-linked PNIPAM-polymer.

Gold-Nanorods in PNIPAM

5. Rotating Rods - Novel Probes for Local Viscosity

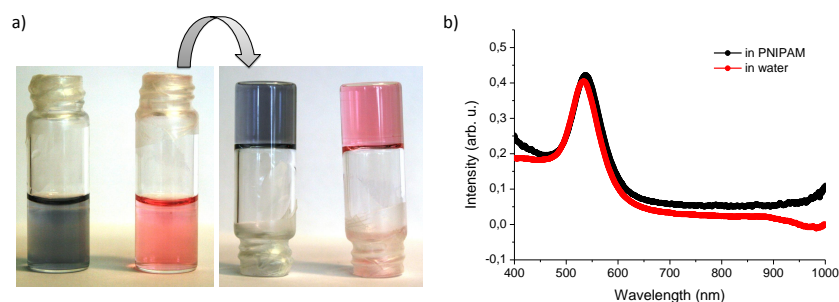


Figure 5.2.: Gold Nanospheres and -rods in PNIPAM

a) Picture of polymerized PNIPAM gels including gold nanorods and -spheres. b) Ensemble-spectra of gold nanospheres in water (red) and polymerized PNIPAM (black). The nanospheres do not aggregate in the gel, neither does the gel scatter or absorb a significant amount of light.

The gold nanoparticles (synthesis see chapter 3 and appendix C.1) can easily be introduced into the PNIPAM by mixing an appropriate amount of nanoparticles with NIPAM monomer and photoinitiator, and polymerizing the gel after this mixing process (details see appendix C.3.1). Macroscopic gels show that the polymerization is not influenced by the gold nanoparticles (figure 5.2a). Ensemble spectra show that the nanoparticles do not aggregate in the gel-matrix (figure 5.2b) and show also that the gel matrix itself does not scatter or absorb light in a distracting amount. In order to analyze single gold nanorods in a dark-field setup, the PNIPAM-gel (including the nanorods) is cast into a self-built gel-chamber, covered by a glass slide (figure 5.3a). True color dark-field images of the sample (figure 5.3b) show that the particles do not aggregate and are distributed throughout the sample. All above mentioned requirements for the use of gold nanorods as sensors rotational sensors are given with the here described method. The nanoparticles scatter light in a non-scattering matrix, are locally fixed, and show rotational movement (see also appendix C.3.2). In the following, their polarized scattered light is used to characterize their rotational movement and therewith the gel matrix properties.

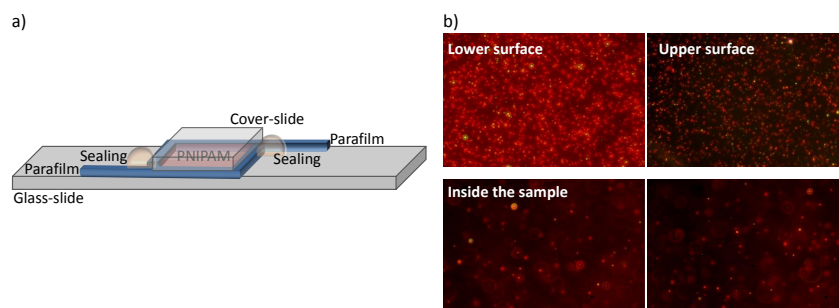


Figure 5.3.: Gold Nanorods in Microscopic PNIPAM

a) Schematic representation of the self-built gel chamber for the microscopy investigation of gold nanorods in PNIPAM. b) True-color dark-field images of gold nanorods in PNIPAM. The nanorods have a tendency to stick to the glass surfaces, but also a high amount of gold nanorods is found throughout the sample. Since nanorods are found in different depths inside the sample, there are always particle defocussed while other are in focus.

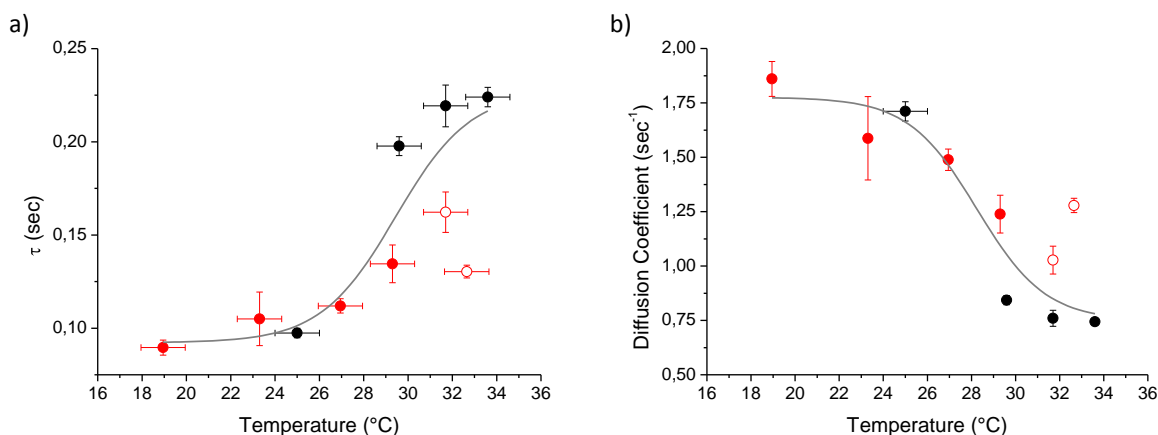


Figure 5.4.: Tau and Diffusion Coefficient for Different Temperatures

Correlation time (a) and diffusion coefficient (b) of gold nanorods in PNIPAM at different temperatures. The data is gained from two different experiments (shown by two different colors, red and black). The two empty red dots correspond to data obtained by keeping the set temperature at 28 °C and let the sample stay at that temperature for 1 (respectively 2) hours. This difference in history of the sample might be responsible for the slight offset of these two points from the sigmoidal curve.

5.3. Results

Single particle scattering intensities are recorded for several particles at different temperatures. Intensity time-traces are transformed into time-traces of the reduced linear dichroism. Those data are autocorrelated. For further details see appendix C.3.2. Assuming a homogeneous environment for all rotating rods, single exponential fits of the first data-points (first 0.1 seconds) of the auto-correlation function of the reduced linear dichroism are performed. All observed correlation times τ_c for one temperature are averaged. As seen in figure 5.4a, the correlation time increases with increasing temperature, following a sigmoidal curve shape. The turning-point is at ~ 29 °C (using a sigmoidal Boltzmann-type fit-function). Using the relation

$$\tau_c = \frac{1}{6D}$$

the diffusion coefficient D can be calculated as well ((Wei *et al.*, 2007), see figure 5.4b). The here-observed characteristic temperature is in good agreement with the transition temperature T_t of PNIPAM from literature (Ahmed *et al.*, 2009), which is 32-35 °C. By assuming a homogeneous environment and averaging over many particles, the here performed analysis of the single particle data recovers the ensemble values. For increasing temperature, the diffusion coefficient decreases, the particles slow down since the gel collapses, the viscosity increases while the mesh-size decreases. The rotational motion of the rods is hindered.

Besides this “ensemble-like” analysis of the data, single particle time traces can in principle be used to determine the local environment of every single particle. By using the KWW-analysis,

5. Rotating Rods - Novel Probes for Local Viscosity

the stretching coefficient β_{KWW} in the fitting function

$$f(t) = \exp\left(\frac{-t}{\tau_{\text{KWW}}}\right)^{\beta_{\text{KWW}}}$$

is used to determine the degree of heterogeneity. From literature (Deschenes & Vanden Bout, 2001) it is known that for long observation times the β_{KWW} value is more likely smaller than one, because molecules can probe different environments during the measurement. If in contrast the observation time is small, β_{KWW} values of 1 are found, because a change in the environment happens on longer time scales. For the here performed measurements, the β_{KWW} values of the stretched exponential fits are all (even for very small time scales) most likely below 0.3 (see appendix C.3.2). This is an extremely low value compared to literature for inhomogeneous environments (Deschenes & Vanden Bout, 2001). This can have different reasons. The gold nanorods might in fact experience a heterogeneous environment on a very small time scale. If this is true, the acquisition frequency needs to be increased in order to have more data-points for shorter times. Also insufficient data recording (too little data points in total) can be a reason for the observed low β_{KWW} . Therefore longer time traces are preferable.

At this point it is unclear how to interpret the obtained time traces with respect to heterogeneous or homogeneous environments for the single gold nanorods. It sounds reasonable that objects of the size of the gold nanorods (of several tens nanometers) experience inhomogeneity, but more detailed experiments (see also chapter 5.4) need to be performed to conclude with higher confidence.

5.4. Summary and Outlook

It is shown that the gold nanorods can be used as rotational orientation sensors in an optical dark-field setup. Embedding the nanorods into the thermoresponsive polymer PNIPAM is possible without altering the properties of one of the components. PNIPAM maintains its thermoresponsive behavior, while the gold nanorods do not aggregate but rotate in the polymerized gel at locally fixed positions. A polarization resolved observation of the scattered light at different temperatures is possible, resulting in diffusion coefficients of the gold nanorods, which can be used as a measure for the transition temperature of the polymer. The here measured transition temperature is 29 °C, close to literature values (32-35 °C (Ahmed *et al.*, 2009)).

Besides this ensemble-averaging data analysis, also a KWW-analysis with stretched exponential fit functions is performed. It results in extremely low values for β_{KWW} (below 0.3), which would account for huge heterogeneity of the system. In order to clarify this speculation, longer time traces with higher frequencies need to be recorded. With this data, more data-points even for short correlation times will be accessible. Furthermore, the time trace of the same nanorod at

different temperatures could be recorded. So far, many particles are lost during the heating and equilibration-time of the microscope. Shortening of these times by improving the setup will help to increase the number of time-traces of the same rods at different temperatures. An additional information could be gained, if at the same time rotational *and* spectral information of the same particle could be recorded. A collapse of the PNIPAM should increase the refractive index around the particles, which would lead to an increase of the resonance wavelength as well.

6. Nanoparticle Assemblies

Plasmonic nanoparticles are a good candidate for sensors, since their plasmon resonance wavelengths depend on internal as well as external parameters. Besides the use of single nanoparticles, also assemblies of them are subject for several studies. The change of the resonance wavelength of a plasmonic particle, if a second one is close by, can be used to determine either the presence of the second one at all (Rong *et al.*, 2008), or to distinguish the distance between them (Sönnichsen *et al.*, 2005). Aggregation, caused by the presence or absence of target molecules (Xia *et al.*, 2010), is also used in sensing applications. Besides the formation of nanoparticle assemblies, also the aggregates themselves, if formed in a controlled way, can be used as sensors. It is known that the sensitivity of 3D-nanoparticle arrangements towards refractive index changes is higher than for single particles (Ye *et al.*, 2008). Therefore, new properties of the assemblies themselves are explored and used.

In the following, two kinds of nanoparticle assemblies are studied. First, the controlled assembly of two particles of the same size (“dimers”) is used to determine the interparticle distance by different methods of calibration. The polarization of the scattered light along or perpendicular to the interparticle axis is used to measure both, refractive index and interparticle distance. Furthermore, the dimer is used to characterize the behaviour of a thermoresponsive linker-molecule upon changes in the temperature and concentration of the linker around the nanoparticle. In the second part of the chapter, core-satellite structures, consisting of a big core particle surrounded by several smaller ones (“flower-like structures”) are used as refractive index sensor. It turns out that they are better suited for refractive index sensing applications than pure spherical particles of the same size, since their sensitivity is much higher.

6.1. Dimers

Nanoscience is an increasing field of research even though this size regime is already used for millions of years by biology. Proteins, protein-transport into cells through pores or channels, and cell-membranes themselves are situated between some few tens of nanometers (Wu & Wong, 2005; Chen & Moy, 2000; Robertson & Roux, 2005). Today, nanomechanics, nanomotors, and nanooptics are topics in research and already in some industrial applications. Therefore, the ability to measure nm-sizes and size-changes is important for both, characterizing and

6. Nanoparticle Assemblies

understanding existing systems, but also developing and manipulating artificial ones. Moreover, (bio)macromolecules and synthetic polymers might show interesting new properties when studied on the nm-scale.

Every distance to be measured needs an adequate technique, which fits the needs of it. Trying to measure the length of the equator with a ten-cm ruler sounds as unrealistic as using it to measure the diameter of a human hair with μm accuracy. In contrast to macroscopic distances, which are usually measured with direct techniques, in the nanometer regime it is common to use optical methods like Förster-resonance energy transfer (FRET, (Jares-Erijman & Jovin, 2003)). In this technique, the energy transfer of a fluorescent donor dye molecule to an acceptor one is measured and by the FRET-efficiency, upper limits for the distance between the molecules can be found. Unfortunately, the transfer works only for distances $< 10\text{nm}$ and continuous evaluation for long timescales is often impossible due to photo-bleaching and blinking. These obstacles can be overcome by using metal nanoparticles as optical labels. They show a high light-scattering efficiency accompanied with quasi unlimited lifetime. With low exposure times and high frame rates, on-line-monitoring of dynamic processes is possible. Furthermore, the particles' resonances can easily be tuned from almost UV to far infrared, including the visible range of the electromagnetic spectrum. This makes an optical observation easy, even though the dimensions of the particles are well below the diffraction limit of a light-microscope. Despite the fact that the particles are much larger than commonly used dyes (some tens nm compared to $\sim 1\text{nm}$), it has already been shown that the size has no huge influence on the processes studied (Sönnichsen *et al.*, 2005).

The resonance position of an individual metal nanoparticle depends on many internal and external conditions such as material, shape, and surrounding refractive index. Additionally, the existence and distance of neighboring particles contributes to the position of the resonance frequency. A system to measure two external conditions autonomously from each other, namely surrounding refractive index and distance between the particles, is a dimer consisting of two spherical gold nanoparticles. This anisotropic construct shows two resonances, which scatter light that is orthogonally polarized. The resonance originating from the longitudinal axis depends on the interparticle distance as well as on the surrounding refractive index, whereas the transverse resonance is only sensitive to the latter.

Since the need for measuring small distances grows more and more important, an evolving number of people are working on nanoparticle dimers (Ghosh & Pal, 2007; Anker *et al.*, 2008), including dimerization in batch (Sheikholeslami *et al.*, 2010) and subsequent separation by gel-electrophoresis (Reinhard *et al.*, 2007), syntheses on surfaces (Brown *et al.*, 2010; Reinhard *et al.*, 2005), and electron beam lithography (Jain & El-Sayed, 2010). Already first attempts are made to use those dimers as in-vitro (Sönnichsen & Alivisatos, 2005; Reinhard *et al.*, 2007; Liu *et al.*, 2006) and in-vivo (Rong *et al.*, 2008) plasmonic rulers. Also theoretical explanations for the dimer-spectrum, which include the hybridization-model in analogy to dimeric molecules

(Nordlander *et al.*, 2004), tunneling of the plasmon between the particles, similar to tunneling effects in quantum mechanics (Su *et al.*, 2003), exciton-coupling model (Jain & El-Sayed, 2010), or the spring-model (Rechberger *et al.*, 2003) are developed (see also section 2.5). Calibration of the distance to spectral shift relation is in general possible by three different approaches: numerical methods, indirect experimental measurements (hydrodynamic radii of linkers determined by dynamic light scattering and calculating to an interparticle distance), or direct experiments, doing imaging and spectral measurements on the same particle pair. Different scaling laws (Jain *et al.*, 2007; Encina & Coronado, 2010; Sönnichsen & Alivisatos, 2005) are found for the spectral dependence on the distance of the particles. Also exotic shapes like gigantic dimers with diameters of 250 nm (Huang & Baumberg, 2010) or heterodimers consisting of different metals or different sized particles (Sheikholeslami *et al.*, 2010; Brown *et al.*, 2010) are examined.

The system used in the following consists of two 60 nm sized gold nanospheres linked by a PEG- or ELP-Biotin-Streptavidin construct. The built sensor is sensitive to both, local refractive index and distance variations. A resonance wavelength to distance calibration is done, using dynamic light scattering and cryo-TEM techniques. By replacing the surrounding medium water by methanol, a decrease in interparticle distance is measured, while exchanging to glycerol, refractive index *and* distance change. It is not only interesting to use formed dimers as sensors to external stimuli as described before. The dimer approach offers also a tool to characterize the linker molecule itself. Besides the PEG dimers, used to study refractive index and distance variations, dimers linked by other polymers are analyzed as well. The aggregation behavior of polymers is one field that is not easy to study. Characterization of aggregated polymers in solution is no longer possible with light scattering techniques, since the solution is often turbid, the polymers of interest precipitate. Therefore, using different polymers as linkers between the dimer offers the chance to study properties, which are maybe not accessible by other techniques.

In contrast to other dimer systems explored so far, the system introduced here offers the possibility to easily exchange the linker molecule/polymer. As long as the alpha-omega functionalization with biotin and thiol is conserved, the nature of the polymer plays only a minor role concerning dimerization. Furthermore, the system is fairly simple (consisting only of a biotinylated polymer and a Streptavidin-protein), what makes interpretation of data feasible. The biotin-streptavidin interaction ensures an overall high yield of dimers, which is mainly important for detection schemes that are limited in the number of observation spots or for data-analysis methods that rely on statistically relevant differences. Moreover, the combination of surface-passivation and dimerization conditions allows for a “clean” surface after forming the dimers. The advantage of the fastSPS-setup (described in (Becker *et al.*, 2007) and (Becker, 2010)) is the ability to measure a lot of particles in a short time. Therefore, statistical conclusions can be made. On the other hand, the polarization dependent spectra taken with a different setup (see appendix B) reveal information on the polarization anisotropy of a lower but still significant number of dimers.

6. Nanoparticle Assemblies

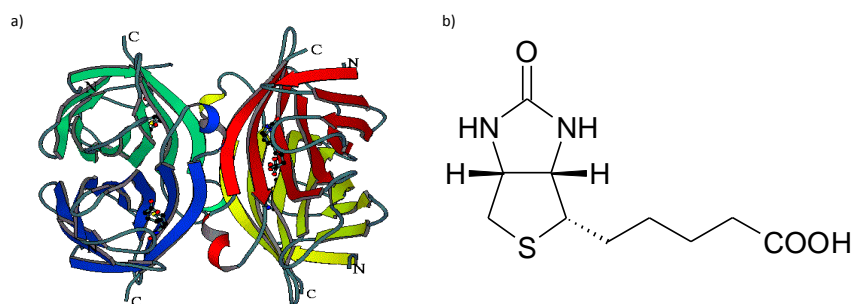


Figure 6.1.: Streptavidin and Biotin

a) Streptavidin is a protein, composed of four subunits, each able to bind one biotin (of Oslo, n.d.). b) Biotin or vitamin H is a small molecule, used in the body in metabolism and regulation of cell-nucleus activity

Biotin, Streptavidin, PEG, and ELP - Introducing the Linkers

The **biotin-streptavidin** system is a nowadays well-established and widely used system in biological engineering and microbiology (Diamandis & Christopoulos, 1991). Although there are many other ligand-binding interactions, streptavidin-biotin has some exceptional properties also useful for the sensing-scheme presented here. The affinity of the non-covalent binding is characterized by a formation constant of $10^{-15} \text{ l}\cdot\text{mol}^{-1}$ (Gonzalez *et al.*, 1997), which is one of the highest ones found in nature. Along with the exceptional stability of streptavidin concerning outer conditions like temperature (Gonzalez *et al.*, 1997), denaturing agents (Waner *et al.*, 2004), or derivatisations of the molecule itself (e.g. solid supports or high-molecular weight macromolecules (Ylikotila *et al.*, 2009)), a once formed biotin-streptavidin bond is not broken easily. Therefore, a linkage mediated by biotin-streptavidin will be very stable. In principle, streptavidin is able to bind four biotin molecules, one to each subunit. By genetic engineering, also mono- and dimeric streptavidins are synthesized (Wu & Wong, 2005).

Polyethylene-glycole (PEG) is a polymer consisting of $[(\text{CH}_2)_2\text{O}]$ building blocks. Its ability to be dissolved in both, organic and inorganic solvents, is one of the reasons why it is used in various applications. Furthermore, it is highly biocompatible and nowadays a common additive for countless products (Laverman *et al.*, 2001; Greenwald *et al.*, 2003; Fruijtier-Polloth, 2005; Heyes *et al.*, 2007; Otsuka *et al.*, 2003). Nevertheless, its structural behavior, especially when it comes to aggregation, is still under discussion (Devanand & Selser, 1991; Khan, 2006). Another advantage of PEG is the possibility to functionalize it on one or both ends with desired end-groups for conjugation, binding, or biorecognition. Many of those functionalizations are commercially available, for example a thiol group on one side, providing gold-anchoring, combined with biotin on the other side, which allows for streptavidin recognition.

Elastin-like polypeptides (ELPs) are interesting candidates for linkers, since they are thermoresponsive and easy to functionalize. Elastin itself is a protein, responsible for the elastic properties of tissue. In the body it is organized in filaments that form larger bundles. The main structural characteristic of elastin is alternating hydrophobic and crosslinking domains, the former ones consisting of hydrophobic amino acids like proline, valine, alanine, and leucine. Synthetic

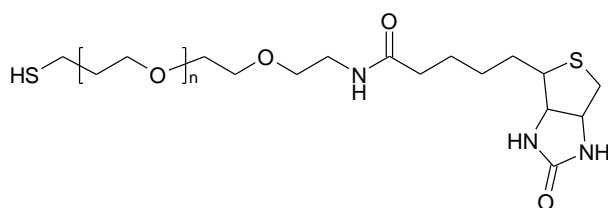


Figure 6.2.: Biotin-PEG

Alpha-Omega functionalization of PEG with thiol and biotin provides both, linkage to the gold surface and recognition by streptavidin.

elastin-like polypeptides consist of repeating units of a certain amino acid sequence (here: Val-Gly-Val-Pro-Gly). By recombinant genetic engineering, precise control over peptide sequence, chain length and stereochemistry is achieved. The ELPs used in this study were provided by Dr. Sabine Flügel (working group of Prof. Dr. Manfred Schmidt, University of Mainz). ELPs have the main advantage that they show an inverse temperature phase transition. The transition temperature T_t decreases with increasing peptide length, peptide concentration and increasing salt concentration. Therefore, T_t can be tuned to external needs. The easy access to synthetic ELPs and the variable transition temperature, along with non-toxicity, biodegradability and good pharmacokinetics, makes them highly interesting for biomedical and biotechnical applications, for example as drug carriers or as gels for the in-vitro synthesis of cartilage.

Dark-Field Microscopy and Flow-Cell Setup - Introducing the Measurement System

All dimerization experiments are done in the flow cell. For the PEG-dimers, the first particles are functionalized with biotin-PEG in batch and introduced (already functionalized) into the flow cell, where the dimerization with the streptavidin functionalized particles takes place. In contrast to dimers carrying PEG as linker molecule, the functionalization of the first particle with biotinylated ELP is, as well as the dimerization itself, carried out on single particle level, avoiding aggregation of functionalized particles in batch. After forming dimers with streptavidin particles as the second ones, the temperature change from room temperature to ~ 4 °C is induced by flowing ice water. Using oil immersion objective and dark-field condenser eliminates defocusing due to condensation of water on the outside of the flow cell. For experimental details see appendix C.4 and C.5.

In contrast to dimerization in batch, the main advantage of forming dimers in the flow cell is the possibility to directly compare spectra of the monomer and the resulting dimer. Non-spherical particles or aggregates are discriminated directly from the beginning and do not perturb later on measurements. Furthermore, aggregation of the monomers (which might occur in solution either

6. Nanoparticle Assemblies

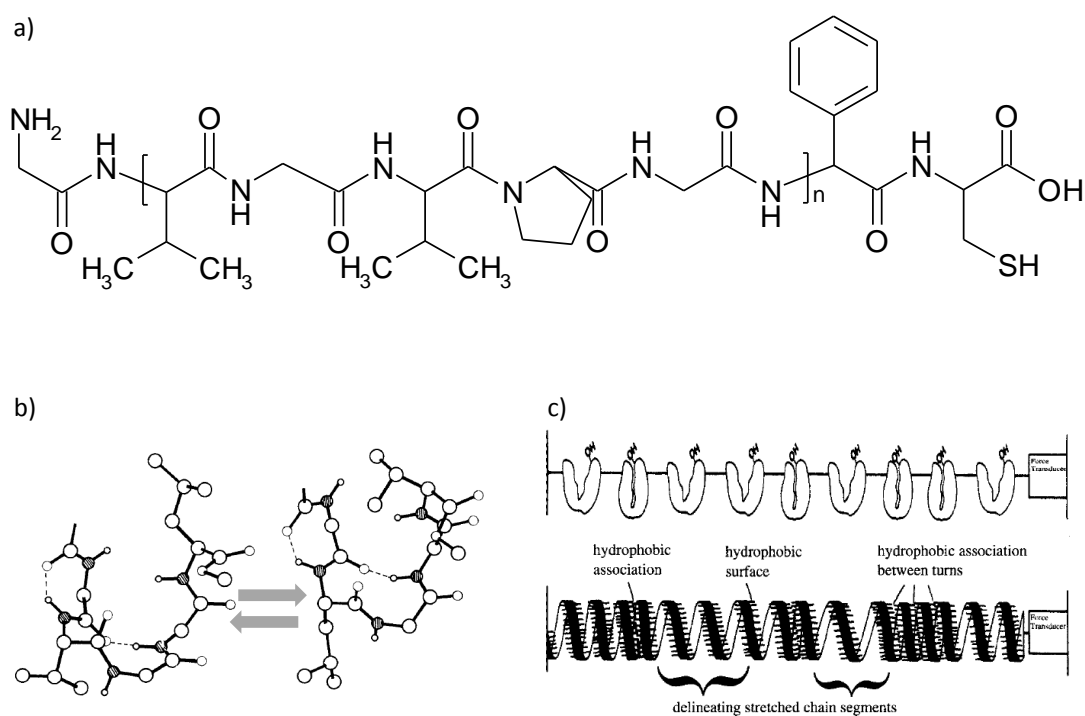


Figure 6.3.: Structure of Elastin

a) Aminoacid-sequence of the ELPs used in this thesis. The number of repeat units n varies from 20 to 120. b) and c) Structural models of elastin: b) model of sliding β -turns proposed by Tamburro (Tamburro *et al.*, 1990), c) β -spiral model by Urry (Urry & Parker, 2002)

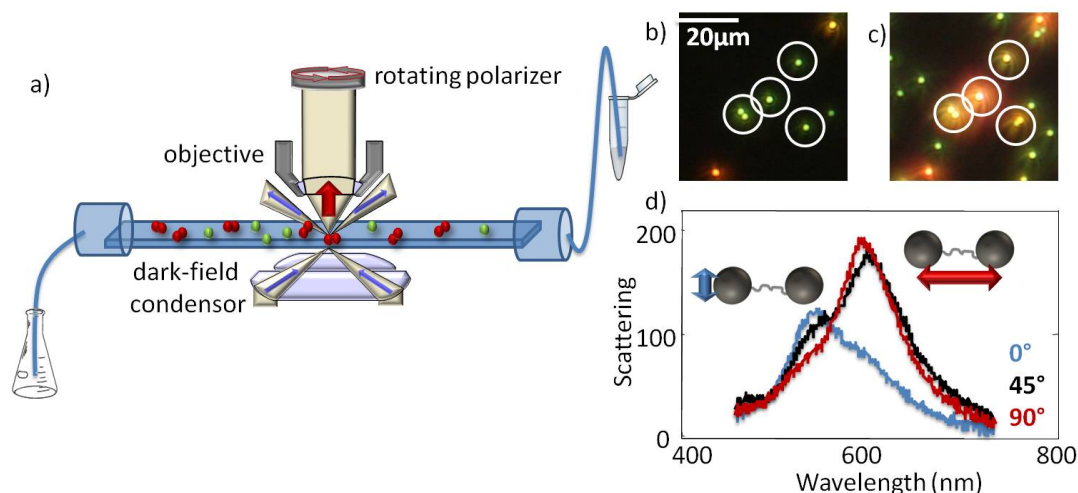


Figure 6.4.: Flow Cell Setup

a) The flow cell setup, consisting of a glass capillary connected via tubings to the reservoir at one side and the waste on the other, allows to easily exchange outer conditions while observing the particles. b) and c) True color photographs of monomers and the resulting dimers in the dark-field setup. d) Polarization resolved spectra of a dimer. 45° polarization shows a spectrum consisting of both peaks, while 0° only represents the transversal and 90° only the longitudinal resonance.

by high salt-concentration or the formation of big aggregates due to multiple binding) does not have to be considered.

Due to the flow-cell setup (figure 6.4), there is an easy way to control outer parameters as solvent or pH. Also particle concentration and flow speed can easily be optimized to ensure a high yield and good reproducibility of the dimerization experiment.

Dimerization in the flow cell always fights with the fact that there is a surface nearby that influences the chemistry of the linking reaction as well as the behavior of the particles. One has to ensure that the first particle stays in its position, the second one reaches the first one to ensure coupling, but on the same time make the free-surface so unattractive for the second particle that it will not (or to very low extent) bind. Salt conditions, flow speed and incubation time have to be carefully adjusted (further details in appendix C.5).

6.1.1. Calibrating the Plasmon Ruler

What is measured in a dimerization experiment are spectral shifts. The monomers turning into dimers, dimers exposed to different refractive indices, or distance-changing dimers, they all show a shift of the resonance position. In order to translate the spectral shift into a distance shift, a calibration is needed, which connects spectral shifts with distance changes. Calibrations of the spectral shift to the distance in between the two particles can be done in different ways. By **theoretical calculations** (BEM-simulations, done by Dr. Jan Becker, working group of Prof. Dr. Carsten Sönnichsen, University of Mainz) two different situations are explored, the “ideal” and the “worst” case. In the ideal case (blue dashed line figure 6.5), the dimer consists of two

6. Nanoparticle Assemblies

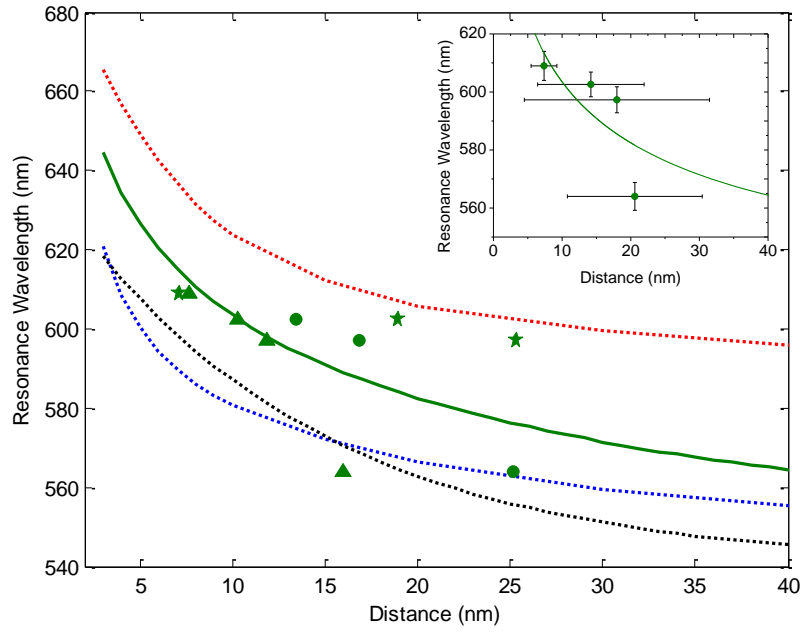


Figure 6.5.: Calibration Plasmon Ruler

Calibration of the plasmon ruler. In order to translate spectral positions into interparticle distances, theoretical simulations (BEM, blue dashed line: two 60 nm spheres in $n=1.33$, red dashed line: 60 nm sphere and rod 60×72 nm in $n=1.5$), the universal scaling law ((Jain *et al.*, 2007) black dashed line), or a fit through the experimental data (green solid line) can be used. The inset shows the mean distances obtained from the experimental data (green stars: cryo-TEM data, green dots: dynamic light scattering of monomers, green triangles: literature sizes of the linker molecules), which are used to fit a stretched exponential function (green solid line).

perfect spheres with a diameter of 60 nm is embedded in a medium of refractive index $n=1.33$. In the worst case (red dashed line figure 6.5), one sphere is substituted by an elongated particle of aspect ratio (length to width ratio) of 1.2, keeping the width constant to 60 nm. The elongation is reasonable when looking at the distribution of sizes and shapes of the spherical sample in TEM (see appendix C.5.4). Furthermore, the dimer is surrounded by a refractive index of 1.5 instead of 1.33, taking into account the glass surface on one side of the dimer and the organic molecules on the surface of each individual particle and especially in between the two. Those simulations yield two stretched exponential fit functions:

$$\lambda_{\text{res,ideal}} [\text{nm}] = 552.2 \text{ nm} \cdot \left(1 - \exp \left(\frac{-\text{distance}[\text{nm}]}{15.2 \text{ nm}} \right) \right)^{-0.067} \quad (6.1)$$

$$\lambda_{\text{res,worst}} [\text{nm}] = 591.5 \text{ nm} \cdot \left(1 - \exp \left(\frac{-\text{distance}[\text{nm}]}{17.5 \text{ nm}} \right) \right)^{-0.066} \quad (6.2)$$

From experiments with **e-beam lithography** synthesized dimers, a universal-scaling law for particle dimers is observed, showing that the shift is constant for a constant gap to diameter ratio. This scaling law results in an exponential function

$$\lambda_{\text{res, e-beam}} [\text{nm}] = \lambda_0 [\text{nm}] + \lambda_0 [\text{nm}] \cdot 0.18 \cdot \exp\left(\frac{-\left(\frac{\text{gap}[\text{nm}]}{\text{diameter}[\text{nm}]}\right)}{0.23}\right)$$

shown as black dashed line in figure 6.5 for two 60 nm diameter spheres with $\lambda_0 = 540$ nm.

Besides those calibrations mentioned above, also **experimental values** can be used to calibrate the plasmon ruler. Using Cryo-TEM techniques, the distance between the dimers can be measured and connected to the mean shift upon dimerization for different spacer lengths (see appendix C.5). It can be seen that the data-points measured with cryo-TEM (green stars figure 6.5) lie within the two simulated situations of perfect spherical particle in $n=1.33$ and a dimer with one elongated particle in $n=1.5$. This shows that none of the simulations shows the real situation in solution. Dynamic light scattering data of the monomers and reconstructing the distance in between the dimers from those hydrodynamic radii also gives distances that, according to simulations, are realistic as well (green dots figure 6.5, appendix C.5.5). Interestingly, cryo-TEM data attributes always bigger distances to the samples than DLS does. Maybe upon binding one end of the PEG via biotin to the streptavidin located at the second particle, the PEG transforms from a random-coil structure (as seen by DLS) to a more stretched configuration. This might explain the offset to higher distances in cryo-TEM compared to DLS of the monomers. Furthermore, the distance can be calculated using literature data for the size of the linker molecules (DTSSP, streptavidin, and the radius of gyration for PEG in water (green triangles figure 6.5, (Pierce, Pierce Protein Research Products; Wong *et al.*, 1999; Devanand & Selser, 1991)). The distances calculated with the literature values are the smallest of those three, but as well within the theoretical predictions. Therefore, a mean value of cryo-TEM, measured hydrodynamic radii of the monomers, and literature data for the linker molecules is calculated (inset figure 6.5) and fitted with a stretched exponential function (green line figure 6.5), resulting in a new calibration:

$$\lambda_{\text{res,exp}} [\text{nm}] = 540\text{nm} \cdot \left(1 - \exp\left(\frac{-\text{distance}[\text{nm}]}{64.6\text{nm}}\right)\right)^{-0.0572} \quad (6.3)$$

The obtained calibration curve has a high slope in the region up to 15 - 20 nm distance between the particles. Therefore, small distance changes cause large spectral shifts, a feature desired for the measurement of small distance changes. Having obtained a calibration, spectral shifts can be translated into distance changes. This new calibration is used to calculate all distances in the following experiments.

6.1.2. Distance and Refractive Index Sensor

In general it would be enough to find (and measure) one single dimerization event and to study it on a single particle level. Nevertheless, it is desirable to achieve dimerization in high yield.

6. Nanoparticle Assemblies

Using the protocol described in the appendix (see chapter C.5), dimerization with 80% yield can be achieved (figure C.29 in appendix C.5). While the dimerization yield can be up to 80%, the surface coverage increases only by a factor of 1.2 (from 0.0137 to 0.0166 part/ μm^2 , see figure C.30 in appendix C.5). These numbers result from counting all bright spots in the region of interest before and after introduction of the second particles. If the experiment is done vice versa (streptavidin-particles first, PEGylated biotin-particles as the second particles), the surface coverage increase is even lower but the formation of dimers is much more time consuming, why this approach is not followed further.

As mentioned before, both resonance frequencies expressed by a dimer depend on the refractive index of the surrounding medium. The interparticle distance is almost irrelevant for the transverse axis (the small blue shift lies, as long as the particles are not touching each other, within the experimental measuring error) but strongly influences the longitudinal one. Measuring both axis separately from each other makes it therefore possible to evaluate the local refractive index around a dimer (by the transversal resonance). Having this knowledge, the longitudinal resonance can give information about the interparticle distance. In order to prove this ability of the sensor, both parameters- namely interparticle distance and refractive index- were changed.

Change the distance

In order to change the interparticle distance without changing the surrounding refractive index, the conformation of the linker between the particles has to change. This is done by exchanging water by methanol (MeOH, $n=1.33$). One can see (figure 6.6) that the transverse axis shows in mean no shift but the longitudinal one clearly does, which is a strong indication that only the distance but not the surrounding refractive index changed. Other experiments show that the reproducibility of this exchange (meaning going back to water and again back to MeOH, see figure C.31 appendix C.5) is not as good as in the other systems but reasonable. It can be suspected that not only the linker changes its conformation but also some other effects (surface-attraction, charging) might take place. Using the calibration (equation 6.3), one can calculate the distance of the dimers in water and in methanol (see figure 6.7a). The median distance in water is 9.5 nm, whereas in methanol it decreases to 6.4 nm. Calculating the distance shift, a decrease of 3.1 nm is found.

Change the refractive index

In order to change the surrounding refractive index, a glycerol/water mixture of $n_{\text{bulk}}=1.41$ is prepared and introduced into the flow-cell. Multiple measurements show a good reversibility of the glycerol/water exchange (see appendix C.5). From theory (Becker, 2010), the sensitivity of the transverse axis is independent from the distance between the two particles forming the dimer and calculates to $132 \frac{\text{nm}}{\text{RIU}}$ (the same as for monomers of 60 nm diameter). The short axis can therefore be used to determine the local refractive index. Knowing n_{local} , the distance between the particles can be calculated by comparing the resonance position for different distances with the measured one.

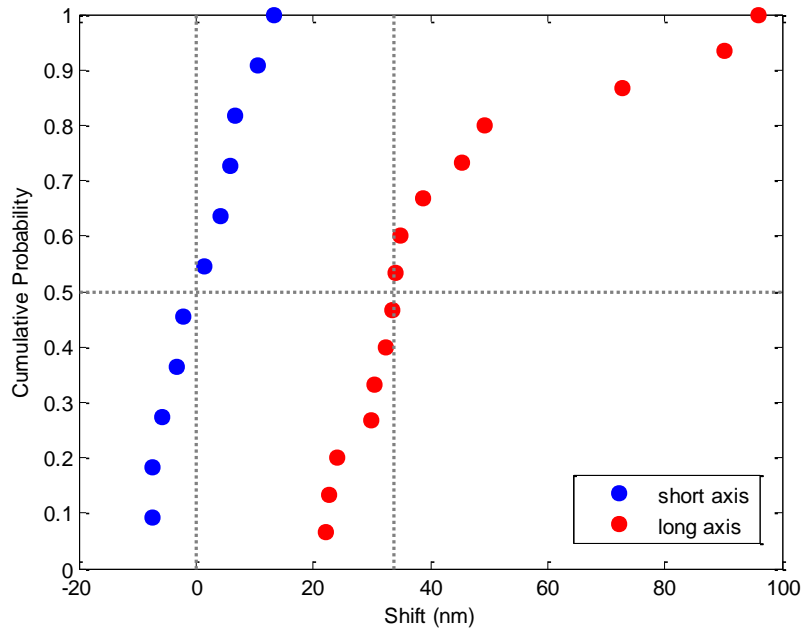


Figure 6.6.: Shift of Long and Short Axis in Methanol

Shift of the transverse (blue) and longitudinal (red) axis of dimers upon the change from water ($n=1.33$) to methanol ($n=1.33$). Since the distance between the particles changes but not the refractive index, only the longitudinal axis shows a (big) shift of about 34 nm compared to water.

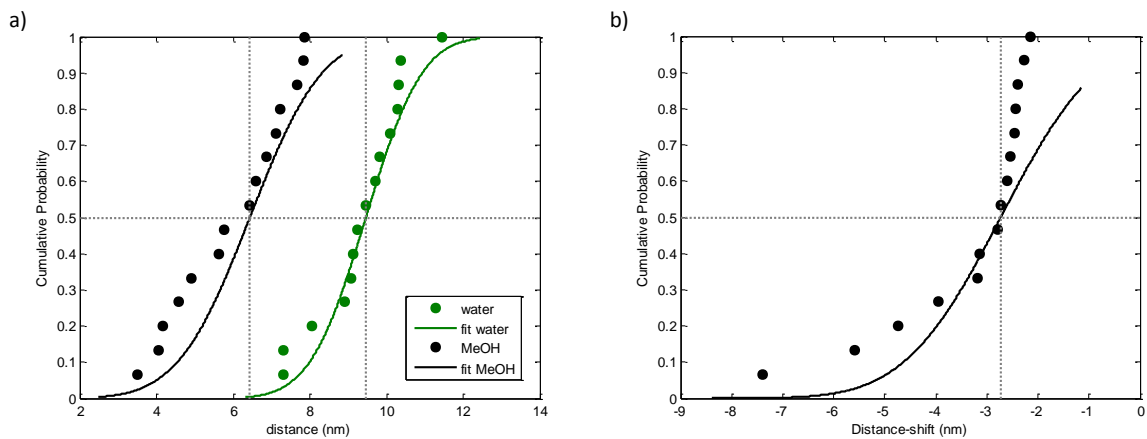


Figure 6.7.: Distances in Water and Methanol

a) From the resonance position of the long axis, the interparticle distance can be calculated using the calibration equation 6.3. The interparticle distance in water is 9.5 nm (green), whereas in methanol it decreases to 6.4 nm (black). b) The mean distance shift is 3.1 nm, indicating that the PEG between the particles collapsed and/or the streptavidin is changed.

6. Nanoparticle Assemblies

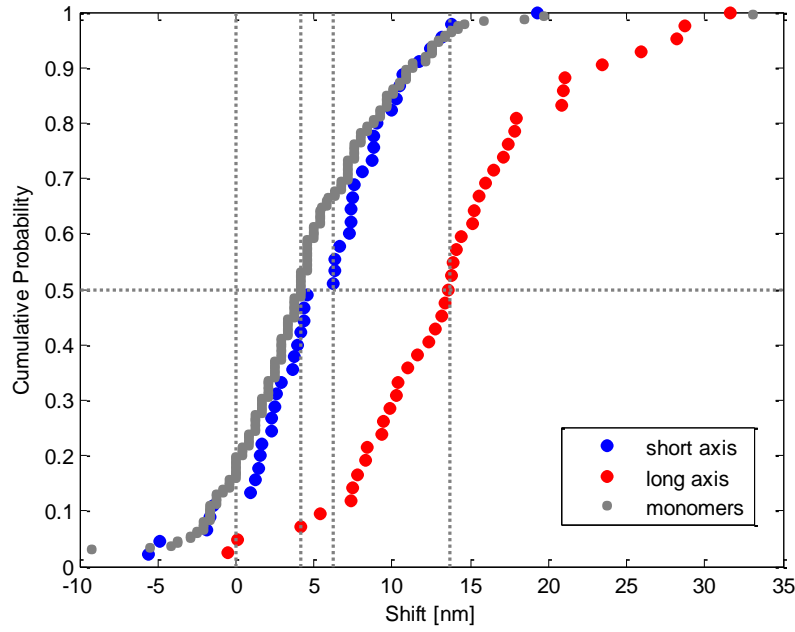


Figure 6.8.: Shift of Long and Short Axis and Monomers in Glycerol

Shift of the transverse (blue) and longitudinal (red) axis of dimers, as well as the shift of monomers (gray) upon introduction of glycerol/water of $n=1.41$. Since all three are sensitive to refractive index changes, shifts of the resonance wavelengths to larger values are observed.

In the system used here, a refractive index of $n=1.41$ is introduced. The median shift of the short axis is 6.2 nm (figure 6.8). This calculates to an effective sensitivity S_{eff} of $77.5 \frac{\text{nm}}{\text{RIU}}$. This is about 60 % of the theoretical expected one, but reasonable, since the dimers are situated on a surface (the refractive index on the bottom is fixed) and the particles are coated by a layer of biomolecules or polymer, which has by itself a higher refractive index than water. Also the monomers (which are always present in a dimerization experiment, since the dimer-yield is not 100 %) show an effective sensitivity lower than the theoretical prediction ($S_{\text{eff,monomers}}=55.2 \frac{\text{nm}}{\text{RIU}}$).

Assuming that the short axis is independent from the distance between the dimers, the relation sensitivity over distance can simply be shifted by $54.5 \frac{\text{nm}}{\text{RIU}}$ to $S_{\text{eff}} = 77.5 \frac{\text{nm}}{\text{RIU}}$ (figure 6.9a). Keeping a constant ratio between sensitivity of short and long axis of the dimers over distance, also the S_{long} is shifted by $54.5 \frac{\text{nm}}{\text{RIU}}$. With those information, a new relation of the resonance position to the refractive index can be established and used to determine the distance of the dimers in a solvent with $n \neq 1.33$. From the theoretical predictions including the corrections done by the experimental data, the distance in any solvent different from water can be calculated via:

$$\begin{aligned} \lambda_{\text{res}} &= \lambda_{\text{res, water}} + \Delta n \left(211.4 \text{nm} \cdot \exp \left(\frac{-d[\text{nm}]}{5.15 \text{nm}} \right) + 84.3 \text{nm} \right) \\ &= 540 \text{nm} \left(1 - \exp \left(\frac{-d[\text{nm}]}{64.6 \text{nm}} \right) \right)^{-0.0572} + \Delta n \left(211.4 \text{nm} \cdot \exp \left(\frac{-d[\text{nm}]}{5.15 \text{nm}} \right) + 84.3 \text{nm} \right) \end{aligned} \quad (6.4)$$

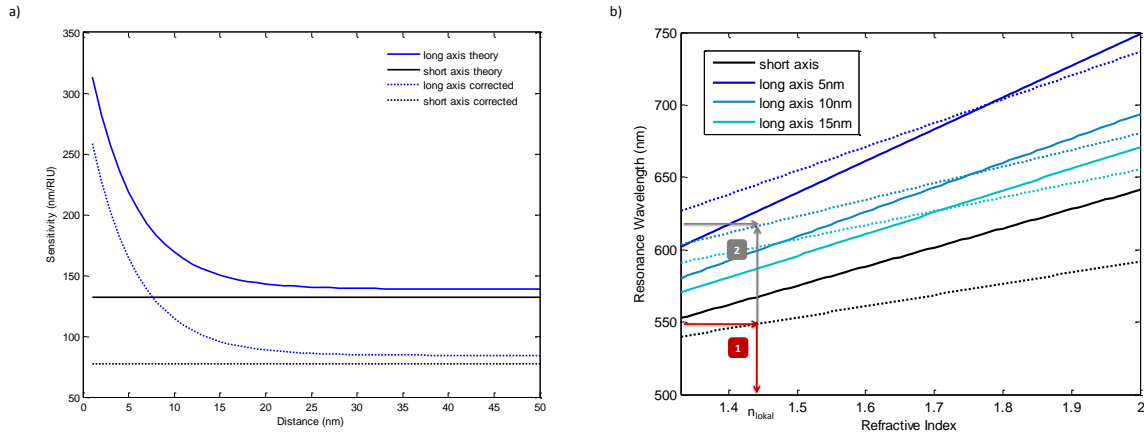


Figure 6.9.: Sensitivity and Resonance of Short and Long Axis

a) While the sensitivity of the short axis (black) shows no dependency on the interparticle distance, the sensitivity of the long axis (blue) is bigger for smaller distances. Using the shift of the short axis caused by $n=1.41$, both theoretical sensitivities (solid lines) are corrected (dashed lines). b) Using the sensitivity of long and short axis and the distance dependency of the resonance wavelength in water (equation 6.3), the resonance wavelength over the refractive index for the short axis (black) and the long axis (blue, numbers indicate interparticle distances) can be calculated.

Knowing the refractive index shift (either from bulk measurements or from calculations using the shift and sensitivity of the short axis), the distance can be calculated. For $n=1.41$ ($\Delta n = 0.08$), the distance calculates to

$$d = -47.8 \cdot \ln \left[1 - \left(\frac{\lambda_{\text{res}}}{550.3\text{nm}} \right)^{-15.442} \right] \quad (6.5)$$

Using equations 2.26 and 6.4, the resonance wavelength over the distance is calculated for both, $n=1.33$ and $n=1.41$. Theoretical calculations are corrected for the measured effective sensitivity.

With the help of equations 6.3 and 6.5, the distances of the dimers in water and glycerol are calculated. The distance in water is 10.8 nm (compared to 9.5 nm in the methanol-experiment), whereas in glycerol the distance is 8.1 nm. Comparing this decrease of the interparticle distance of the dimers, with the behavior of a PEO-block (of a PEO-PPO-PEO block copolymer) in water and glycerol, the decrease in distance can be compared to the deswelling and contraction of the PEO-block in glycerol or glucose (Alexandridis *et al.*, 2000).

6. Nanoparticle Assemblies

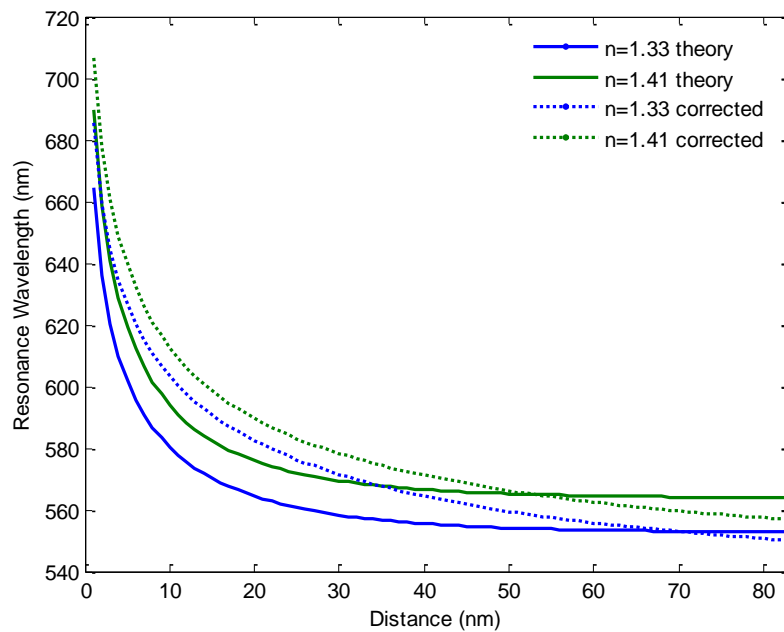


Figure 6.10.: Resonance Wavelength over Distance in Water and Glycerol

Using the theoretical (solid) and experimentally obtained/corrected (dashed) values for the resonance wavelength and the sensitivity (6.1, 6.3) the dependency of the resonance position over the distance in water (blue) and $n=1.41$ (green) are calculated.

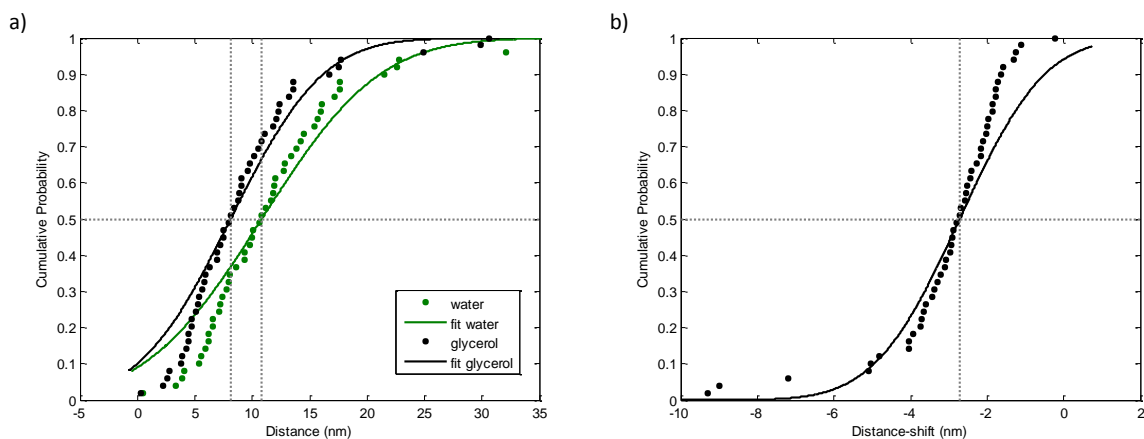


Figure 6.11.: Distances in Water and Glycerol

a) The distances of the dimers in water and glycerol are calculated using the plasmon ruler equation (6.3) and the relation resonance to distance in glycerol (6.5). While the mean distance in water is 10.8 nm, the dimers shift to smaller distances in glycerol (8.1 nm). b) The mean distance shift is -2.7 nm.

Summary and Outlook

It is possible to create dimers in high yield (up to 80 %) with a low surface coverage using Biotin-PEGylated gold spheres and connect them on a glass surface to streptavidin-functionalized gold nanospheres. The created dimers can serve as both, refractive index and distance sensors. If the microscope-setup is equipped with a polarized detection system, both refractive index and distance can be measured at once. Furthermore, it is shown that also monomers instead of the transverse axis of the dimers can serve as internal refractive index sensors. The calibration of such a plasmonic ruler can be done via simulations, but it is shown that small changes in the simulated shape or surrounding refractive index have dramatic effects. Therefore, an experimental calibration using cryo-TEM techniques (among others) is given, which accounts better for the “real” situation. The best would be to measure distance and spectra of exactly the same dimer in exactly the same environment. Unfortunately this is not possible at the moment with our setups but might be realistic with “environmental” SEM techniques, which allow for the use of higher pressures while imaging and mapping larger areas in order to relocate back the particle pairs evaluated in optical microscopy.

6.1.3. Characterization of Elastin-Like Polypeptides

The general structure of the dimers, making the linkage between the two gold spheres via a biotin-streptavidin mediated interaction, allows for generalization of this approach to systems using a different polymer connected to the biotin part. The only requirements are that the polymer binds to the gold surface (preferentially via a thiol group) and can be functionalized with biotin on the other end. Elastin-like polypeptides (ELPs) fulfill these requirements. They can easily be functionalized with biotin via a biotin-NHS ester and due to the thiol-group of the ending cysteine amino acid, direct binding to the gold surface is possible (see appendix C.4). Furthermore, ELPs show the interesting property that they have an inverse temperature transition. Heating above the transition temperature T_t causes aggregation of the polymer, a transition from hydrophilic to hydrophobic. Macroscopically, the polymer-suspension turns turbid. This observation is used to determine the “cloud point temperature” by heating a sample while measuring the transmission intensity. The same fact (turbidity) also indicates that light scattering experiments, which are commonly used to characterize polymeric samples, are not possible in the collapsed state and other techniques are required to study the polymer and its properties. Using the ELP as a linker between two spherical gold nano particles makes it possible to determine the size of the ELP-biotin-streptavidin construct under various conditions like different temperatures, different ELPs, different surface coverages... Since this technique only depends on the scattering of the gold nanoparticles, a collapse of the polymer does not hinder measurements.

6. Nanoparticle Assemblies

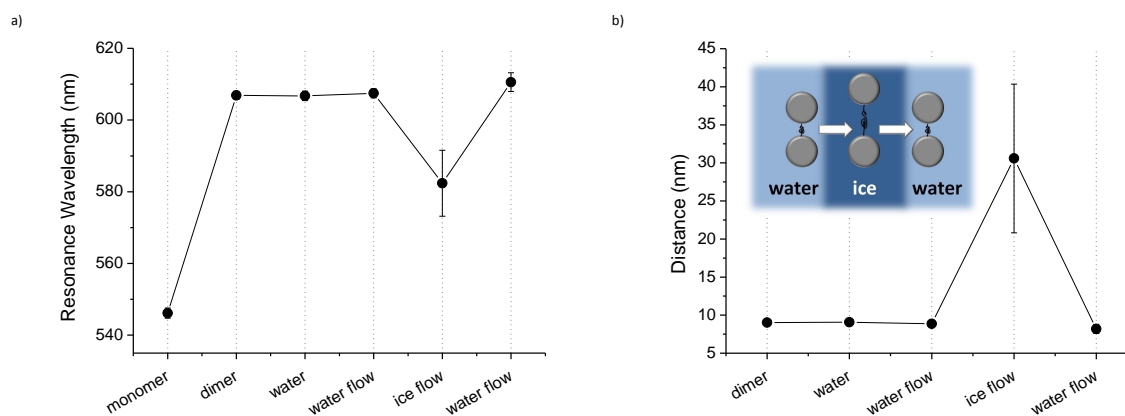


Figure 6.12.: ELP-Dimers at Different Temperatures

a) Resonance wavelength of monomers and dimers (connected via streptavidin-biotin-ELP) in different environments. Dimerization causes a big red-shift of the resonance. In ice-water ($\sim 4^{\circ}\text{C}$), a blue-shift is observed. b) Distance of dimers calculated with equation 6.3. In ice-water, the distance increases by 20 nm to 30 nm, indicating that the ELP transforms from collapsed to stretched state.

Using the same approach as for the PEG dimers, also dimers with ELP as linking molecule are synthesized in the flow cell (experimental details see appendix C.4 and C.5).

ELP-dimers at different temperatures

Introducing ice-water into the flow cell containing flow-cell-made dimers linked by 10% ELP (90% mPEG), a blue-shift of the dimer spectrum of 25 nm compared to room-temperature water (flowing with the same speed) is observed. Translating this shift into a distance via equation 6.3, the interparticle distance increases about 20 nm to 30 nm (using only those dimers for the calculation which shift back to the same value before and after ice water flow). The refractive index of water increases with decreasing temperature (Mitra *et al.*, 1972). Therefore, an increase in the resonance wavelength of the dimer at constant distance is expected upon ice-water introduction, since higher refractive indices shift the resonance more into the infrared (see also chapter 6.1). Anyhow, a decrease in the resonance wavelength is observed. This blueshift is reversible, introducing room-temperature water shifts the resonance wavelength back to the initial one. It is known that ELPs have a lower critical solution temperature (LCST). Above this temperature they are in a collapsed state, below they are stretched. Decreasing the temperature by introducing ice-water lowers the temperature in the gap between the particles below this LCST, the ELP can transform from the collapsed into the stretched state. The size of the streptavidin-biotin-ELP construct increases by 20 nm. Assuming that streptavidin and biotin do not change their conformation and size in the new environment, the collapsed state of ELP on the surface is 20 nm smaller than the stretched one.

Differently sized ELPs between the dimers

Introducing streptavidin-functionalized particles in a flow cell that contains biotinylated ELP particles, dimerization is possible (experimental details see appendix C.5). In order to prove that

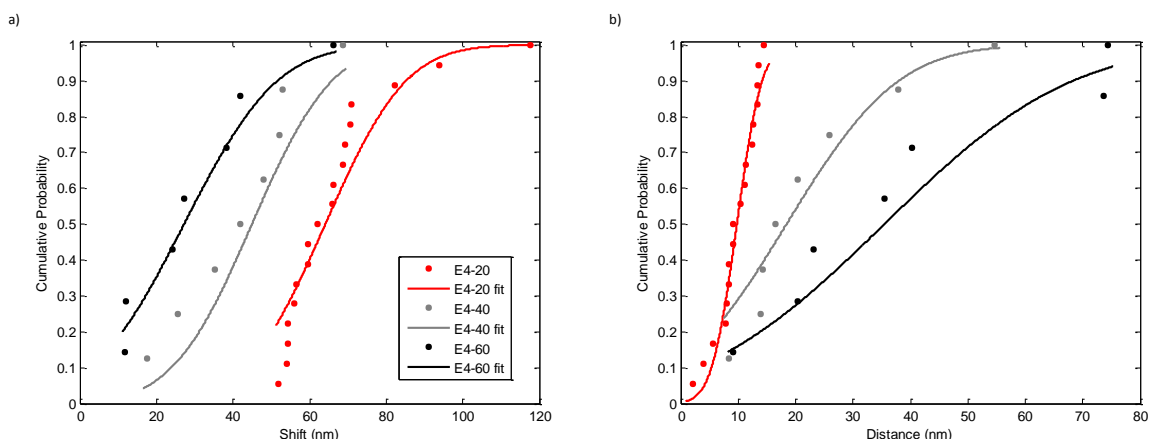


Figure 6.13.: Shift and Distance for Different ELPs

a) Shift of the resonance wavelength upon dimerization with different ELPs as linker molecules. Bigger ELPs cause smaller shifts. b) Distance between the two gold spheres of a dimer for different ELPs. Bigger ELPs cause bigger distances.

the synthesized dimers carry ELP as linker molecule, different ELPs are used and the shift upon dimerization is recorded (table 6.1). For increasing molecular weight of the ELP, a decrease in the shift can be observed. For the highest molecular weight ELP (E4-120, $M_W = 49400 \frac{\text{g}}{\text{mol}}$) no dimerization could be measured due to “dirt” in the flow-cell.

This dirt is probably ELP itself, which aggregates in the buffer needed for the dimerization reaction due to high salt concentrations. Nevertheless, also E4-120 binds to the particles, as measured by a red-shift of the spheres-spectrum of 2 nm (see figure C.23 in appendix). The reason for the decreased shift upon increasing molecular weight of the ELP is the size of the linker molecule. The higher the molecular weight, the bigger the linker, and the further apart are the two spheres. For increasing distances, a decrease in the shift is expected from theory (see also chapter 6.1). Since the dimers differ only in the length of ELP, being part of the streptavidin-biotin-ELP linker, one can be sure that ELP is working as a linker molecule. The distance in between the dimers is calculated using the calibration from chapter 6.1.1. A plot of the distance versus the size (hydrodynamic diameter of ELP obtained by DLS (Flügel, 2010) shows a linear behavior. It is known that the hydrodynamic radius scales with the molecular weight

| Name | Repeat Units | Molecular Mass (kDa) |
|--------|--------------|----------------------|
| E4-20 | 20 | 8.4 |
| E4-40 | 40 | 16.5 |
| E4-60 | 60 | 25.2 |
| E4-120 | 120 | 49.4 |

Table 6.1.: Different ELPs

$$M_W \sim R^v$$

with v being the fractional dimension. A double-logarithmic plot of the hydrodynamic radius

6. Nanoparticle Assemblies

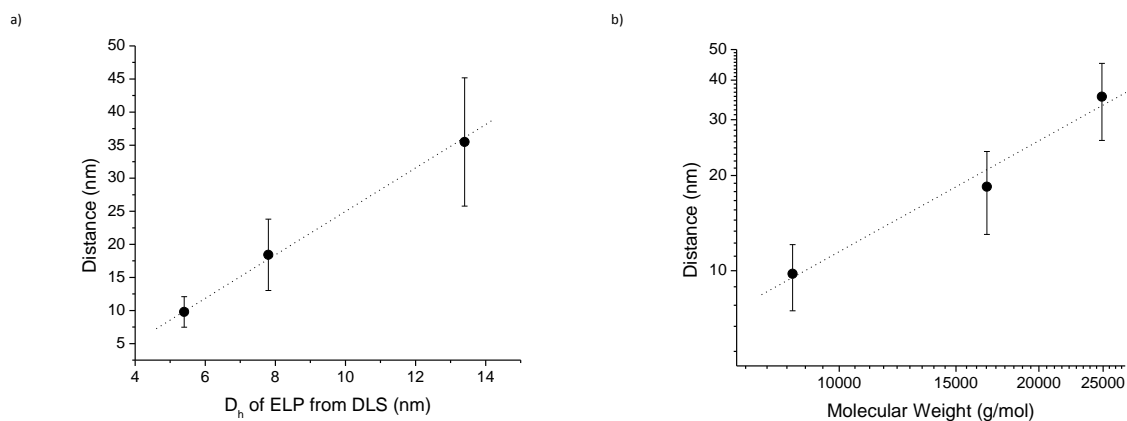


Figure 6.14.: Distance between Dimers over D_h and M_W

a) The distance between the dimers depends linearly on the hydrodynamic diameter of ELP determined by dynamic light scattering (Flügel, 2010), whereas the dependency on the molecular weight of the ELP (b) shows a linear behavior only in a double logarithmic plot.

versus the molecular weight reveals ν as slope of a linear fit. An ideal coil in theta solution has a fractional dimension of 0.5. For bad solvents bigger fractional dimensions are expected. The linear fit of the distance versus the molecular weight in figure 6.14b has a slope of 1.16. A fractional dimension of 1 would correspond to an infinitely thin rod, 2 to a circle or plate, 3 to a solid sphere. It can therefore be stated that the streptavidin-biotin-ELP complex in between the dimers is *not* an ideal coil but probably better represented by a rod-shaped geometry, confirming the fact that the ELP at room-temperature is in a more collapsed state.

Different % of ELP between the dimers

The concentration of ELP on the first particle can be varied by incubating the particles with a mixture of biotinylated ELP and mPEG. Doing this in batch shows via an agarose gel electrophoresis (see appendix figure C.28) that different ratios of ELP and mPEG show different running speeds. The observed running speeds do not depend linearly on the ratio between ELP and mPEG, neither from batch, nor from surface coverage (appendix figure C.28). Therefore, it cannot be stated if both species have the same binding affinity or not, but it is confirmed that a variation in the concentration of ELP on the surface is present.

In single particle dimerization experiments, one sees that dimers are formed for 10, 50, and 100 % of biotinylated ELP in batch (figure 6.15). The higher the percentage of biotinylated ELP, the bigger the shift upon dimerization. Since a bigger shift corresponds to a smaller distance, a higher percentage of ELP seems to account for a more aggregated state of the streptavidin-biotin-ELP complex. The distance in between the dimers depends linear on the % of ELP in solution. The smallest distance is measured for a 100% coverage by ELP

The percentage of the surface covered by ELP is in general comparable to a concentration of ELP in solution. For ELP solutions it is known that the cloud point temperature (or LCST, temperature where the collapse of the stretched form is observed) decreases with increasing

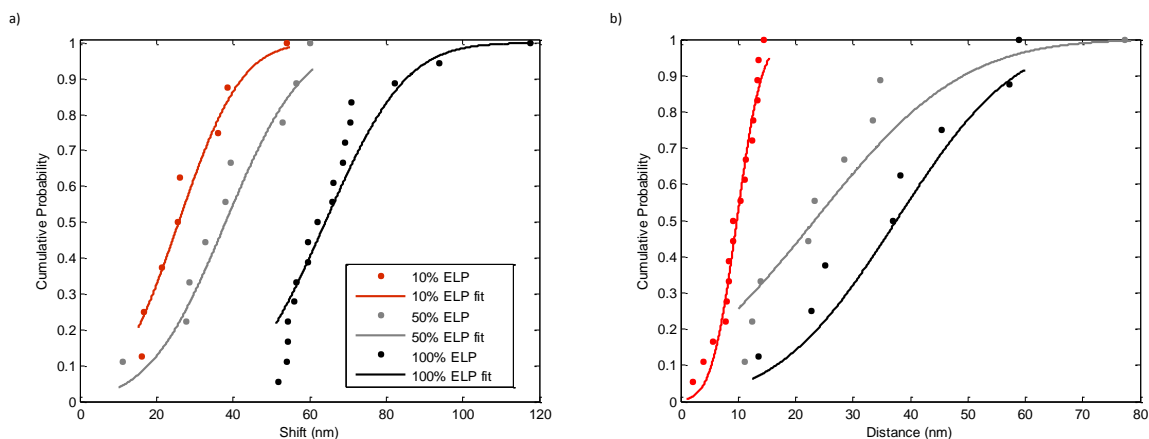


Figure 6.15.: Resonance Shift and Distance for Different % of ELP

a) Shift of the resonance wavelength upon dimerization with different % of ELP (legend corresponds to % ELP in batch). Higher % of ELP cause bigger shifts. b) Distance between the two spheres of a dimer for different % of ELP. Bigger % of ELP cause smaller distances, indicating that the ELP is in a more collapsed state.

ELP concentration (Flügel, 2010). It sounds plausible that for higher percentages of ELP on the surface the local concentration of ELP is higher and the ELP is more likely in a collapsed state (meaning the transition temperature is below room temperature). Another hint that higher % of ELPs have lower transition temperatures is the fact that a blueshift upon introduction of ice-water is only observed in the case where only 10 % of ELP is used. In the experiments with 50 or 100 % ELP, no blueshift can be measured. Since the blueshift is only observed if the temperature in the gap is below the transition temperature, the local concentration in the case of 50 and 100 % ELP is probably too high (the transition temperature too low) to be fallen below. It is known that for ELP in solution there exists a linear relationship between the transition temperature T_t and the logarithm of the concentration (Flügel, 2010). For the ELP used here, this relation is

$$T_t = 61.9 - 11.4 \log C \quad (6.6)$$

with T_t in $^{\circ}\text{C}$ and C in μM . Assuming a 100 % coverage of a 60 nm gold sphere with close-packed ELP, the concentration of ELP in the shell around the particle (shell-thickness of 5.4 nm, representing the hydrodynamic diameter of the ELP in solution in its uncollapsed state) is 8.82 mM. This yields a transition temperature of 17 $^{\circ}\text{C}$ (using equation 6.6), which is well below room temperature. For the other concentrations, either the concentration from bulk can be used (50 and 10%, resulting in 4.41 mM and 882 μM and transition temperatures of 20 and 28 $^{\circ}\text{C}$ respectively) or the surface coverage of ELP can be considered (see appendix figure C.27) and the concentrations from bulk convert into 87.5 and 44 % (7.7 and 3.9 mM, transition temperatures of 18 and 21 $^{\circ}\text{C}$ respectively, figure 6.16). From those calculations it should be possible for all investigated concentrations to transform the ELP from a collapsed to a stretched state by introducing ice-water. Since this is not the case, the behavior of ELP on the surface of a gold nanoparticle (or in between the surfaces of two spheres) differs from its batch characteristics.

6. Nanoparticle Assemblies

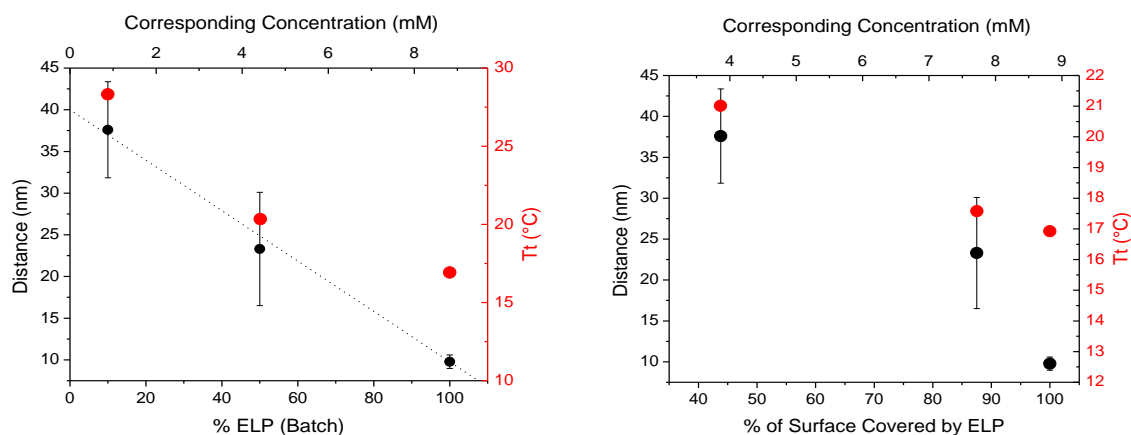


Figure 6.16.: Comparing % ELP/Distance with Concentration/Transition Temperature

a) The distance between the dimers depends linear on the concentration of ELP in batch (and the corresponding concentration), while the transition temperature shows an exponential behavior. b) Converting the concentration from batch into a concentration on the surface of the gold nano particle, the distance does not show a linear behavior anymore.

Summary and Outlook

It could be shown that the general strategy of linking two gold nanospheres by a biotin-streptavidin-interaction is applicable to other polymers instead of PEG. ELP-linked dimers are formed and the transition from collapsed to stretched of the ELP is measured by spectral shifts of the dimer. It is shown that ELP on the surface behaves different from ELP in solution, concerning the temperature of the transition.

6.2. Core-Satellite Structures

For the detection of small changes in the environment caused by binding, adsorption and desorption of biomolecules, a highly responsive sensor is required. This sensor is supposed to be chemically stable and easy to synthesize. Furthermore, a resonance position tunable to external needs is desired. Combining brightness, tunable resonance wavelength, sensitivity to their local environment, and specifically addressable recognition, conjugates of nanoparticles with biomolecules form the basis of sensors based on optical recognition techniques. In the previous chapter, dimeric structures were explored and mainly used to determine the interparticle distance. Core-satellite structures, composed of a (big) plasmonic core particle combined with smaller plasmonic satellites, offer a route for sensing distance (conformational) changes caused by assembly, disassembly or rearrangement driven by binding or desorbing biomolecules. At the same time they are also sensitive to global refractive index changes. Their sensitivity is thought to be much higher than pure spherical particles. In contrast to dimeric structures, they can easily be produced in batch. The drawback is that from a theoretical point of view, they are much harder to treat.

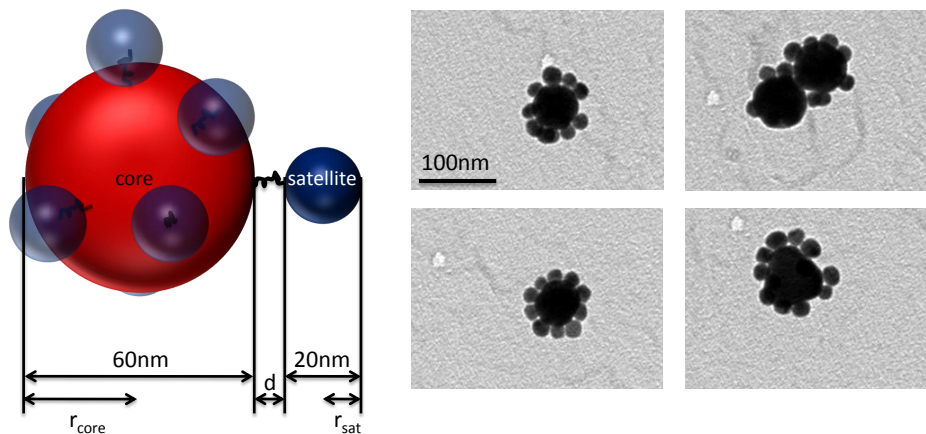


Figure 6.17.: Flowers

Model and TEM images of the flower-like assemblies consisting of a 60 nm gold core decorated with 20 nm satellite gold particles. The scalebar (100 nm) is the same for all images.

In this section I show that 60 nm core particles decorated with ~ 7 20 nm sized satellite particles have a much higher sensitivity to local refractive index changes compared to “naked” 60 nm spheres. Furthermore, they have a simple synthesis and are chemically stable in high ionic strength environments and under an applied electric field.

From a theoretical point of view, core-satellite nanostructures are a promising geometry for plasmonic sensing applications. The basic question, which geometry will show the highest sensitivity, is still not solved to full extent. Ross (Ross *et al.*, 2009) shows in a theoretical study using the Generalized Multiparticle Mie formalism (GMM) that there are four variables to consider while describing core-satellite structures:

- $n_{\text{satellites}}$ -the number of attached small particles,
- $r_{\text{satellites}}$ -the size of the small particles,
- r_{core} -the size of the core,
- $d_{\text{satellites}}$ -the distance between core and satellites.

Additionally, also the number of cores n_{cores} may vary. Furthermore, the composition of the assembly can be altered, for example by forming mixed flowers, composed either of a gold core with silver satellites or vice versa (Sebba *et al.*, 2008a). For their theoretical studies, Sebba *et al.* (Sebba *et al.*, 2008a) use a system in which all satellites are identical in size and distance from the core, and arranged accidentally around it. The core is composed either of gold or glass,

6. Nanoparticle Assemblies

the satellites are always made out of gold. Using the Johnson-Cristy (Johnson & Christy, 1972) values for the dielectric function of gold, they come to the following results: Increasing $n_{\text{satellites}}$ increases the observed resonance position, while the peakwidth is decreasing. Both effects are attributed to plasmon coupling between core and satellites. Also for an increase in $r_{\text{satellites}}$ a linear increase of the resonance wavelength is seen, accompanied by a broadening of the peak. This broadening is strongly increasing with the size of the satellites, because the whole flower-like assembly becomes closer to the size of the wavelength of light and retardation effects become more prominent. Additionally to those two relationships, the resonance wavelength decreases with both, increasing r_{core} and increasing distance between core and satellites. This relation is more or less linear for satellites $< 50\text{nm}$, which corresponds to the quasi-static regime. For bigger satellites, a non-linear behavior is observed. BEM-simulations (performed by Dr. Jan Becker, working group of Prof. Dr. Carsten Sönnichsen) of core-satellite assemblies ($r_{\text{core}}=30\text{ nm}$, $r_{\text{satellites}}=10\text{ nm}$, $n_{\text{satellites}}=6$) predict a sensitivity of $150 \frac{\text{nm}}{\text{RIU}}$ (compared to $97 \frac{\text{nm}}{\text{RIU}}$ for the “naked” core, see also appendix C.6).

Sebba et al. (Sebba *et al.*, 2008b) show experimentally that variations of the distance between an assembly of 20 $r_{\text{satellites}}=6.5\text{ nm}$ gold satellites around a $r_{\text{core}}=25\text{ nm}$ gold core cause shifts in the resonance positions. Unfortunately they ignore shifts in the local refractive index while the linker-DNA is stretched or compressed. Therefore, a need for pure refractive index sensing measurements is given.

6.2.1. Sensing Refractive Index Changes

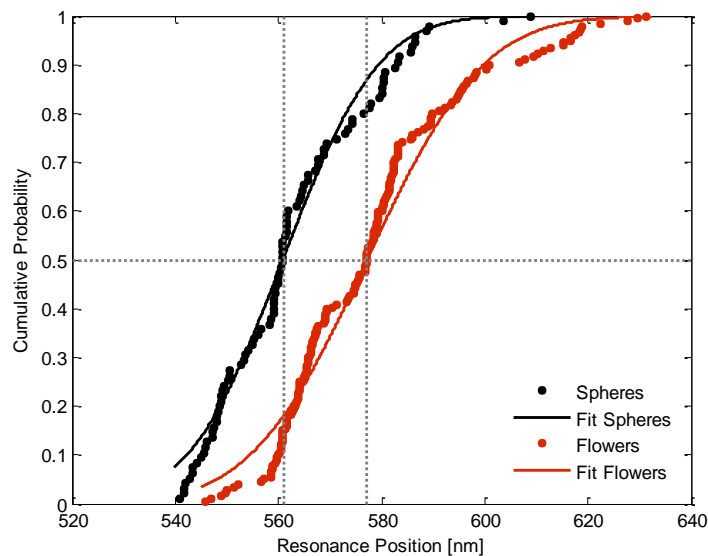


Figure 6.18.: Single Particle Resonance Positions of Spheres and Flowers

In single-particle measurements, flowers (red) show an increased resonance wavelength compared to naked spheres of the same core-size (black).

Table 6.2.: Sensitivity and FOM of Spheres and Flowers

| | $\lambda_{\text{res,water}}(\text{nm})$ | $\lambda_{\text{res,DMSO}}(\text{nm})$ | $S (\text{nm/RIU})$ | FOM |
|---------|---|--|---------------------|------|
| spheres | 563 | 568 | 43 | 0.13 |
| flowers | 578 | 640 | 535 | 1.6 |

Upon the formation of the flowers in water, the ensemble spectrum shows a peak shift of 21 nm to longer wavelengths (see appendix C.6). Single particle scattering spectra of the same spheres and flowers as in the ensemble measurement, immobilized on the glass surface ($n=1.5$) are recorded. The mean resonance wavelength of the flowers in water is 578 nm. This is 16 nm red-shifted compared to 60 nm spheres in water, which have a mean resonance wavelength of 563 nm. The red-shift is slightly smaller than in the ensemble spectrum. The reason for this might be the fact that for the single particle measurements only the fraction of the sample supposed to be single-core aggregates is investigated while the ensemble spectrum includes aggregates with multiple cores, which are supposed to have an increased wavelength. The shift upon changing from water ($n=1.33$) to 75 %DMSO ($n=1.446$) is 62 nm for flowers and 5 nm for spheres (mean of the measured resonance positions). In order to characterize the samples concerning possible sensing applications, sensitivity S and figure of merit FOM can be considered (Becker *et al.*, 2010).

$$S = \frac{\Delta\lambda}{\Delta n} \quad (6.7)$$

$$\text{FOM} = \frac{S}{FWHM} \quad (6.8)$$

Comparing the sensitivity of both samples, flowers show a 100 x higher sensitivity than spheres, while the FOM increases by a factor of about 12 (see table 6.2). This makes flowers in general very desirable for sensing applications. From the BEM-simulations, the sensitivity for single spheres is supposed to be $97 \frac{\text{nm}}{\text{RIU}}$ (see appendix C.6). The experimentally observed lower (effective) sensitivity $S_{\text{eff}}=43 \frac{\text{nm}}{\text{RIU}}$ might be due to the underlying glass substrate, which does not contribute to the refractive index change. It remains the question if the shift in resonance position of the core-satellite structures is only caused by a shift in the surrounding refractive index, or if additionally the distance between core and satellites might change. Since BEM-simulations (see appendix C.6) predict a much lower sensitivity of $150 \frac{\text{nm}}{\text{RIU}}$ for the flower-like assemblies, a change in the separation distance upon introduction of DMSO is likely. To exclude this effect, further experiments with other refractive index changing media are planned.

6.2.2. Synthesis and Separation

The presented core-satellite assemblies are easy to make. In order to prepare core-satellite structures (“flowers”), the first particle (core-particle) is functionalized with a dithiol-PEG, which

6. Nanoparticle Assemblies

offers on both ends binding sites for gold. In order to avoid loop-formation and back-binding to the initial particle, dithiol-PEG is used in big excess. After functionalization of the first particle, satellite particles along with a reducing agent (which destroys unwanted dithiol-bridges) are incubated and create the desired flower-like structure. Further details of the reaction and reaction conditions are found in appendix C.6. For the single particle measurements, the as-synthesized samples are separated via a gel electrophoresis into single- and multi-core structures. Using agarose gel-electrophoresis in a preparative way (besides the starting pocket there is a second collecting pocket -introduced while casting the gel-, from which the sample can be removed at a desired time, details see appendix C.6), single-core assemblies can be separated from multi-core ones. This is important, since for the single particle measurements only the single-core assemblies are desired. In ensemble spectra one can see that besides a shift of ~ 17 nm to longer wavelengths (see appendix C.6), an increase in FWHM (full width at half the maximum intensity) can be observed as well. This is a hint that not all of the built structures are homogeneous.

Table 6.3.: Separation of Flowers by Gel-Electrophoresis

| lane | collection time | $n_{\text{satellites}}$ | n_{cores} |
|------|-----------------|-------------------------|--------------------|
| A1 | 120-170 min | 7.0 | 1.21 |
| A2 | 175-200 min | 6.4 | 2.15 |
| A3 | 205-240 min | 7.1 | 3.71 |

particle-spectrum and TEM images (which would tell about the “true” structure) is not possible. The knowledge that multi-core assemblies can be separated from single-core ones enables for the use of the flowers in single particle experiments. Analyzing only the fastest lane from the gel (A1, see appendix C.6), the probability to measure homogeneous samples in single particle experiments is high (see table 6.3). Therefore, only this fraction of the sample was investigated for the DMSO-sensitivity measurements in chapter 6.2.1. Originally it was thought that the number of satellite particles can be controlled by the ratio of dithiol-PEG to monofunctional one. Interestingly this is not the case. No matter how much dithiol-PEG compared to monothiol-PEG is present, the average number of satellites is around 8 per core (Gaussian fits of distribution, see table 6.4).

They can differ in number of cores (n_{cores}) and number of satellites ($n_{\text{satellites}}$). The distance between core and satellites as well as satellite and core size can be supposed to be constant since the same particles and linker molecules are used throughout the study. The homogeneity of a flower sample in both, n_{cores} and $n_{\text{satellites}}$, is a need for single-particle studies, since so far a correlation between single-

Table 6.4.: Variation of Dithiol-PEG

| sample | $n_{\text{satellites}}$ | σ |
|------------------|-------------------------|----------|
| 100% dithiol-PEG | 9.3 | 1.5 |
| 25% dithiol-PEG | 7.2 | 1.4 |
| 0% dithiol-PEG | 8.3 | 1.3 |

This can be due to different reasons. Either the dithiol-PEG does make back-binding to the core and looks from the point of view of the satellite particle the same as monofunctional PEG, or the entanglement of small particles inside the PEG chain (the interaction of small particles with the polymer chain) is much stronger than interaction with the second thiol functionality. No matter which of these facts is true, the strategy of having a dithiol-PEG as a controlled linker between dimers of particles is not followed (see chapter dimers 6.1), since dimerization can not be performed in a controlled way.

6.2.3. Summary and Outlook

The presented core-satellite structures, consisting of a 60 nm gold nano particle as core, decorated with 20 nm sized satellite particles, show a much higher sensitivity to refractive index changes than naked spheres of the same size. The “flowers” are easy to synthesize and stable even in high salt conditions and in an applied electrical field (TBE-buffer, 150 V). This makes them versatile plasmonic sensors for changes to the local environment.

Unfortunately it is hard to separate the observed shift due to refractive index changes from a shift caused by changes in the distance between core and satellites. For this reason, investigations of more easy structures (dimers, see chapter 6.1) need to be done in order to be able to separate those two effects. Furthermore, additional experiments with other refractive index changing media are planned, also concerning reversibility. More simulations, concerning distance changes as well as symmetrical/ asymmetrical assembly of the satellites around the core, need to be run. With this knowledge, a better prediction of the expected shift and a separation between distance and refractive index changes, will be possible.

7. Summary and Outlook

Metal nanoparticles show bright colors upon illumination with light, due to their small size and the fact that they are metallic. This color is already used, for example, in colored glass windows. Also metal nanoparticle suspensions are intensively colored, the whole visible spectrum up to the IR-region is accessible. In this thesis I present the synthesis of those plasmonic nanostructures, including gold nanorods, silver-coated gold nanorods, nanoparticle dimers, and core-satellite structures. Furthermore, their plasmonic properties are characterized and used in different sensing applications.

In order to have access to high quality nanoparticles, specially designed for external needs like fixed laser-wavelengths or pre-selected resonance positions, it is crucial to know the growth mechanism of the particles. In chapter 3, a model for the growth of gold nanorods is developed. It shows that besides the presence of surfactants to stabilize the growing nanoparticles, it is crucial to ensure a low growth speed and high selectivity of growth to obtain anisotropic shapes. The low speed of growth is achieved by a small difference in the redox potentials between reduced and oxidized reaction partners. This aspect of the gold nanorod synthesis is not yet reported or discussed in detail in literature and helps to clarify the effects of pH, counterions, and ionic strength, leading to changes in the synthesized particles. Knowing the importance of the electrochemical potential, fine tuning of the gold nanorod synthesis with the help of different reducing agents will be possible. Furthermore, this knowledge might help to improve the synthesis of other metallic nanoparticles like silver nanorods, which are not as nicely accessible as gold nanorods.

Following the determination of a growth model for the synthesis of pure gold nanorods, the growth of silver on top of a pre-formed gold nanorod is studied (chapter 4). Upon coating the gold nanorods with a thin shell of silver, a reduction in the ensemble linewidth is observed, a desired feature for optical sensors, since a reduced linewidth implies a higher figure of merit. This reduction, the so called “plasmonic focusing effect”, is caused by a change in the plasmon-shape relation. By theoretical modeling, the observed ensemble effect can be divided into three contributions (single particle linewidth, distribution of aspect ratios, plasmon-shape relation). With this knowledge, the experimental spectra can be theoretically recovered. Furthermore, the kinetics of the coating process are explored. Determination of the reaction order and activation energy allow to predict the reaction time in order to stop the reaction at a desired resonance wavelength. With this knowledge, the synthesis of well-designed plasmonic particles is possible.

7. Summary and Outlook

In order to control temperature and reaction time more precisely, an automated stop-flow or continuous-flow setup might be desirable.

Gold nanorods have the property that the light they scatter is polarized. Therefore, by introducing a detection scheme which accounts for this polarization, their orientation can be determined. In chapter 5, gold nanorods are embedded in a polymer matrix. By recording time traces of their intensity in two orthogonally polarized channels, their rotation inside the gel is determined at different temperatures. The rotational motion is used to measure the transition temperature of the gel matrix. In order to determine if the environment of the gold nanorods is heterogeneous or homogeneous, longer time-traces with higher acquisition frequencies need to be recorded. With an improved setup, concerning illumination and data processing, gold nanorods as rotational sensors will measure up with conventional single molecule probes and eventually overtake in special applications.

Besides the use of single nanoparticles, also assemblies of nanoparticles can be used as sensors. Dimers of gold nanoparticles (chapter 6.1) offer a system to measure both, refractive index and interparticle distance at once. After calibrating the resonance wavelength to distance relation by external methods, the interparticle distance in different media is measured. Furthermore, elastin-like polypeptides (ELPs, thermoresponsive bio-mimetic polymers) are characterized with the help of the dimeric-assembly. Since the crucial factor for using gold nanoparticle dimers as distance sensors is the calibration, increasing the confidence of the used calibration method or employing others, like correlated spectral and electron-microscopy investigations of the same particle (in the same environment), are future areas of research. Also theoretical calculations taking into account surface contributions and the polymer matrix around the particles are worthwhile to elucidate the calibration-problem. More complex nanoparticle assemblies (core-satellite structures) are synthesized as well and used as sensor for refractive index variations (chapter 6.2). They show theoretically and experimentally an increased sensitivity compared to naked core-particles of the same size. While the performed measurements probably show a combined spectral response to refractive index *and* interparticle distance changes, measurements in different media and concerning reversibility need to be performed.

The thesis presented here shows many applications for plasmonic nanoparticles and nanoparticle assemblies, and initiates a lot of future projects. With the help of the presented data and the experimental details given in the appendix, new and interesting results and conclusions are expected to derive from the highlighted topics.

Appendix

A. Analytical Methods

A.1. Ensemble-Spectra

So called “ensemble-spectra” are taken from solution, representing the extinction (absorbance and scattering) of a high number of particles (an ensemble). From these spectra, general features of the sample can be derived. One characteristic feature is the resonance wavelength of the nanoobjects. While gold nanospheres have only one plasmon resonance wavelength, nanorods show two resonance peaks in their spectra, according to plasmon resonances for the longitudinal and transverse resonance mode (see figure A.1). The position of the resonance peak is connected to the size of the particles (diameter of gold nanospheres, aspect ratio of gold nanorods), the refractive index of the surrounding medium, and the interparticle distance. For gold nanorods, the position of the longitudinal resonance peak in a medium with refractive index, n , can be used to estimate the mean aspect ratio of the sample by using the following relation (Becker, 2010):

$$\lambda_{\text{res}} (\text{nm}) = (91 \cdot \text{aspect ratio} + 138) \left(\frac{\text{nm}}{\text{RIU}} \right) \cdot n - (15 \cdot \text{aspect ratio} - 215) (\text{nm})$$

In addition, the particle concentration can be calculated from the extinction E , using Lambert-Beer’s law, if the extinction coefficient ϵ is known.

$$E = c \cdot d \cdot \epsilon \tag{A.1}$$

$$E = \text{extinction} = -\log_{10} \frac{I_{\text{trans}}}{I_{\text{ref}}}$$

c = concentration

d = distance, the light traveled through the absorbing media

$$\epsilon = \text{molar decade extinction coefficient} = \frac{N_A \cdot \sigma}{\ln(10)}$$

σ = extinction cross section of one single particle

The extinction is the ratio between transmitted and reference intensity. This linear relationship between concentration and extinction is true for dilute solutions with $E < 1$, but might change at higher concentrations due to a possible change of the ϵ values and multiple scattering events. Since in the case of gold nanoparticle solutions the concentration is usually very low, the particle concentration is one value that can be derived from an ensemble spectrum, as soon as the extinction coefficient is known (BBInternational, <http://www.bbighgold.com/>; Orendorff & Murphy, 2006).

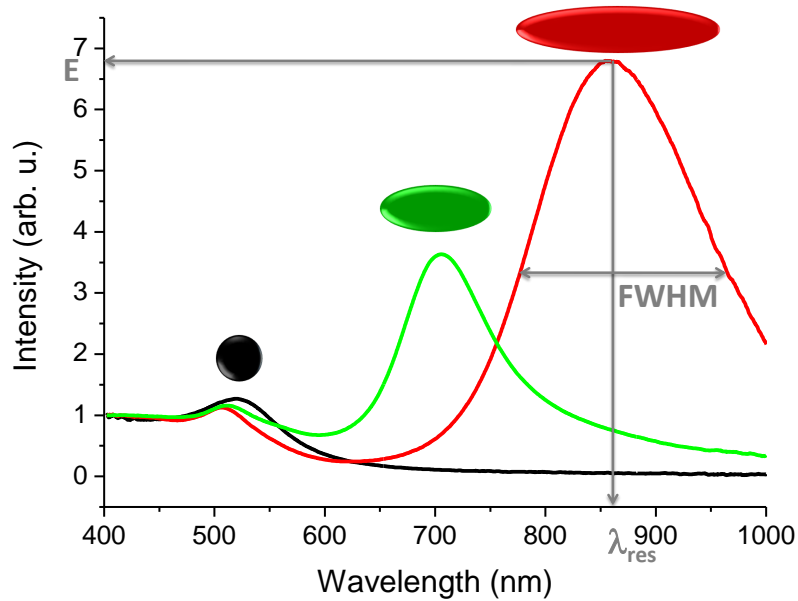


Figure A.1.: Typical Ensemble Spectra

Ensemble spectra (normalized at 400 nm) for gold nanospheres (black), small (green), and large (red) aspect ratio gold nanorods.

An additional source information in the extinction spectrum is the full width at half maximum of the peak (FWHM or linewidth). In contrast to single particle spectra, where the width is directly connected to the plasmon lifetime, the peak width in ensemble spectra is also connected to the polydispersity of the sample. The more monodisperse a sample is, the thinner the peak becomes. Therefore, the spectrum gives a hint about sample quality.

The ensemble spectra presented in the thesis are recorded using a fiber optic spectrometer (Ocean Optics, USB-2000) and a fiber coupled tungsten light source (Ocean Optics, FL 2000 FHSA).

A.2. Single-Particle-Spectra

In contrast to ensemble spectra, which show general features of a nanoparticle sample, single particle spectra only give information about the scattering characteristics of one single particle. Statistics over a large number of single particle spectra will result in ensemble information.

Single particle spectra of gold nanoparticles are taken combining the technique of dark field microscopy (see section A.3) with a spectrometer (Becker *et al.*, 2007). In general, the scattered light from one particle is no longer directed to the ocular, but to a spectrometer, which records a spectrum. Further details of the used setups are given in appendix B.

The peak position reveals (in first approximation) the aspect ratio of a gold nanorod, the diameter of a gold nanosphere, or the distance between a particle pair. Furthermore, it is connected to

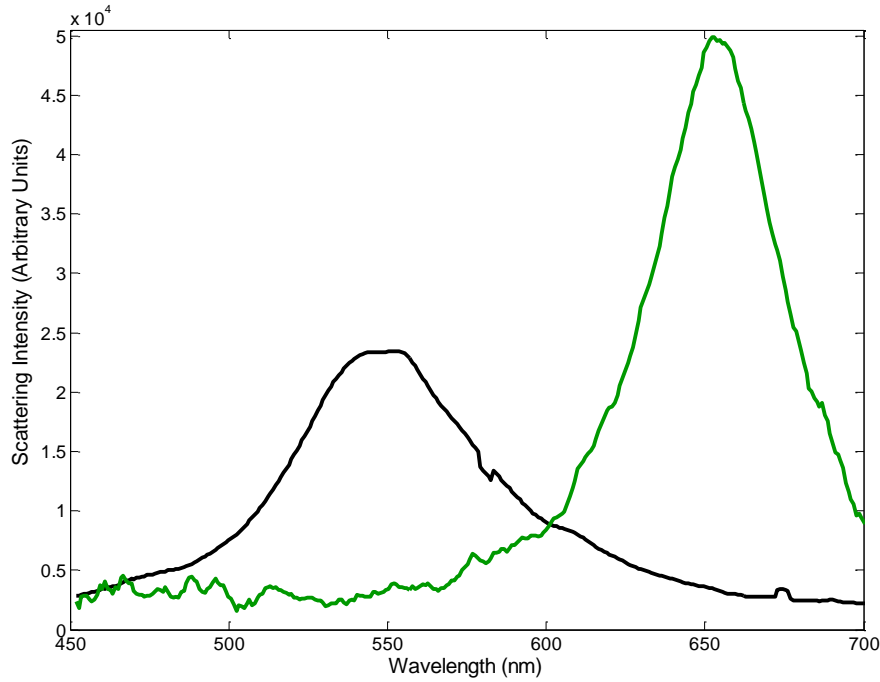


Figure A.2.: Typical Single Particle Spectra
Single particle scattering spectra of gold nanospheres (black) and nanorods (green).

the refractive index of the surrounding medium. The higher the refractive index, the larger the observed resonance wavelength. The exact prediction of the resonance wavelength upon changes in the surrounding medium is subject to theoretical studies in order to determine the nanoparticle's sensitivity and thereafter using the nanoparticles as refractive index sensors.

The intensity, in contrast to ensemble spectra where it attributes to the concentration of the sample, can now be used to determine the scattering efficiency of the observed nanoobject (in comparison to a standard, e.g. glass beads of a known size). Since the scattering coefficient can be used as a measure for the volume of a plasmonic particle of known shape, it is possible to yield information about the size of the nanoparticles from the intensity.

Also the linewidth of the single particle spectrum has a totally different meaning compared to ensemble spectra, where it indicates the polydispersity of the sample. For single particle spectra the peakwidth Γ is directly connected to the plasmon lifetime τ via equation A.2. The narrower the peak, the longer the plasmon lifetime. For sensing applications it is desirable to have a narrow peakwidth and big figure of merit (FOM, see equation 6.8).

$$\tau = \frac{2\hbar}{\Gamma} \quad (\text{A.2})$$

A.3. Dark-Field-Microscopy

Microscopy in general is used to image structures or particles that are too small to be seen with the naked eye. Many different microscopes are available to see objects far smaller than the resolution of the eye, the most popular one being probably the light microscope, consisting of a set of lenses that make it possible to resolve structures down to the size of some 100 nm. In its simplest possible form the microscope consists of two lenses: An objective that creates an intermediate image, and an eyepiece, acting as a simple magnifying glass for the intermediate image.

The optical resolution d_{\min} (smallest distance to be resolved) of a microscope is given by equation A.3. From this equation it can be seen that one way of increasing the resolution of a microscope is to use light of smaller wavelengths (e.g. UV light or electrons, see section A.4). An other approach is to increase the refractive index, n , of the immersion media, going from air to water to immersion oil ($n_{\text{air}}= 1$, $n_{\text{water}}= 1.33$, $n_{\text{immersion oil}}= 1.518$ (CRC, 2004)). Furthermore, increasing the numerical aperture of the objective N.A. by increasing the opening angle α increases the optical resolution as well.

$$d_{\min} = \frac{\lambda}{n \cdot \sin\alpha} = \frac{\lambda}{\text{N.A.}} \quad (\text{A.3})$$

In standard bright field optical microscopes, light passing the (in general very thin and translucent) object is used to create an image. This image will show a dark object in front of a bright background. In contrast to this, a dark field (DF) microscope does not illuminate the sample directly but uses only light scattered by the sample to create an image.

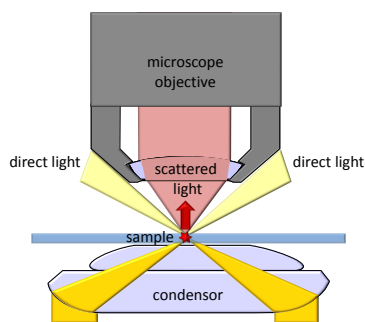


Figure A.3.: Dark-field Illumination

The dark-field condenser allows for indirect illumination of the sample with a hollow cone of light.

This image will show a dark background behind bright objects. The most important part in a dark-field microscope is the dark-field condenser (figure A.3). It provides a hollow cone of light to illuminate the sample and makes sure that only scattered light reaches the objective.

In order to obtain good images, it is important to adjust the condenser very carefully. Otherwise, contrast and brightness will not be optimized for imaging objects in the dark field mode. Since gold nanorods are smaller than visible light (400-700 nm), they cannot be resolved in an optical microscope. Nevertheless, a dark field microscopy is a common tool to investigate metal nanoparticle samples. The reason is the high scattering intensity of metal nanoparticles combined with a plasmon resonance wavelength in the visible range, making it possible to see

the scattered light as bright spots in a dark field image as long as the sample is so much diluted that the distance in between nanoparticles is larger than the resolution of the microscope.

A.4. Electron-Microscopy

Transmission Electron Microscopy (TEM) is used for imaging samples too small for common light microscopy (meaning objects smaller than the wavelength of light, see section A.3). Nevertheless, a TEM works similarly to a light microscope, substituting photons for electrons and optical for magnetic lenses (Fultz & Howe, 2001).

Electrons, sent out from an electron source (hot cathode, LaB_6) and traveling through a system of magnetic lenses, cross the specimen and hit a viewing screen (see figure A.4).

Usually, all transmitted and diffracted rays are combined to form an image there. This image reveals the nanoscale morphology of the particles. The “mass-thickness” contrast in the TEM image results from the electron capture cross-section of the particular element (increasing with increasing atomic number Z) and the thickness of the material. This is the reason why gold appears darker than silver in a TEM image and some organic materials can not be seen at all (accompanied with the possible burning of the sample under electron irradiation). In order to avoid collisions between electrons and air molecules, the TEM is operated in high vacuum. Imaged samples therefore need to be dry and stable under these conditions.

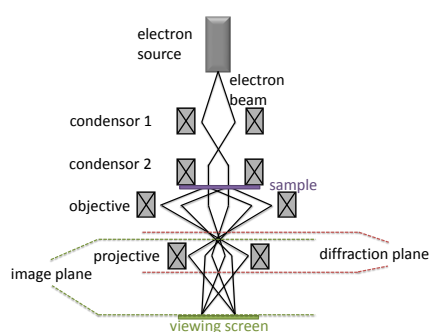


Figure A.4.: Transmission Electron Microscope Schematic design of a transmission electron microscope. The electron-beam is focused by a set of magnetic lenses and hits a viewing screen. Diffraction patterns can also be obtained.

The transmission electron microscopes used here are a Philips CM12, a Philips EM420, and a FEI Tecnai-12. A gold nanoparticle sample is generally prepared by drying 5-7 μl of a concentrated nanoparticle solution on the carbon coated copper TEM grid (Plano). Usually, the sample is washed once with millipore water before drying on the grid in order to remove excess organics, which cause contamination of the TEM and a bad resolution for the obtained images.

Cryo-Electron Microscopy (cryo-TEM)

For many species (especially in biology), dryness and high vacuum are far from their natural environment, which makes it hard to compare structures from TEM images with structure in solution. Cryo-TEM is a technique that enables imaging of liquid samples close to their natural state. The aqueous sample solution is placed on a copper grid that carries a holey carbon film on top. After removing excess solution, a thin water film covers the whole grid and spans

A. Analytical Methods

the holes. Since the holes are of defined size, the formed water films have a regular thickness of about 100 nm. This film is “vitrified” in liquid ethane (ca. -90°C) or liquid propane (ca. -40°C). Since the vitrification process is extremely fast, no ice crystals are shaped, the film stays almost invisible for TEM investigations. For imaging, a TEM grid holder equipped with a liquid-nitrogen cooling system ensures that the sample remains in its vitrified state. Images done with cryo-TEM are therefore closer to the situation found in solution (see also chapter C.5.4).

A.5. Gel-Electrophoresis

Electrophoretic techniques depend on the migration of charged particles (ions, macromolecules, colloidal particles) in an electric field. In general, one can distinguish between carrier-free electrophoresis, which is based on the migration of ions in buffers that are layered above the sample solution, and carrier electrophoresis. Among the various types of carriers used, gel electrophoresis is very common in biological applications (Serwer, 1983; Tietz, 1987; Viovy, 2000), but has also been shown to be an appropriate tool to separate gold nanoparticles according to the number of attached DNA chains (Zanchet *et al.*, 2001; Zanchet *et al.*, 2002).

The velocity of the moving particles depends mainly on their size and charge. In order to achieve a separation by electrophoresis, the electrophoretic mobilities μ_E of the particles have to differ. The electrophoretic mobility is given by the velocity of the moving particle v divided by the applied electric field E (see equation A.4).

$$\mu_E = \frac{v}{E} \quad (\text{A.4})$$

In a carrier-free electrophoresis (no matrix is present, the electrolyte is infinitely diluted), the only two forces acting simultaneously on the particle are the accelerating force F_{acc} due to the charge of the particle, and a retarding friction force F_{fric} , described by Stokes’s law for a spherical particle of radius r with charge q in an electrolyte with viscosity η . In equilibrium, $F_{\text{acc}} = F_{\text{fric}}$, leading to the following expression for μ_E (equation A.5) for spherical particles.

$$F_{\text{acc}} = qE$$

$$F_{\text{fric}} = 6\pi\eta r v$$

$$\mu_E = \frac{q}{6\pi\eta r} \quad (\text{A.5})$$

Introducing a matrix (for example an agarose or polyacrylamide gel) leads to additional forces on the moving particles, for example restraining the migration of the particles if their sizes are in

a comparable range to the pores. Also the charge of the matrix and existing counterions have to be considered.

In polyacrylamide (PAGE) gels, the matrix itself is not charged, not net-flow of ions in the buffer (electro-osmotic effect) need to be considered. This technique is usually used to separate and analyze small DNA-fragments and proteins (Barron & Blanch, 1995). If used for proteins (as in chapter C.4), sodiumdodecyl (SDS)-PAGE is a standard technique. For this method, the anionic detergent SDS is added in excess to the sample and the running buffer. The SDS covers the peptide charge and forms micelles with a constant negative charge per mass unit: 1.4g SDS per 1g protein. Hence, the separation in SDS-PAGE is simply due to the molecular size of the proteins.

For agarose gel-electrophoresis, an electro-osmotic flow can be observed, which is due to the fact that the agarose matrix binds negatively charged ions from the buffer, leading to an excess of positive charge (Ghosh & Moss, 1974). These charges are not fixed and after applying an electric field, they move to the minus pole, tracking water along with them, creating a flow. This flow causes an offset in the mobilities, meaning that also uncharged particles move in the electric field. A common marker for the strength of this phenomenon is vitamin B₁₂ (Vit B₁₂), which is uncharged at a wide range of pH and intensely colored (Serwer & Hayes, 1982). If mobilities are compared, they have to be corrected by the electro-osmotic effect. In order to be able to recover samples separated by gel-electrophoresis, a gel is cast with two sets of pockets, one for loading and one collecting the samples.

A.6. Dynamic Light Scattering

Dynamic light scattering (DLS) is used to measure the diffusion coefficient of scatterers in solution, which allows for determination of the hydrodynamic radius R_h . The fluctuations in the scattering intensity at a constant angle are recorded. They are described by an intensity-time correlation function. This correlation function describes the interaction of two particles at time $t=t$ and at $t=t+\tau$ with the correlation time τ . The function decays exponentially with time, because the particles diffuse away from each other and their correlation decreases. The diffusion coefficient of the scatterers is determined by converting the intensity autocorrelation function into the amplitude autocorrelation function with the help of the Siegert relation. The hydrodynamic radius R_h can be calculated from the diffusion coefficient D_z using the Stokes-Einstein relation:

$$R_h = \frac{kT}{6\pi\eta D_z}$$

The DLS is used to determine the size of the monomers in chapter 6.1 and the size of the elastin-like polypeptides chapter 6.1.3. For further details on light scattering see (Schärfl, 2007).

B. Darkfield Setups

B.1. FastSPS Setup

In the fastSPS setup a standard dark field microscope (Zeiss, Axioplan; 100 W halogen lamp) is coupled to a spectrometer (SP-2150i, Acton) and a CCD-camera (Pixis400, Princeton Instruments). The entrance slit of the spectrometer is replaced by a LCD (LC2002, Holo-eye), which serves as an electronically spacial addressable shutter that allows the investigation of almost all particles in the field of view in a relatively short time. Due to the fact that within a short time a high number of particles is investigated, I mainly used this setup for high-statistic measurements (chapters 6.1, 4, 6.2) . For more details on the setup see (Becker *et al.*, 2007) and “Plasmons as Sensors” (Becker, 2010).

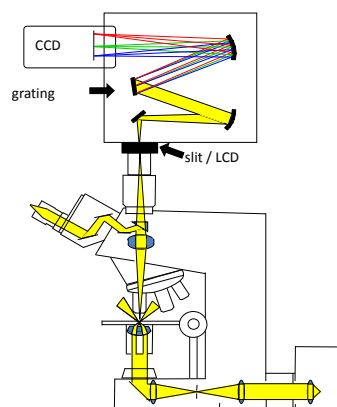


Figure B.1.: FastSPS-Setup

Schematics of the dark-field microscope setup. The scattered light is directed either to the ocular or to an imaging spectrometer, where the light is dispersed and the resulting spectrum captured by a CCD camera. The image is taken from reference (Becker *et al.*, 2007).

B.2. Rotation Setup

In contrast to the fastSPS setup, the entrance to the spectrometer in the rotation setup is defined by a simple slit. In order to conserve high statistical data, the sample is moved through the field of view by moving the sample stage with a piezo scanner. In addition to the fastSPS setup, a polarizer is introduced in the analysis pathway. This makes it possible to distinguish between the light scattered off the longitudinal axis and the light scattered off the transverse one. The rotation setup was used to measure the spectra of gold nanoparticle dimers in different environments for different polarization directions (chapter 6.1)

B.3. Polarization Contrast Setup

Both, fastSPS and rotation setup collect the scattered light (via a grating) in a spectrometer to get spectral information of the particles. In contrast to this, the polarization contrast setup has a polarization beam splitter in the detection pathway. This allows for two orthogonal polarization directions of the same area of the sample to be investigated at once. The two intensity signals from the two polarization directions are recorded on either half of an EM-CCD chip. Further details are found in reference (Pierrat *et al.*, 2009). The polarization contrast setup was used to record time traces of rotating gold nanorods in PNIPAM (chapter 5). Instead of the 63x water immersion objective, a 40x air objective was used.

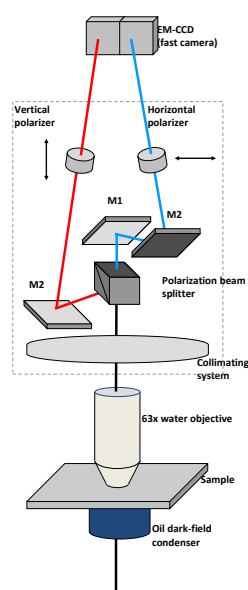


Figure B.2.: Polarization Contrast Setup

Schematic representation of the experimental setup. The sample is illuminated by a dark-field condenser (oil immersion) and the light scattered by the gold nanorods is collected by a water immersion objective. A two-channel polarization system (Dual-View® represented in the gray-dashed box) is then mounted on the microscope, allowing the separation of two orthogonal polarization directions. The two signals are then recorded by a electron-multiplying CCD camera on a single frame, half of the picture corresponding to one polarization direction, the other half to the orthogonal one. The image is taken from reference (Pierrat *et al.*, 2009).

C. Experimental Methods

C.1. General Synthesis of Gold Nanorods

The general procedure for synthesizing gold nanorods is described in the following. In a first step, small gold seeds are produced by reducing 10 ml of a solution of 0.5 mM tetrachloroauric acid ($\text{HAuCl}_4 \cdot 3\text{H}_2\text{O}$, Sigma) and 0.1 M of cetyltrimethylammonium bromide (CTAB, Sigma) with 600 μl ice-cold 0.1 M sodium borohydride (NaBH_4 , Sigma-Aldrich), a strong reducing agent. Adding CTAB to the aqueous HAuCl_4 solution causes a color change from light yellow to darker yellow or slightly orange, due to the creation of gold-bromide complexes (Johnson *et al.*, 2002). Addition of NaBH_4 leads to the formation of small gold colloids with a diameter of 2-4 nm, showing a brownish color. These seeds can be used after storing them for 2 h at 37° C, which causes the decomposition of excessive NaBH_4 . Keeping the solution at room temperature for some days, it turns red, which indicates the appearance of larger, more or less spherical gold colloids, henceforth indicated as gold nano spheres. In a second step, 5 ml of a 1 mM HAuCl_4 solution are prepared and mixed with 5 ml 0.2 M aqueous CTAB solution. A small amount of 0.04 M silver nitrate (AgNO_3 , Sigma-Aldrich) is added (typically in the range of 5-20 μl). This solution is mixed with 70 μl 0.0788 M ascorbic acid (Sigma-Aldrich), which causes decolorization and is later on referred to as "growth solution". Finally, a small amount of seed solution (usually 12 μl) is injected in the growth solution in order to promote the growth of gold nanorods. This process is accompanied by a color change from colorless to blue (if rods with a resonance wavelength of around 650 nm are prepared), or reddish (resonance wavelength over 750 nm). The reaction is typically carried out at 28° C. At temperatures below 28° C, the CTAB precipitates. Using higher temperatures, the resulting rods will be more spherical in shape and show lower resonance wavelengths. It takes about 30-60 min for the reaction to complete. Nevertheless, the rods change over a much larger timescale. Unreacted metal salts and the excess of surfactants are removed from the growth solution through two centrifugation steps at 6000 g for 20 min. In each centrifugation step, after removing the supernatant, the precipitated pellet is resolubilised in 1 ml of Millipore water (18M Ω) the first time and in 50-100 μl of water the second time. A detailed overview of the carried out syntheses is given in the following section.

C. Experimental Methods

C.1.1. Overview Over the Carried out Syntheses

Seed dilution

| name | corresponds to original seeds | water | CTAB | seeds |
|------|-------------------------------|-----------|--------------|-----------|
| | | | 0.2 M | |
| | µl | ml | ml | µl |
| A | 0 | 10 | 10 | 0 |
| B | 6 | 9.94 | 9.94 | 120 |
| C | 12 | 9.88 | 9.88 | 240 |
| D | 24 | 9.76 | 9.76 | 480 |
| E | 48 | 9.52 | 9.52 | 960 |
| F | 96 | 9.04 | 9.04 | 1920 |
| G | 192 | 8.08 | 8.08 | 3840 |
| H | 384 | 6.16 | 6.16 | 7680 |

Variation of silver concentration and seeds

| name | water | HAuCl ₄ | CTAB | AgNO ₃ | Ascorbic Acid | seeds | seeds sample |
|-------|-----------|--------------------|-------------|-------------------|---------------|-----------|--------------|
| | | 0.1M | 0.2M | 0.04M | 0.078M | | |
| | µl | µl | µl | µl | µl | µl | |
| 1i | 4380 | 50 | 4500 | 0 | 70 | 1000 | A |
| 1ii | 4380 | 50 | 4500 | 0 | 70 | 1000 | B |
| 1iii | 4380 | 50 | 4500 | 0 | 70 | 1000 | C |
| 1iv | 4380 | 50 | 4500 | 0 | 70 | 1000 | D |
| 1v | 4380 | 50 | 4500 | 0 | 70 | 1000 | E |
| 1vi | 4380 | 50 | 4500 | 0 | 70 | 1000 | F |
| 1vii | 4380 | 50 | 4500 | 0 | 70 | 1000 | G |
| 1viii | 4380 | 50 | 4500 | 0 | 70 | 1000 | H |
| | | | | | | | |
| 2i | 4375 | 50 | 4500 | 5 | 70 | 1000 | A |
| 2ii | 4375 | 50 | 4500 | 5 | 70 | 1000 | B |
| 2iii | 4375 | 50 | 4500 | 5 | 70 | 1000 | C |

| name | water | HAuCl₄ | CTAB | AgNO₃ | Ascorbic Acid | seeds | seeds sample |
|-------------|--------------|--------------------------|-------------|-------------------------|----------------------|--------------|---------------------|
| 2iv | 4375 | 50 | 4500 | 5 | 70 | 1000 | D |
| 2v | 4375 | 50 | 4500 | 5 | 70 | 1000 | E |
| 2vi | 4375 | 50 | 4500 | 5 | 70 | 1000 | F |
| 2vii | 4375 | 50 | 4500 | 5 | 70 | 1000 | G |
| 2viii | 4375 | 50 | 4500 | 5 | 70 | 1000 | H |
| | | | | | | | |
| 3i | 4370 | 50 | 4500 | 10 | 70 | 1000 | A |
| 3ii | 4370 | 50 | 4500 | 10 | 70 | 1000 | B |
| 3iii | 4370 | 50 | 4500 | 10 | 70 | 1000 | C |
| 3iv | 4370 | 50 | 4500 | 10 | 70 | 1000 | D |
| 3v | 4370 | 50 | 4500 | 10 | 70 | 1000 | E |
| 3vi | 4370 | 50 | 4500 | 10 | 70 | 1000 | F |
| 3vii | 4370 | 50 | 4500 | 10 | 70 | 1000 | G |
| 3viii | 4370 | 50 | 4500 | 10 | 70 | 1000 | H |
| | | | | | | | |
| 4i | 4355 | 50 | 4500 | 25 | 70 | 1000 | A |
| 4ii | 4355 | 50 | 4500 | 25 | 70 | 1000 | B |
| 4iii | 4355 | 50 | 4500 | 25 | 70 | 1000 | C |
| 4iv | 4355 | 50 | 4500 | 25 | 70 | 1000 | D |
| 4v | 4355 | 50 | 4500 | 25 | 70 | 1000 | E |
| 4vi | 4355 | 50 | 4500 | 25 | 70 | 1000 | F |
| 4vii | 4355 | 50 | 4500 | 25 | 70 | 1000 | G |
| 4viii | 4355 | 50 | 4500 | 25 | 70 | 1000 | H |
| | | | | | | | |
| 5i | 4330 | 50 | 4500 | 50 | 70 | 1000 | A |
| 5ii | 4330 | 50 | 4500 | 50 | 70 | 1000 | B |
| 5iii | 4330 | 50 | 4500 | 50 | 70 | 1000 | C |
| 5iv | 4330 | 50 | 4500 | 50 | 70 | 1000 | D |
| 5v | 4330 | 50 | 4500 | 50 | 70 | 1000 | E |
| 5vi | 4330 | 50 | 4500 | 50 | 70 | 1000 | F |
| 5vii | 4330 | 50 | 4500 | 50 | 70 | 1000 | G |
| 5viii | 4330 | 50 | 4500 | 50 | 70 | 1000 | H |
| | | | | | | | |
| 6i | 4305 | 50 | 4500 | 75 | 70 | 1000 | A |
| 6ii | 4305 | 50 | 4500 | 75 | 70 | 1000 | B |

C. Experimental Methods

| name | water | HAuCl ₄ | CTAB | AgNO ₃ | Ascorbic Acid | seeds | seeds sample |
|-------|-------|--------------------|------|-------------------|---------------|-------|--------------|
| 6iii | 4305 | 50 | 4500 | 75 | 70 | 1000 | C |
| 6iv | 4305 | 50 | 4500 | 75 | 70 | 1000 | D |
| 6v | 4305 | 50 | 4500 | 75 | 70 | 1000 | E |
| 6vi | 4305 | 50 | 4500 | 75 | 70 | 1000 | F |
| 6vii | 4305 | 50 | 4500 | 75 | 70 | 1000 | G |
| 6viii | 4305 | 50 | 4500 | 75 | 70 | 1000 | H |
| | | | | | | | |
| 7i | 4280 | 50 | 4500 | 100 | 70 | 1000 | A |
| 7ii | 4280 | 50 | 4500 | 100 | 70 | 1000 | B |
| 7iii | 4280 | 50 | 4500 | 100 | 70 | 1000 | C |
| 7iv | 4280 | 50 | 4500 | 100 | 70 | 1000 | D |
| 7v | 4280 | 50 | 4500 | 100 | 70 | 1000 | E |
| 7vi | 4280 | 50 | 4500 | 100 | 70 | 1000 | F |
| 7vii | 4280 | 50 | 4500 | 100 | 70 | 1000 | G |
| 7viii | 4280 | 50 | 4500 | 100 | 70 | 1000 | H |

Variation of HNO₃ concentration

| name | water | HAuCl ₄ | CTAB | AgNO ₃ | AscAcid | HNO ₃ | seeds |
|-------|-----------|--------------------|-------------|-------------------|---------------|------------------|-----------|
| | | 0,1M | 0.2M | 0.04M | 0.078M | 0.1M | |
| | μl | μl | μl | μl | μl | μl | μl |
| 8i | 4868 | 50 | 5000 | 0 | 70 | 0 | 12 |
| 8ii | 4858 | 50 | 5000 | 0 | 70 | 10 | 12 |
| 8iii | 4818 | 50 | 5000 | 0 | 70 | 50 | 12 |
| 8iv | 4768 | 50 | 5000 | 0 | 70 | 100 | 12 |
| 8v | 4618 | 50 | 5000 | 0 | 70 | 250 | 12 |
| 8vi | 4368 | 50 | 5000 | 0 | 70 | 500 | 12 |
| 8vii | 4118 | 50 | 5000 | 0 | 70 | 750 | 12 |
| 8viii | 3868 | 50 | 5000 | 0 | 70 | 1000 | 12 |
| | | | | | | | |
| 9i | 4856 | 50 | 5000 | 0 | 70 | 0 | 24 |
| 9ii | 4846 | 50 | 5000 | 0 | 70 | 10 | 24 |
| 9iii | 4806 | 50 | 5000 | 0 | 70 | 50 | 24 |
| 9iv | 4756 | 50 | 5000 | 0 | 70 | 100 | 24 |

| | | | | | | | |
|--------|------|----|------|----|----|------|----|
| 9v | 4606 | 50 | 5000 | 0 | 70 | 250 | 24 |
| 9vi | 4356 | 50 | 5000 | 0 | 70 | 500 | 24 |
| 9vii | 4106 | 50 | 5000 | 0 | 70 | 750 | 24 |
| 9viii | 3856 | 50 | 5000 | 0 | 70 | 1000 | 24 |
| | | | | | | | |
| 10i | 4848 | 50 | 5000 | 20 | 70 | 0 | 12 |
| 10ii | 4838 | 50 | 5000 | 20 | 70 | 10 | 12 |
| 10iii | 4798 | 50 | 5000 | 20 | 70 | 50 | 12 |
| 10iv | 4748 | 50 | 5000 | 20 | 70 | 100 | 12 |
| 10v | 4598 | 50 | 5000 | 20 | 70 | 250 | 12 |
| 10vi | 4348 | 50 | 5000 | 20 | 70 | 500 | 12 |
| 10vii | 4098 | 50 | 5000 | 20 | 70 | 750 | 12 |
| 10viii | 3848 | 50 | 5000 | 20 | 70 | 1000 | 12 |
| | | | | | | | |
| 11i | 4836 | 50 | 5000 | 20 | 70 | 0 | 24 |
| 11ii | 4826 | 50 | 5000 | 20 | 70 | 10 | 24 |
| 11iii | 4786 | 50 | 5000 | 20 | 70 | 50 | 24 |
| 11iv | 4736 | 50 | 5000 | 20 | 70 | 100 | 24 |
| 11v | 4586 | 50 | 5000 | 20 | 70 | 250 | 24 |
| 11vi | 4336 | 50 | 5000 | 20 | 70 | 500 | 24 |
| 11vii | 4086 | 50 | 5000 | 20 | 70 | 750 | 24 |
| 11viii | 3836 | 50 | 5000 | 20 | 70 | 1000 | 24 |

Variation of CTAB concentration

| name | water | HAuCl ₄ | CTAB | AgNO ₃ | AscAcid | seeds |
|--------|-------|--------------------|------|-------------------|---------|-------|
| | | 0.1M | 0.2M | 0.04M | 0.078M | |
| | µl | µl | µl | µl | µl | µl |
| 12i | 9868 | 50 | 0 | 0 | 70 | 12 |
| 12ii | 9843 | 50 | 25 | 0 | 70 | 12 |
| 12iii | 9768 | 50 | 100 | 0 | 70 | 12 |
| 12iv | 8868 | 50 | 1000 | 0 | 70 | 12 |
| 12v | 7368 | 50 | 2500 | 0 | 70 | 12 |
| 12vi | 4868 | 50 | 5000 | 0 | 70 | 12 |
| 12vii | 2368 | 50 | 7500 | 0 | 70 | 12 |
| 12viii | 868 | 50 | 9000 | 0 | 70 | 12 |

C. Experimental Methods

| name | water | HAuCl ₄ | CTAB | AgNO ₃ | AscAcid | seeds |
|--------|-------|--------------------|------|-------------------|---------|-------|
| | | | | | | |
| 13i | 9856 | 50 | 0 | 0 | 70 | 24 |
| 13ii | 9831 | 50 | 25 | 0 | 70 | 24 |
| 13iii | 9756 | 50 | 100 | 0 | 70 | 24 |
| 13iv | 8856 | 50 | 1000 | 0 | 70 | 24 |
| 13v | 7356 | 50 | 2500 | 0 | 70 | 24 |
| 13vi | 4856 | 50 | 5000 | 0 | 70 | 24 |
| 13vii | 2356 | 50 | 7500 | 0 | 70 | 24 |
| 13viii | 856 | 50 | 9000 | 0 | 70 | 24 |
| | | | | | | |
| 14i | 9848 | 50 | 0 | 20 | 70 | 12 |
| 14ii | 9823 | 50 | 25 | 20 | 70 | 12 |
| 14iii | 9748 | 50 | 100 | 20 | 70 | 12 |
| 14iv | 8848 | 50 | 1000 | 20 | 70 | 12 |
| 14v | 7348 | 50 | 2500 | 20 | 70 | 12 |
| 14vi | 4848 | 50 | 5000 | 20 | 70 | 12 |
| 14vii | 2348 | 50 | 7500 | 20 | 70 | 12 |
| 14viii | 848 | 50 | 9000 | 20 | 70 | 12 |
| | | | | | | |
| 15i | 9836 | 50 | 0 | 20 | 70 | 24 |
| 15ii | 9811 | 50 | 25 | 20 | 70 | 24 |
| 15iii | 9736 | 50 | 100 | 20 | 70 | 24 |
| 15iv | 8836 | 50 | 1000 | 20 | 70 | 24 |
| 15v | 7336 | 50 | 2500 | 20 | 70 | 24 |
| 15vi | 4836 | 50 | 5000 | 20 | 70 | 24 |
| 15vii | 2336 | 50 | 7500 | 20 | 70 | 24 |
| 15viii | 836 | 50 | 9000 | 20 | 70 | 24 |

Variation of CTAB/CTAC ratio

| name | water | HAuCl ₄ | CTAB | CTAC | AgNO ₃ | AscAcid | seeds |
|------|-----------|--------------------|-------------|-------------|-------------------|---------------|-----------|
| | | 0.1M | 0.2M | 0.2M | 0.04M | 0.078M | |
| | μl | μl | μl | μl | μl | μl | μl |
| 16i | 4868 | 50 | 4975 | 25 | 0 | 70 | 12 |
| 16ii | 4868 | 50 | 4900 | 100 | 0 | 70 | 12 |

| name | water | HAuCl₄ | CTAB | CTAC | AgNO₃ | AscAcid | seeds |
|-------------|--------------|--------------------------|-------------|-------------|-------------------------|----------------|--------------|
| 16iii | 4868 | 50 | 3750 | 1250 | 0 | 70 | 12 |
| 16iv | 4868 | 50 | 2500 | 2500 | 0 | 70 | 12 |
| 16v | 4868 | 50 | 1250 | 3750 | 0 | 70 | 12 |
| 16vi | 4868 | 50 | 100 | 4900 | 0 | 70 | 12 |
| 16vii | 4868 | 50 | 25 | 4975 | 0 | 70 | 12 |
| 16viii | 4868 | 50 | 0 | 5000 | 0 | 70 | 12 |
| | | | | | | | |
| 17i | 4856 | 50 | 4975 | 25 | 0 | 70 | 24 |
| 17ii | 4856 | 50 | 4900 | 100 | 0 | 70 | 24 |
| 17iii | 4856 | 50 | 3750 | 1250 | 0 | 70 | 24 |
| 17iv | 4856 | 50 | 2500 | 2500 | 0 | 70 | 24 |
| 17v | 4856 | 50 | 1250 | 3750 | 0 | 70 | 24 |
| 17vi | 4856 | 50 | 100 | 4900 | 0 | 70 | 24 |
| 17vii | 4856 | 50 | 25 | 4975 | 0 | 70 | 24 |
| 17viii | 4856 | 50 | 0 | 5000 | 0 | 70 | 24 |
| | | | | | | | |
| 18i | 4848 | 50 | 4975 | 25 | 20 | 70 | 12 |
| 18ii | 4848 | 50 | 4900 | 100 | 20 | 70 | 12 |
| 18iii | 4848 | 50 | 3750 | 1250 | 20 | 70 | 12 |
| 18iv | 4848 | 50 | 2500 | 2500 | 20 | 70 | 12 |
| 18v | 4848 | 50 | 1250 | 3750 | 20 | 70 | 12 |
| 18vi | 4848 | 50 | 100 | 4900 | 20 | 70 | 12 |
| 18vii | 4848 | 50 | 25 | 4975 | 20 | 70 | 12 |
| 18viii | 4848 | 50 | 0 | 5000 | 20 | 70 | 12 |
| | | | | | | | |
| 18i2010 | 4848 | 50 | 2500 | 2500 | 20 | 70 | 12 |
| 18ii2010 | 4848 | 50 | 1429 | 3571 | 20 | 70 | 12 |
| 18iii2010 | 4848 | 50 | 1297 | 3703 | 20 | 70 | 12 |
| 18iv2010 | 4848 | 50 | 1154 | 3846 | 20 | 70 | 12 |
| 18v2010 | 4848 | 50 | 1000 | 4000 | 20 | 70 | 12 |
| 18vi2010 | 4848 | 50 | 834 | 4166 | 20 | 70 | 12 |
| 18vii2010 | 4848 | 50 | 652 | 4348 | 20 | 70 | 12 |
| 18viii2010 | 4848 | 50 | 98 | 4902 | 20 | 70 | 12 |
| | | | | | | | |
| 19i | 4836 | 50 | 4975 | 25 | 20 | 70 | 24 |
| 19ii | 4836 | 50 | 4900 | 100 | 20 | 70 | 24 |
| 19iii | 4836 | 50 | 3750 | 1250 | 20 | 70 | 24 |

C. Experimental Methods

| name | water | HAuCl ₄ | CTAB | CTAC | AgNO ₃ | AscAcid | seeds |
|--------|-------|--------------------|------|------|-------------------|---------|-------|
| 19iv | 4836 | 50 | 2500 | 2500 | 20 | 70 | 24 |
| 19v | 4836 | 50 | 1250 | 3750 | 20 | 70 | 24 |
| 19vi | 4836 | 50 | 100 | 4900 | 20 | 70 | 24 |
| 19vii | 4836 | 50 | 25 | 4975 | 20 | 70 | 24 |
| 19viii | 4836 | 50 | 0 | 5000 | 20 | 70 | 24 |

Variation of CTAC/NaBr ratio

| name | water | HAuCl ₄ | CTAC | NaBr | AgNO ₃ | AscAcid | seeds |
|--------|-------|--------------------|------|-------|-------------------|---------|-------|
| | | 0.1M | 0.2M | 0.25M | 0.04M | 0.078M | |
| | μl | μl | μl | μl | μl | μl | μl |
| 20i | 4868 | 50 | 5000 | 0 | 0 | 70 | 12 |
| 20ii | 4848 | 50 | 5000 | 20 | 0 | 70 | 12 |
| 20iii | 4788 | 50 | 5000 | 80 | 0 | 70 | 12 |
| 20iv | 4668 | 50 | 5000 | 200 | 0 | 70 | 12 |
| 20v | 4468 | 50 | 5000 | 400 | 0 | 70 | 12 |
| 20vi | 3868 | 50 | 5000 | 1000 | 0 | 70 | 12 |
| 20vii | 2868 | 50 | 5000 | 2000 | 0 | 70 | 12 |
| 20viii | 868 | 50 | 5000 | 4000 | 0 | 70 | 12 |
| | | | | | | | |
| 21i | 4856 | 50 | 5000 | 0 | 0 | 70 | 24 |
| 21ii | 4836 | 50 | 5000 | 20 | 0 | 70 | 24 |
| 21iii | 4776 | 50 | 5000 | 80 | 0 | 70 | 24 |
| 21iv | 4656 | 50 | 5000 | 200 | 0 | 70 | 24 |
| 21v | 4456 | 50 | 5000 | 400 | 0 | 70 | 24 |
| 21vi | 3856 | 50 | 5000 | 1000 | 0 | 70 | 24 |
| 21vii | 2856 | 50 | 5000 | 2000 | 0 | 70 | 24 |
| 21viii | 856 | 50 | 5000 | 4000 | 0 | 70 | 24 |
| | | | | | | | |
| 22i | 4848 | 50 | 5000 | 0 | 20 | 70 | 12 |
| 22ii | 4828 | 50 | 5000 | 20 | 20 | 70 | 12 |
| 22iii | 4768 | 50 | 5000 | 80 | 20 | 70 | 12 |
| 22iv | 4648 | 50 | 5000 | 200 | 20 | 70 | 12 |
| 22v | 4448 | 50 | 5000 | 400 | 20 | 70 | 12 |
| 22vi | 3848 | 50 | 5000 | 1000 | 20 | 70 | 12 |

| name | water | HAuCl ₄ | CTAC | NaBr | AgNO ₃ | AscAcid | seeds |
|------------|-------|--------------------|------|------|-------------------|---------|-------|
| 22vii | 2848 | 50 | 5000 | 2000 | 20 | 70 | 12 |
| 22viii | 848 | 50 | 5000 | 4000 | 20 | 70 | 12 |
| | | | | | | | |
| 22i2010 | 4768 | 50 | 5000 | 80 | 20 | 70 | 12 |
| 22ii2010 | 4248 | 50 | 5000 | 600 | 20 | 70 | 12 |
| 22iii2010 | 4048 | 50 | 5000 | 800 | 20 | 70 | 12 |
| 22iv2010 | 3848 | 50 | 5000 | 1000 | 20 | 70 | 12 |
| 22v2010 | 3648 | 50 | 5000 | 1200 | 20 | 70 | 12 |
| 22vi2010 | 3448 | 50 | 5000 | 1400 | 20 | 70 | 12 |
| 22vii2010 | 3248 | 50 | 5000 | 1600 | 20 | 70 | 12 |
| 22viii2010 | 848 | 50 | 5000 | 4000 | 20 | 70 | 12 |
| | | | | | | | |
| 23i | 4836 | 50 | 5000 | 0 | 20 | 70 | 24 |
| 23ii | 4816 | 50 | 5000 | 20 | 20 | 70 | 24 |
| 23iii | 4756 | 50 | 5000 | 80 | 20 | 70 | 24 |
| 23iv | 4636 | 50 | 5000 | 200 | 20 | 70 | 24 |
| 23v | 4436 | 50 | 5000 | 400 | 20 | 70 | 24 |
| 23vi | 3836 | 50 | 5000 | 1000 | 20 | 70 | 24 |
| 23vii | 2836 | 50 | 5000 | 2000 | 20 | 70 | 24 |
| 23viii | 836 | 50 | 5000 | 4000 | 20 | 70 | 24 |

Variation of CTAB/NaCl ratio

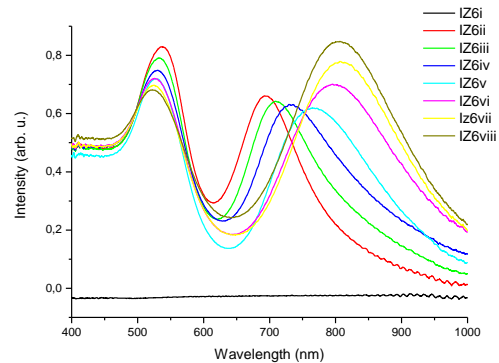
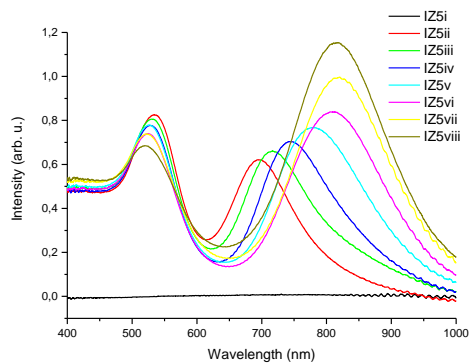
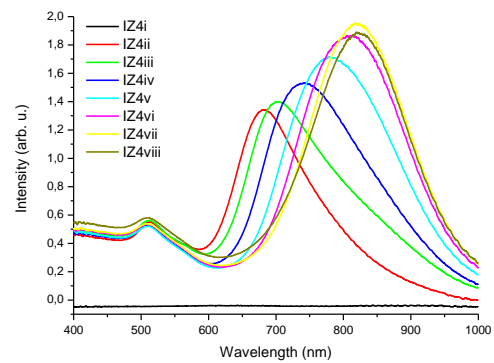
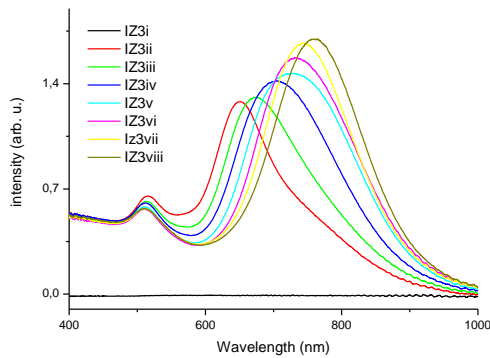
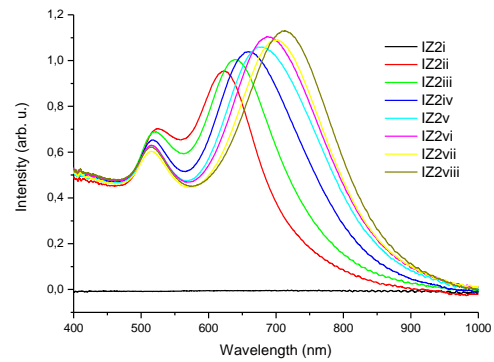
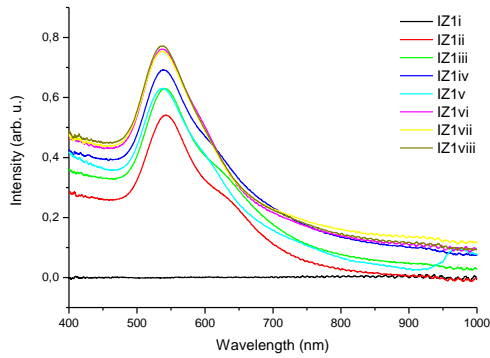
| name | water | HAuCl ₄ | CTAB | NaCl | AgNO ₃ | AscAcid | seeds |
|--------|-----------|--------------------|-------------|--------------|-------------------|---------------|-----------|
| | | 0.1M | 0.2M | 0.25M | 0.04M | 0.078M | |
| | μl | μl | μl | μl | μl | μl | μl |
| 24i | 4868 | 50 | 5000 | 0 | 0 | 70 | 12 |
| 24ii | 4848 | 50 | 5000 | 20 | 0 | 70 | 12 |
| 24iii | 4788 | 50 | 5000 | 80 | 0 | 70 | 12 |
| 24iv | 4668 | 50 | 5000 | 200 | 0 | 70 | 12 |
| 24v | 4468 | 50 | 5000 | 400 | 0 | 70 | 12 |
| 24vi | 3868 | 50 | 5000 | 1000 | 0 | 70 | 12 |
| 24vii | 2868 | 50 | 5000 | 2000 | 0 | 70 | 12 |
| 24viii | 868 | 50 | 5000 | 4000 | 0 | 70 | 12 |
| | | | | | | | |

C. Experimental Methods

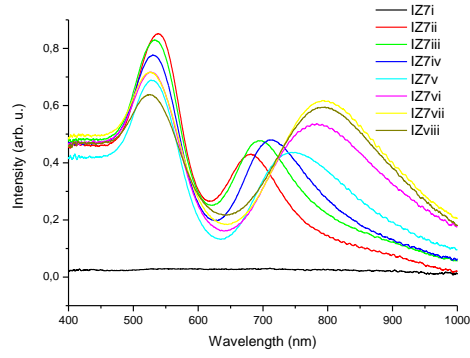
| name | water | HAuCl₄ | CTAB | NaCl | AgNO₃ | AscAcid | seeds |
|-------------|--------------|--------------------------|-------------|-------------|-------------------------|----------------|--------------|
| 25i | 4856 | 50 | 5000 | 0 | 0 | 70 | 24 |
| 25ii | 4836 | 50 | 5000 | 20 | 0 | 70 | 24 |
| 25iii | 4776 | 50 | 5000 | 80 | 0 | 70 | 24 |
| 25iv | 4656 | 50 | 5000 | 200 | 0 | 70 | 24 |
| 25v | 4456 | 50 | 5000 | 400 | 0 | 70 | 24 |
| 25vi | 3856 | 50 | 5000 | 1000 | 0 | 70 | 24 |
| 25vii | 2856 | 50 | 5000 | 2000 | 0 | 70 | 24 |
| 25viii | 856 | 50 | 5000 | 4000 | 0 | 70 | 24 |
| | | | | | | | |
| 26i | 4848 | 50 | 5000 | 0 | 20 | 70 | 12 |
| 26ii | 4828 | 50 | 5000 | 20 | 20 | 70 | 12 |
| 26iii | 4768 | 50 | 5000 | 80 | 20 | 70 | 12 |
| 26iv | 4648 | 50 | 5000 | 200 | 20 | 70 | 12 |
| 26v | 4448 | 50 | 5000 | 400 | 20 | 70 | 12 |
| 26vi | 3848 | 50 | 5000 | 1000 | 20 | 70 | 12 |
| 26vii | 2848 | 50 | 5000 | 2000 | 20 | 70 | 12 |
| 26viii | 848 | 50 | 5000 | 4000 | 20 | 70 | 12 |
| | | | | | | | |
| 27i | 4836 | 50 | 5000 | 0 | 20 | 70 | 24 |
| 27ii | 4816 | 50 | 5000 | 20 | 20 | 70 | 24 |
| 27iii | 4756 | 50 | 5000 | 80 | 20 | 70 | 24 |
| 27iv | 4636 | 50 | 5000 | 200 | 20 | 70 | 24 |
| 27v | 4436 | 50 | 5000 | 400 | 20 | 70 | 24 |
| 27vi | 3836 | 50 | 5000 | 1000 | 20 | 70 | 24 |
| 27vii | 2836 | 50 | 5000 | 2000 | 20 | 70 | 24 |
| 27viii | 836 | 50 | 5000 | 4000 | 20 | 70 | 24 |

C.1.2. Spectra of the Carried out Syntheses

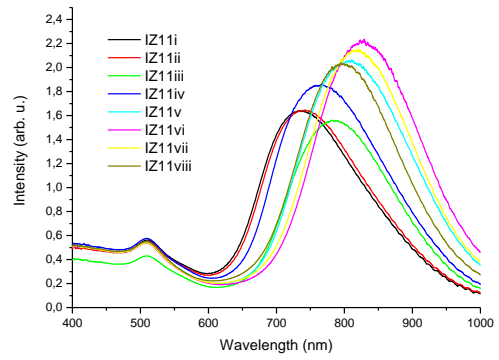
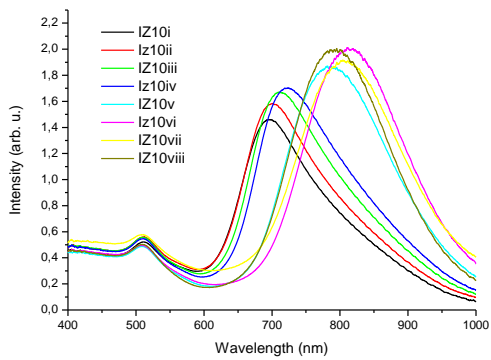
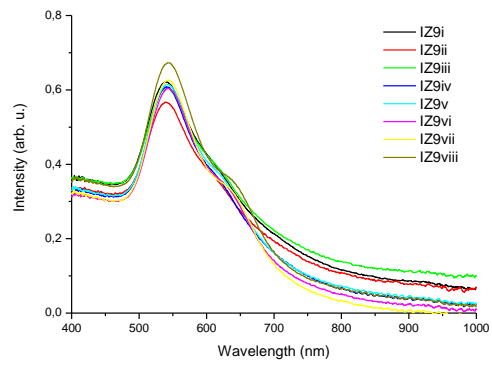
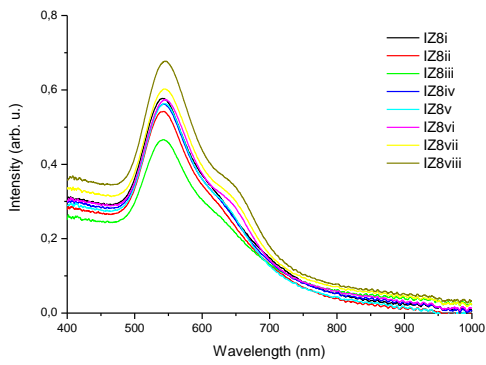
Variation of silver concentration and seeds



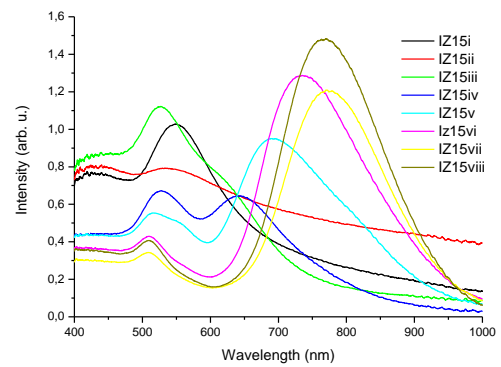
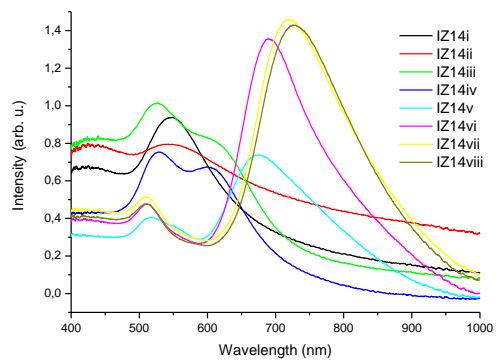
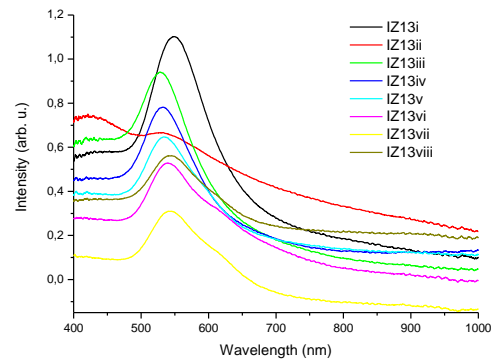
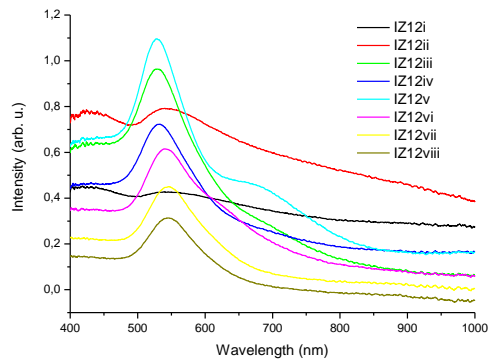
C. Experimental Methods



Variation of HNO₃ concentration

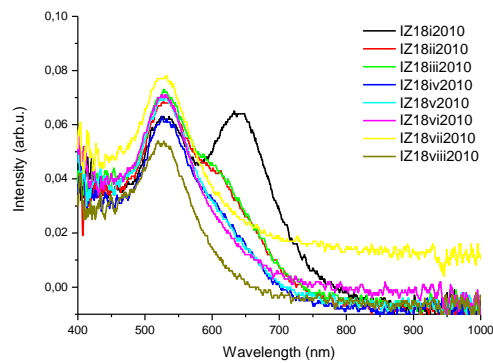
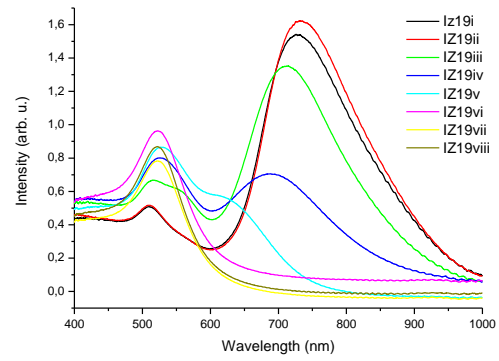
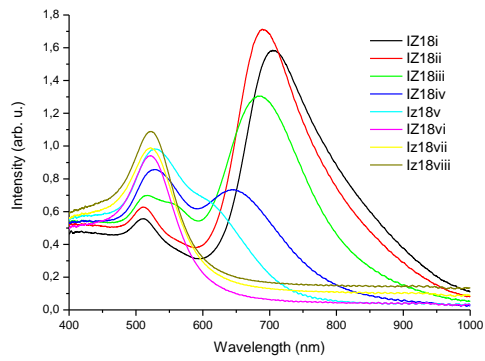
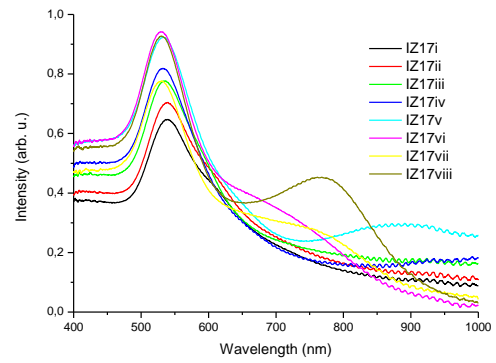
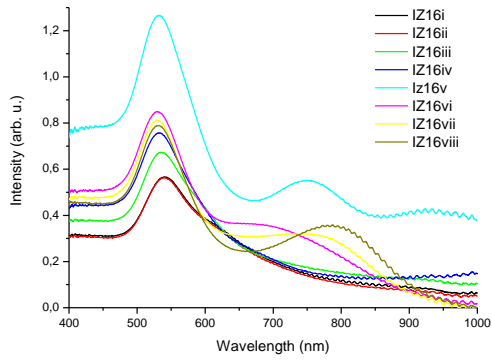


Variation of CTAB concentration

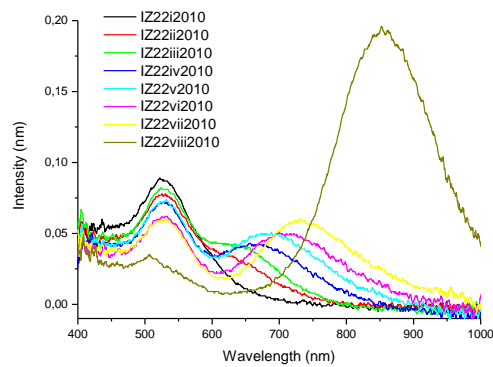
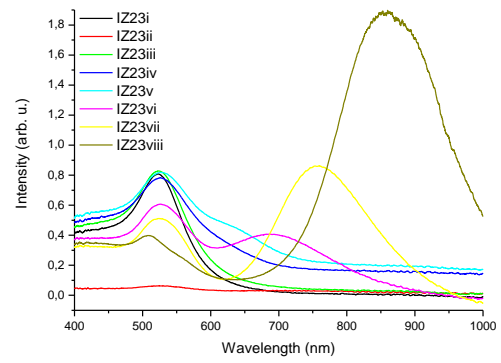
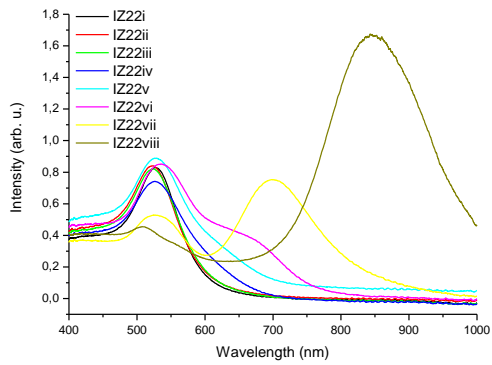
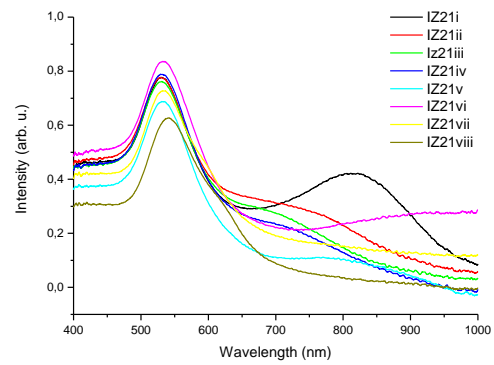
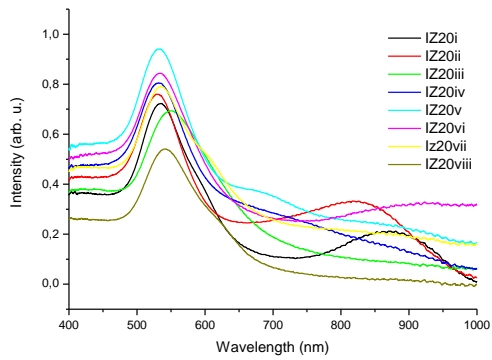


C. Experimental Methods

Variation of CTAB/ CTAC ratio

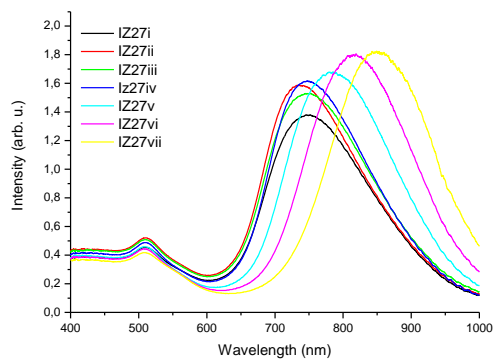
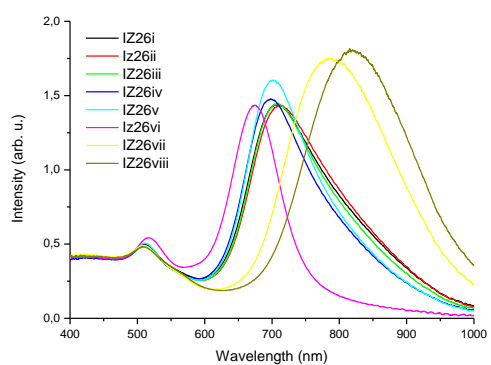
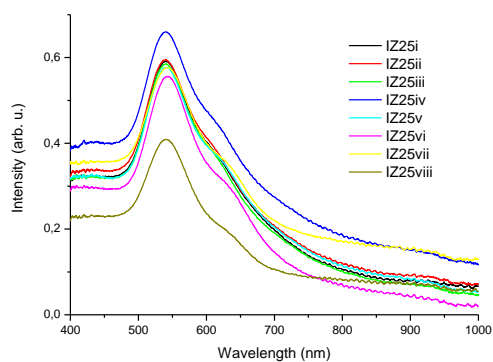
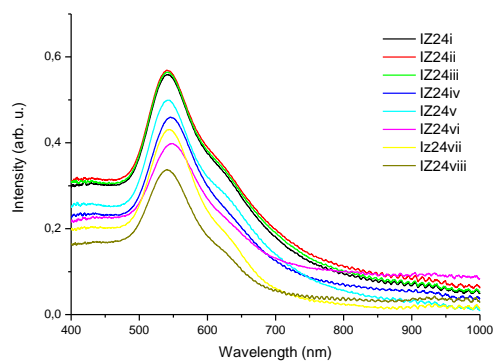


Variation of CTAC/ NaBr ratio



C. Experimental Methods

Variation of CTAB/ NaCl ratio



In order to calculate a yield of rods from the spectra, the absolute size of the particles needs to be known. For this, TEM images of all samples need to be taken. This was not practical considering the number of samples, only TEM images of selected samples are available (appendix C.1.3). In order to approximate a yield of rods from the ensemble spectra, theoretical spectra were calculated by simulating 10000 rods with a mean width of 13.4 nm and a distribution of 20 % (mean of all TEM data). For these fixed values, the ratio of the intensities for the longitudinal and transverse peak is calculated using QSA theory (see chapter 2 and figure C.1). In order to calculate the yield of rods from the spectrum, the measured ratio $\frac{I_{\text{long,exp}}}{I_{\text{short,exp}}}$ is divided by the theoretical one $\frac{I_{\text{long,theo}}}{I_{\text{short,theo}}}$, which gives the ratio for 100 % rod yield. The closer the corrected ratio is to 1, the higher the yield of rods. If the experimental ratio is the same as the theoretical one, 100 % of rods are synthesized.

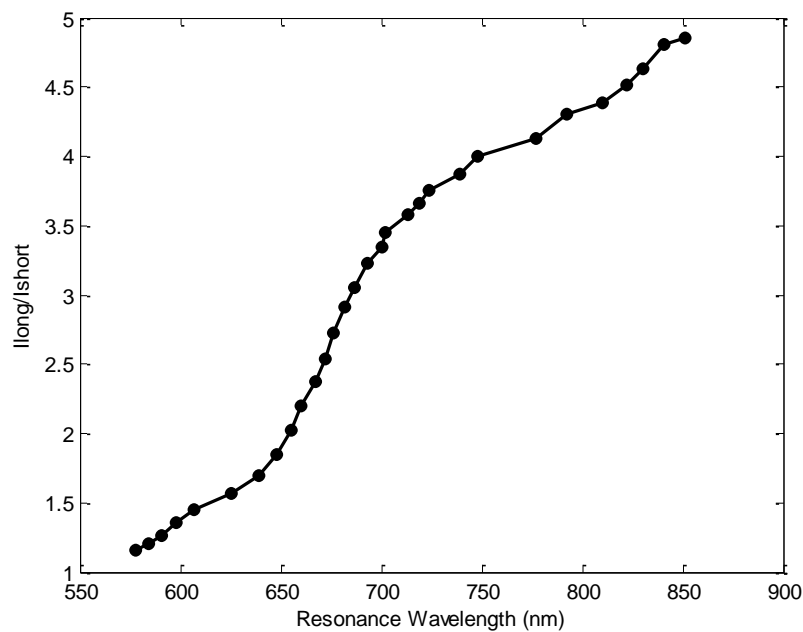


Figure C.1.: $I_{\text{long}}/I_{\text{short}}$ Calculated by QSA

QSA simulations of gold nanorods with a diameter of 13.4 nm and a polydispersity of 20 % (representing the mean of the TEM data) are done to evaluate the theoretical ratio of intensities of long and short axis for 100 % rod yield for rods with different aspect ratios (resonance wavelengths).

Variation of silver concentration and seeds

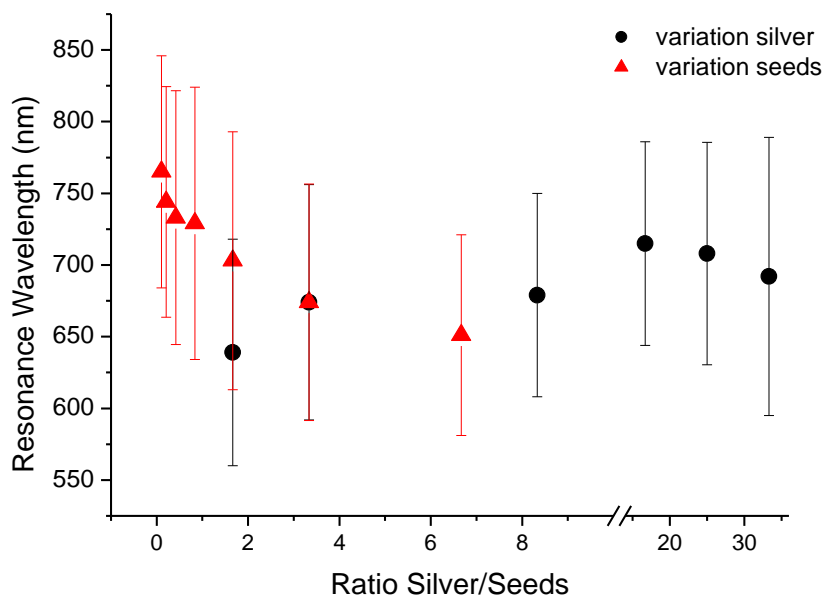
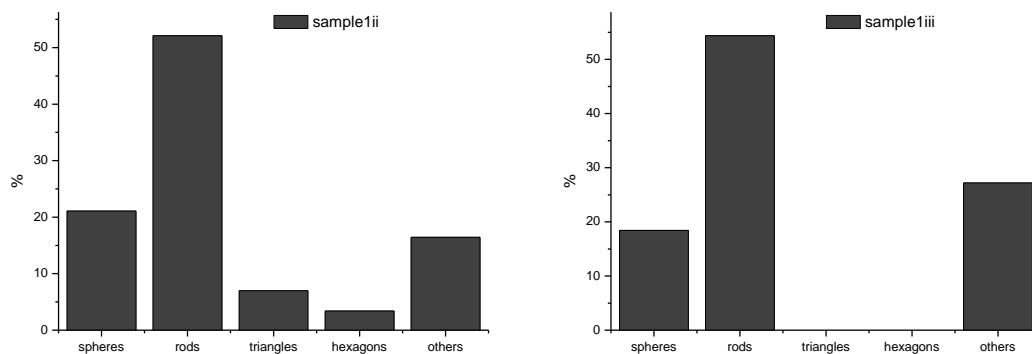


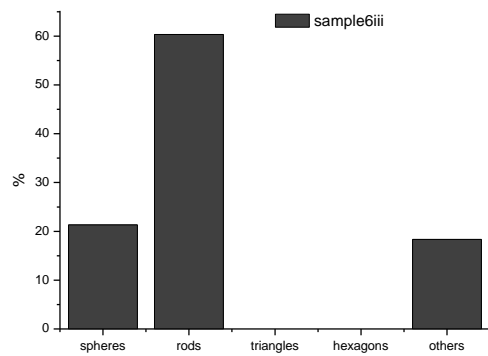
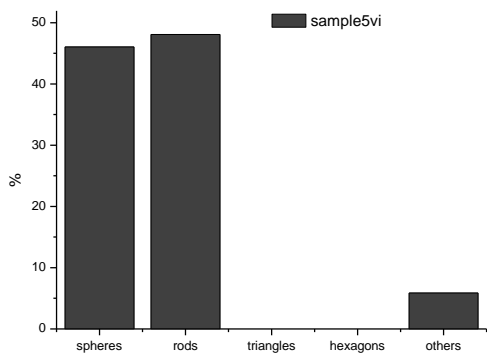
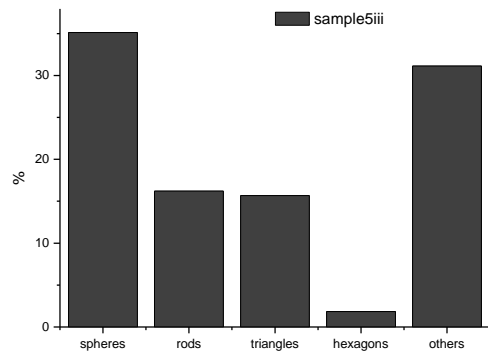
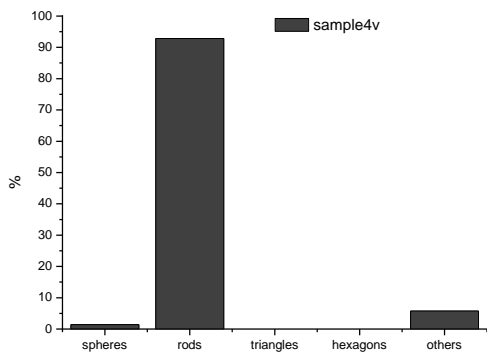
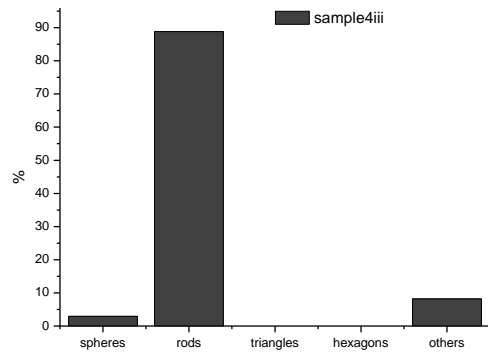
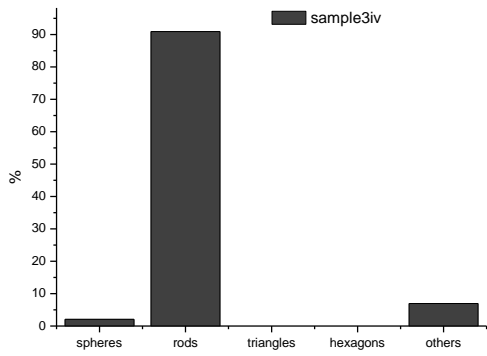
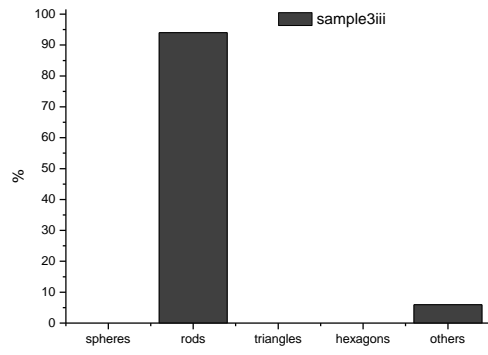
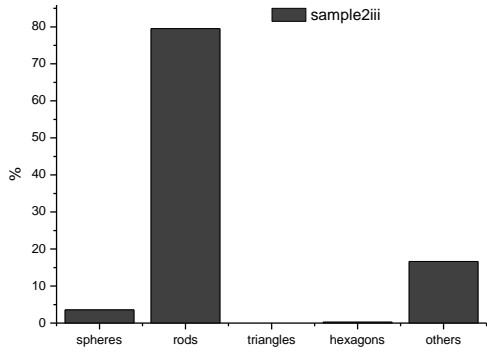
Figure C.2.: Seeds and Silver Variations

The series characterizing the variation in seeds (series 4) and the one representing the variation in silver concentration (series 1-7iii) cover different regions in the silver/seeds regime.

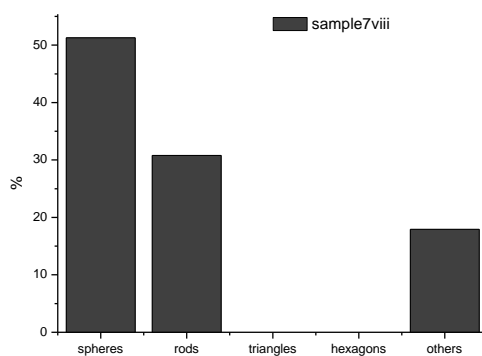
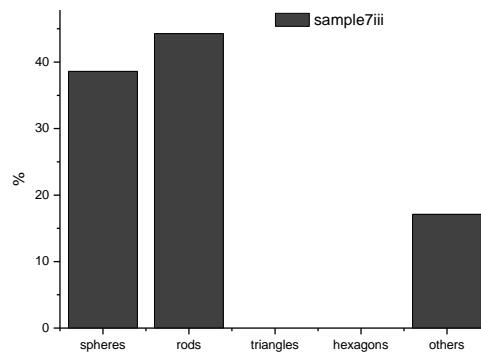
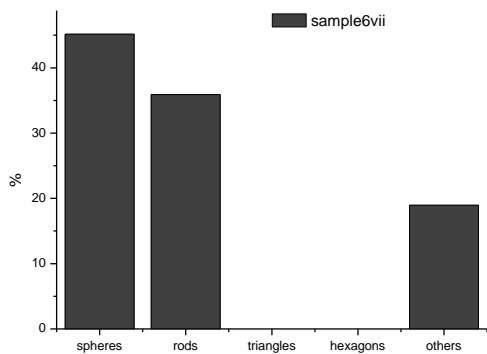
C.1.3. TEM-data of the Carried out Syntheses

Variation of silver concentration and seeds

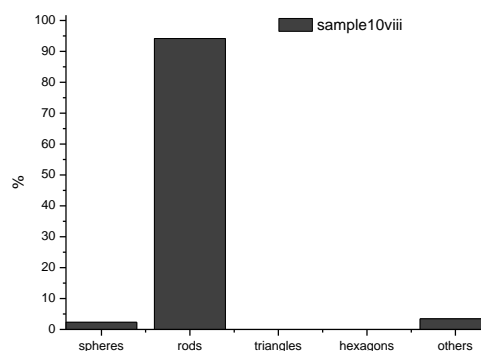
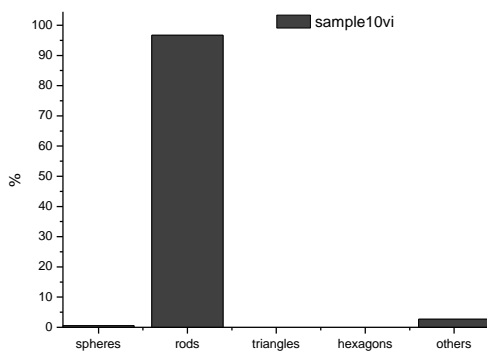
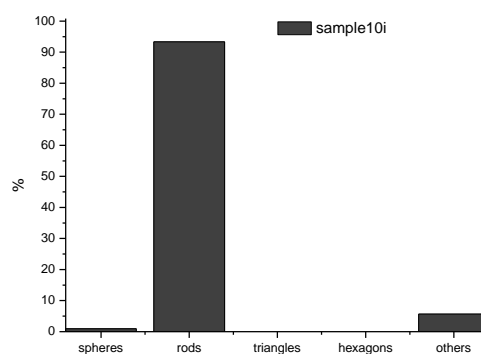
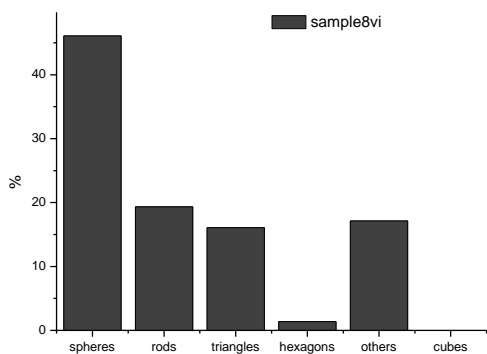


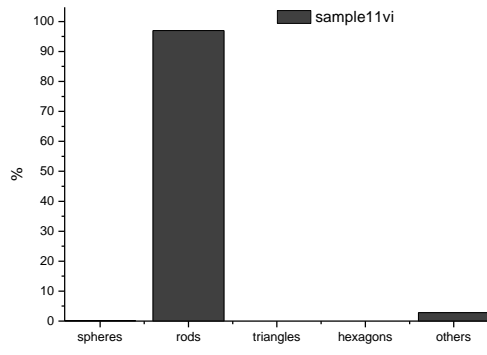


C. Experimental Methods



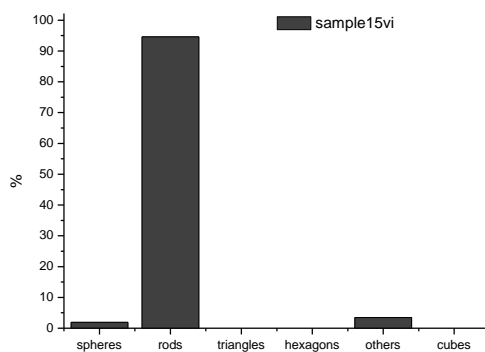
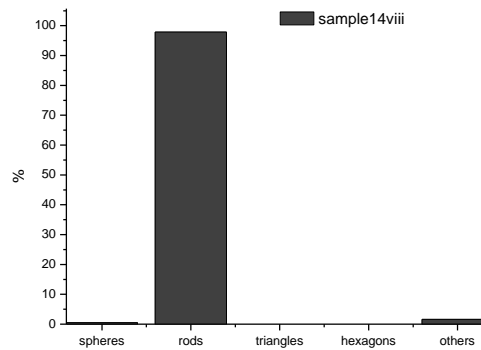
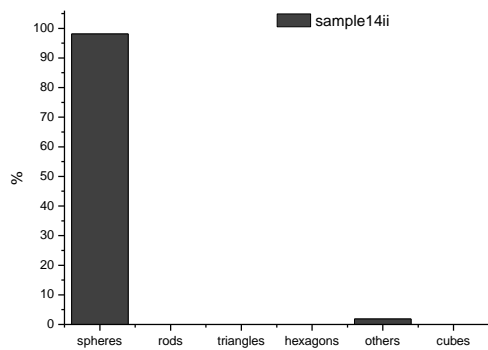
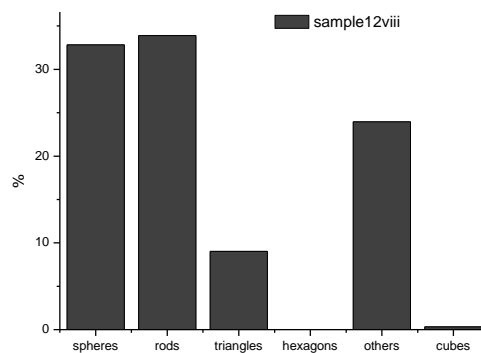
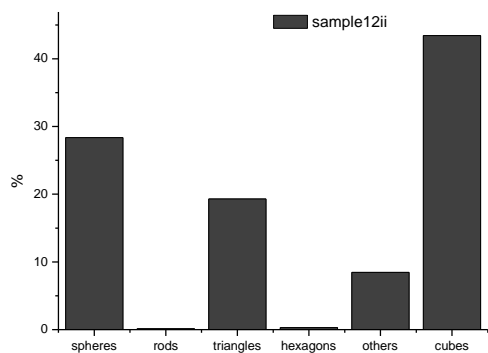
Variation of HNO₃ concentration



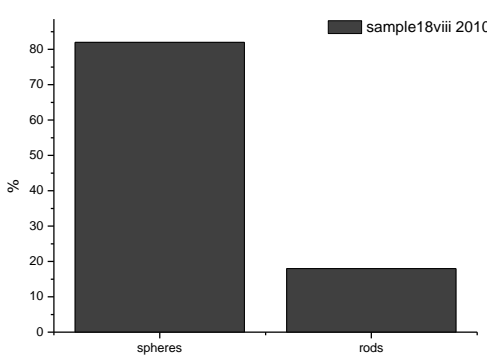
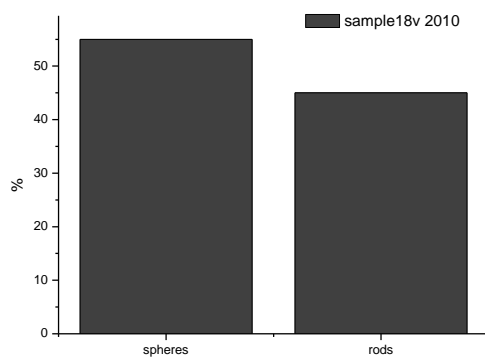
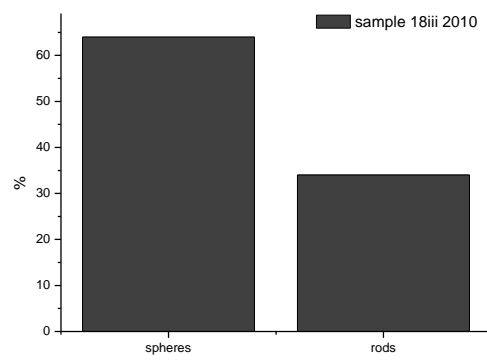
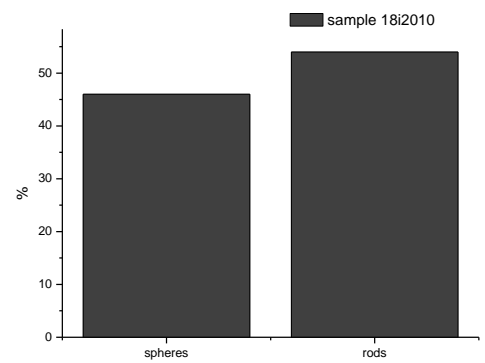
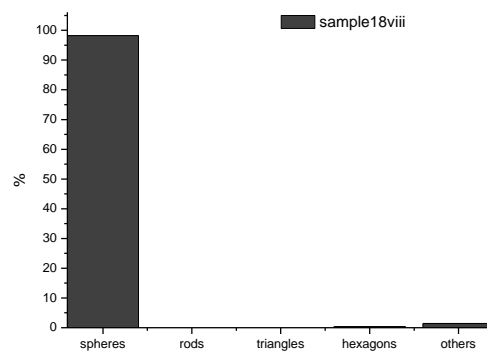
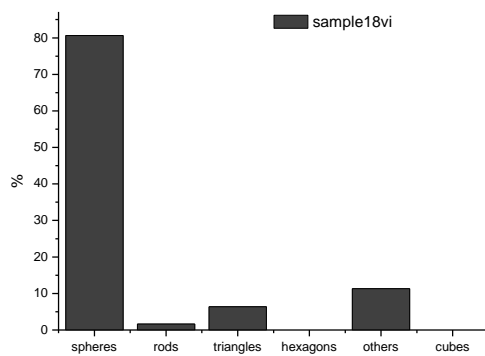
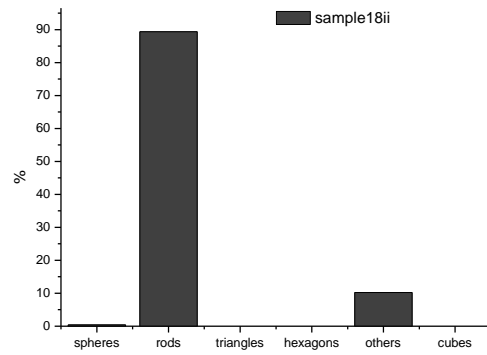
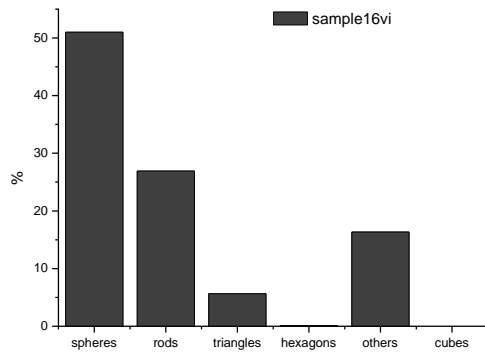


C. Experimental Methods

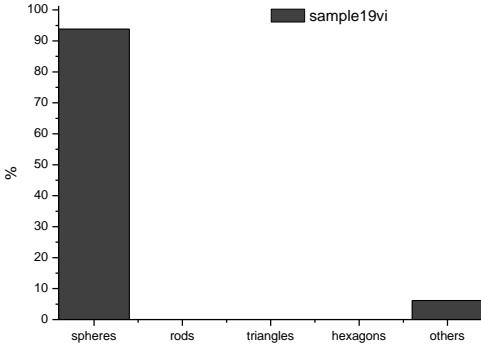
Variation of CTAB concentration



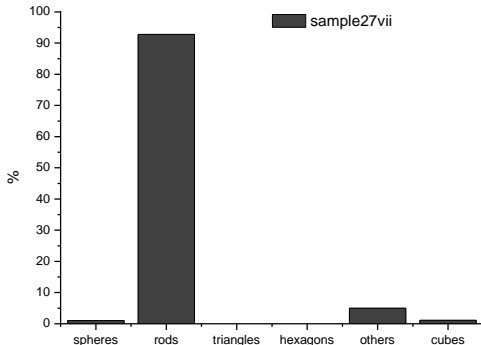
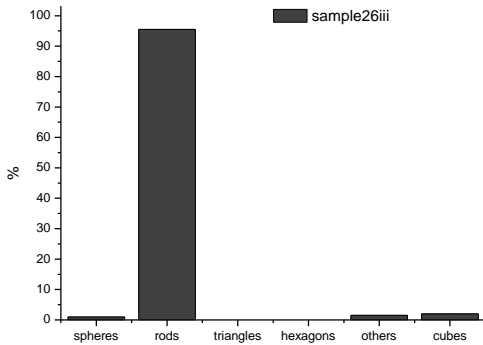
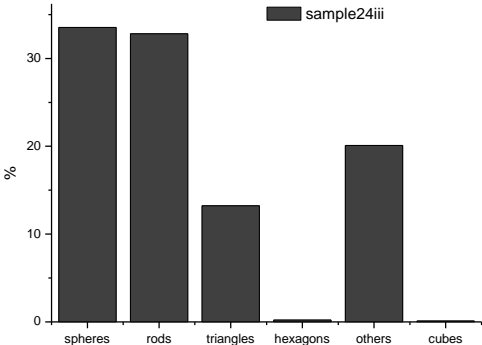
Variation of CTAB/ CTAC ratio



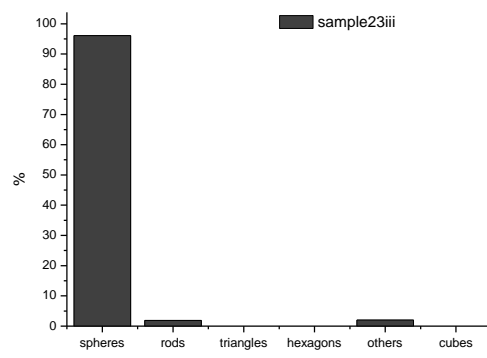
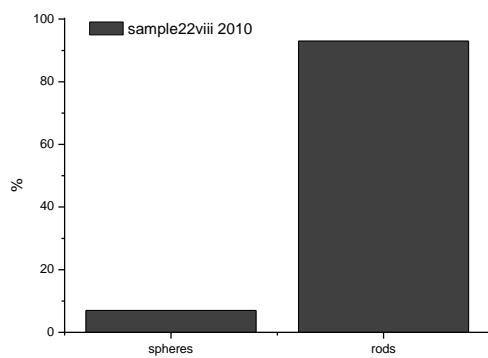
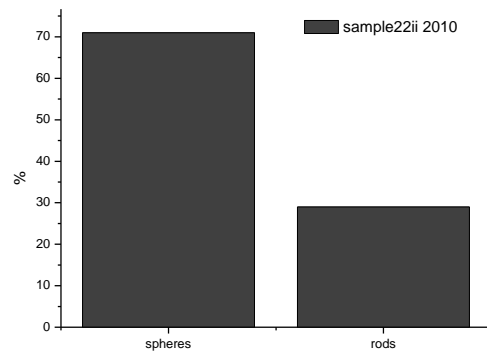
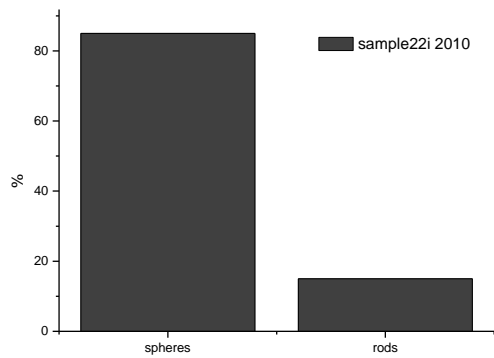
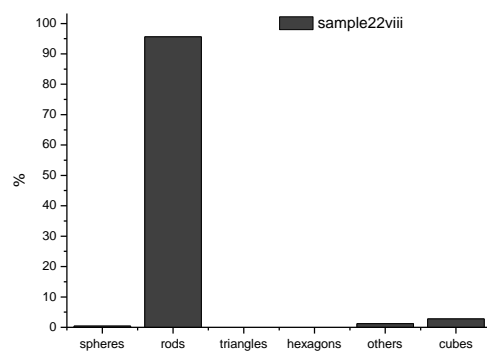
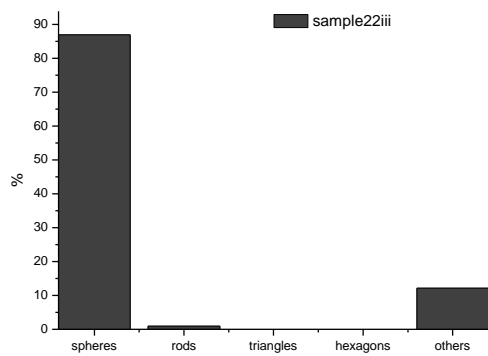
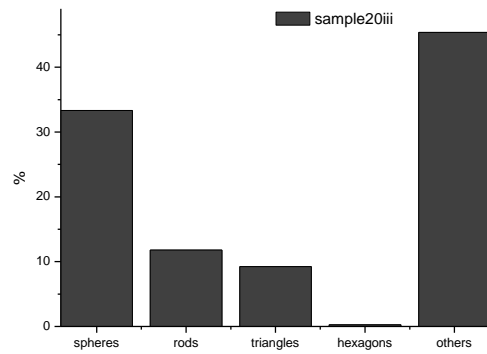
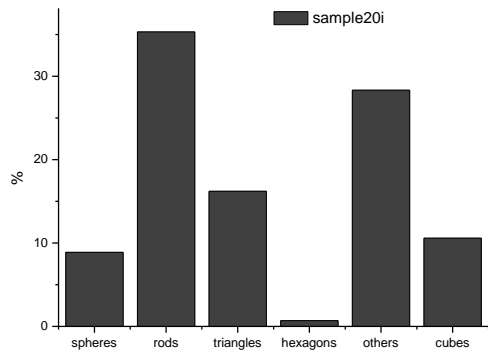
C. Experimental Methods



Variation of CTAB/ NaCl ratio



Variation CTAC and NaBr



C.1.4. Electrochemical Potential of the Growth Solution

In order to calculate the electrochemical potential of the growth solution, one has to consider 5 steps:

1. Which gold complexes are formed?
2. How much bromide/ chloride is left?
3. How much bromide/ chloride is in solution or bound to micelles?
4. Redox-potential for gold complexes
5. Electrochemical potential of the growth solution

1. Which gold complexes are formed?

In mixtures of chlorides and bromides, Au^{3+} has the possibility to form 5 different complexes (see figure C.3). The fraction of each complex depends on the concentration of gold, chloride, and bromide in solution. Knowing the dissociation (or formation) constants and expressing the laws of mass action and charge balance, it is possible to calculate for each concentration the distribution of complexes (for details see (Usher *et al.*, 2009)). In principle, laws of mass action of the following form need to be solved:

$$k = \frac{[\text{Au}^{3+}] \cdot [\text{Br}^-]^n \cdot [\text{Cl}^-]^{(4-n)}}{[\text{AuBr}_n\text{Cl}_{(4-n)}]} \quad n = 1, 2, 3, 4$$

Including also mass and charge balance equations like:

$$\begin{aligned} [\text{Au}^{3+}]_{\text{total}} &= [\text{AuBr}_4^-] + [\text{AuBr}_3\text{Cl}^-] + [\text{AuBr}_2\text{Cl}_2^-] + [\text{AuBrCl}_3^-] + [\text{AuCl}_4^-] \\ [\text{Cl}^-]_{\text{total}} &= [\text{AuBr}_3\text{Cl}^-] + 2 \cdot [\text{AuBr}_2\text{Cl}_2^-] + 3 \cdot [\text{AuBrCl}_3^-] + 4 \cdot [\text{AuCl}_4^-] \\ [\text{Br}^-]_{\text{total}} &= 4 \cdot [\text{AuBr}_4^-] + 3 \cdot [\text{AuBr}_3\text{Cl}^-] + 2 \cdot [\text{AuBr}_2\text{Cl}_2^-] + [\text{AuBrCl}_3^-] \end{aligned}$$

Despite the fact that those complexes occur, the gold species that is finally reduced to elemental gold is not Au^{3+} but Au^+ . Therefore, the matching complexes for Au^+ have to be evaluated. Since it is not possible to find a dissociation or formation constant for the $[\text{AuClBr}]^-$ mixed complex, only $[\text{AuBr}_2]^-$ and $[\text{AuCl}_2]^-$ are considered (see figure C.4, (CRC, 2004). Since the formation constants are extremely big (several orders of magnitude higher than the dissociation of CTAB), they will form at any concentration of bromide and chloride. It is assumed that they form by ripping off all needed ions from the CTA^+ micelles.

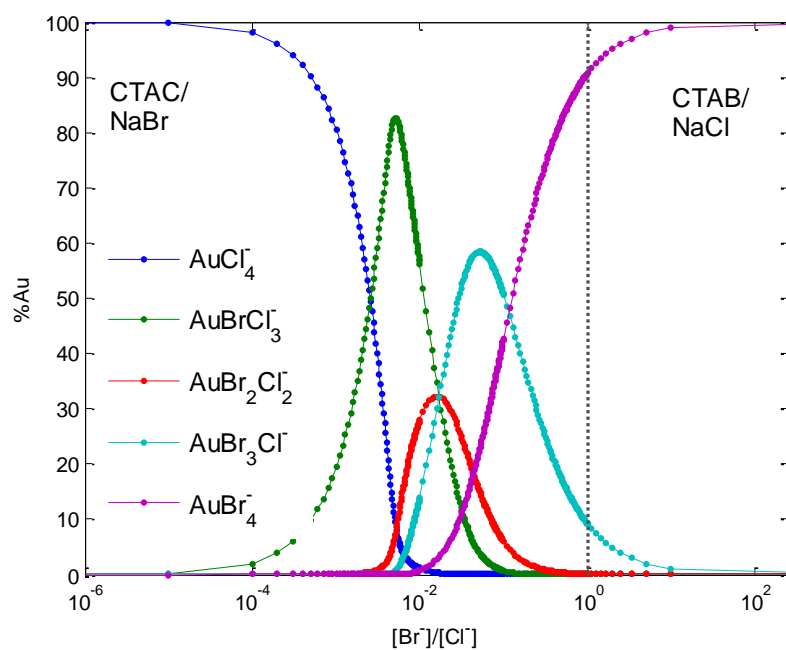


Figure C.3.: Distribution of Au^{3+} Complexes

For different ratios of bromide to chloride, different amounts of the gold-complexes are formed. At high bromide excess, almost only AuBr_4^- is formed. In the series with CTAC and increasing NaBr, all samples are found on the left, while in the series CTAB/NaCl, all samples are found in the right side of the graph.

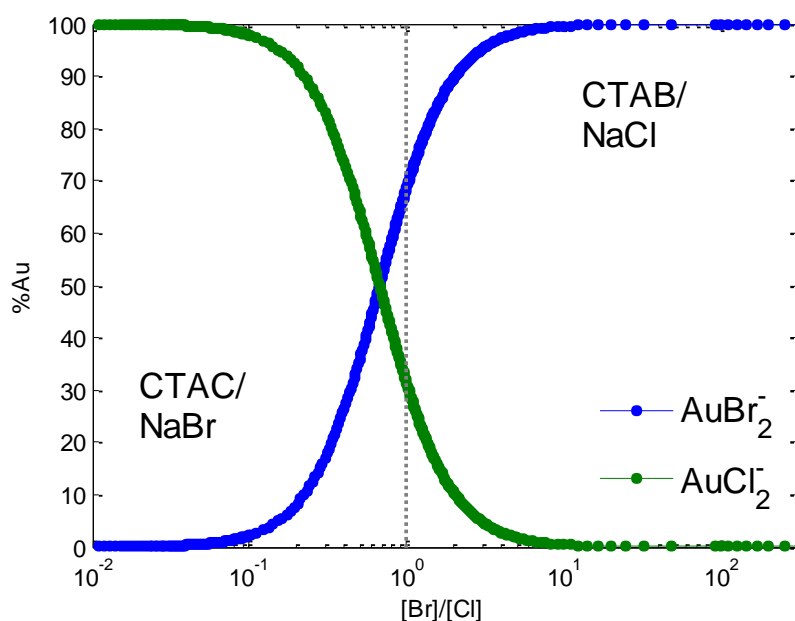


Figure C.4.: Distribution of Au^+ Complexes

Increasing the ratio of bromide to chloride, more AuBr_2^- is formed. Since the formation constants are different for the two complexes, at a ratio of 1 for Br/Cl, more of the bromo-complex is present. In the series with CTAC and increasing NaBr, all samples are found on the left, while in the series CTAB/NaCl, all samples are found on the right side of the graph.

C. Experimental Methods

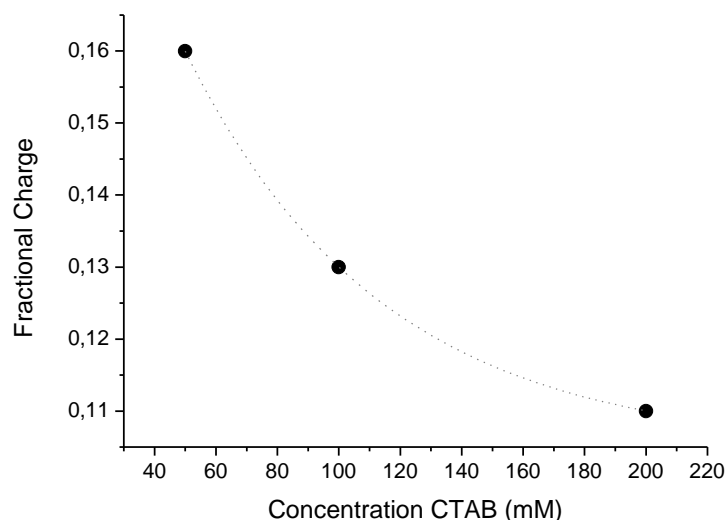


Figure C.5.: Fractional Charge

The fractional charge of CTAB depends on its concentration. The higher the CTAB concentration, the lower the fractional charge. Meaning for higher CTAB concentrations, a smaller percentage of the bromide is in solution, the bigger fraction is bound on the micelles.

2. How much bromide/ chloride is left?

From the synthesis plan (appendix C.1.1) one knows the total concentration of chloride and bromide used. The corrected halogenide concentrations are calculated by simply subtracting $2x [\text{AuBr}_2]^-$ from the bromide and $2x [\text{AuCl}_2]^-$ from the chloride concentration. These concentration are now termed $[\text{Br}]_{\text{corrected}}$ and $[\text{Cl}]_{\text{corrected}}$.

3. How much bromide/ chloride is in solution or bound to micelles?

Introducing CTAB into water at concentrations higher than the first CMC, positively charged micelles are formed, which bind a certain amount of bromides. The fractional charge β quantifies this effect by dividing the total charge of the micelle Z by the aggregation number N .

$$\beta = \frac{Z}{N}$$

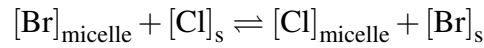
In order to calculate the concentration of bromide in solution $[\text{Br}]_s$, for pure CTAB solutions the fractional charge β corresponds to the fraction of bromides dissolved from the micelles.

$$[\text{Br}]_s = \beta \cdot [\text{Br}]_{\text{corrected}}$$

For pure CTAB solutions, β depends on the concentration of CTAB (van Stam *et al.*, 1998). The relation can be fitted by an exponential function, connecting β and concentration via

$$\beta = 0.12088 \exp\left(\frac{-[\text{CTAB}]}{0.06393}\right) + 0.10471$$

For mixtures of CTA^+ with bromides and chlorides, the concentration of halides (bromides *and* chlorides) in solution depends on the fractional charge of the mixture (which is assumed to be the mean of β_{Cl} and β_{Br} , $\beta_{\text{mixture}} = x \cdot \beta_{\text{Cl}} + (1 - x) \cdot \beta_{\text{Br}}$, x is the molar fraction of bromide (Aswal & Goyal, 1998)). Furthermore, the exchange constant K_e of bromide and chloride on the micelles has to be taken into account (Gamboa *et al.*, 1981).



$$K_e = \frac{[\text{Cl}]_{\text{micelle}} \cdot [\text{Br}]_{\text{s}}}{[\text{Br}]_{\text{micelle}} \cdot [\text{Cl}]_{\text{s}}} = 0.2$$

Using additionally the relations

$$\begin{aligned} [\text{halogenide}]_{\text{corrected}} &= [\text{Br}]_{\text{corrected}} + [\text{Cl}]_{\text{corrected}} \\ &= [\text{Br}]_{\text{micelle}} + [\text{Cl}]_{\text{micelle}} + [\text{Br}]_{\text{s}} + [\text{Cl}]_{\text{s}} \\ [\text{halogenide}]_{\text{s}} &= \beta \cdot [\text{halogenide}]_{\text{corrected}} \\ &= [\text{Br}]_{\text{s}} + [\text{Cl}]_{\text{s}} \end{aligned}$$

one can calculate the concentration of bromide and chloride in solution for different mixtures of CTAB/CTAC, CTAC/NaBr, CTAB/NaCl (figure C.6).

C. Experimental Methods

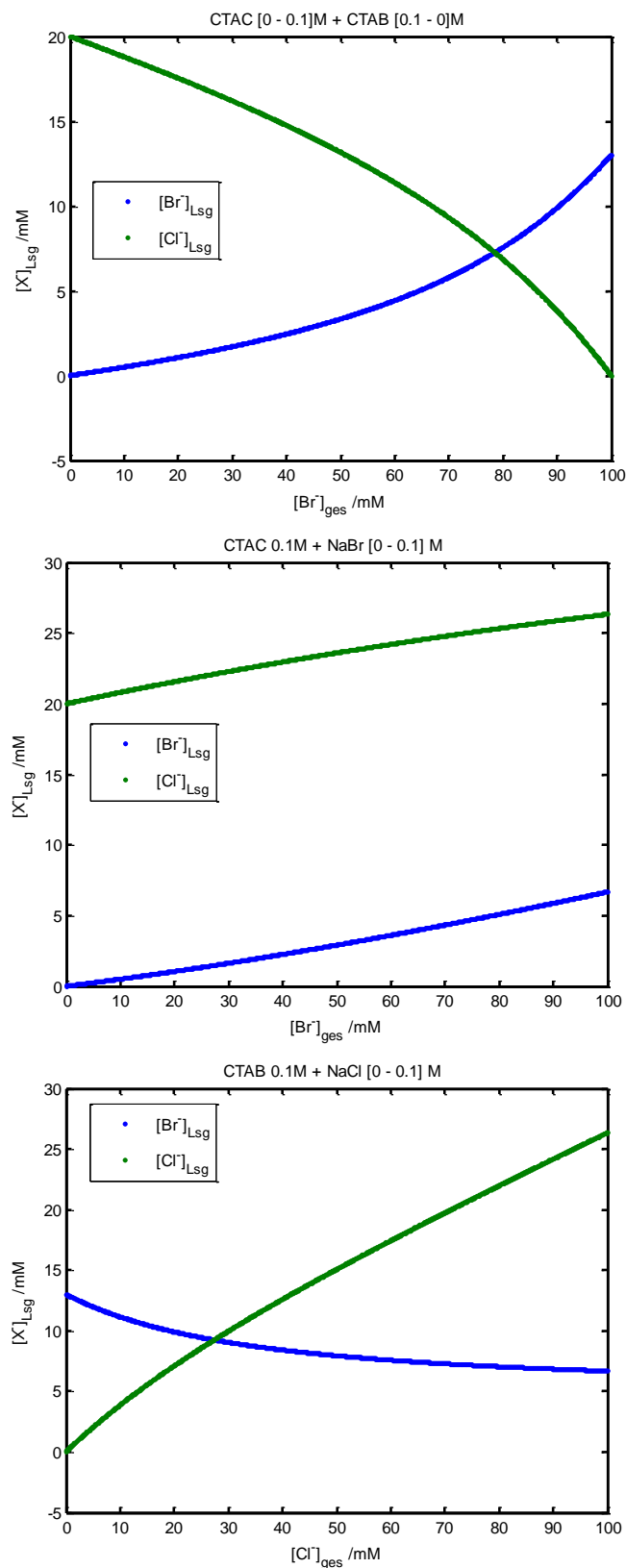


Figure C.6.: Halogenides in Solution

The concentration of halogenides in solution depends on the concentration of chloride and/or bromide used. For the three series (CTAC/CTAB, CTAC/NaBr, CTAB/NaCl), three different graphs are found.

4. Redox-potential for gold complexes

The standard redox potentials of the gold-halide complexes are known (CRC, 2004):

$$E^\theta ([\text{AuBr}_2]^-) = 0.959 \text{ V}$$

$$E^\theta ([\text{AuCl}_2]^-) = 1.119 \text{ V}$$

Using the Nernst-equation, the potentials for a given concentration of chloride or bromide in solution can be calculated:

$$E ([\text{AuBr}_2]^-) = E^\theta ([\text{AuBr}_2]^-) + 0.059 \log \left(\frac{[\text{AuBr}_2]^-}{[\text{Br}^-]^2} \right)$$

$$E ([\text{AuCl}_2]^-) = E^\theta ([\text{AuCl}_2]^-) + 0.059 \log \left(\frac{[\text{AuCl}_2]^-}{[\text{Cl}^-]^2} \right)$$

5. Electrochemical potential of the growth solution

In order to calculate an effective electrochemical potential of the growth solution E_{eff} , the potentials of the pure $[\text{AuBr}_2]^-$ and $[\text{AuCl}_2]^-$ are weighted with their proportion calculated in step 1:

$$E_{\text{eff}} = E ([\text{AuBr}_2]^-) \cdot \frac{[\text{AuBr}_2]^-}{[\text{AuCl}_2]^- + [\text{AuBr}_2]^-} + E ([\text{AuCl}_2]^-) \cdot \frac{[\text{AuCl}_2]^-}{[\text{AuCl}_2]^- + [\text{AuBr}_2]^-}$$

C.2. Silver-Coating

The silver coating follows a procedure described by Liu and Guyot-Sionnest (Liu & Guyot-Sionnest, 2004). In contrast to Liu and Guyot-Sionnest, we first remove excessive growth solution from the gold rods, which contains additional silver and gold ions, by centrifuging once and re-dispersing in 0.1 M CTAB. 0.8 ml of the CTAB-gold rods solution is diluted in 4 ml of 1 wt % aqueous polyvinyl pyrrolidone (PVP, Aldrich). To the mixture of PVP, CTAB and gold nanoparticles, different amounts of 1 mM AgNO_3 (Sigma-Aldrich, typically 180 μL) and typically 100 μL 0.1 M ascorbic acid (Sigma) are added. Raising the pH by adding 200 μL of 0.1 M NaOH (Merck) initiates the coating reaction and leads to a color change within a few minutes. We keep the molar ratio between AgNO_3 , ascorbic acid and NaOH constant (0.6:25:50) when the concentration of silver nitrate is changed.

C. Experimental Methods

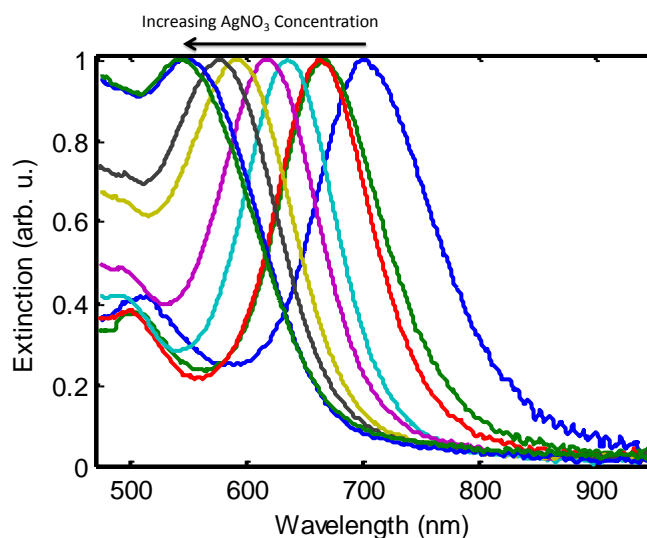


Figure C.7.: Extinction Spectra Au@Ag-Nanorods

Normalized extinction spectra of silver coated gold-nanorods with increasing silver concentration in the coating solution. The silver concentrations are given in figure 4.2c.

Single particle observations

In order to observe coating of single particles with the dark-field microscope, gold nanorods are first immobilized on the glass surface via the addition of NaCl. After extensive washing with deionized water, they are immersed in 40 μ L 0.01 M NaOH (Merck), which is simultaneously used as the immersion medium for a water immersion objective (100x, NA 1.0). Best results are obtained when detaching the drop of NaOH from the objective, mixing it with 80 μ L growth solution containing PVP, AgNO₃ and ascorbic acid in the same ratios as mentioned above and reattaching the solution again to the objective. If the experiment is performed the other way around (first putting in the growth solution, then mixing with NaOH), silver particles form all over the glass surface and completely cover the (silver coated) gold rods. All solutions are filtered through a syringe filter (0.02 μ m) to prevent the introduction of dust.

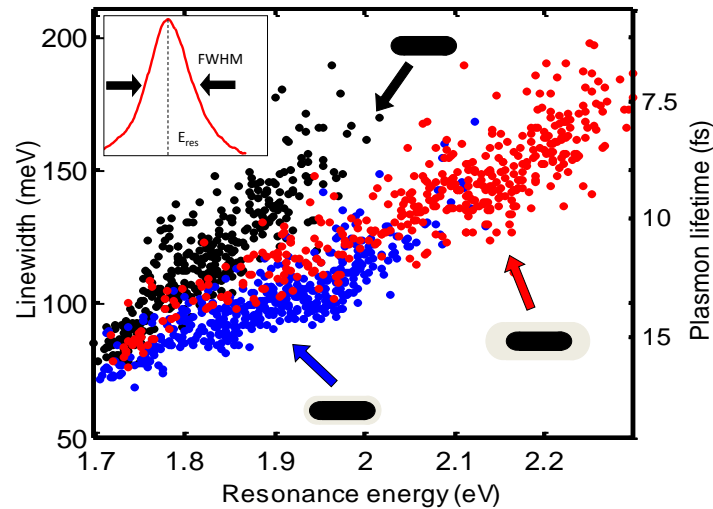


Figure C.8.: Extinction Spectra Au@Ag-Nanorods

Plasmon linewidth and resonance energy in energy units determined for single particles (pure gold nanorods (black dots), thin (blue dots), thick silver coating (red dots)). The linewidth in meV directly corresponds to a plasmon lifetime in fs (second axis on the right).

Electrodynamic model

We calculate extinction spectra (for example to extract the plasmon-shape relation in figure 4.3) using the electrodynamic solution for coated ellipsoids in the quasi-static approximation and the dielectric constants for gold and silver published by Johnson and Christy (Johnson & Christy, 1972). We replace the geometric ‘L-factor’ in the equations for coated ellipsoids by recently reported corrections for the end-cap geometry, which were obtained in the discrete dipole approximation (DDA). We generate a large distribution of ‘particles’ with the same mean and standard deviation of their width and length as determined by TEM for a given sample. For each ‘particle’, we simulate the extinction spectrum and add up all spectra to a simulated ensemble spectrum. We choose the end-cap geometry and therefore the ‘L-factor’ relation such that the peak resonance of the simulated and measured ensemble spectrum of the uncoated nanorods coincides. We keep this geometry fixed and introduce a silver coating with a thickness determined from TEM images (one half of the average widths of the coated particles minus the average width of the uncoated particles).

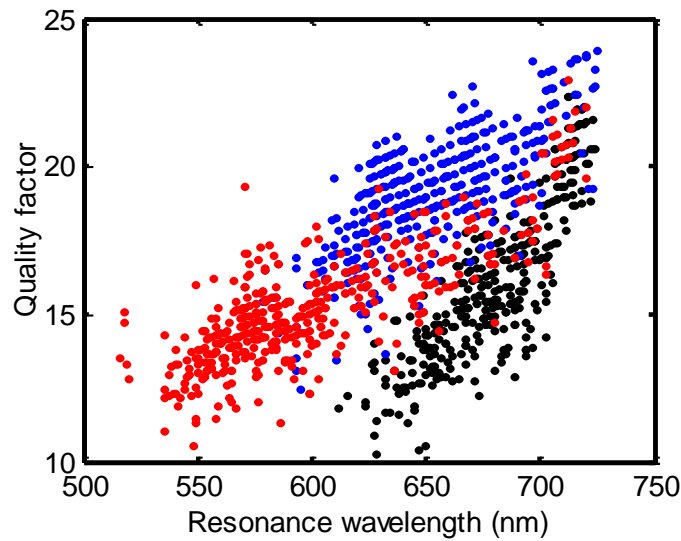


Figure C.9.: Quality Factor Au@Ag Nanorods

The quality factor Q of a harmonic oscillator is related to the linewidth Γ and the resonance wavelength λ_{res} by $Q = \Gamma/\lambda_{\text{res}}$. The quality factor gives the amount of energy stored in an externally driven oscillator and is thus a measure for the field enhancement around the particles. The quality factor extracted from single particle scattering spectra are shown here for pure gold nanorods (black dots), those rods with a thin silver coating (blue dots) and thick silver coating (red dots). The silver coating increases the quality factor up to 2 fold.

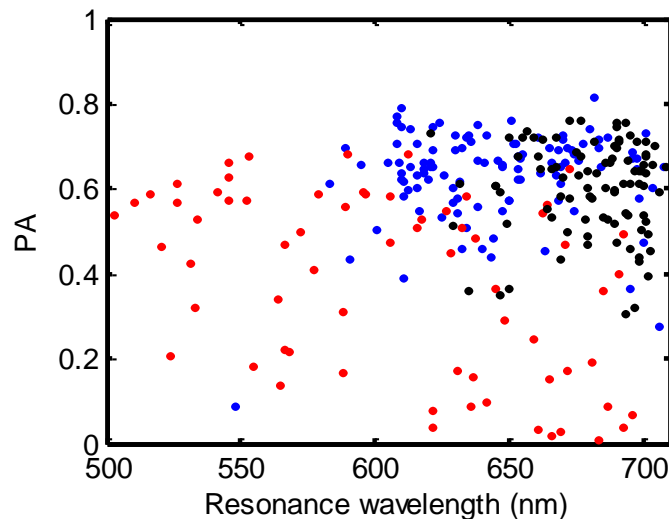


Figure C.10.: Polarization Anisotropy Au@Ag Nanorods

Polarization anisotropy (PA) for pure gold nanorods (black dots), with a thin silver coating (blue dots), and with a thick silver coating (red dots). The polarization anisotropy is given by the scattering intensity at the resonance wavelength of the long axis plasmon resonance with the polarization along this axis divided by the scattering intensity with the polarization perpendicular to the long axis – normalized to the sum of both intensities. PA is a measure for the degree of rod-like shape: it is expected to be close to 1 for perfect rods and close to 0 for perfect spheres. Clearly, the PA decreases for particles with thick coating.

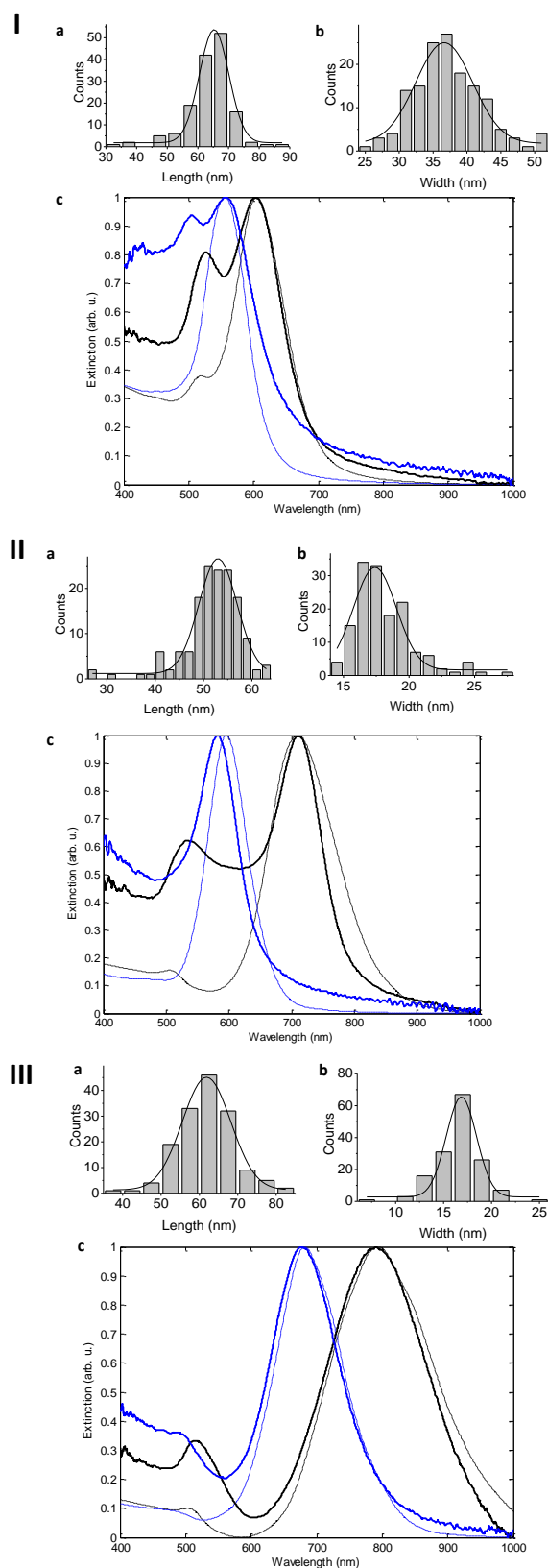


Figure C.11.: Modeled Ensemble Spectra Au@Ag Nanorods

Modeling the ensemble extinction spectra of uncoated and silver-coated gold nanorods. I-III show the length and width distribution of three samples of gold nanorods (a, b) and their extinction spectra (c, black: uncoated, blue: silver coated). The spectra calculated theoretically from the size distributions are shown in dashed lines. The parameters used for the calculations are:

I length: 64.9 ± 7.4 nm width: 36.4 ± 5.0 nm coating thickness: 4.4 nm eccentricity: 0.95

II length: 52.6 ± 6.0 nm width: 17.6 ± 2.3 nm coating thickness: 4.2 nm eccentricity: 0.8

III length: 61.8 ± 7.3 nm width: 16.6 ± 2.3 nm coating thickness: 2.6 nm eccentricity: 0.0 (spherical)

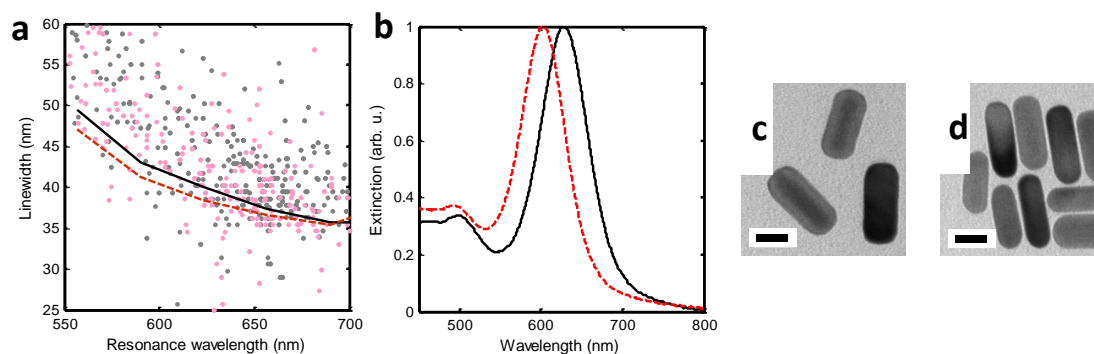


Figure C.12.: Linewidth Narrowing for Au@Ag Nanorods

Single particle and ensemble spectra of silver coated gold nanorods a) Linewidth vs. resonance-wavelength for bare (gray dots) and silver coated (reddish dots) gold-rods measured on over 400 single particles in each sample using an automated setup. This setup has a relatively high error in the linewidth determination. The lines show the trend with 90% of the particles above and 10% below (at each wavelength) for pure (black line) and silver coated (red line) gold rods. The line for silver coated nanoparticles is below the line for pure rods indicating a linewidth narrowing due to silver coating comparing particles at the same wavelength. b) Ensemble extinction spectra for bare gold (black line) and silver coated gold particles (red line). The silver-coated particles exhibit a blue shifted maximum. c)/d) TEM images of the pure (c) and silver-coated (d) gold particles, respectively. Scalebars are 20 nm.

Kinetic Measurements

In order to exclude effects by other chemicals different from gold nanorods and silver nitrate on the kinetics of the Ag-coating reaction, also ascorbic acid is varied. Furthermore, the addition of HCl after the end of the reaction is tested. This is done to exclude effects on the final particles, when HCl is used to quench the reaction at a certain point in time.

Ascorbic Acid Variation

Ascorbic acid is the reducing agent responsible for the reduction of Ag^+ to Ag^0 . Furthermore, it decreases the pH of the solution due to its acidic properties. Therefore, “enough” NaOH needs to be added to overcome this acidic effect. If no ascorbic acid is present in the solution no reaction occurs and no shift can be observed (see black data points figure C.13a). Adding only small amounts of ascorbic acid to the coating solution results in a small shift of the resonance wavelength. It can be imagined that only a part of the silver nitrate is reduced until ascorbic acid

is used up. Silver ions might stay in solution. Upon a certain threshold of ascorbic acid, a further increase does neither change the final resonance wavelength (see figure C.13b), nor the kinetics of the reaction.

Silver and Ascorbic Acid Variation

Changing ascorbic acid and silver nitrate at the same time but keeping the ratio between the two constant should eliminate the effect of one species decreasing below or above the optimum reaction stoichiometry. It can be seen that the end resonance wavelength behaves similarly as in the pure silver-variation experiment (see chapter 4.2). Adding more silver results in a bigger shift. Therefore, it has to be ensured to have enough ascorbic acid to completely reduce all silver present.

Adding HCl

Adding HCl while the coating reaction is running stops the reaction at the time the HCl is added. The pH of the reaction mixture is decreased, the redox potential of the ascorbic acid is decreased and ascorbic acid loses its ability to reduce silver on the gold nanorods (see figure C.15). If HCl is added after the coating reaction is over, no additional shift is observed.

Calculation of Gibbs Energy

The reaction potential of silver is calculated using the Nernst equation:

$$E(\text{Ag}^+ \rightarrow \text{Ag}) = E^\theta(\text{Ag}^+ \rightarrow \text{Ag}) + 0.059 \cdot \log([\text{Ag}^+])$$

for the reducing agent ascorbic acid, the reaction potential depends on the pH (Ando *et al.*, 1997):

$$E(\text{pH}) = 0.37\text{V} - 0.009\text{V} \cdot \text{pH}$$

Using $c(\text{Ag})=100\ \mu\text{M}$ (which is a mean value for the carried out reactions) and $\text{pH}=8$, the difference ΔE calculates to $\Delta E=0.5636\ \text{V}$. In order to calculate the Gibbs Energy, Faraday's law can be used:

$$\Delta G = z \cdot E \cdot F$$

with z = valency number of ions of the substance and $F = 96485\ \text{Cmol}^{-1}$, the Faraday constant. With this, $\Delta G = 26.5\ \text{kJmol}^{-1}$ results.

C. Experimental Methods

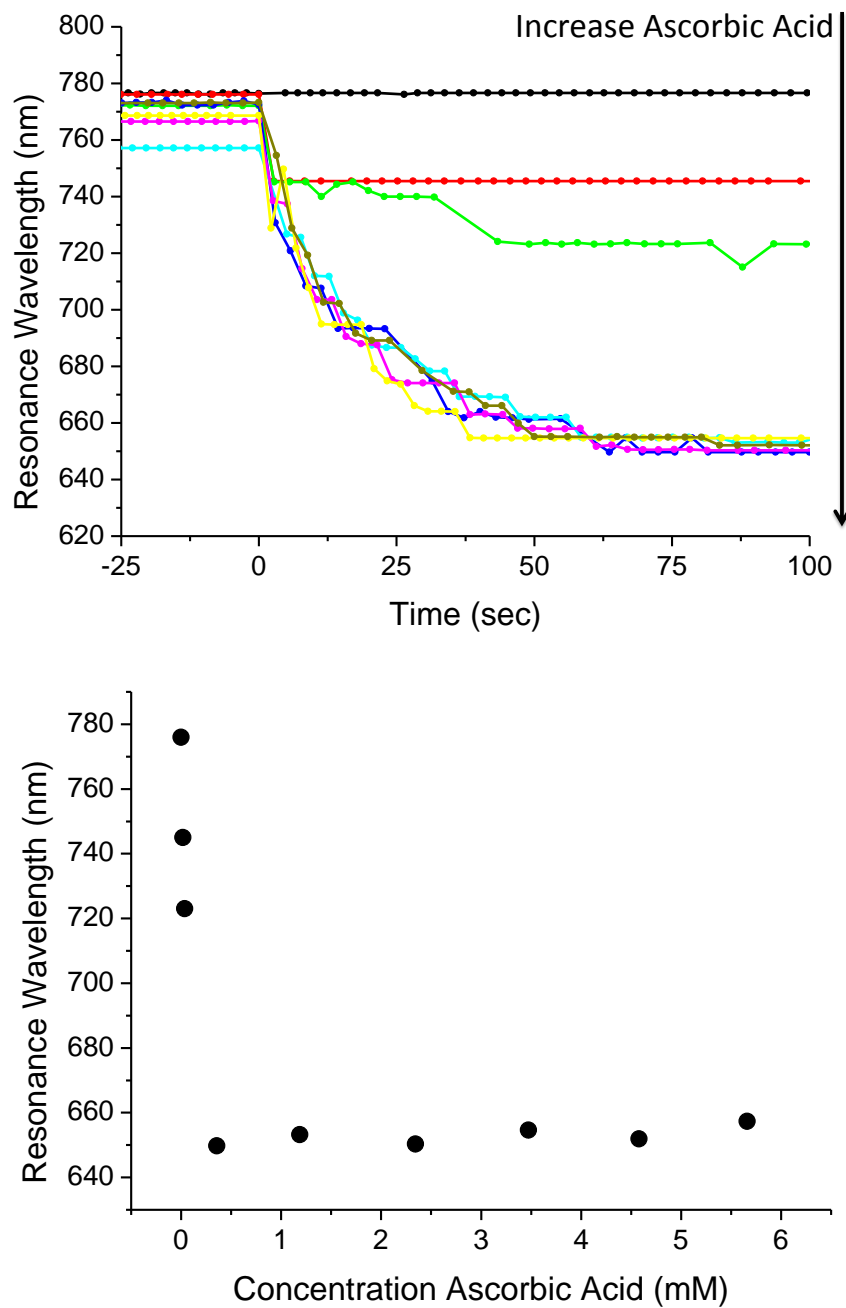


Figure C.13.: Different Ascorbic Acid Concentrations

a) If too little ascorbic acid is added, the silver is not reduced completely (red and green data points). If no ascorbic acid is present, no reaction is observed (black data points). b) Changing the concentration of ascorbic acid does not change the reaction kinetics as long as enough ascorbic acid is present to reduce all silver.

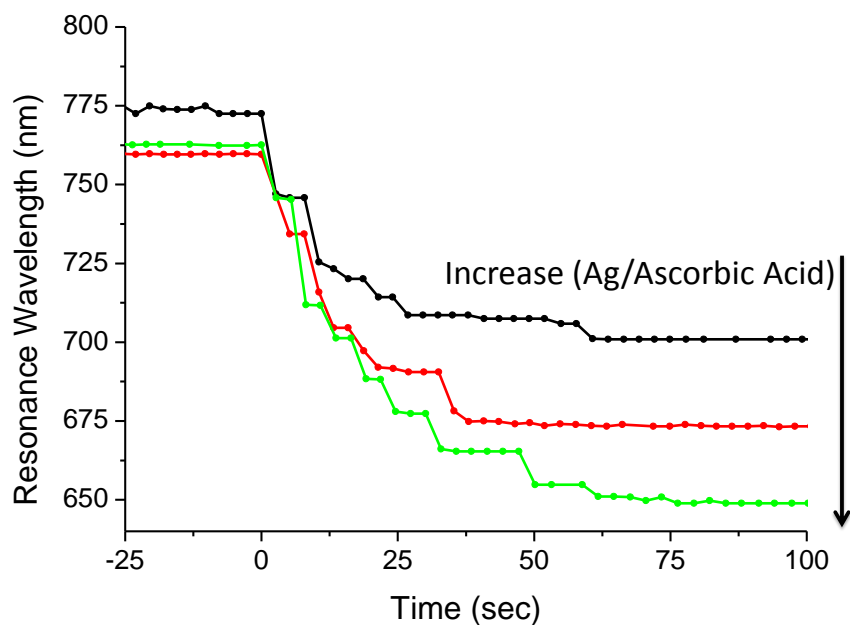


Figure C.14.: Vary Silver and Ascorbic Acid

Increasing the silver and ascorbic acid concentration, but keeping the *ratio* between the two species constant results in an increased shift of the resonance wavelength upon increasing the concentration. The behavior is the same as for the pure silver-variation case.

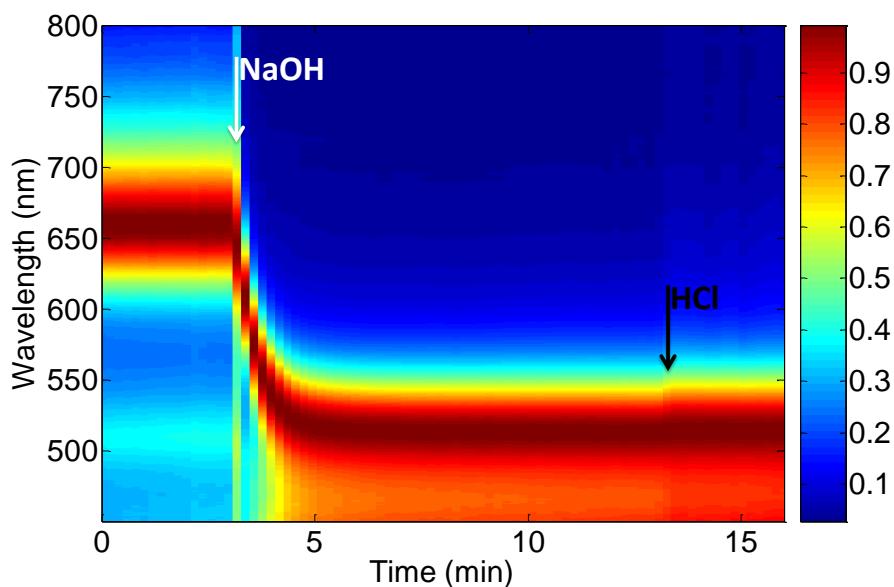


Figure C.15.: Adding HCl after the Coating Reaction

If HCl is added after the coating reaction is finished, no additional shift is observed.

C.3. Gold Nanorods in Gels

C.3.1. PNIPAM-Gels

For the synthesis of PNIPAM-polymer, the monomer N-Isopropylacrylamide (NIPAM, Acros) is mixed with the cross-linker N,N'-Methylen-Bis-Acrylamide (BIS, Sigma-Aldrich) and the photoinitiator Ammoniumpersulfate (APS, Sigma-Aldrich), typically in the molar ratio 531:1:3 (NIPAM:BIS:APS). The final concentration of NIPAM in the monomer-solution is 345 mM. In order to start the polymerization, the mixture is illuminated with a UV lamp (Hg/Xe 200, Amko, shortpass filter 400 nm) for 60 minutes. Heating during the polymerization (which causes turbidity of the gel) is avoided by cooling the sample slightly by a fan on top of a rotating plate, which ensures homogeneous illumination.

Introducing a certain amount of gold spheres or gold rods into the system of NIPAM, BIS and photoinitiator is possible without aggregation of the nanoparticles. The ratio between gold nanoparticle solution and monomer-solution is 1:3, the final concentration of NIPAM is kept to 345 mM. Polymerization works in the same way as without nanoparticles. The gel hardens within one hour of UV-illumination and is stiff enough to be turned upside down without losing its form (see also figure 5.2).

The thermoresponsive properties of the gel are conserved as well. Upon heating the gels in an incubator to 37 °C, clouding is observed (see figure C.16). When the sample is cooled down to room temperature again, the cloudiness is lost and the samples finally look the same as before heating. It can be noticed that the sample does not cool down homogeneously but the cooling starts from the outside walls of the vial. Inside the sample the higher temperature stays longer, which can easily be seen as cloudy sphere, which shrinks over time. Furthermore, it can be noticed that the gels stay in the gel constitution and do not melt into some liquid form.

Spectra

NIPAM itself shows an increased absorption below 500 nm and above 900 nm (see figure C.17). Upon polymerization, the overall extinction increases, dramatically below 500 nm. It is therefore crucial to take a polymerized PNIPAM sample as reference for the spectra of particles inside the gels. For this purpose, particles are mixed with NIPAM, BIS, and APS, filled into a cuvette and polymerized by UV-light inside the cuvette.

For both, spheres and rods, it can be seen that the particles do not aggregate in the gel (figure C.18). The background-correction for spheres worked out much better than for rods, but also the rod-sample still shows the distinct peak at about the same position as the particles in water.

Gels in Flow Cell

For the microscopic investigations it is desired to have a thin sample of PNIPAM gel including nanoparticles between two glass slides. This is achieved by a self-built flow-cell setup (see

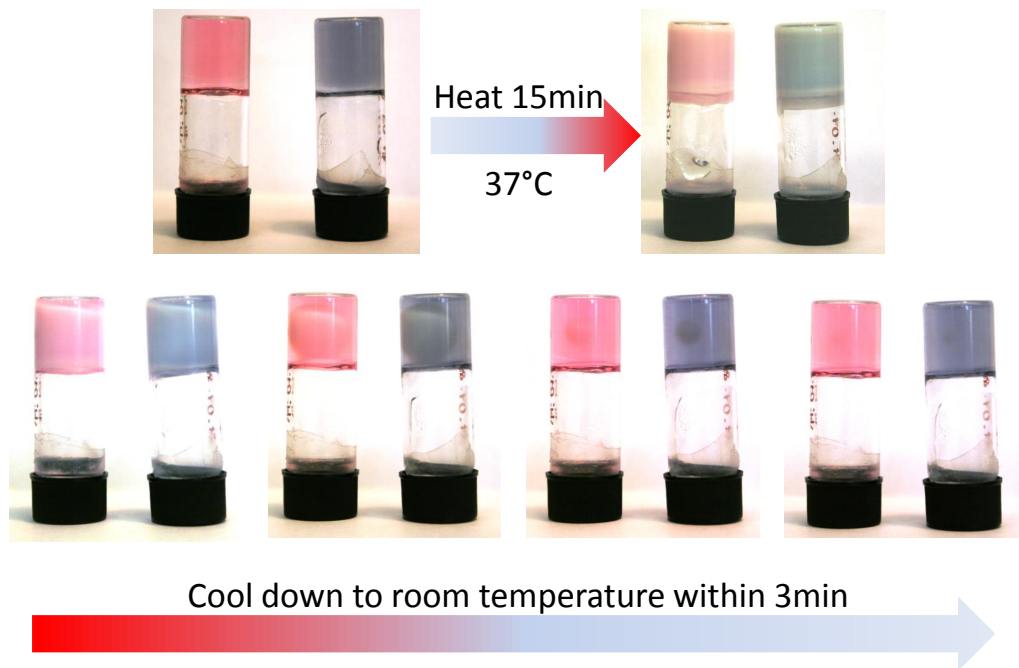


Figure C.16.: Heating Gold Nanorods and -spheres in PNIPAM

Gold nanorods and -spheres are introduced into the unpolymerized NIPAM monomer solution. The gel is polymerized by exposing it to UV-light. After the polymerization process, a clear gel is obtained, which turns turbid after heating to 37 °C. A clear gel is recovered upon cooling back to room temperature.

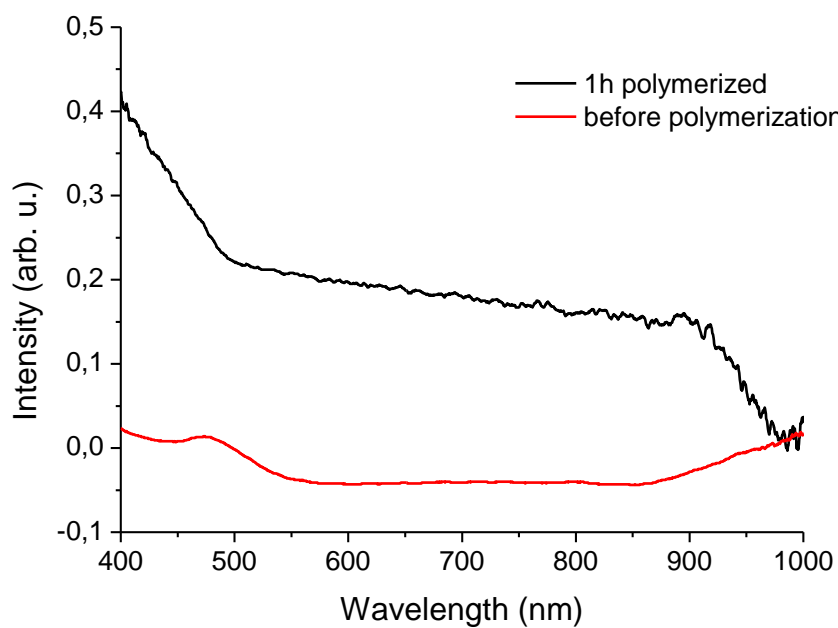


Figure C.17.: Spectra NIPAM and PNIPAM

UV-Vis spectra of unpolymerized (red) and polymerized (black) (P)NIPAM. The polymerized sample shows an increased absorption below 500 nm.

C. Experimental Methods

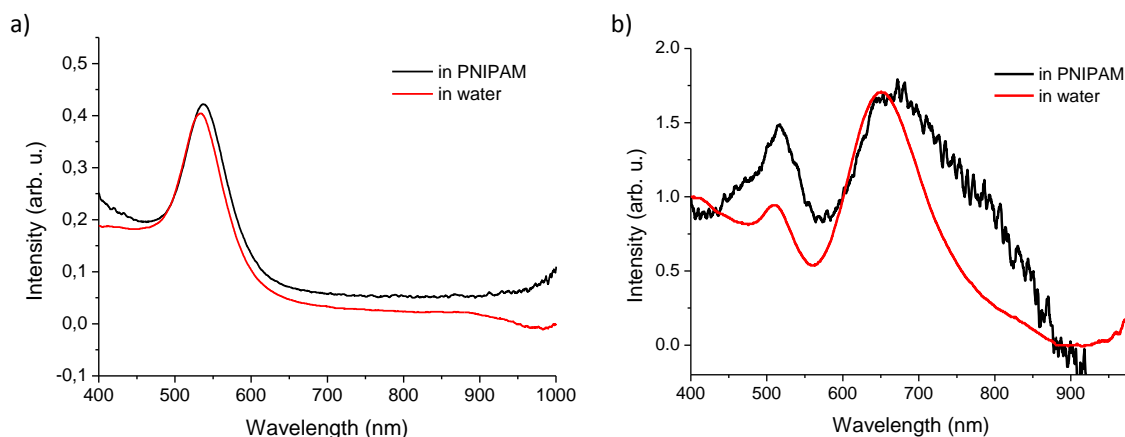


Figure C.18.: Spectra Gold Nanorods and -spheres in PNIPAM

For mixtures of gold nanospheres (a) and -rods (ba) ensemble spectra are recorded in water (red) and PNIPAM (black). It can be seen that the particles do not aggregate in the polymer matrix but still show their characteristic plasmon peak.

figure 5.3), consisting of a microscope slide and a cover glass, kept apart at a small distance by parafilm. After cleaning the glass slides with 10 % Hellmanex II solution (Hellma GmbH, two washing steps including heating to 60 °C and sonication in an ultrasonic bath) and glueing them together by parafilm, the unpolymerized mixture of NIPAM, BIS, APS, and gold nanorods is filled into the cell. The openings are sealed by vacuum grease, and the assembly is placed in front of the UV-lamp (see above “PNIPAM Gels”). Looking at the polymerized sample in a dark-field microscope, one can see that the particles have a tendency to stick to the glass surfaces (therefore they have to be cleaned beforehand). But also a significant amount of particles stay “inside” the gel. The particles do not aggregate, but most of them still scatter the characteristic red light of isolated gold rods. The gel itself does not scatter light in high amounts, except some impurities like dust, which might as well be on the glass surface itself. The particles inside the gel are locally fixed and do not show any lateral movement, an intrinsic indicator that the polymerization worked (also tested by breaking the flow cell apart after the experiment).

C.3.2. Rotational Data Acquisition and Analysis

The gold nanorods inside the polymerized PNIPAM gel do not show any lateral movement. By introducing a polarizing beam splitter in front of a CCD camera (for further setup-information see chapter B.3), the particles light up in either one of the channels according to their orientation. The two channels are recorded on one CCD-chip, spacially separated. Figure C.19 shows some selected snapshots of a movie, recorded originally with a frequency of 116.9 Hz (5 msec exposure time, gain 4000, 2500 frames). Channel one corresponds to the upper part of the image, channel two to the lower one. Arrows point to the same particles in both channels. If a particle is bright in one channel, it appears dark(er) in the other one. With time, the particles change their orientation from bright to dark in the one channel and correspondingly from dark to bright in the other one.

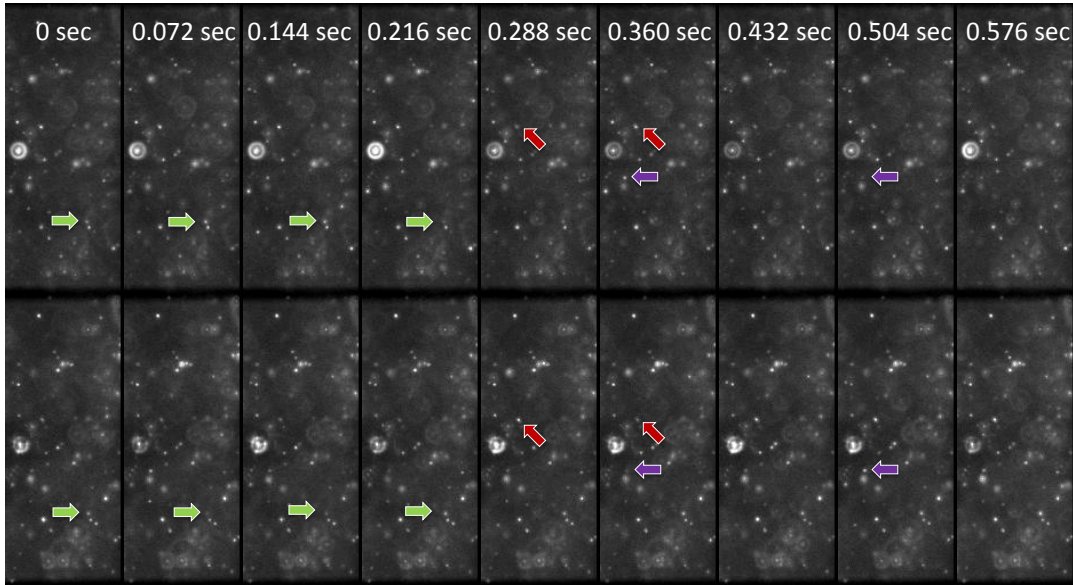


Figure C.19.: Snapshots of Rotating Rods in PNIPAM

Snapshots of a movie showing rotating gold nanorods at different times. The upper part of the image corresponds to one polarization channel, the lower part to the orthogonally polarized one. Arrows mark particles, which show rotation by changing from bright to dark in one channel, while switching from dark to bright in the other.

Besides “blinking” particles, there are also some which are always bright in both channels. They account either for spheres or aggregates, which do not scatter polarized light.

Following one particle over time in both channels results in a time trace as shown in figure C.20. The intensity in the channels fluctuates around a median position, an increase of the intensity in one channel corresponds to a decrease of the intensity in the other one. The recording of two channels instead of one, which would in principle already be enough to calculate the autocorrelation of the signal, ensures that the particle is truly rotating and the fluctuations are not caused by overall intensity changes.

For the same reason -getting rid of overall intensity fluctuation- the reduced linear dichroism (RedInt) is calculated and used as signal to further on handle the data. The reduced linear dichroism (see figure C.21a) is calculated as the following, the difference between the intensities of the two channels (Int1 and Int2) is normalized by their sum.

$$\text{RedInt} = \frac{\text{Int1} - \text{Int2}}{\text{Int1} + \text{Int2}} \quad (\text{C.1})$$

The obtained signal is autocorrelated, resulting in an autocorrelation function over time (figure C.21b).

C. Experimental Methods

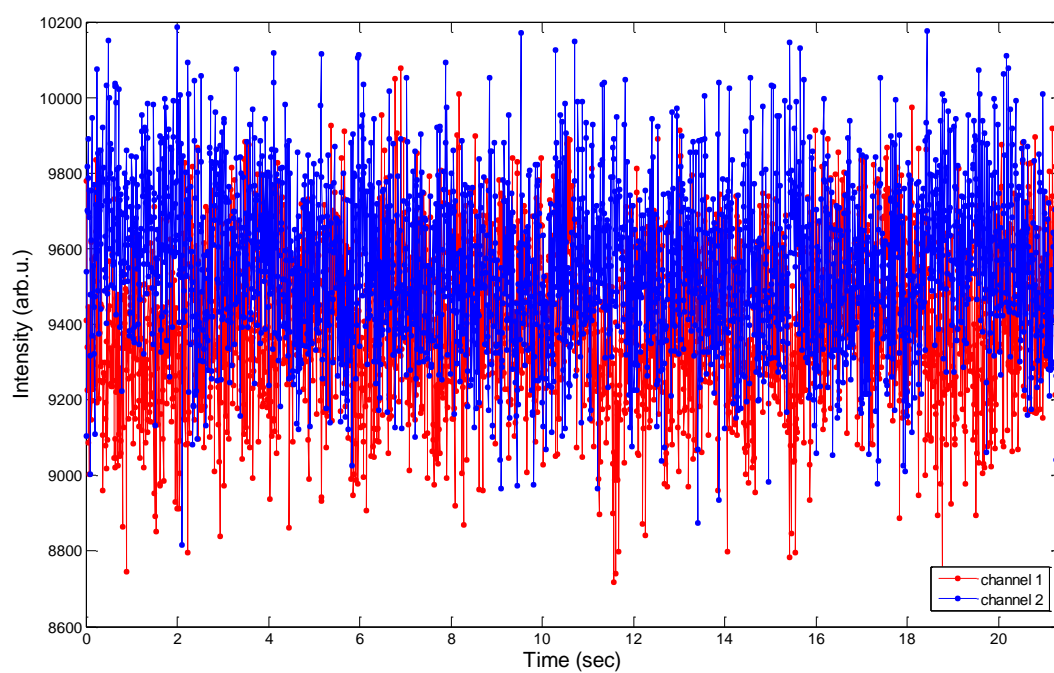


Figure C.20.: Typical Time Trace of a Rotating Gold Nanorod

Time-trace for a rotating gold nanorod for both polarization channels. While the intensity in channel one (red) is increasing, an intensity drop in channel two (blue) is observed and vice versa.

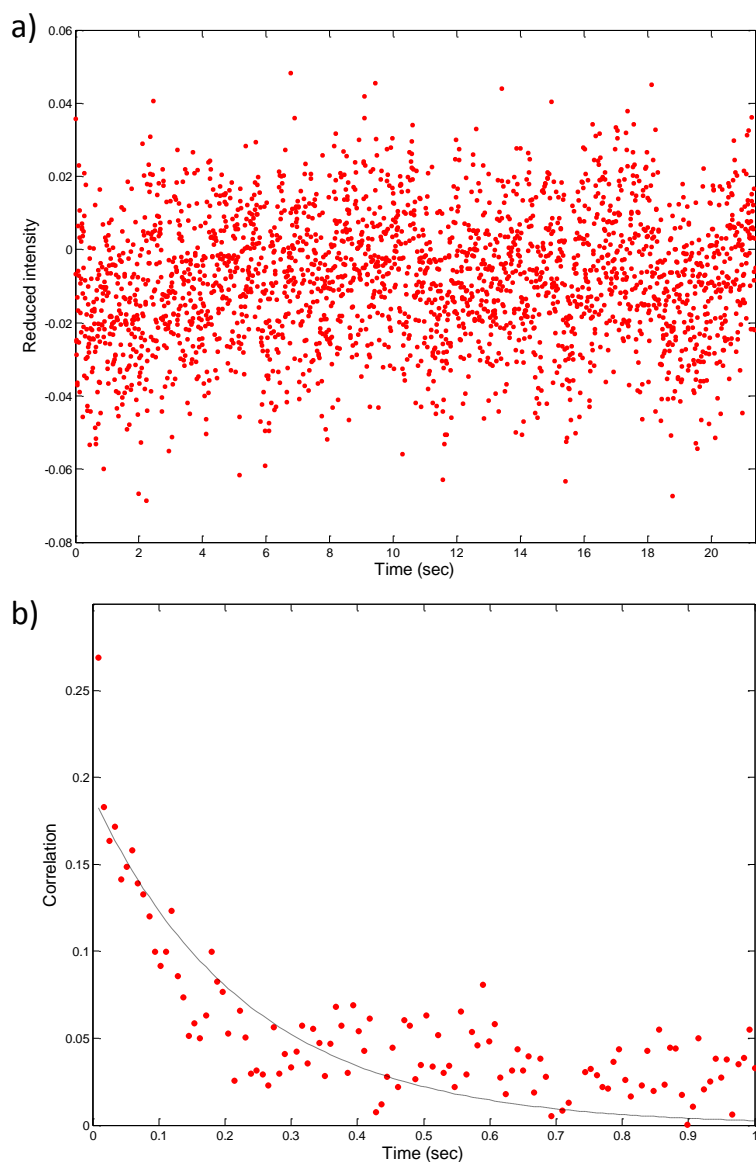
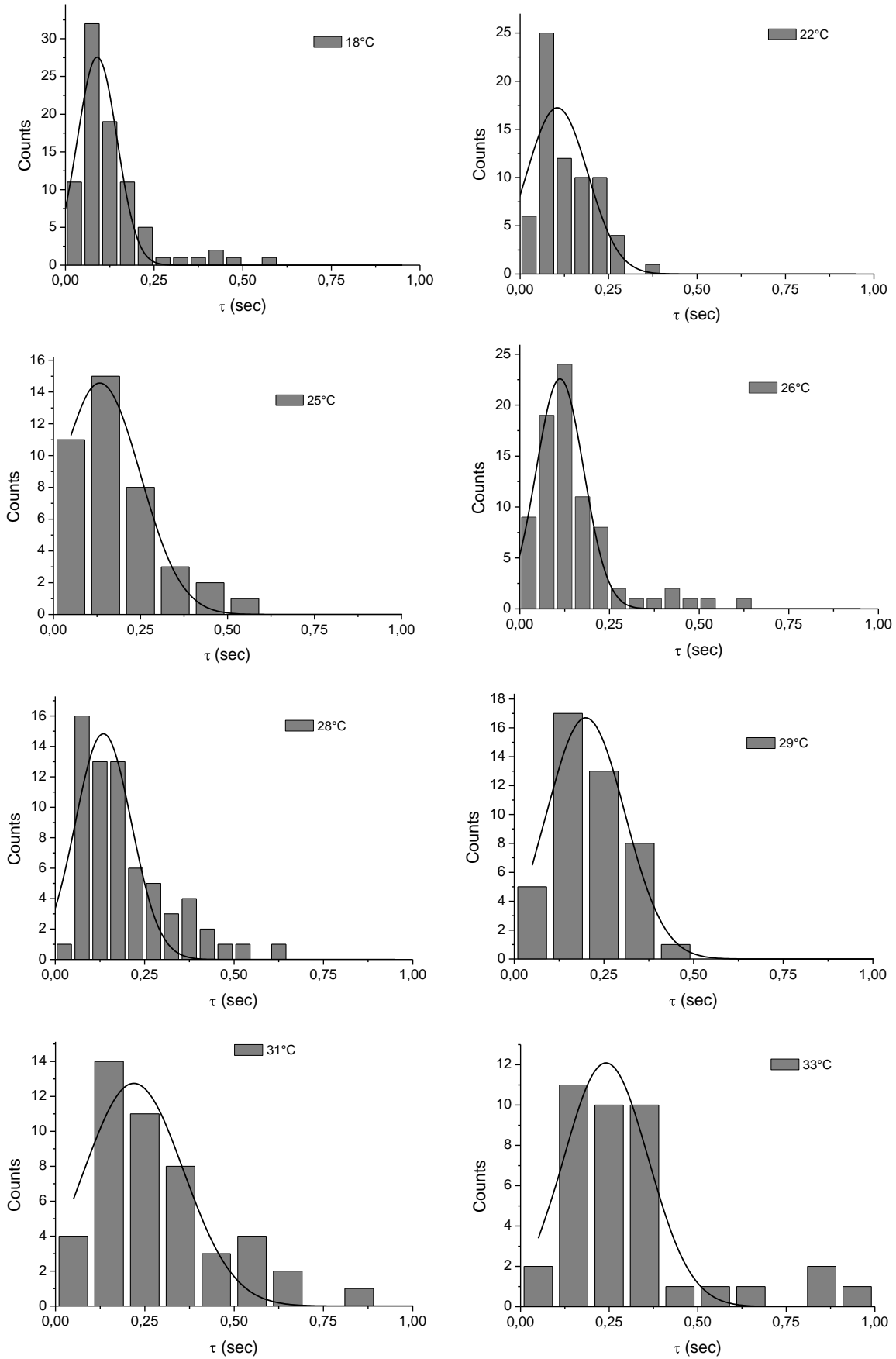


Figure C.21.: Reduced Linear Dichroism and Autocorrelation

a) Time-trace of the reduced linear dichroism of a rotating gold nanorod calculated according to equation C.1. b) Autocorrelation of the reduced linear dichroism signal of part a). A single exponential fit for the first 0.1 seconds is shown as a gray line.

The first 0.1 seconds of the autocorrelation function of the reduced linear dichroism are fit by a single exponential decay, assuming a homogeneous environment for the rotating particles. The obtained correlation times for all rotating particles are collected and the histograms are fitted by gaussian distributions. All correlation times are given in table C.8.

C. Experimental Methods



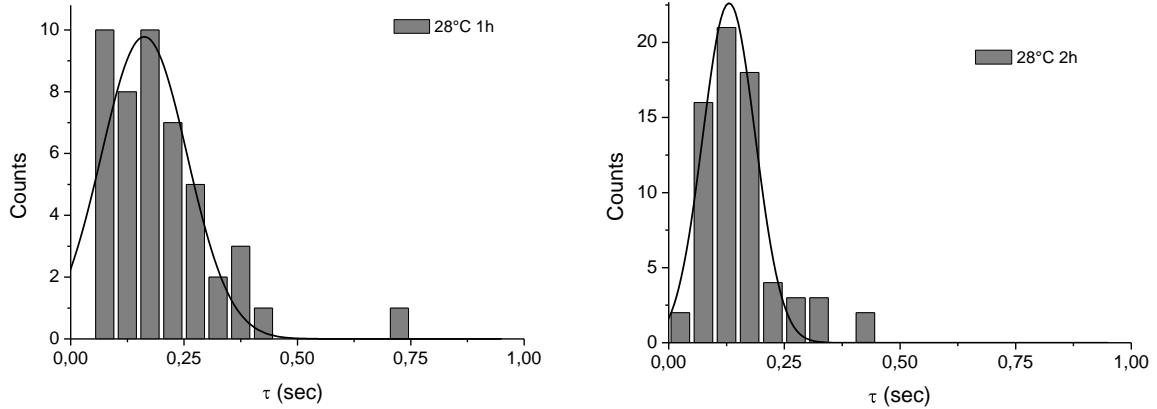


Table C.8.: Decay Times at Different Temperatures

| set T (°C) | T at the sample (°C) | τ (sec) |
|------------|----------------------|--------------|
| 18 | 19 | 0.09 |
| 22 | 23.3 | 0.11 |
| 25 | 25 | 0.1 |
| 26 | 27 | 0.11 |
| 28 | 29.3 | 0.13 |
| 29 | 29.6 | 0.2 |
| 31 | 31.7 | 0.22 |
| 33 | 33.6 | 0.22 |
| 28°C, 1h | 31.7 | 0.16 |
| 28°C, 2h | 32.7 | 0.13 |

Besides this “simple” analysis, the autocorrelation data can as well be fitted by a stretched exponential function of the form

$$f(t) = \exp\left(\frac{-t}{\tau_{KWW}}\right)^{\beta_{KWW}}$$

This analysis is known as Kohlrausch-Williams-Watt, yielding τ_{KWW} and β_{KWW} . While the correlation time τ_c can be calculated using

$$\tau_c = \int f(t)dt = \frac{\tau_{KWW}}{\beta_{KWW}} \Gamma\left(\frac{1}{\beta_{KWW}}\right)$$

the parameter β_{KWW} accounts for the inhomogeneity of the system. While for homogeneous systems β_{KWW} turns into 1 (a single exponential fit function is recovered), heterogeneous systems show $\beta_{KWW} < 1$. Using stretched exponential fit functions for the autocorrelation signal of the reduced linear dichroism, very small β_{KWW} values are obtained.

C. Experimental Methods

| set T (°C) | time range used for fit (sec) | β_{KWW} |
|------------|-------------------------------|----------------------|
| 18 | 0-1.5 | 0.3 |
| 18 | 0-5 | 0.28 |
| 22 | 0-1.5 | 0.32 |
| 22 | 0-5 | 0.25 |
| 25 | 0-0.1 | 0.18 |
| 25 | 0-1.5 | 0.24 |
| 25 | 0-5 | 0.19 |
| 26 | 0-1.5 | 0.3 |
| 26 | 0-5 | 0.22 |
| 28 | 0-1.5 | 0.25 |
| 28 | 0-5 | 0.23 |
| 29 | 0-0.1 | 0.17 |
| 29 | 0-1.5 | 0.29 |
| 29 | 0-5 | 0.2 |
| 31 | 0-0.1 | 0.16 |
| 31 | 0-1.5 | 0.3 |
| 31 | 0-5 | 0.2 |
| 33 | 0-0.1 | 0.16 |
| 33 | 0-1.5 | 0.32 |
| 33 | 0-5 | 0.21 |
| 28, 1h | 0-1.5 | 0.28 |
| 28, 1h | 0-5 | 0.21 |
| 28, 2h | 0-1.5 | 0.25 |
| 28, 2h | 0-5 | 0.19 |

These β_{KWW} values are significantly smaller than values reported in literature for inhomogeneous systems (Deschenes & Vanden Bout, 2001). This can have different reasons. The gold nanorods might in fact experience a heterogeneous environment on a very small time scale. If this is true, the acquisition frequency needs to be increased in order to have more data-points for shorter times. Also insufficient data recording (too little data points in total) can be a reason for the observed low β_{KWW} . Therefore, longer timetraces are as well preferable. Both problems might be overcome by improving the experimental setup. A stronger light source, which enables for shorter exposure times, as well as a more powerful camera and data-acquisition system will allow for higher frequencies and longer time traces.

C.4. Biological Coatings (Bio-functionalization)

C.4.1. Biotin-PEG

Biotin-PEG-SH

For the two high-molecular weight PEGs (PEG₆₂: MW= 3000 g/mol and PEG₁₀₇: MW= 5000 g/mol, Iris Biotech GmbH), a direct functionalization of the gold nanospheres is possible, since those PEGs carry a thiol-group at the end. 500 µl gold nanoparticles are centrifuged (9720 rcf, 5 min) and resuspended in 100 µl freshly prepared 2 mM aqueous PEG solution. The mixture is incubated for at least 2 hours at room temperature on a shaking table. To remove the excess of PEG, 400 µl deionized water (18 MΩ) are added and the solution is centrifuged again. After removing the supernatant, the pellet is taken up in 20 µl deionized water and stored at 4 °C until use.

Biotin-PEG-NH₂

The low-molecular weight PEGs (PEG₁₀: MW= 683 g/mol and PEG₂: MW= 525.6 g/mol, Iris Biotech GmbH) carry an amino-group at their end. Therefore, the gold nanoparticles are pre-functionalized with 3,3'-Dithiobis(sulfosuccinimidylpropionate) (DTSSP, Pierce). For this purpose, 200 µl gold nanoparticle solution are centrifuged (9720 rcf, 5 min). After the removal of the supernatant, 100 µl freshly prepared 5 mM aqueous DTSSP solution are added and the mixture is incubated for 20 minutes at room temperature under shaking. Prior to the functionalization with PEG-Biotin, excess DTSSP is removed via centrifugation (9720 rcf, 5 min). Collecting the supernatant leaves a pellet, which is incubated with 100 µl freshly prepared 5 mM aqueous PEG solution for at least 2 hours. To remove the excess of PEG, 400 µl deionized water (18 MΩ) are added and the solution is centrifuged again. After removing the supernatant, the pellet is taken up in 20 µl deionized water and stored at 4 °C until use.

C.4.2. Streptavidin

In order to bind streptavidin covalently to the gold nanoparticle surface (British Biocell), disulfide groups are introduced to the protein via 3,3'-Dithiobis(sulfosuccinimidylpropionate) (DTSSP, Pierce). 50 µl of a 1 mg/ml streptavidin solution (Calbiochem) in phosphate buffered saline (PBS, 0.01 M, Sigma) are incubated for 30 minutes at room temperature with 50 µl 0.3 mM DTSSP in PBS. Afterward, the unreacted DTSSP is removed with a Zeba Spin Desalting Column 7K MWCO (Pierce). To clean the gold nanoparticles from their storage solution, 500 µl are centrifuged (9720 rcf, 5min) and the supernatant is removed. 50 µl of the modified streptavidin are added and the spheres are left for incubation over night at room temperature under shaking. The next day, 400 µl deionized water (18 MΩ) are added and the spheres are centrifuged again

C. Experimental Methods

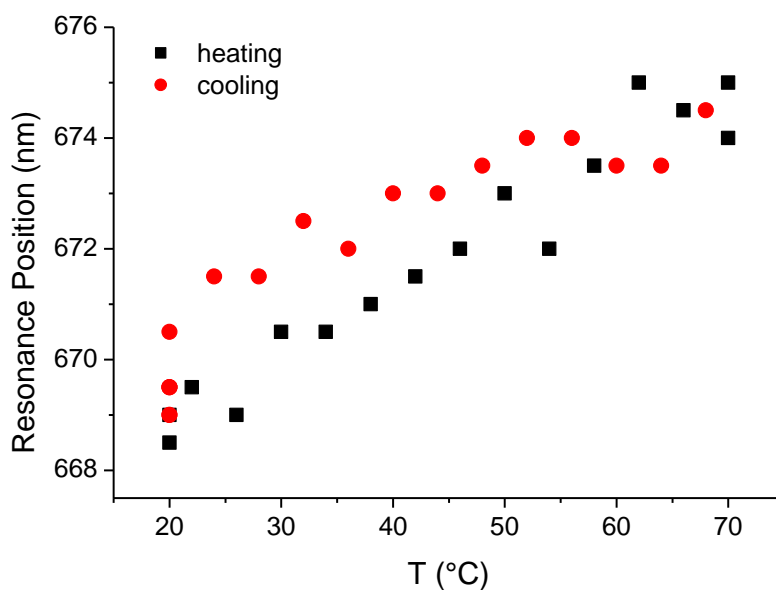


Figure C.22.: Heating of ELP-Functionalized Gold Nanorods

Resonance position of gold nanorods coated with elastin-like polypeptide in water at different temperatures. Black squares show the heating process while red circles show the cooling. Increasing the temperature increases the resonance position since ELP collapses at higher temperatures and increases the refractive index around the particles. The process is reversible.

(9720 rcf, 5 min). The supernatant, including unbound streptavidin, is discarded. 20 μ l deionized water are added and the streptavidin-modified spheres are stored at 4 $^{\circ}$ C until use.

C.4.3. ELP

In batch: 100 μ l ELP (125 μ M) and 100 μ l hydroxylamine (0.1 mM, Sigma Aldrich) are mixed with a pellet of gold nanoparticles gained from 1 ml of nanoparticle stock solution by centrifugation. The reaction mixture is incubated over night at 4 $^{\circ}$ C and cleaned the next day by adding 500 μ l of water, followed by centrifugation (2430 rpm, 5 min) and redispersion in water. It has to be mentioned that the ELP-functionalized particles tend to aggregate or stick on the walls of the reaction vessel. This tendency is stronger for higher molecular weight ELPs (E4-40, -60, and -120) than for the E4-20.

It is also possible to functionalize gold nanorods with ELP, using the same protocol as described for spheres. Those rods show a reversible redshift of the resonance position upon heating (and cooling). The higher the temperature, the more red-shifted the resonance position. This can be explained by a collapse of the ELP at higher temperatures and an increase in the local refractive index around the rods, causing a redshift of the resonance. The ELP's ability to respond to temperature changes seems unaffected by the gold nanoparticle. No aggregation of the particles is observed here as well as in the sphere case.

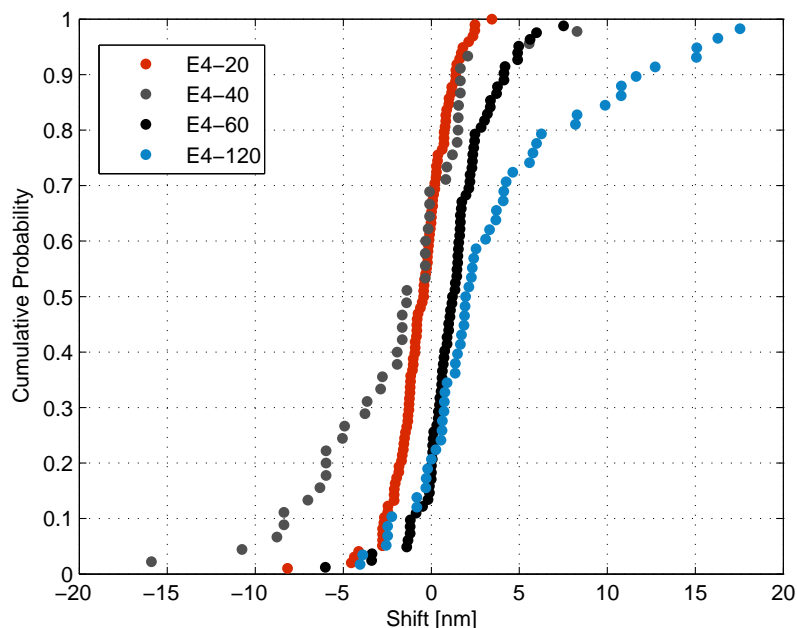


Figure C.23.: Different ELPs Bind to Particles in a Flow-Cell

Different ELPs bind to spherical gold nano particles in the flow cell. While the two smaller ELPs (E4-20 and -40, red and gray circles) show no shift, the two bigger ELPs (E4-60 and -120, black and blue circles) show a small redshift of the resonance wavelength upon binding onto the gold spheres.

In the flow cell: Functionalization of gold nanoparticles with ELP in a flow cell starts from “naked” gold nanoparticles immobilized on the glass surface via the introduction of 1 M NaCl. These particles are exposed to a mixture of 300 μ l 125 μ M ELP in water, 3 μ l of Tris(2-chlorethyl)phosphat (TCEP, 100 mM, Aldrich), and 100 μ l of conjugation buffer (2.5 mM Tris-HCl pH 7.5, 0.25 mM EDTA, 0.5 M NaCl, 0.025 % Tween 20, all Sigma). Two rinsing periods (5 min each) with this mixture are interrupted by two incubation periods (45 min each). Afterward, the flow cell is rinsed with a mixture of superbloc and conjugation buffer in a 60:40 ratio to remove excess ELP.

Single particle spectra are taken before incubation with ELP (spectra in a mixture of superbloc and conjugation buffer in a 60:40 ratio) and after binding ELP (spectra again in a mixture of superbloc and conjugation buffer in a 60:40 ratio). Binding the small ELPs (E4-20 and -40), practically no shift can be observed. The bigger ELPs cause a redshift of 1.3 nm and 2 nm. An increased shift for bigger ELPs is observed, which can be explained by the fact that the local refractive index is increased in a bigger space around the sphere.

| Name | Repeat Units | Molecular Mass (kDa) |
|--------|--------------|----------------------|
| E4-20 | 20 | 8.4 |
| E4-40 | 40 | 16.5 |
| E4-60 | 60 | 25.2 |
| E4-120 | 120 | 49.4 |

Table C.10.: Different ELPs

C. Experimental Methods

| ELP | shift | error of the mean |
|--------|----------|-------------------|
| E4-20 | -0.44 nm | 0.17 nm |
| E4-40 | -0.86 nm | 1.43 nm |
| E4-60 | 1.27 nm | 0.39 nm |
| E4-120 | 2.04 nm | 0.72 nm |

Table C.11.: Shift upon binding of different size ELP

C.4.4. Biotin-ELP

Biotin-Functionalization of ELP

The ELP-structures carry, by themselves, a thiol-group on one end and an amino functionality on the other. The latter one can be used to attach a biotin-N-hydroxysuccinimid-ester (NHS-biotin, Pierce). The ELP is diluted in PBS (0.01 M, Sigma) to a final concentration of 125 μ M. 500 μ l of this solution are mixed with 300 μ l of a 3.33 mg/ml solution of NHS-biotin (Thermo Scientific) in DMSO (Sigma Aldrich). The reaction mixture is incubated for at least 2 h at room temperature.

In order to prove “biotinylation”, a SDS-PAGE gel is run. Samples to be tested are pure ELP, ELP functionalized with biotin, pure streptavidin and the mixtures of both types of ELP with streptavidin. Streptavidin itself runs according to its molar mass of about 60 kDa. Furthermore, one or two smaller fragments can be seen in the range of 35 kDa. Since streptavidin is a protein consisting of four subunits, those fragments might be assigned to dimers of two subunits. The ELP and biotinylated ELP differ only in the fact that pure ELP shows a much higher tendency to form dimers (interconnected by a dithiol-bond) than the biotin-functionalized one. The main band here is the one of the monomer with a molecular mass of 8000 Da. Mixing of unfunctionalized ELP with streptavidin and incubation in a conjugation buffer over night does not show any binding of the ELP to the protein. The observed bands look like mixtures of the bands for the pure reaction partners. In contrast, a mixture of biotinylated ELP with streptavidin shows a lot of additional bands, which might be due to binding of biotinylated ELP to streptavidin and streptavidin-subunit-fragments. Possible molecular masses are assigned in table C.12 and sketched in figure C.24.

Functionalization of particles with biotinylated ELP

In batch: Prior to incubation of gold nanoparticles with biotinylated ELP, unreacted NHS-biotin and DMSO are removed with a Zeba Spin Desalting Column 7K MWCO (Pierce). Thereafter, 100 μ l (biotinylated) ELP (125 μ M) and 100 μ l hydroxylamine (0.1 mM, Sigma Aldrich) are mixed with a pellet of gold nanoparticles gained from 1 ml of nanoparticle stock solution by centrifugation. The reaction mixture is incubated over night at 4 °C and cleaned the next day by adding 500 μ l of water, followed by centrifugation (2430 rpm, 5 min) and redispersion in water. In contrast to the pure ELP-functionalized particles, biotinylation of the ELP helps to stabilize the particle in solution, even for the higher molecular weights.

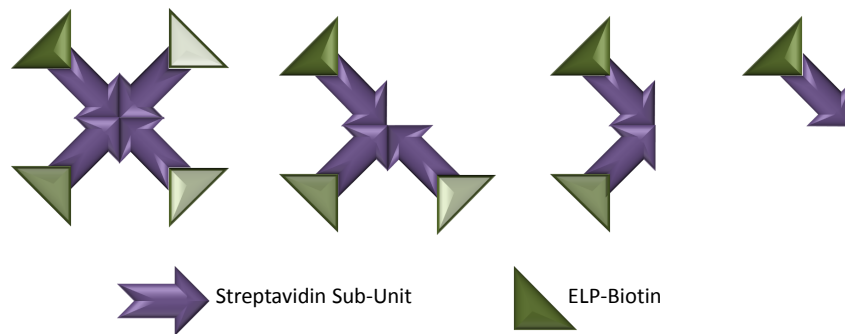


Figure C.24.: Streptavidin Binds Biotinylated ELP

Streptavidin (violet) consists of four subunits, each able to bind one biotinylated ELP (green). The scheme represents all possible configurations, if streptavidin-rupture and different numbers of bound ELPs are considered.

| Number Streptavidin Subunits | Number ELP | Final Molecular Mass (kDa) |
|------------------------------|------------|----------------------------|
| 1 | 1 | 23 |
| 2 | 1 | 38 |
| 2 | 2 | 46 |
| 3 | 1 | 53 |
| 3 | 2 | 61 |
| 3 | 3 | 69 |
| 4 | 1 | 68 |
| 4 | 2 | 76 |
| 4 | 3 | 84 |
| 4 | 4 | 92 |

Table C.12.: Possible Configurations upon Binding of Biotin-ELP to Streptavidin

C. Experimental Methods

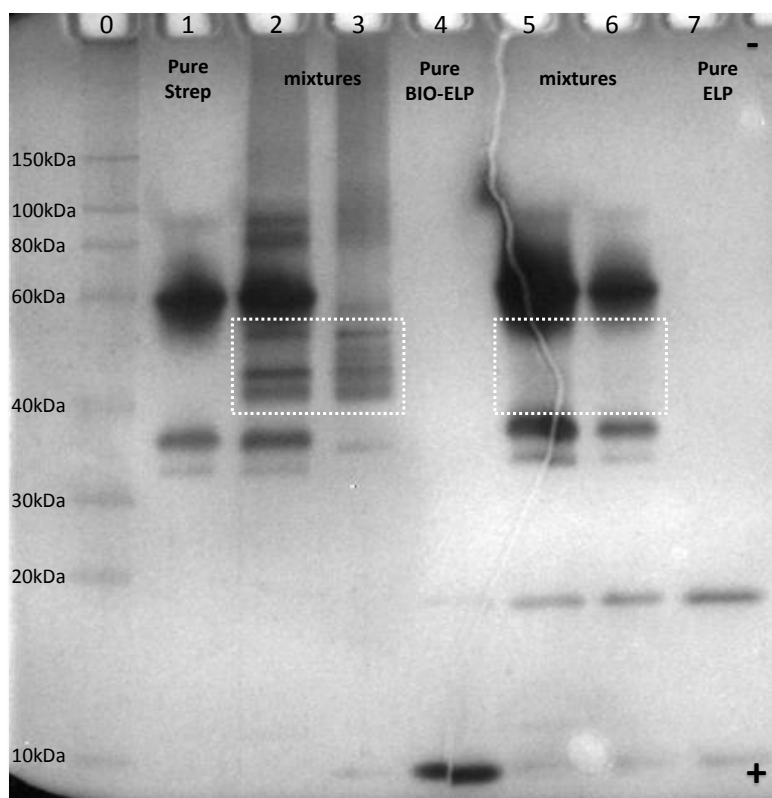


Figure C.25.: PAGE gel of ELP, Bio-ELP, and Streptavidin

Lane 1, 4, and 7 show pure streptavidin, pure biotin-ELP, and pure ELP. Lane 2 and 3 are mixtures of streptavidin and biotin-ELP in 3:2 and 6:1 ratios, lane 5 and 6 the same mixtures but with unfunctionalized ELP. Only the lanes 2 and 3 show additional bands that are attributable to streptavidin-biotin-ELP complexes. Lane 0 is the marker with assigned molecular masses.

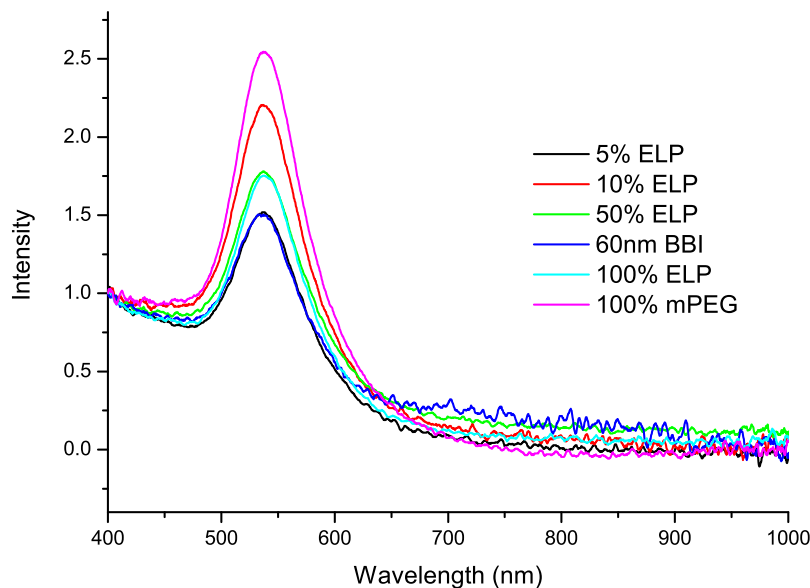


Figure C.26.: Spectra of ELP- and mPEG-Functionalized Spheres

UV-Vis spectra of 60 nm gold nanoparticles (blue) functionalized with different ratios of ELP (E4-20) and mPEG ($M_w = 750$ g/mol). No aggregation is observed.

Furthermore, different fractions of ELP are mixable with mPEG (Iris Biotech). For this purpose, mixtures of $125 \mu\text{M}$ mPEG and $125 \mu\text{M}$ biotinylated ELP prepared. $100 \mu\text{l}$ of this mixture are put together with $100 \mu\text{l}$ hydroxylamine (0.1 mM, Sigma Aldrich) and added to a pellet gained from centrifugation of 1 ml of nanoparticle stock solution (see description above). No aggregation is observed here as well. In an ensemble spectrum (figure C.26) the peak position stays constant, no red-shift is observed. The intensities are normalized to one at 400 nm.

By comparing the size of ELP and mPEG, one sees that the fraction of them from batch does not coincide with the fraction of surface of the nanoparticle covered by one or the other (see figure C.27).

Running an agarose gel of the functionalized particles shows that different fractions of ELP cause different running speeds. The distance observed in the agarose gel does neither depend linearly on the % ELP in batch, nor linearly on the % of surface covered by ELP (see figure C.28).

In the flow cell: Functionalization of gold nanoparticles with (biotinylated) ELP in a flow cell starts from “naked” gold nanoparticles immobilized on the glass surface via the introduction of 1 M NaCl. These particles are exposed to a mixture of $300 \mu\text{l}$ $125 \mu\text{M}$ (biotinylated) ELP in water, $3 \mu\text{l}$ of Tris(2-chlorethyl)phosphat (TCEP, 100 mM, Aldrich), and $100 \mu\text{l}$ of conjugation buffer. Two rinsing periods (5 min each) with this mixture are interrupted by two incubation periods (45 min each). Afterward, the flow cell is rinsed with a mixture of superbloc and conjugation buffer in a $60:40$ ratio to remove excess biotinylated ELP.

C. Experimental Methods

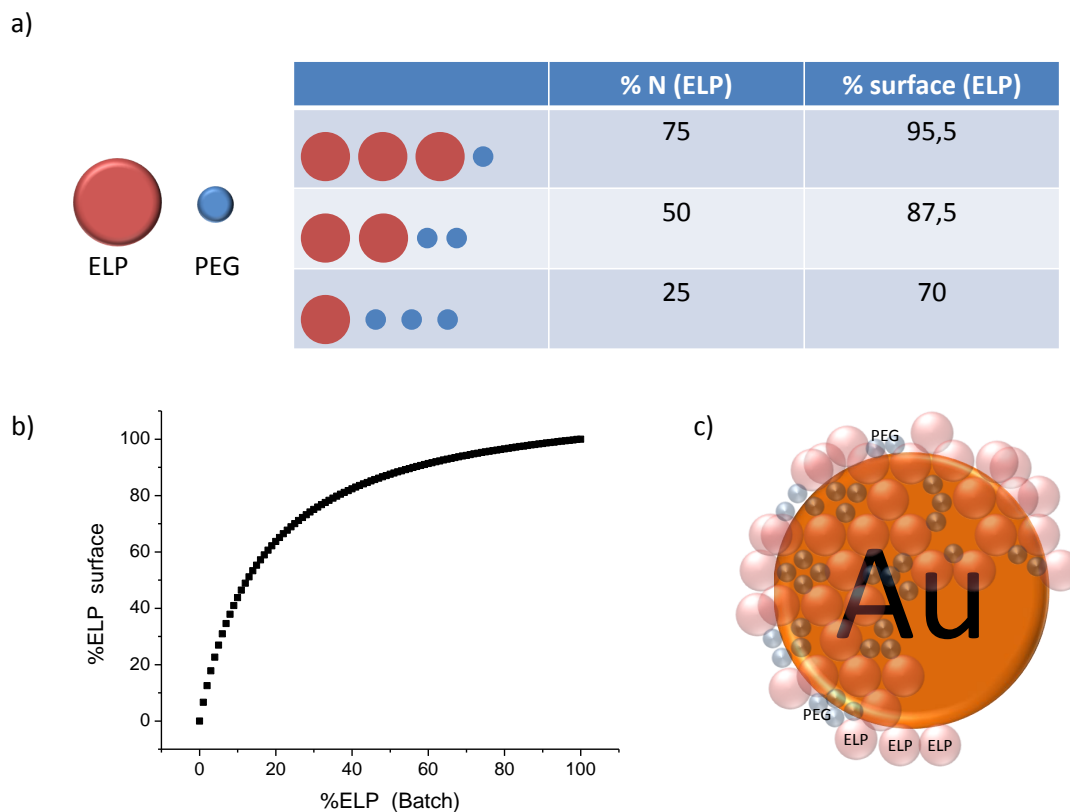


Figure C.27.: Batch and Surface % ELP

a) Since ELP ($R_h=2.7$ nm) is much bigger than the mPEG used here ($R_h=0.95$), the ratio/concentration in batch does not represent the % of the surface (of the gold nano particle) covered by ELP. b) The relation of % surface covered by ELP depends logarithmically on the % of ELP from batch. c) Sketch of mPEG and ELP covering a gold nano sphere. The sphere is not to scale.

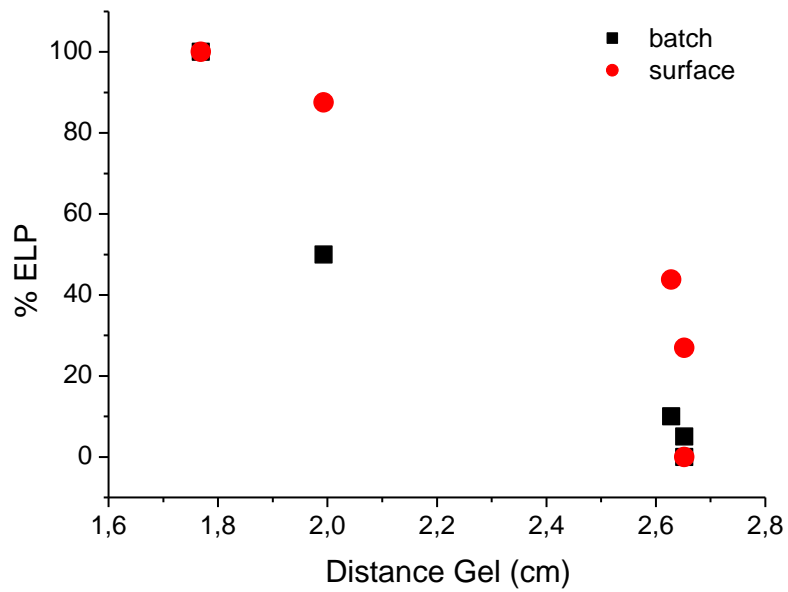
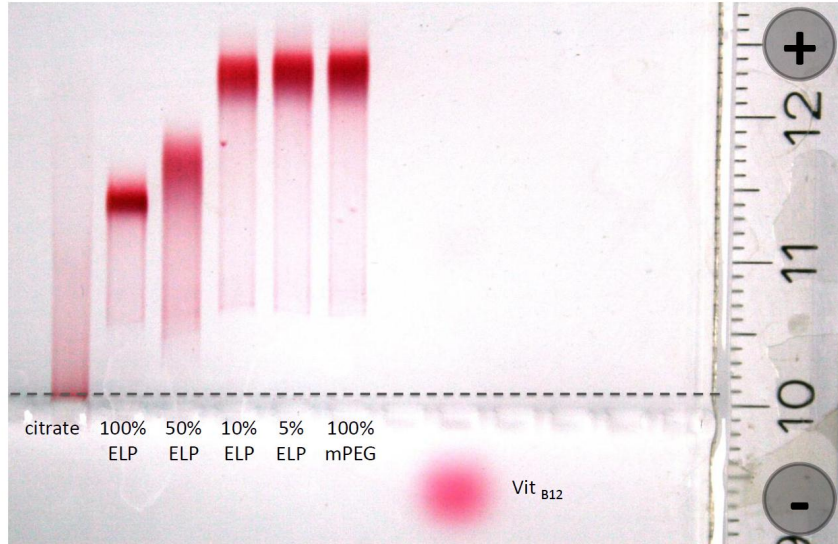


Figure C.28.: Agarose Gel of ELP/mPEG Functionalized Particles

Gel electrophoresis (0.5 % agarose gel, 0.5 x TBE, 150 V, 30 min) of 60 nm gold particles functionalized with different ratios of biotinylated ELP and mPEG. Neither the concentration of ELP in batch, nor the concentration on the surface does linearly depend on the distance traveled in the gel.

C.5. Dimers

C.5.1. Synthesis in Batch

In principle it is possible to form two different kinds of dimers, consisting either of two equally functionalized particles connected via a linker that binds both particles (homodimers), or of two oppositely functionalized ones (heterodimers).

Heterodimers (Biotin-Streptavidin)

For the formation of dimers in batch, 2 μl of streptavidin-modified gold nanoparticles are mixed with 2 μl Biotin-PEG gold nanoparticles and 2 μl conjugation-buffer (in the case of high-molecular weight PEGs) or 2 μl deionized water (low-molecular weight PEG). The mixtures are incubated at least over night at room-temperature under shaking. For the preparation of TEM-grids, 4 μl deionized water are added.

Homodimers (Biotin-Streptavidin-Biotin)

In order to link two PEG-Biotin functionalized gold nanospheres, 20 μl of functionalized gold nanospheres ($C=1.17 \cdot 10^{-9}\text{M}$) are mixed with 10 μl $1.17 \cdot 10^{-7}\text{M}$ streptavidin in water. This reaction mixture is incubated over night at room temperature.

C.5.2. Synthesis in the Flow-Cell

Self-built flow cells consist of UV-cleaned (15 minutes, Navascan PSD-UV) glass slides (Vitro-tubes, 0.1x2 mm), which are connected to a PE-tubing on both sides, sealed with epoxy-glye. Using this cell-setup, a flow can simply be exerted by gravitational forces.

PEG-Dimers

Fast but dirty method: Prior to the introduction of any particle into the flow-cell, it is washed with deionized water for 5 minutes. PEG-biotin-modified spheres are diluted 1:100 in deionized water and flown through the cell for 3-4 minutes. In order to immobilize them on the surface, 1 M sodium chloride (NaCl, Ambion) solution is introduced until the particles settle down. In the next step the glass-surface is passivated with a mixture of superbloc (Pierce) and conjugation buffer (2.5 mM Tris-HCl pH 7.5, 0.25 mM EDTA, 0.5 M NaCl, 0.025 % Tween 20, all Sigma) in a 60:40 ratio. The passivation is done within 1 hour, while 10 minutes of flow alternate twice with 20 minutes of rest periods. At this stage, true color images and single-particle spectra are acquired. A 1:50 dilution of streptavidin-modified particles in a 60:40 mixture of superbloc and conjugation buffer is introduced in the flow cell. Flow- and rest periods rotate in 2 minute time intervals 2 times. Unbound particles are removed by rinsing 10 minutes with a 60:40 mixture of superbloc and conjugation buffer. A second set of true color images and single-particle spectra is recorded.

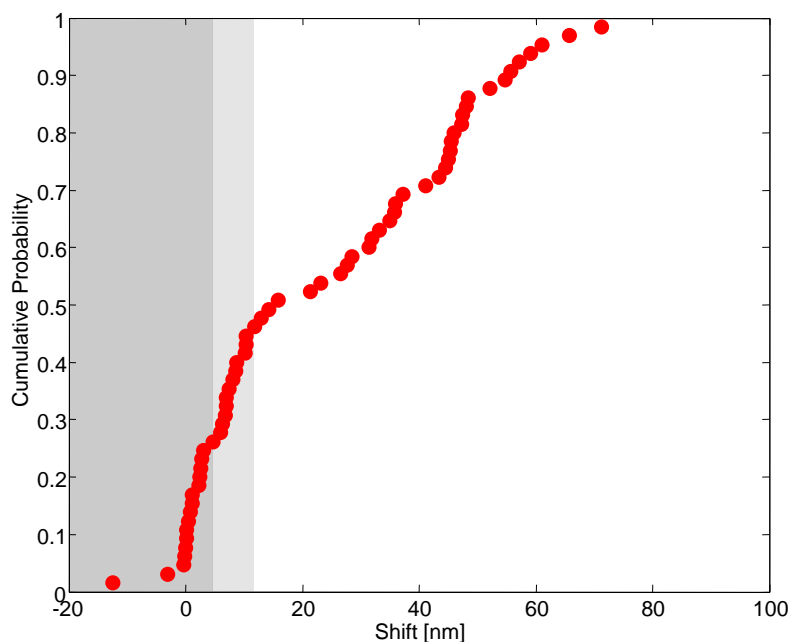


Figure C.29.: Typical Dimerization Experiment

Cumulative probability of the shifts observed for a typical dimerization experiment with biotin-PEGylated 60 nm gold spheres as first, and streptavidin-functionalized 60 nm gold spheres as second particles. Some particles do not form dimers at all (dark gray). A minor fraction of spheres (light gray) shows a small shift that is attributed to the binding of free streptavidin. The majority of the particles (white) shows a shift between 10 and 80 nm due to the formation of dimers. All shift are compared to monomers in conjugation buffer.

Clean but slow method: In contrast to the “fast-but-dirty” method, the streptavidin particles serve here as the first particles. They are diluted 1:100 in deionized water and flown through the flow cell for some minutes. Even without the addition of salt, particles settle down on the surface. Surface-passivation is done as described before. A 1:50 dilution of PEG-biotin modified nanoparticles in a 60:40 mixture of superbloc and conjugation buffer form dimers while flowing two times for 2 min and resting 2 h in between. Since this method is much more time-consuming but does not have relevant advantages compared to the first one, it is not explored further.

Figure C.29 shows an example of a typical dimerization experiment using Biotin-PEG as linker. Some of the monomers do not shift at all (dark gray). This is not a problem but in contrast they are a useful internal standard for later experiments concerning distance and refractive index changes within the dimers. Furthermore, a part of the monomers shows a very small shift (light gray), which might be due to binding of free streptavidin. This fraction is bigger if un-washed streptavidin particles are used and almost vanishes when the streptavidin-particles are carefully cleaned.

The surface coverage before and after dimerization does not significantly increase (from 0.0137 to 0.0166 part/ μm^2), while the yield of dimerization is about 80 %.

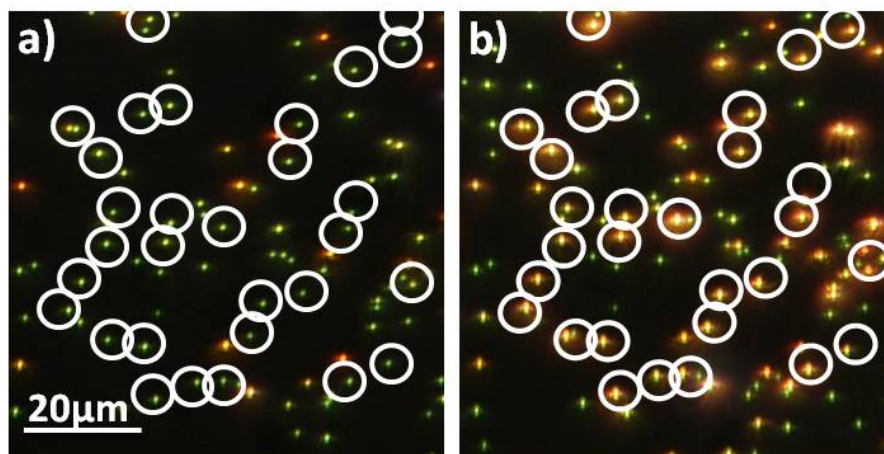


Figure C.30.: Yield and Surface Coverage by Counting

True color images of biotin-PEGylated 60 nm gold spheres in a dark-field microscope before (a) and after (b) dimerization. The yield counts to 80 % while the surface coverage stays low.

ELP-Dimers

After functionalization of the gold nanospheres with biotinylated ELP and passivation of the free surface (see above), true color images and single-particle spectra are acquired. A 1:50 dilution of streptavidin-modified particles in a 60:40 mixture of superbloc and conjugation buffer is introduced in the flow cell. 2 flow- periods of 10 minutes alternate with 2 rest-periods of 20 minutes. Unbound particles are removed by rinsing 10 minutes with a 60:40 mixture of superbloc and conjugation buffer. A second set of true color images and single-particle spectra is recorded.

C.5.3. Sensing with Dimers

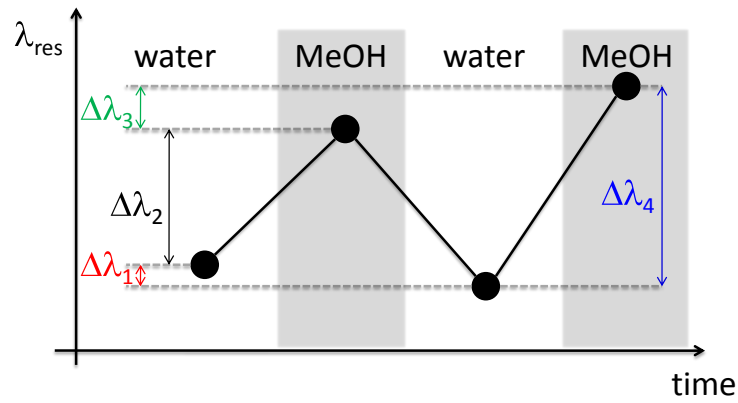
Sensing distance changes by methanol

After measuring the dimers in water, methanol is flown in for 10 minutes and the dimers are measured again. Thereafter, water is flown for 10 minutes and a second water measurement is done. One can see that the dimers shift back almost completely (see red dots figure C.31). A second methanol-measurement does not end at the same resonance position as the first one but is in mean shifted by 4 nm to lower wavelengths. Therefore, the distance change between the dimers seems not to be completely reversible. Also the shift between water and MeOH is different from the first (black dots, figure C.31) to the second (blue dots figure C.31) cycle, indicating that additional things might happen.

Sensing refractive index changes

The environment of the dimers is changed to higher refractive indices by sucrose, glucose and glycerol (all $n=1.41$). The new medium is introduced by flowing the solution for 10 minutes and measuring thereafter. In order to ensure that the linker molecule doesn't change, a second

a)



b)

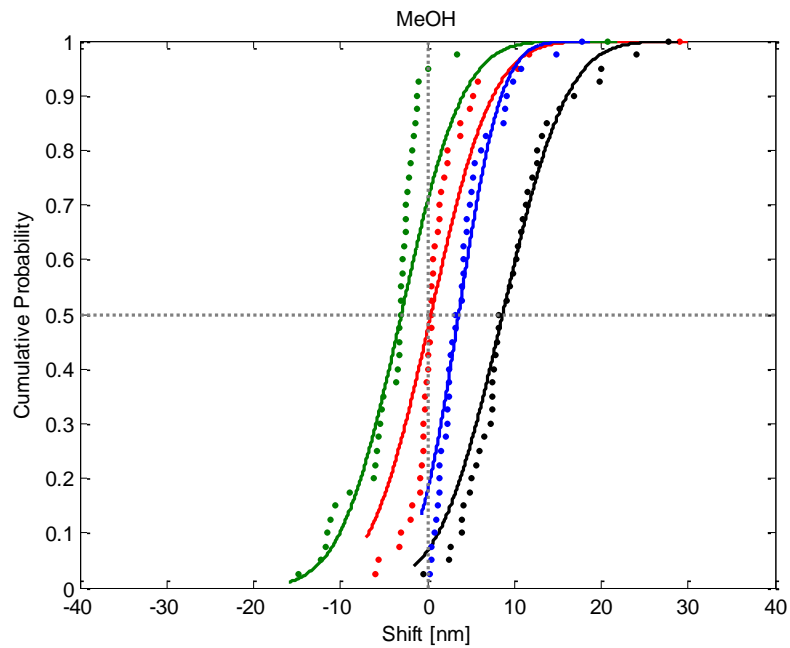


Figure C.31.: Reversibility Methanol

a) Principle of the reversible distance-change experiment. b) Shift observed for dimers used in two cycles of a distance-sensing experiment. The reversibility between the first and second water measurement (red) is good (zero shift), while the difference between the two methanol measurements (green) is bigger. Also the measured shifts between water and methanol (black and blue) differ, representing not 100 % reversibility.

C. Experimental Methods

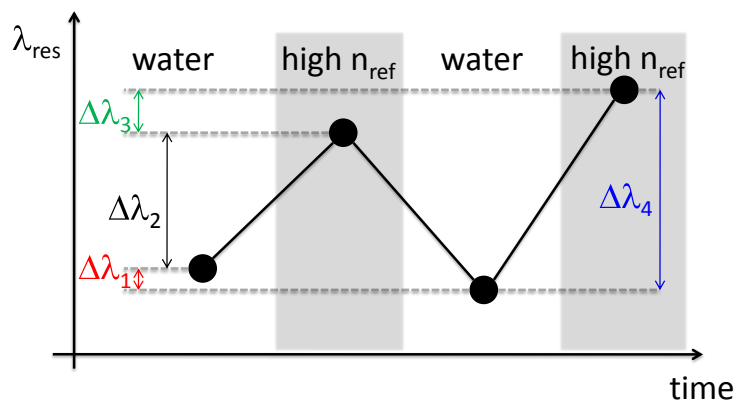


Figure C.32.: Principle of Reversibility Measurement

In order to check for reversibility, two cycles of water and higher refractive index measurements are recorded.

measurement in water and the higher refractive index solvent is done. For all three solutions a good reversibility is achieved, concerning both, shift between water and higher refractive index and comparison between two measurements in the same environment. Furthermore, all solutions show a shift of ~ 7 nm, indicating that the dimers behave very similar in all environments.

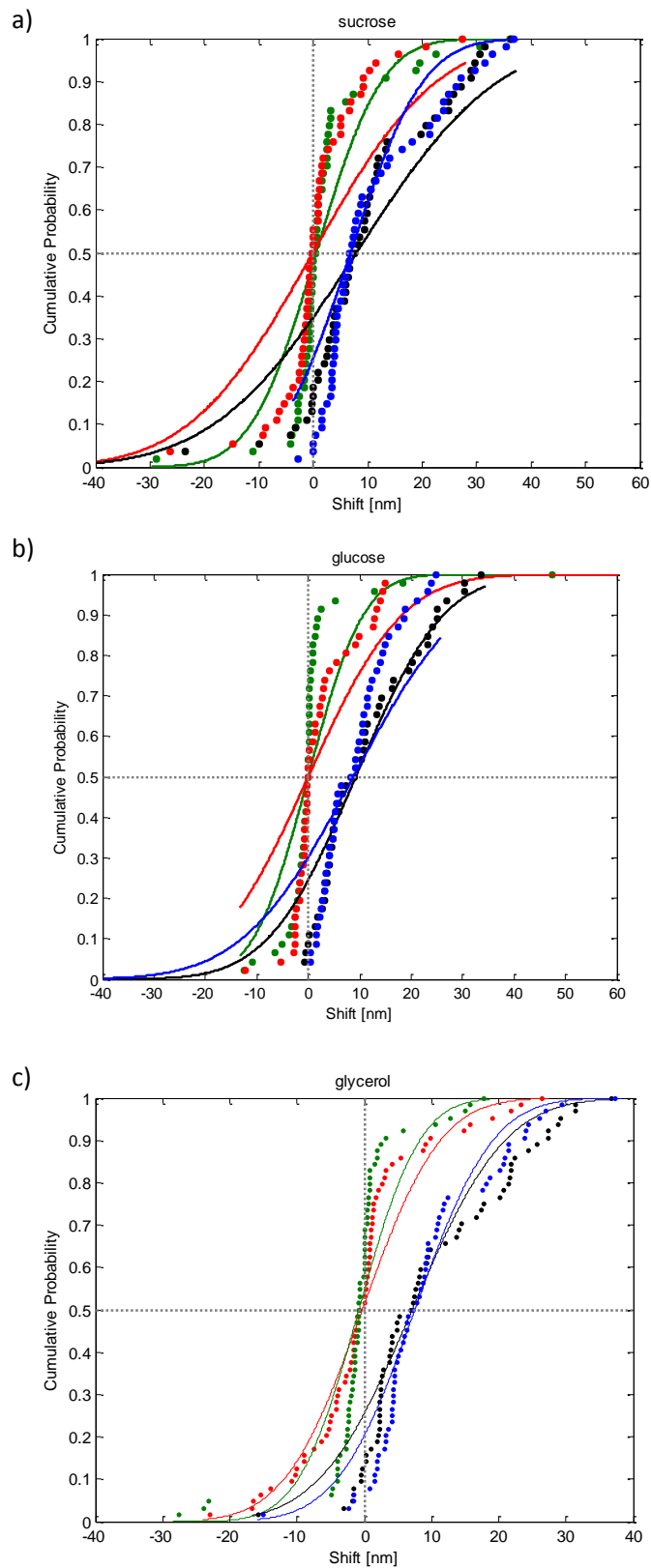


Figure C.33.: Reversibility Sucrose, Glucose and Glycerol

Repeated measurements of dimers in water and higher refractive index media ($n=1.41$, a) sucrose, b) glucose, c) glycerol) show that the reversibility (shift between two water (red) or two higher refractive index media (green) measurements) as well as the sensitivity (shift between water and the second media, black and blue) are good.

Sensing ELP conformational changes

In order to induce a change in the conformation of ELP and with this simultaneously a change in the interparticle distance, the dimers are exposed to a different temperature. In order to change the environment of the dimers from room temperature water to ice-water ($\sim 4^\circ\text{C}$), a syringe pump is connected to one end of the flow cell, while the other end is immersed in an ice-water reservoir. With a flow speed of 3 ml/min, the ice-water is pulled through the flow cell. This high flow-speed ensures that the water does not heat extensively while running through the tubings and cell, seen by condensing water on the outside of the flow cell. After 5 minutes of flow, spectra are recorded while flowing ice-water. In order to exclude effects due to the flow itself, as comparison also spectra under the same flow conditions but with room temperature water are recorded as well. Since water is condensing on the outside of the flow-cell, oil-immersion condenser *and* objective are used (see figure C.34).

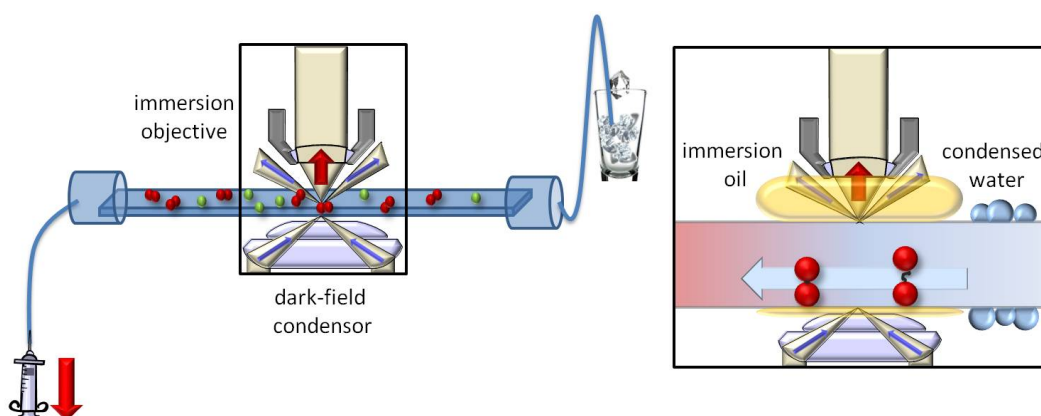


Figure C.34.: Introducing the system

In order to avoid condensation of water on the outside of the flow cell while 4°C water is flown through, oil-immersion condenser *and* objective are used.

C.5.4. TEM

TEM

Not all spheres that build dimers are perfectly spherical. As seen by TEM experiments, the aspect ratio distribution shows a tail up to an aspect ratio of 1.4, while the distribution of the mean diameter centers around 57 nm.

TEM-experiments can also be used to determine the yield of dimerization in batch. For this purpose, after forming dimers in batch (see above), 5-7 μl of the concentrated solution are dried on the carbon coated copper TEM grid (Plano). In order to avoid dimerization or aggregation due to gravitational forces, the washing step used in a “usual” TEM-grid preparation (involving centrifugation) is skipped. That’s probably the reason why in some parts of the TEM grid “dirt” (organic remaining) can be found next to the particles. Thereafter, images of the samples are

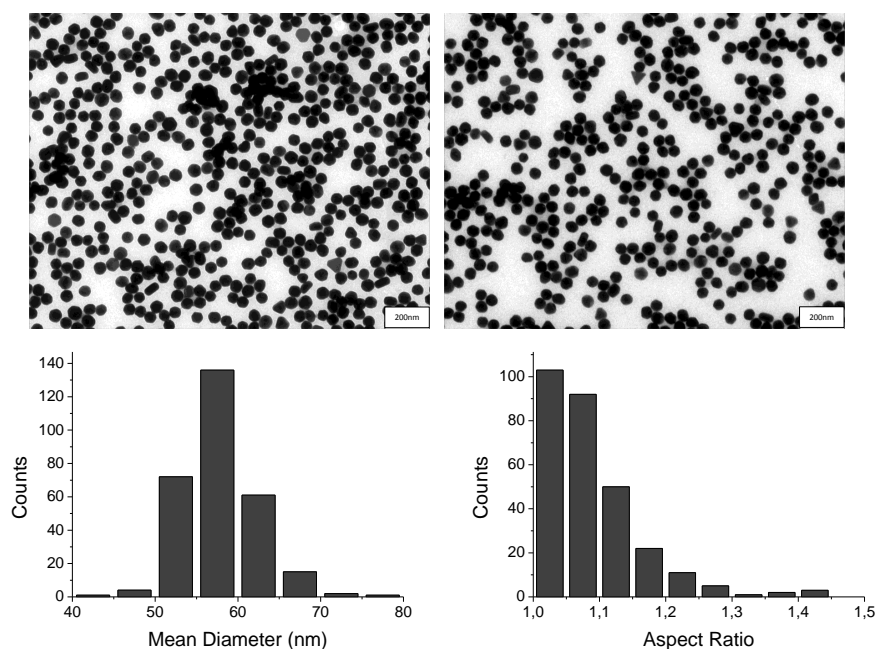


Figure C.35.: TEM-images of the 60nm Gold spheres

TEM images show that the spherical gold spheres show a mean diameter of 57 nm and an aspect ratio of up to 1.4 .

taken and the occurrence of the different species (monomers, dimers, trimers...) is evaluated. In the sample with the highest dimer yield, ~20% of dimers were formed.

Cryo-TEM

In contrast to standard TEM-techniques, which include drying of the sample, Cryo-TEM is a technique that allows to resemble conditions similar to those in solution or in a flow cell. The dimers are created in solution (see above “dimers in batch”) and vitrified on the TEM grid without any further treatment. For this purpose a vitrobot (FEI) is used. The TEM-grids (Quantifoil ‘Holey Carbon Films’ R2/1) are plasma-cleaned (30s, Ar) prior to use. The atmosphere in the vitrobot-preparation chamber is set to 20 °C and 80-100 % humidity. The applied sample volume is 5 μ l. Quick-freezing of the sample is done in condensed propane. The measured distance in between the particles can be attributed to be the “real” distance in solution.

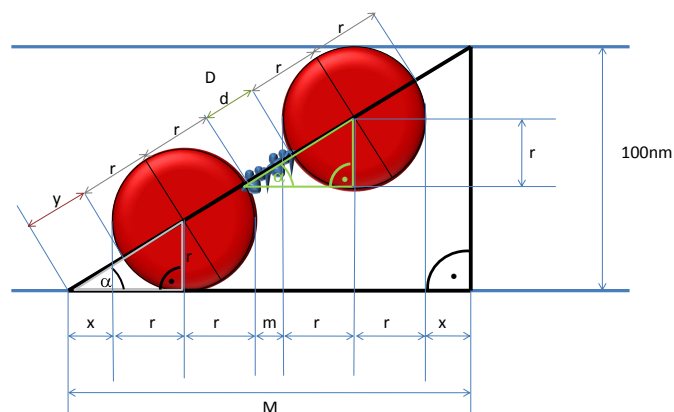


Figure C.37.: Evaluation of Cryo-TEM Images
Schematic representation of the evaluation of cryo-TEM data. The projection “m” of the distance between the particles is converted into the real distance “d” via geometrical relations.

Since TEM-images always show only the projection and tilting experiments were not done for

C. Experimental Methods

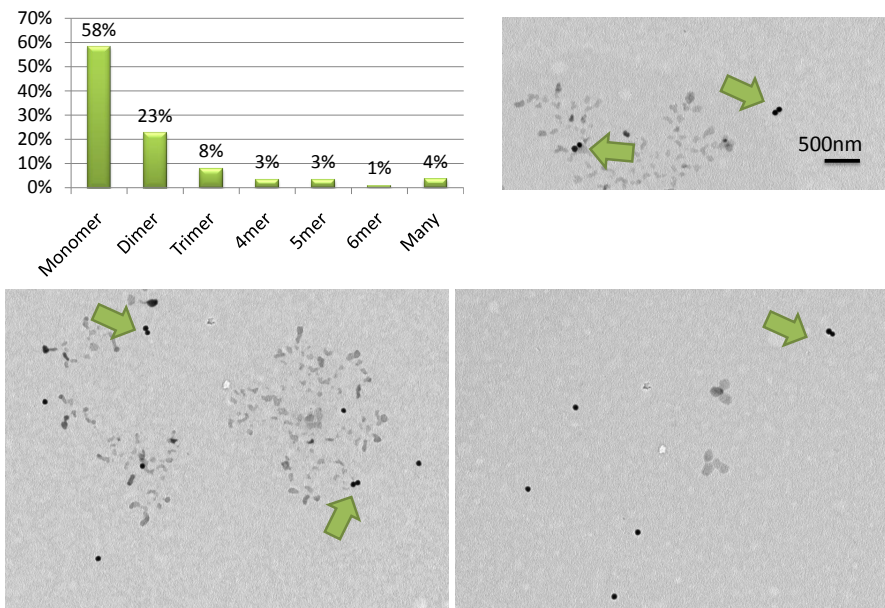


Figure C.36.: Yield of Dimers by TEM

The yield of dimerization in batch can be evaluated by counting the dimers in various TEM images. In the best case, a yield of 23 % of dimers could be achieved.

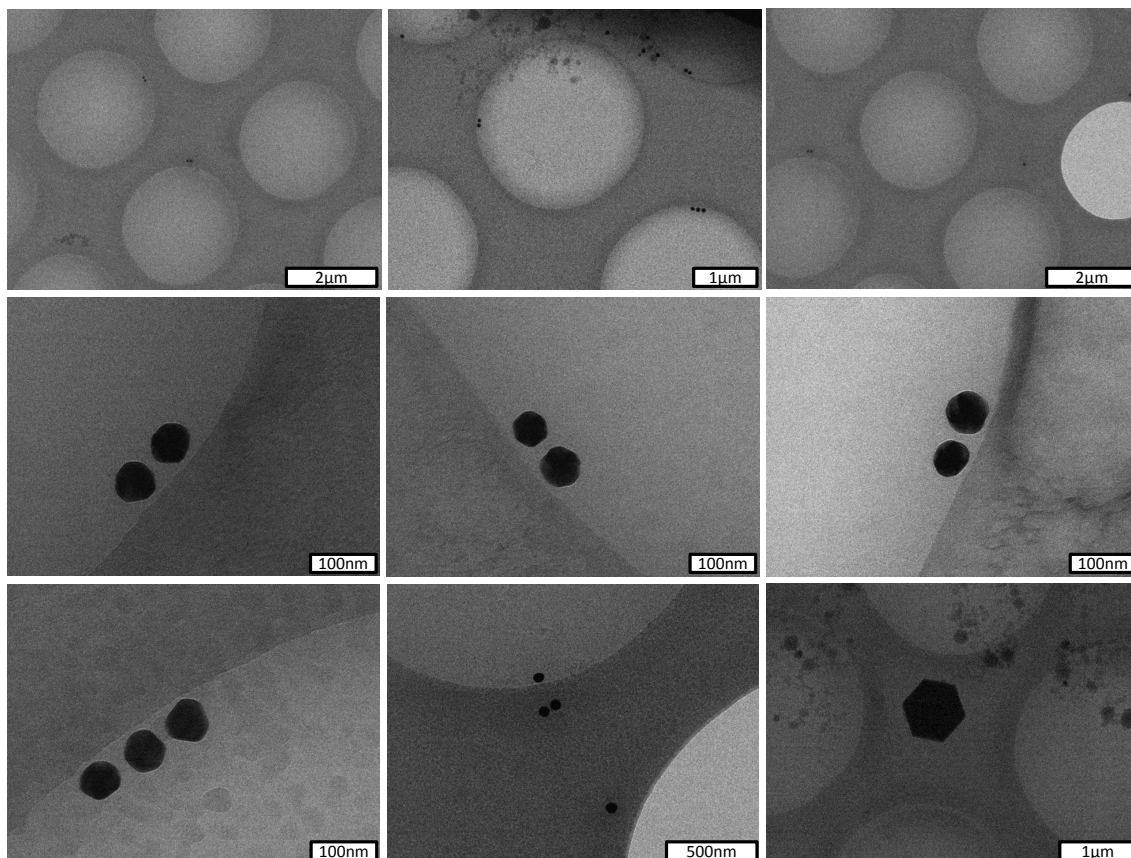


Figure C.38.: Cryo-TEM images

Overview of cryo-TEM images showing monomers, dimers, and trimers of 60 nm gold spheres linked by PEG-Biotin-Streptavidin. Also visible is the holy carbon grid as well as an ice-crystal in the last image.

all dimers, evaluation of the measured distances has to be done carefully. The film-thickness is set to 100 nm and for a given distance between two 60 nm spheres, the maximum angle (α_{\max}) of possible tilting in that film without exposing a sphere outside the film is calculated. All angles between 0° and α_{\max} are set to have the same probability. For the fixed distance all projections are calculated and the median is determined. This median is compared to the median of the measured distribution of distances. By this, the “real” distance could be evaluated. For the sample with the lowest shift in resonance, the yield of dimers in solution was too low to see them in the cryo-TEM experiments.

C. Experimental Methods

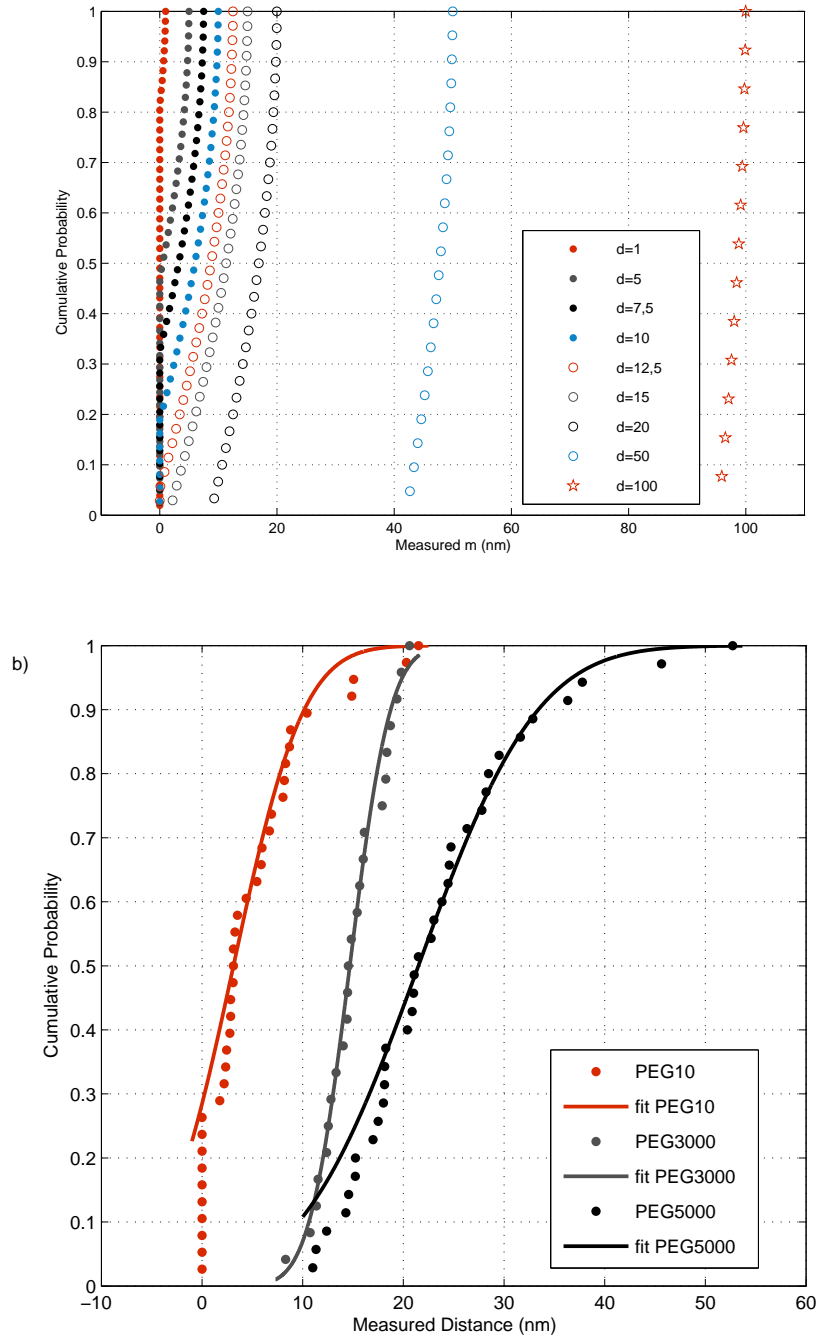


Figure C.39.: Convert measured to real distance

a) Simulated cumulative probability of measured projections "m" of dimers for different given real distances "d". b) Measured cumulative probabilities of projections "m" from cryo-TEM experiments of different linkers.

C.5.5. DLS of monomers

Dynamic light scattering experiments of the monomers (60 nm gold nanospheres coated with streptavidin or biotin-PEG) are performed by Dr. Frauke Kühn (working group of Prof. Dr. Manfred Schmidt, University of Mainz). Due to low yield of dimers in solution (maximum 20 %),

| M _w PEG (g/mol) | m (nm) | d (nm) |
|-------------------------------|--------|--------|
| 683 | 5.7 | 7.1 |
| 3000 | 14.7 | 18.9 |
| 5000 | 21.5 | 25.3 |

Table C.13.: Distances PEG

| Coating | R _h (nm) |
|--------------|---------------------|
| Citrate | 41.1 |
| Streptavidin | 52.9 |
| PEG-3000 | 42.7 |
| PEG-5000 | 46.1 |

Table C.14.: DLS Data of Monomers

it is not possible to directly do DLS on the dimers. Furthermore, this would in the best case lead to the hydrodynamic radius (R_h) of a dimer, but not directly to the distance between two particles. PEGylated and streptavidin-functionalized particles are measured as well as citrate-stabilized spheres. The latter one serves as reference specimen to calculate the thickness of PEG- or Streptavidin-layer. From the difference between R_h (functionalized) and R_h (citrate), distances of the dimers are calculated by adding up the proper linker-sizes. Since the spheres functionalized with the smallest Biotin-PEG-derivative don't allow for filtration through a syringe filter, no DLS experiment could be performed with them.

C.6. Core-Satellite Assemblies

For the synthesis of flower-like structures, the core particle is functionalized with dithiol-PEG ($M=5000$ g/mol). 1 ml of the citrate stabilized particles (60 nm diameter, BBI) is centrifuged with a speed of 6000 g for 10 min. After removing the supernatant, 100 μ l of a 2 mM dithiol-PEG solution are added and the reaction mixture is incubated over night. The PEGylated particles are cleaned in one washing step, adding 400 μ l water and centrifuging at 6000 g for 10 minutes. The pellet is resuspended in 10 μ l water and mixed with 1 μ l hydroxylamine (100 mM) in order to break possible dithiol bonds. Then 10 μ l of 50 x concentrated 20 nm citrate spheres are added and incubated for 1 hour.

Ensemble-Spectrum

In the ensemble spectrum a shift of 17 nm to higher wavelengths is observed upon formation of the flowers. Additionally, an increase of the peak-width is observed, possibly due to multi-core assemblies.

C. Experimental Methods

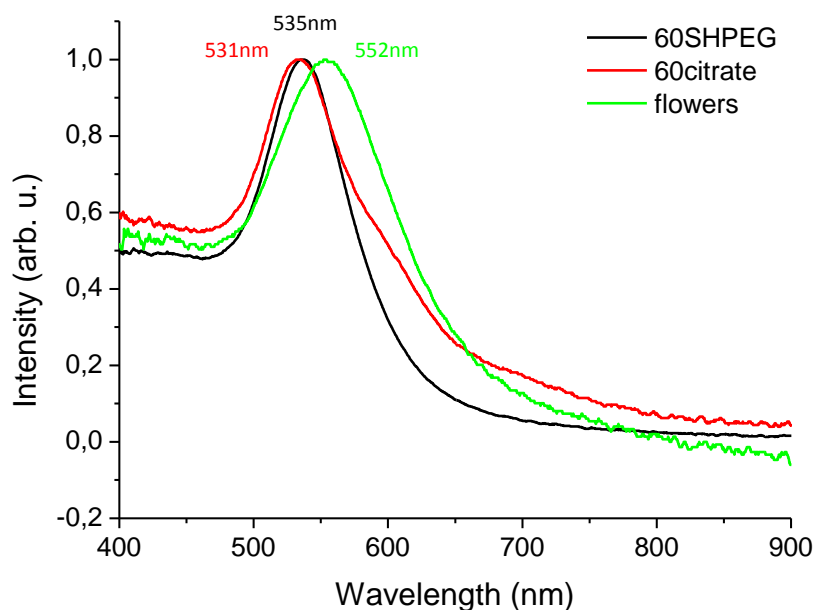


Figure C.40.: Ensemble Spectra of Spheres and Flowers

Ensemble spectra of citrate (red) and SH-PEG-coated (black) 60 nm gold spheres as well as of flower-like assemblies (green), which show a shift to higher wavelengths.

TEM-images

A TEM image of the samples shows that mainly core-satellite structures with one core are produced. The satellites are clearly visible and tend to arrange on the sides of the core (possibly due to drying). Sometimes they are found above (or below) the core.

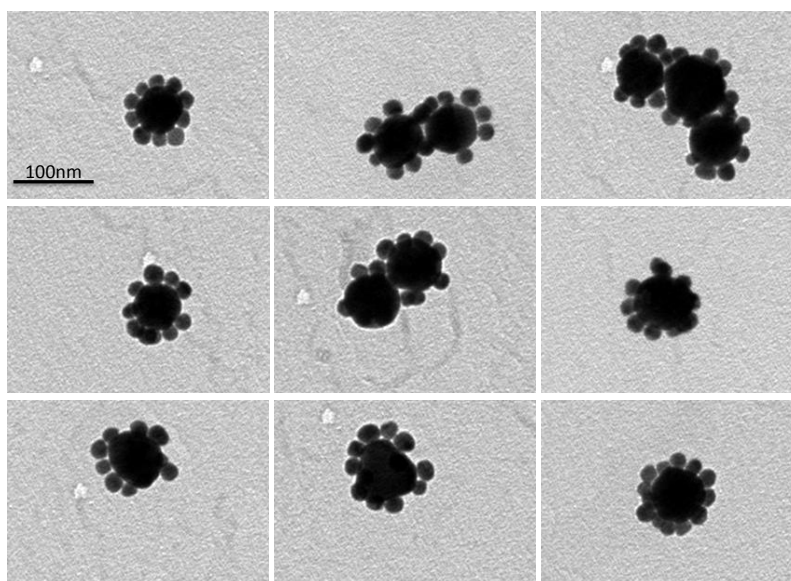


Figure C.41.: TEM Images of Flower-Like Structures

Representative TEM-images of flower-like assemblies. Most of the assemblies show single-cores. The satellites are found around the core, sometime on top or below. The scalebar (100 nm) is the same for all images.

Gel-Electrophoresis

The as-synthesized flower samples can be separated via an agarose gel-electrophoresis. Instead of casting a gel with only one pocket, a second (“collection”) pocket is introduced, from which the samples can be collected at different times. Lane B figure C.42 shows a sample that was already collected at several times. One can see that the remaining sample runs after the pocket in the same manner as before, the collected parts can be seen as “empty” parts in the lane. Lane A is the sample used for the single particle investigation in chapter 6.2.1, lane C and D show the 20 nm citrate and 60 nm dithiol-PEG particles.

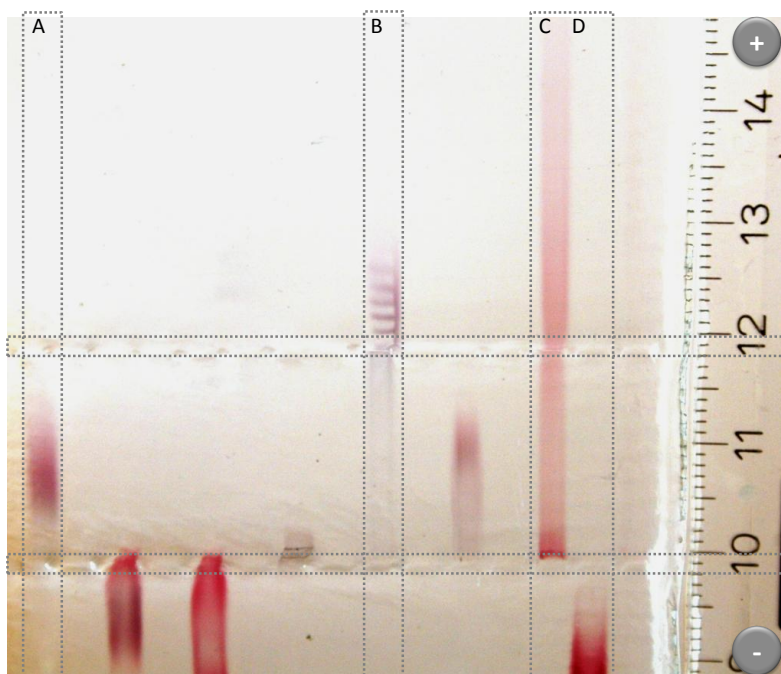


Figure C.42.: Separation Gel

Agarose gel-electrophoresis of the flower-like assemblies (lane A) as well as of the pure cores (lane D) and pure satellites (lane C). One can see the starting pockets (~ at the 10 cm mark) and the collection pockets (~ at the 12 cm mark). The sample in lane B was already collected at several times, left over sample is running further.

After the collection from the gel, TEM images are taken from three fractions collected from the gel, A1 being the fastest running species, A3 the slowest one. One can see that the number of small satellites per core is more or less constant while the slower running fractions show a tendency to have more core particles per assembly.

C. Experimental Methods

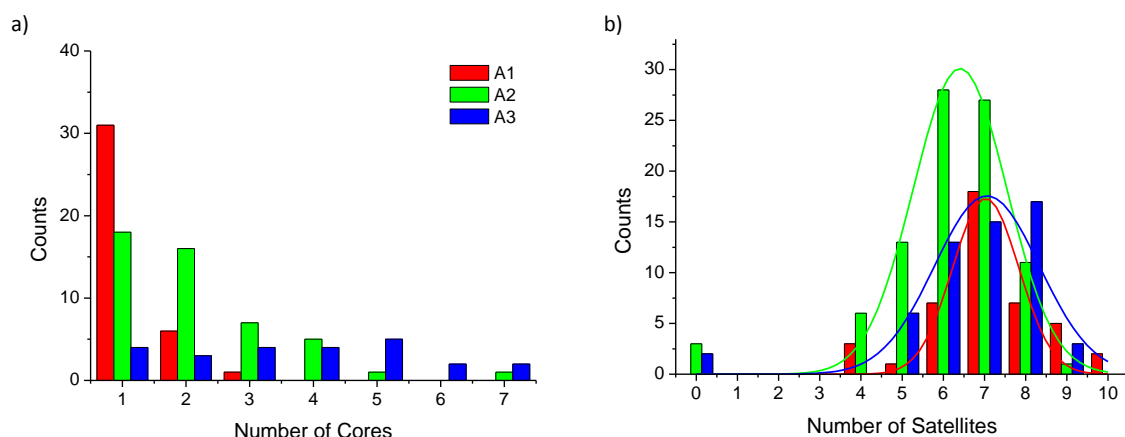


Figure C.43.: Number of Cores and Satellites after Gel-Electrophoresis

By counting TEM-images with more than 100 assemblies, the number of cores per assembly (a) and the number of satellites per core (b) is determined. While the fastest fraction (A1) shows mainly single-core structures and the slowest one (A3) has a significant amount of multi-core ones, no trend can be seen in the number of satellites per core.

Different % Dithiol-PEG

Different ratios of dithiol- to monothiol-PEG do not show any effect on the number of satellite or core particles.

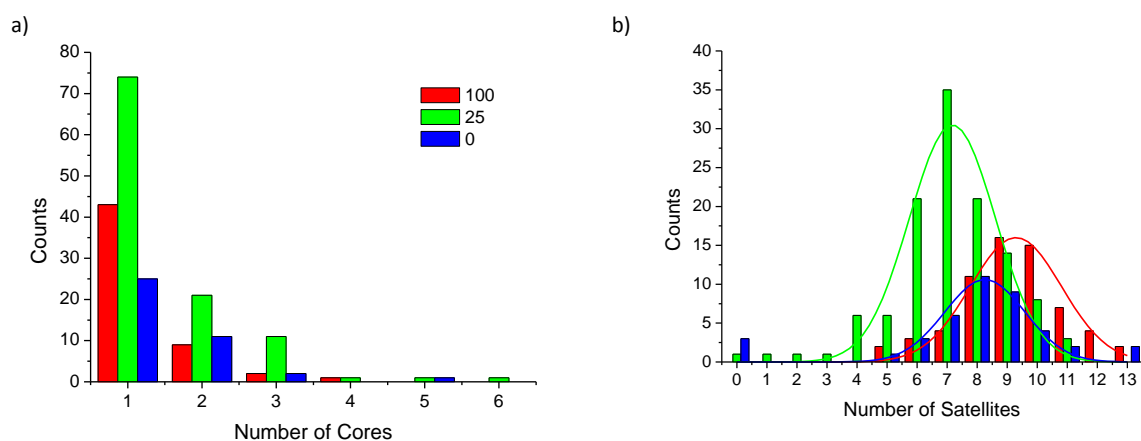


Figure C.44.: Number of Cores and Satellites for Different % Dithiol-PEG

Doing statistics on assemblies counted on TEM-images, the number of cores per assembly (a) and the number of satellites per core (b) is determined. Neither for the number of cores, nor for the number of satellites, a major difference between the different fractions of PEG is found.

BEM-simulations

BEM-simulations of flowers (performed by Dr. Jan Becker, working group of Prof. Dr. Carsten Sönnichsen) show the following results:

| $r_{\text{core}}(\text{nm})$ | $r_{\text{core}}(\text{nm})$ | n_{sat} | $d_{\text{sat}}(\text{nm})$ | $\lambda_{\text{res,water}}(\text{nm})$ | S (nm/RIU) |
|------------------------------|------------------------------|------------------|-----------------------------|---|--------------|
| 60 | 20 | 0 | – | 541.6 | 97 |
| 60 | 20 | 6 | 5 | 564.6 | 151 |
| 60 | 20 | 6 | 4 | 568.7 | 150 |

Table C.15.: BEM-Simulations of Core-Satellite Structures

References

- Ah, Chil Seong, Hong, Seung Do, & Jang, Du-Jeon. 2001. Preparation of Au-core-Ag-shell Nanorods and Characterization of Their Surface Plasmon Resonances. *The Journal of Physical Chemistry B*, **105**(33), 7871–7873.
- Ahmed, Z., Gooding, E. A., Pimenov, K. V., Wang, L. L., & Asher, S. A. 2009. UV Resonance Raman Determination of Molecular Mechanism of Poly(N-isopropylacrylamide) Volume Phase Transition. *Journal of Physical Chemistry B*, **113**(13), 4248–4256.
- Aizenberg, J., Tkachenko, A., Weiner, S., Addadi, L., & Hendler, G. 2001. Calcitic microlenses as part of the photoreceptor system in brittlestars. *Nature*, **412**, 819–822.
- Alexandridis, Paschalis, Ivanova, Rouja, & Lindman, Björn. 2000. Effect of Glycols on the Self-Assembly of Amphiphilic Block Copolymers in Water. 2. Glycol Location in the Microstructure. *Langmuir*, **16**, 3676–3689.
- Ando, Isao, Chofuku, Hiroshi, Ujimoto, Kikujiro, & Kurihara, Hirono. 1997. Activation of a Gold Electrode for the Oxidation of L-Ascorbic Acid. Adsorbed Substrate as a Catalyst. *Bulletin of the Chemical Society of Japan*, **70**, 2187–2192.
- Anker, J. N., Hall, W. P., Lyandres, O., Shah, N. C., Zhao, J., & Van Duyne, R. P. 2008. Biosensing with plasmonic nanosensors. *Nature Materials*, **7**(6), 442–453.
- Aswal, V. K., & Goyal, P. S. 1998. Mixed micelles of alkyltrimethylammonium halides - A small-angle neutron-scattering study. *Physica B*, **245**, 73–80.
- Atkins, Peter, & de Paula, Julio. 2006. *Atkins's Physical Chemistry*. Oxford.
- Baciu, Cristina L., Becker, Jan, Janshoff, Andreas, & Sönnichsen, Carsten. 2008. Protein-Membrane Interaction Probed by Single Plasmonic Nanoparticles. *Nano Letters*, **8**, 1724–1728.
- Barron, Annelise E., & Blanch, Harvey W. 1995. DNA Separations by Slab Gel, and Capillary Electrophoresis: Theory and Practice. *Separation and Purification Methods*, **24**, 1–118.
- BBInternational. <http://www.bbigold.com/>. <http://www.bbigold.com/>.
- Becker, Dr. Jan. 2010. *Plasmons as Sensors*. Ph.D. thesis, Johannes-Gutenberg-Universität Mainz.

REFERENCES

- Becker, J., Schubert, O., & Sönnichsen, C. 2007. Gold nanoparticle growth monitored in situ using a novel fast optical single-particle spectroscopy method. *Nano Letters*, **7**, 1664–1669.
- Becker, J., Trügler, A., Jakab, A., Hohenester, U., & Sönnichsen, C. 2010. The Optimal Aspect Ratio of Gold Nanorods for Plasmonic Bio-sensing. *Plasmonics*, **5**(2), 161–167.
- Becker, Jan, Zins, Inga, Jakab, Arpad, Khalavka, Yuriy, Schubert, Olaf, & Sönnichsen, Carsten. 2008. Plasmonic Focusing Reduces Ensemble Linewidth of Silver-Coated Gold Nanorods. *Nano Letters*, **8**, 1719–1723.
- Bek, Alpan, Jansen, Reiner, Ringler, Moritz, Mayilo, Sergiy, Klar, Thomas A., & Feldmann, Jochen. 2008. Fluorescence Enhancement in Hot Spots of AFM-Designed Gold Nanoparticle Sandwiches. *Nano Letters*, **8**, 485–490.
- Berr, S., Jones, R. R. M., & Johnson, J. S. 1992. Effect of Counterion On the Size and Charge of Alkyltrimethylammonium Halide Micelles As A Function of Chain-length and Concentration As Determined By Small-angle Neutron-scattering. *Journal of Physical Chemistry*, **96**, 5611–5614.
- Bohren, Craig F., & Huffman, Donald R. 1983. *Absorption and Scattering of Light by Small Particles*. Wiley-Interscience.
- Brigger, Irène, Dubernet, Catherine, & Couvreur, Patrick. 2002. Nanoparticles in cancer therapy and diagnosis. *Advanced Drug Delivery Reviews*, **54**(5), 631 – 651.
- Brown, L. V., Sobhani, H., Lassiter, J. B., Nordlander, P., & Halas, N. J. 2010. Heterodimers: Plasmonic Properties of Mismatched Nanoparticle Pairs. *Acs Nano*, **4**(2), 819–832.
- Bryant, Garnett W., Garcia de Abajo, F. Javier, & Aizpurua, Javier. 2008. Mapping the Plasmon Resonances of Metallic Nanoantennas. *Nano Letters*, **8**(2), 631–636.
- Campion, A., & Kambhampati, P. 1998. Surface-enhanced Raman scattering. *Chemical Society Reviews*, **27**(4), 241–250.
- Caswell, K. K., Wilson, James N., Bunz, Uwe H. F., & Murphy, Catherine J. 2003. Preferential End-to-End Assembly of Gold Nanorods by Biotin-Streptavidin Connectors. *Journal of the American Chemical Society*, **125**(46), 13914–13915.
- Chen, A., & Moy, V. T. 2000. Cross-linking of cell surface receptors enhances cooperativity of molecular adhesion. *Biophysical Journal*, **78**(6), 2814–2820.
- CRC. 2004. *CRC Handbook of Chemistry and Physics*. CRC Press.
- Deschenes, L. A., & Vanden Bout, D. A. 2001. Single-molecule studies of heterogeneous dynamics in polymer melts near the glass transition (Retracted article. See vol 312, pg 195, 2006). *Science*, **292**(5515), 255–258.
- Devanand, K., & Selser, J. C. 1991. Asymptotic-Behavior and Long-Range Interactions in Aqueous-Solutions of Poly(Ethylene Oxide). *Macromolecules*, **24**(22), 5943–5947.

- Diamandis, E. P., & Christopoulos, T. K. 1991. The Biotin (Strept)Avidin System - Principles and Applications in Biotechnology. *Clinical Chemistry*, **37**(5), 625–636.
- Draine. <http://arXiv.org>. <http://arXiv.org/abs/1002.1505v1>.
- El-Sayed, Mostafa A. 2001. Some Interesting Properties of Metals Confined in Time and Nanometer Space of Different Shapes. *Accounts of Chemical Research*, **34**(4), 257–264.
- Elghanian, R., Storhoff, J. J., Mucic, R. C., Letsinger, R. L., & Mirkin, C. A. 1997. Selective colorimetric detection of polynucleotides based on the distance-dependent optical properties of gold nanoparticles. *Science*, **277**(5329), 1078–1081.
- Encina, E. R., & Coronado, E. A. 2010. Plasmon Coupling in Silver Nanosphere Pairs. *Journal of Physical Chemistry C*, **114**(9), 3918–3923.
- Ensikat, Hans J., Schulte, Anna J., Koch, Kerstin, & Barthlott, Wilhelm. 2009. Droplets on Superhydrophobic Surfaces: Visualization of the Contact Area by Cryo-Scanning Electron Microscopy. *Langmuir*, **25**(22), 13077–13083.
- Eustis, Susie, & El-Sayed, Mostafa A. 2006. Why gold nanoparticles are more precious than pretty gold: Noble metal surface plasmon resonance and its enhancement of the radiative and nonradiative properties of nanocrystals of different shapes. *Chem. Soc. Rev.*, **35**(3), 209–217.
- Flügel, Dr. Sabine. 2010. *Oligodeoxynucleotide-Polypeptide Block Copolymers*. Ph.D. thesis, Johannes-Gutenberg-Universität Mainz.
- Frujtier-Polloth, C. 2005. Safety assessment on polyethylene glycols (PEGs) and their derivatives as used in cosmetic products. *Toxicology*, **214**(1-2), 1–38.
- Fultz, B., & Howe, J. M. 2001. *Transmission Electron Microscopy and Diffractometry of Materials*. Springer.
- Gamboa, C., Sepulveda, L., & Soto, R. 1981. Free-energies of Transfer of Anions From Water To Cationic Micelles From Ionic Exchange Measurements. *Journal of Physical Chemistry*, **85**(10), 1429–1434.
- Gao, Jinxin, Bender, Christopher M., & Murphy, Catherine J. 2003. Dependence of the Gold Nanorod Aspect Ratio on the Nature of the Directing Surfactant in Aqueous Solution. *Langmuir*, **19**(21), 9065–9070.
- Garg, N., Scholl, C., Mohanty, A., & Jin, R. C. 2010. The Role of Bromide Ions in Seeding Growth of Au Nanorods. *Langmuir*, **26**(12), 10271–10276.
- geogebra. www.geogebra.org.
- Ghosh, S., & Moss, D. B. 1974. Electroendosmosis Correction for Electrophoretic Mobility Determined in Gels. *Analytical Biochemistry*, **62**, 365–370.

REFERENCES

- Ghosh, S. K., & Pal, T. 2007. Interparticle coupling effect on the surface plasmon resonance of gold nanoparticles: From theory to applications. *Chemical Reviews*, **107**(11), 4797–4862.
- Gonzalez, M., Bagatolli, L. A., Echabe, I., Arrondo, J. L. R., Argarana, C. E., Cantor, C. R., & Fidelio, G. D. 1997. Interaction of biotin with streptavidin - Thermostability and conformational changes upon binding. *Journal of Biological Chemistry*, **272**(17), 11288–11294.
- Greenwald, R. B., Choe, Y. H., McGuire, J., & Conover, C. D. 2003. Effective drug delivery by PEGylated drug conjugates. *Advanced Drug Delivery Reviews*, **55**(2), 217–250.
- Gu, J. X., Xia, F., Wu, Y., Qu, X. Z., Yang, Z. Z., & Jiang, L. 2007. Programmable delivery of hydrophilic drug using dually responsive hydrogel cages. *Journal of Controlled Release*, **117**(3), 396–402.
- Hansen, W. R., & Autumn, K. 2005. Evidence for self-cleaning in gecko setae. *Proceedings of the National Academy of Sciences of the United States of America*, **102**(2), 385–389.
- Hecht, Eugene. 2009. *Optik*. Oldenbourg.
- Henkel, Andreas, Schubert, Olaf, Plech, Anton, & Sönnichsen, Carsten. 2009. Growth Kinetic of a Rod-Shaped Metal Nanocrystal. *The Journal of Physical Chemistry C*, **113**(24), 10390–10394.
- Heyes, C. D., Groll, J., Moller, M., & Nienhaus, G. U. 2007. Synthesis, patterning and applications of star-shaped poly(ethylene glycol) biofunctionalized surfaces. *Molecular Biosystems*, **3**(6), 419–430.
- Hirsch, L. R., Stafford, R. J., Bankson, J. A., Sershen, S. R., Rivera, B., Price, R. E., Hazle, J. D., Halas, N. J., & West, J. L. 2003. Nanoshell-mediated near-infrared thermal therapy of tumors under magnetic resonance guidance. *Proceedings of the National Academy of Sciences of the United States of America*, **100**(23), 13549–13554.
- Hodak, Jose H., Henglein, Arnim, Giersig, Michael, & Hartland, Gregory V. 2000. Laser-Induced Inter-Diffusion in AuAg Core-Shell Nanoparticles. *The Journal of Physical Chemistry B*, **104**(49), 11708–11718.
- Huang, F. M., & Baumberg, J. J. 2010. Actively Tuned Plasmons on Elastomerically Driven Au Nanoparticle Dimers. *Nano Letters*, **10**(5), 1787–1792.
- Huang, X. H., Neretina, S., & El-Sayed, M. A. 2009. Gold Nanorods: From Synthesis and Properties to Biological and Biomedical Applications. *Advanced Materials*, **21**(48), 4880–4910.
- Hubert, F., Testard, F., & Spalla, O. 2008. Cetyltrimethylammonium bromide silver bromide complex as the capping agent of gold nanorods. *Langmuir*, **24**(17), 9219–9222.
- Jain, P. K., & El-Sayed, M. A. 2008. Noble Metal Nanoparticle Pairs: Effect of Medium for Enhanced Nanosensing. *Nano Letters*, **8**(12), 4347–4352.

- Jain, P. K., & El-Sayed, M. A. 2010. Plasmonic coupling in noble metal nanostructures. *Chemical Physics Letters*, **487**(4-6), 153–164.
- Jain, Prashant K., Eustis, Susie, & El-Sayed, Mostafa A. 2006. Plasmon Coupling in Nanorod Assemblies: Optical Absorption, Discrete Dipole Approximation Simulation, and Exciton-Coupling Model. *The Journal of Physical Chemistry B*, **110**(37), 18243–18253.
- Jain, Prashant K., Huang, Wenyu, & El-Sayed, Mostafa A. 2007. On the Universal Scaling Behavior of the Distance Decay of Plasmon Coupling in Metal Nanoparticle Pairs: A Plasmon Ruler Equation. *Nano Letters*, **7**(7), 2080–2088.
- Jain, Prashant K., Huang, Xiaohua, El-Sayed, Ivan H., & El-Sayed, Mostafa A. 2008. Noble Metals on the Nanoscale: Optical and Photothermal Properties and Some Applications in Imaging, Sensing, Biology, and Medicine. *Accounts of Chemical Research*, **41**(12), 1578–1586.
- Jana, Nikhil R., Gearheart, Latha, & Murphy, Catherine J. 2001. Wet Chemical Synthesis of High Aspect Ratio Cylindrical Gold Nanorods. *The Journal of Physical Chemistry B*, **105**(19), 4065–4067.
- Jares-Erijman, E. A., & Jovin, T. M. 2003. FRET imaging. *Nature Biotechnology*, **21**(11), 1387–1395.
- Johnson, C. J., Dujardin, E., Davis, S. A., Murphy, C. J., & Mann, S. 2002. Growth and form of gold nanorods prepared by seed-mediated, surfactant-directed synthesis. *Journal of Materials Chemistry*, **12**(6), 1765–1770.
- Johnson, P. B., & Christy, R. W. 1972. Optical-Constants Of Noble-Metals. *Physical Review B*, **6**(12), 4370–4379.
- Khan, M. S. 2006. Aggregate formation in poly(ethylene oxide) solutions. *Journal of Applied Polymer Science*, **102**(3), 2578–2583.
- Kim, Franklin, Song, Jae Hee, & Yang, Peidong. 2002. Photochemical Synthesis of Gold Nanorods. *Journal of the American Chemical Society*, **124**(48), 14316–14317.
- Kimling, J., Maier, M., Okenve, B., Kotaidis, V., Ballot, H., & Plech, A. 2006. Turkevich method for gold nanoparticle synthesis revisited. *Journal of Physical Chemistry B*, **110**(32), 15700–15707.
- Kneipp, Katrin, Wang, Yang, Kneipp, Harald, Perelman, Lev T., Itzkan, Irving, Dasari, Ramachandra R., & Feld, Michael S. 1997. Single Molecule Detection Using Surface-Enhanced Raman Scattering (SERS). *Phys. Rev. Lett.*, **78**(9), 1667–1670.
- Laverman, P., Boerman, O. C., Oyen, W. J. G., Corstens, F. H. M., & Storm, G. 2001. In vivo applications of PEG liposomes: Unexpected observations. *Critical Reviews in Therapeutic Drug Carrier Systems*, **18**(6), 551–566.

REFERENCES

- Lee, H., Habas, S. E., Kwekin, S., Butcher, D., Somorjai, G. A., & Yang, P. 2006. Morphological Control of Catalytically Active Platinum Nanocrystals. *Angewandte Chemie International Edition*, **45**(46), 7824–7828.
- Link, S., & El-Sayed, M. A. 2005. Simulation of the Optical Absorption Spectra of Gold Nanorods as a Function of Their Aspect Ratio and the Effect of the Medium Dielectric Constant. *The Journal of Physical Chemistry B*, **109**(20), 10531–10532.
- Liu, & Guyot-Sionnest, Philippe. 2004. Synthesis and Optical Characterization of Au/Ag Core/Shell Nanorods. *The Journal of Physical Chemistry B*, **108**(19), 5882–5888.
- Liu, & Guyot-Sionnest, Philippe. 2005. Mechanism of Silver(I)-Assisted Growth of Gold Nanorods and Bipyramids. *The Journal of Physical Chemistry B*, **109**(47), 22192–22200.
- Liu, G. L., Yin, Y. D., Kunchakarra, S., Mukherjee, B., Gerion, D., Jett, S. D., Bear, D. G., Gray, J. W., Alivisatos, A. P., Lee, L. P., & Chen, F. Q. F. 2006. A nanoplasmonic molecular ruler for measuring nuclease activity and DNA footprinting. *Nature Nanotechnology*, **1**(1), 47–52.
- Liu, Jingyu, & Hurt, Robert H. 2010. Ion Release Kinetics and Particle Persistence in Aqueous Nano-Silver Colloids. *Environmental Science & Technology*, **44**(6), 2169–2175.
- Maier, S. A., Brongersma, M. L., Kik, P. G., Meltzer, S., Requicha, A. A. G., & Atwater, H. A. 2001. Plasmonics: A Route to Nanoscale Optical Devices. *Adv. Mater.*, **13**(19), 1501–1505.
- Maier, Stefan A. 2007. *Plasmonics Fundamentals and Applications*. Springer.
- Mandal, Madhuri, Ranjan Jana, Nikhil, Kundu, Subrata, Kumar Ghosh, Sujit, Panigrahi, Mru-ganka, & Pal, Tarasankar. 2004. Synthesis of Au-core-Ag-shell type bimetallic nanoparticles for single molecule detection in solution by SERS method. *Journal of Nanoparticle Research*, **6**, 53–61.
- McFarland, Adam D., & Van Duyne, Richard P. 2003. Single Silver Nanoparticles as Real-Time Optical Sensors with Zeptomole Sensitivity. *Nano Letters*, **3**(8), 1057–1062.
- Millstone, Jill E., Wei, Wei, Jones, Matthew R., Yoo, Hyojong, & Mirkin, Chad A. 2008. Iodide Ions Control Seed-Mediated Growth of Anisotropic Gold Nanoparticles. *Nano Letters*, **8**(8), 2526–2529.
- Mitra, S. K., Varshney, N. C., & Dass, N. 1972. Temperature Dependence of Refractive-index Water. *Journal of Chemical Physics*, **57**(4), 1798–&.
- Mock, Jack J., Smith, David R., & Schultz, Sheldon. 2003. Local Refractive Index Dependence of Plasmon Resonance Spectra from Individual Nanoparticles. *Nano Letters*, **3**(4), 485–491.
- Murphy, Catherine J., Sau, Tapan K., Gole, Anand M., Orendorff, Christopher J., Gao, Jinxin, Gou, Linfeng, Hunyadi, Simona E., & Li, Tan. 2005. Anisotropic Metal Nanoparticles: Synthesis, Assembly, and Optical Applications. *The Journal of Physical Chemistry B*, **109**(29), 13857–13870.

- Murray, C. B., Kagan, C. R., & Bawendi, M. G. 2000. Synthesis and characterization of monodisperse nanocrystals and close-packed nanocrystal assemblies. *Annual Review Of Materials Science*, **30**, 545–610.
- Myroshnychenko, Viktor, Rodriguez-Fernandez, Jessica, Pastoriza-Santos, Isabel, Funston, Alison M., Novo, Carolina, Mulvaney, Paul, Liz-Marzan, Luis M., & Garcia de Abajo, F. Javier. 2008. Modelling the optical response of gold nanoparticles. *Chem. Soc. Rev.*, **37**(9), 1792–1805.
- Nie, Shuming, & Emory, Steven R. 1997. Probing Single Molecules and Single Nanoparticles by Surface-Enhanced Raman Scattering. *Science*, **275**, 1102–1106.
- Nikoobakht, B., & El-Sayed, M. A. 2003. Preparation and growth mechanism of gold nanorods (NRs) using seed-mediated growth method. *Chemistry of Materials*, **15**(10), 1957–1962.
- Nikoobakht, B., Wang, Z. L., & El-Sayed, M. A. 2000. Self-Assembly of Gold Nanorods. *The Journal of Physical Chemistry B*, **104**(36), 8635–8640.
- Nordlander, P., Oubre, C., Prodan, E., Li, K., & Stockman, M. I. 2004. Plasmon Hybridization in Nanoparticle Dimers. *Nano Letters*, **4**(5), 899–903.
- of Oslo, University. www.iob.uio.no.
- Ono, Y., Kawasaki, H., Annaka, M., & Maeda, H. 2005. Effects of micelle-to-vesicle transitions on the degree of counterion binding. *Journal of Colloid and Interface Science*, **287**(2), 685–693.
- Orendorff, C. J., & Murphy, C. J. 2006. Quantitation of metal content in the silver-assisted growth of gold nanorods. *Journal of Physical Chemistry B*, **110**(9), 3990–3994.
- Otsuka, H., Nagasaki, Y., & Kataoka, K. 2003. PEGylated nanoparticles for biological and pharmaceutical applications. *Advanced Drug Delivery Reviews*, **55**(3), 403–419.
- Peng, Xiaogang, Wickham, J., & Alivisatos, A. P. 1998. Kinetics of II-VI and III-V Colloidal Semiconductor Nanocrystal Growth: Focusing of Size Distributions. *Journal of the American Chemical Society*, **120**(21), 5343–5344.
- Perez-Juste, J., Liz-Marzán, L., Carnie, S., Chan, D., & Mulvaney, P. 2004. Electric-Field-Directed Growth of Gold Nanorods in Aqueous Surfactant Solutions. *Adv. Funct. Mater.*, **14**(6), 571–579.
- Pierce. Pierce Protein Research Products. <http://www.piercenet.com/>.
- Pierrat, S., Hartinger, E., Faiss, S., Janshoff, A., & Sönnichsen, C. 2009. Rotational Dynamics of Laterally Frozen Nanoparticles Specifically Attached to Biomembranes. *Journal of Physical Chemistry C*, **113**(26), 11179–11183.
- Prescott, S. W., & Mulvaney, P. 2006. Gold nanorod extinction spectra. *Journal of Applied Physics*, **99**(12), 123504.

REFERENCES

- Pérez-Juste, Jorge, Pastoriza-Santos, Isabel, Liz-Marzán, Luis M., & Mulvaney, Paul. 2005. Gold nanorods: Synthesis, characterization and applications. *Coordination Chemistry Reviews*, **249**(17-18), 1870 – 1901.
- Quinten, M., Leitner, A., Krenn, J. R., & Aussenegg, F. R. 1998. Electromagnetic energy transport via linear chains of silver nanoparticles. *Opt. Lett.*, **23**(17), 1331–1333.
- Raschke, G., Kowarik, S., Franzl, T., Sönnichsen, C., Klar, T. A., Feldmann, J., Nichtl, A., & Kärzinger, K. 2003. Biomolecular Recognition Based on Single Gold Nanoparticle Light Scattering. *Nano Letters*, **3**(7), 935–938.
- Rayavarapu, Raja Gopal, Ungureanu, Constantin, Krystek, Petra, van Leeuwen, Ton. G., & Manohar, Srirang. 2010. Iodide Impurities in Hexadecyltrimethylammonium Bromide (CTAB) Products: Lot-Lot Variations and Influence on Gold Nanorod Synthesis. *Langmuir*, **26**(7), 5050–5055.
- Rechberger, W., Hohenau, A., Leitner, A., Krenn, J. R., Lamprecht, B., & Aussenegg, F. R. 2003. Optical properties of two interacting gold nanoparticles. *Optics Communications*, **220**(1-3), 137 – 141.
- Reinhard, B. M., Siu, M., Agarwal, H., Alivisatos, A. P., & Liphardt, J. 2005. Calibration of dynamic molecular ruler based on plasmon coupling between gold nanoparticles. *Nano Letters*, **5**(11), 2246–2252.
- Reinhard, B. M., Sheikholeslami, S., Mastroianni, A., Alivisatos, A. P., & Liphardt, J. 2007. Use of plasmon coupling to reveal the dynamics of DNA bending and cleavage by single EcoRV restriction enzymes. *Proceedings of the National Academy of Sciences of the United States of America*, **104**(8), 2667–2672.
- Reiss, H. 1951. The Growth of Uniform Colloidal Dispersions. *Journal of Chemical Physics*, **19**(4), 482–487.
- Robertson, J. L., & Roux, B. 2005. One channel: Open and closed. *Structure*, **13**(10), 1398–1400.
- Rong, G. X., Wang, H. Y., Skewis, L. R., & Reinhard, B. M. 2008. Resolving Sub-Diffraction Limit Encounters in Nanoparticle Tracking Using Live Cell Plasmon Coupling Microscopy. *Nano Letters*, **8**(10), 3386–3393.
- Ross, Benjamin M., Waldeisen, John R., Wang, Tim, & Lee, Luke P. 2009. Strategies for nanoplasmonic core-satellite biomolecular sensors: Theory-based Design. *Applied Physics Letters*, **95**(19), 193112.
- Sanchez, A., Abbet, S., Heiz, U., Schneider, W.-D., Hakkinen, H., Barnett, R. N., & Landman, Uzi. 1999. When Gold Is Not Noble: Nanoscale Gold Catalysts. *The Journal of Physical Chemistry A*, **103**(48), 9573–9578.
- Schärtl, Wolfgang. 2007. *Light Scattering from Polymer Solutions and Nanoparticle Dispersions*. Springer.

- Schultz, Sheldon, Smith, David R., Mock, Jack J., & Schultz, David A. 2000. Single-target molecule detection with nonbleaching multicolor optical immunolabels. *Proceedings of the National Academy of Sciences of the United States of America*, **97**(3), 996–1001.
- Sebba, D., LaBean, T., & Lazarides, A. 2008a. Plasmon coupling in binary metal core-satellite assemblies. *Applied Physics B: Lasers and Optics*, **93**, 69–78.
- Sebba, David S., Mock, Jack J., Smith, David R., LaBean, Thomas H., & Lazarides, Anne A. 2008b. Reconfigurable Core-Satellite Nanoassemblies as Molecularly-Driven Plasmonic Switches. *Nano Letters*, **8**(7), 1803–1808.
- Serwer, P. 1983. Agarose gels: Properties and use for electrophoresis. *Electrophoresis*, **4**(6), 375–382.
- Serwer, P., & Hayes, S. J. 1982. Agarose gel electrophoresis of bacteriophages and related particles. II. Correction of electrophoretic mobilities for the electro-osmosis of agarose. *Electrophoresis*, **3**(2), 80–85.
- Seyed-Razavi, Alireza, Snook, Ian K., & Barnard, Amanda S. 2011. Surface Area Limited Model for Predicting Anisotropic Coarsening of Faceted Nanoparticles. *Crystal Growth & Design*, **11**(1), 158–165.
- Sheikholeslami, Sassan, Jun, Young-wook, Jain, Prashant K., & Alivisatos, A. Paul. 2010. Coupling of Optical Resonances in a Compositionally Asymmetric Plasmonic Nanoparticle Dimer. *Nano Letters*.
- Sönnichsen, C., & Alivisatos, A. P. 2005. Gold nanorods as novel nonbleaching plasmon-based orientation sensors for polarized single-particle microscopy. *Nano Letters*, **5**(2), 301–304.
- Sönnichsen, C., Franzl, T., Wilk, T., von Plessen, G., Feldmann, J., Wilson, O., & Mulvaney, P. 2002. Drastic reduction of plasmon damping in gold nanorods. *Physical Review Letters*, **88**(7).
- Sönnichsen, C., Reinhard, B. M., Liphardt, J., & Alivisatos, A. P. 2005. A molecular ruler based on plasmon coupling of single gold and silver nanoparticles. *Nature Biotechnology*, **23**(6), 741–745.
- Sönnichsen, Dr. Carsten. 2001. *Plasmons in metal nanostructures*. Ph.D. thesis, University of Munich.
- Song, J. H., Kim, F., Kim, D., & Yang, P. D. 2005. Crystal overgrowth on gold nanorods: Tuning the shape, facet, aspect ratio, and composition of the nanorods. *Chemistry-a European Journal*, **11**(3), 910–916.
- Su, K.-H., Wei, Q.-H., Zhang, X., Mock, J. J., Smith, D. R., & Schultz, S. 2003. Interparticle Coupling Effects on Plasmon Resonances of Nanogold Particles. *Nano Letters*, **3**(8), 1087–1090.

REFERENCES

- Tamburro, A. M., Guantieri, V., Pandolfo, L., & Scopa, A. 1990. Synthetic Fragments and Analogs of Elastin .2. Conformational Studies. *Biopolymers*, **29**(4-5), 855–870.
- Tietz, Dietmar. 1987. Gel Electrophoresis of Intact Subcellular Particles. *Journal of Chromatography*, **418**, 305–344.
- Tomalia, D. A., Naylor, A. M., & Goddard, W. A. 1990. Starburst Dendrimers - Molecular-level Control of Size, Shape, Surface-chemistry, Topology, and Flexibility From Atoms To Macroscopic Matter. *Angewandte Chemie-international Edition In English*, **29**(2), 138–175.
- Tong, Wei, Zheng, Qing, Shao, Shuang, Lei, Qunfang, & Fang, Wenjun. 2010. Critical Micellar Concentrations of Quaternary Ammonium Surfactants with Hydroxyethyl Substituents on Headgroups Determined by Isothermal Titration Calorimetry. *Journal of Chemical & Engineering Data*, **55**(9), 3766–3771.
- Tsuji, Masaharu, Miyamae, Nobuhiro, Lim, Seongyop, Kimura, Kousuke, Zhang, Xu, Hikino, Sachie, & Nishio, Michiko. 2006. Crystal Structures and Growth Mechanisms of Au@Ag Core-Shell Nanoparticles Prepared by the Microwave-Polyol Method. *Crystal Growth & Design*, **6**(8), 1801–1807.
- Turkevich, J., Stevenson, P. C., & Hillier, J. 1951. A Study of the Nucleation and Growth Processes In the Synthesis of Colloidal Gold. *Discussions of the Faraday Society*, 55–&.
- Uji-i, H., Melnikov, S. M., Deres, A., Bergamini, G., De Schryver, F., Herrmann, A., Mullen, K., Enderlein, J., & Hofkens, J. 2006. Visualizing spatial and temporal heterogeneity of single molecule rotational diffusion in a glassy polymer by defocused wide-field imaging. *Polymer*, **47**(7), 2511–2518.
- Urry, D. W., & Parker, T. M. 2002. Mechanics of elastin: molecular mechanism of biological elasticity and its relationship to contraction. *Journal of Muscle Research and Cell Motility*, **23**(5-6), 543–559.
- Usher, A., McPhail, D. C., & Brugger, J. 2009. A spectrophotometric study of aqueous Au(III) halide-hydroxide complexes at 25-80 degrees C. *Geochimica Et Cosmochimica Acta*, **73**(11), 3359–3380.
- van Stam, Jan, Depaemelaere, Sigrid, & De Schryver, Frans C. 1998. Micellar Aggregation Numbers - A Fluorescence Study. *Journal of Chemical Education*, **75**(1), 93.
- Viovy, J. L. 2000. Electrophoresis of DNA and other polyelectrolytes: Physical mechanisms. *Reviews of Modern Physics*, **72**(3), 813–872.
- Waner, Mark J., Navrotskaya, Irina, Bain, Amanda, Oldham, Edward Davis, & Mascotti, David P. 2004. Thermal and Sodium Dodecylsulfate Induced Transitions of Streptavidin. *Biophysical Journal*, **87**(4), 2701–2713.
- Wang, S. G., Tian, E. K., & Lung, C. W. 2000. Surface energy of arbitrary crystal plane of bcc and fcc metals. *Journal of Physics and Chemistry of Solids*, **61**(8), 1295 – 1300.

- Wang, Xuan, Zhang, Zhenyuan, & Hartland, Gregory V. 2005. Electronic Dephasing in Bimetallic Gold-Silver Nanoparticles Examined by Single Particle Spectroscopy. *The Journal of Physical Chemistry B*, **109**(43), 20324–20330.
- Wang, Z. L., Mohamed, M. B., Link, S., & El-Sayed, M. A. 1999. Crystallographic facets and shapes of gold nanorods of different aspect ratios. *Surface Science*, **440**(1-2), L809 – L814.
- Wei, C. Y. J., Lu, C. Y., Kim, Y. H., & Bout, D. A. V. 2007. Determining if a system is heterogeneous: The analysis of single molecule rotational correlation functions and their limitations. *Journal of Fluorescence*, **17**(6), 797–804.
- Wei, Chia-Yin J., Kim, Yeon Ho, Darst, Richard K., Rossky, Peter J., & Vanden Bout, David A. 2005. Origins of Nonexponential Decay in Single Molecule Measurements of Rotational Dynamics. *Phys. Rev. Lett.*, **95**(17), 173001.
- Wong, J., Chilkoti, A., & Moy, V. T. 1999. Direct force measurements of the streptavidin-biotin interaction. *Biomolecular Engineering*, **16**(1-4), 45–55.
- Wu, Hsiang-Yang, Chu, Hsin-Cheng, Kuo, Tz-Jun, Kuo, Chi-Liang, & Huang, Michael H. 2005. Seed-Mediated Synthesis of High Aspect Ratio Gold Nanorods with Nitric Acid. *Chemistry of Materials*, **17**(25), 6447–6451.
- Wu, S. C., & Wong, S. L. 2005. Engineering soluble monomeric streptavidin with reversible biotin binding capability. *Journal of Biological Chemistry*, **280**(24), 23225–23231.
- Xia, F., Zuo, X. L., Yang, R. Q., Xiao, Y., Kang, D., Vallee-Belisle, A., Gong, X., Yuen, J. D., Hsu, B. B. Y., Heeger, A. J., & Plaxco, K. W. 2010. Colorimetric detection of DNA, small molecules, proteins, and ions using unmodified gold nanoparticles and conjugated polyelectrolytes. *Proceedings of the National Academy of Sciences of the United States of America*, **107**(24), 10837–10841.
- Ye, J., Bonroy, K., Nelis, D., Frederix, F., D’Haen, J., Maes, G., & Borghs, G. 2008. Enhanced localized surface plasmon resonance sensing on three-dimensional gold nanoparticles assemblies. *Colloids and Surfaces A-physicochemical and Engineering Aspects*, **321**(1-3), 313–317.
- Yin, Y., & Alivisatos, A. P. 2005. Colloidal nanocrystal synthesis and the organic-inorganic interface. *Nature*, **437**, 664–670.
- Ylikotila, J., Valimaa, L., Takalo, H., & Pettersson, K. 2009. Improved surface stability and biotin binding properties of streptavidin coating on polystyrene. *Colloids and Surfaces B-biointerfaces*, **70**(2), 271–277.
- Yu, Chang, Ser-Sing, Lee, Chien-Liang, & Wang, C. R. Chris. 1997. Gold Nanorods: Electrochemical Synthesis and Optical Properties. *The Journal of Physical Chemistry B*, **101**(34), 6661–6664.

REFERENCES

- Zanchet, D., Micheel, C.M., Parak, W.J., Gerion, D., & Alivisatos, A.P. 2001. Electrophoretic Isolation of Discrete Au Nanocrystal/DNA Conjugates. *Nano Lett.*, **1**(1), 32–35.
- Zanchet, D., Micheel, C.M., Parak, W.J., Gerion, D., Williams, S.C., & Alivisatos, A.P. 2002. Electrophoretic and Structural Studies of DNA-Directed Au Nanoparticle Groupings. *J. Phys. Chem. B*, **106**(45), 11758–11763.
- Zhang, Yawen, Grass, Michael E., Kuhn, John N., Tao, Feng, Habas, Susan E., Huang, Wenyu, Yang, Peidong, & Somorjai, Gabor A. 2008. Highly Selective Synthesis of Catalytically Active Monodisperse Rhodium Nanocubes. *Journal of the American Chemical Society*, **130**(18), 5868–5869.
- Zhao, J., Pinchuk, A. O., McMahon, J. M., Li, S. Z., Ausman, L. K., Atkinson, A. L., & Schatz, G. C. 2008. Methods for Describing the Electromagnetic Properties of Silver and Gold Nanoparticles. *Accounts of Chemical Research*, **41**(12), 1710–1720.
- Zijlstra, Peter, Bullen, Craig, Chon, James W. M., & Gu, Min. 2006. High-Temperature Seedless Synthesis of Gold Nanorods. *The Journal of Physical Chemistry B*, **110**(39), 19315–19318.

Acknowledgement

Curriculum Vitae

University and Highschool Education

| | |
|-----------------|--|
| 01/2007-present | Doctoral Studies in the Nanobiotechnology group (Prof. Dr. Carsten Sönnichsen) at the Institute of Physical Chemistry, Johannes-Gutenberg-University Mainz |
| 09/2007 | Diploma in chemistry (1.0), Johannes-Gutenberg-University, Mainz, thesis entitled “Optimizing Gold Nanoparticles for their Use as Sensors in Biological Systems” |
| 09/2005-06/2006 | Exchange semester at the University of Toronto, Canada, Group of Prof. Dr. Geoff Ozin |
| 10/2004 | “Vordiplom” in chemistry (intermediate diploma, 1.2) |
| 06/2002 | “Abitur” (1.2), Carl-von-Ossietzky Schule Wiesbaden, major courses: mathematics and chemistry |

Scholarships

| | |
|-----------------|--|
| 10/2007-10/2010 | PhD-Scholarship of the Graduate School of Excellence, MAINZ |
| 04/2007-09/2007 | Diploma-Scholarship of the Johannes-Gutenberg-University, Mainz |
| 09/2005-02/2006 | DAAD (German Academic Exchange Program) scholarship |
| 10/2002-06/2004 | Undergraduate-Studies-Scholarship of the “Fond der Chemischen Industrie” |

Awards and Certificates

| | |
|------|--|
| 2010 | Soft-Skill Certificate of the Johannes-Gutenberg-University, Mainz |
| 2007 | Poster prize at the MWFZ annual meeting Adolf-Todt Prize for excellent studies |
| 2002 | Second round of the county youth competition in chemistry Third place national youth competition in mathematics |

Publications

“LbL multilayer capsules: recent progress and future outlook for their use in life sciences”

L. del Mercato, P. Rivera-Gil, A.Z. Abbasi, M. Ochs, C. Ganas, I. Zins, C. Sönnichsen, W. Parak
Nanoscale, 2010, Vol. 2, Pages 458-467

“Quantitative optical trapping of single gold nanorods”

C. Selhuber-Unkel, I. Zins, O. Schubert, C. Sönnichsen, L.B. Oddershede
Nano Letters, 2008, Vol. 8, Pages 2998-3003

“Mapping the polarization pattern of plasmon modes reveals nanoparticle symmetry”

O. Schubert, J. Becker, L. Carbone, Y. Khalavka, T. Provalska, I. Zins, c. Sönnichsen
Nano Letters, 2008, Vol. 8, Pages 2345-2350

“Plasmonic focusing reduces ensemble linewidth of silver-coated gold nanorods”

J. Becker, I. Zins, A. Jakob, Y. Khalavka, O. Schubert, C. Sönnichsen
Nano Letters, 2008, Vol. 8, Pages 1719-1723

“Separation of nanoparticles by gel electrophoresis according to size-and shape”

M. Hanauer, S. Pierrat, I. Zins, A. Lotz, C. Sönnichsen
Nano Letters, 2007, Vol. 7, Pages 2881-2885

“Self-assembly of small gold colloids with functionalized gold nanorods”

S. Pierrat, I. Zins, A. Breivogel, C. Sönnichsen
Nano Letters, 2007, Vol. 7, Pages 259-263